FEDERAL UNIVERSITY OF AMAZONAS (UFAM)
INSTITUTE OF EXACT SCIENCES (ICE)
GRADUATE PROGRAM IN PHYSICS (PPGFIS)

JARDSON BRAZ DA SILVA

Structural, Thermal, and Electrical Properties of POMA Composites with Li-Doped Sodium Titanate and Mg/Sr-Codoped LLZO

Manaus-AM
2026

JARDSON BRAZ DA SILVA

Structural, Thermal, and Electrical Properties of POMA Composites with Li-Doped Sodium Titanate and Mg/Sr-Codoped LLZO

Thesis submitted to the Graduate Program in Physics, Federal University of Amazonas, in partial fulfillment of the requirements for the degree of Doctor in Physics.

Advisor: Prof. Dr. Yurimiler Leyet Ruiz

Manaus-AM

2026

Ficha Catalográfica

Elaborada automaticamente de acordo com os dados fornecidos pelo(a) autor(a).

S586s Silva, Jardson Braz da

Structural, thermal, and electrical properties of POMA composites with Li-doped sodium titanate and Mg/Sr-codoped LLZO / Jardson Braz da Silva. - 2026.

193 f. : il., color. ; 31 cm.

Orientador(a): Yurimiler Leyet Ruiz .

Tese (doutorado) - Universidade Federal do Amazonas, Programa de Pós-Graduação em Física, Manaus (AM), 2026.

1. Solid-state electrolytes. 2. Ceramic–polymer composites. 3. Poly(omethoxyaniline). 4. Lithium-doped sodium titanate. 5. Garnet-type LLZO. I. Ruiz, Yurimiler Leyet. II. Universidade Federal do Amazonas. Programa de Pós-Graduação em Física. III. Título

---

Structural, Thermal, and Electrical Properties of POMA Composites with Li-Doped Sodium Titanate and Mg/Sr-Codoped LLZO

JARDSON BRAZ DA SILVA

Thesis submitted to the Graduate Program in Physics, Federal University of Amazonas, in partial fulfillment of the requirements for the degree of Doctor in Physics.

Approved by:

Prof. Dr. Yurimiler Leyet Ruiz
Advisor (PPGFIS/UFAM)

Prof. Dr. Fidel Guerrero Zayas
Committee Member (PPGFIS/UFAM)

Prof. Dr. Henrique Duarte da Fonseca Filho
Committee Member (PPGFIS/UFAM)

Prof.Dr. Michel Venet Zambrano
Committee Member (UFSCAR)

Dr. Ramon Raudel Peña Garcia
Committee Member (UFRP)

Manaus-AM, 28 de agosto de 2026.

To the memory of Professor José Wilson,
who taught me that generosity is
the greatest quality of an educator.

ACKNOWLEDGEMENTS

I would like to express my sincere gratitude to my supervisor, Professor Yurimiler Leyet Ruiz, for his trust, constant availability, and dedication throughout this research.

To my partner, Nadia Rio, for her patience, understanding, and unwavering support. To my parents, Anastácio Passos and Antonia Braz, for their encouragement, invaluable teachings, and unconditional support throughout my life.

I am grateful to the professors of the Graduate Program in Physics at the Federal University of Amazonas for their teachings, academic contributions, and commitment to the education of researchers. I would especially like to thank Angsula Ghosh, Fidel Guerrero Zayas, Henrique Fonseca, Puspitapallab Chaudhuri, Hidembergue Frota, Edgar Sanches, and Daniela Trichês, with whom I had the pleasure of taking courses during my doctoral studies.

I also thank my colleagues from the Graduate Program and my friends at the Laboratory for the Processing of Technological Materials (LPMAT) for their companionship, discussions, exchange of experiences, and support. In particular, I would like to thank Yan Pinto, Juliana Pereira, Lianet Dominguez, José Milério, Rodrigo Lavareda, Salomão Costa, Carlos Batista, José Gamboa, Hamdan Danamah, Victoria Lira, Letícia Alves, Marcos Colares, Ruan Raposo, Sávio Bentes, Ariel Delgado, Eliezer Costa, Ana Carolina, Raphaella Cabral, Edézio Júnior, Thomás Correa, Jamilton Boaes, Luã Catique, Vitor Brasil, Clilton Vasconcelos, and everyone else who shared this journey with me.

I gratefully acknowledge the Federal University of Amazonas, the Graduate Program in Physics, the institutions and laboratories that contributed to the experimental characterizations, and the professionals who provided technical support throughout this work.

I also acknowledge the financial support provided by CAPES, CNPq, and FAPEAM.

Finally, I express my sincere gratitude to everyone who contributed to the completion of this thesis.

RESUMO

Esta tese investiga a influência da poli(o-metoxianilina) dopada com HCl (POMA) sobre a estrutura, a morfologia, a estabilidade térmica e a resposta elétrica de dois sistemas cerâmica–polímero: titanato de sódio nominalmente dopado com 3 mol% de Li (NLTO/POMA) e $Li_{6.95}Mg_{0.15}La_{2.75}Sr_{0.25}Zr_2O_{12}$ (LLZO/POMA). Os materiais foram analisados por difração de raios X com refinamento de Rietveld, espectroscopia FTIR, microscopia eletrônica de varredura, análises TG/DTG/DSC e espectroscopia de impedância. No sistema NLTO/POMA, a adição de polímero foi acompanhada pela redução relativa da fase cristalina $Na_2Ti_3O_7$ e pelo aparecimento de $H_2Ti_3O_7$ e NaCl nas composições com maior teor de POMA, o que é compatível com reações de troca iônica e com a química do polímero protonado. No sistema LLZO/POMA, a fase cúbica do LLZO permaneceu entre as fases cristalinas majoritárias, mas coexistiu com a fase tetragonal do LLZO e com quantidades relevantes de Li_2CO_3 e LiOH, evidenciando degradação superficial durante o processamento e a exposição ao ambiente. A espectroscopia FTIR confirmou as características vibracionais dos constituintes dos compósitos, enquanto as análises térmicas indicaram estabilidade relativa acima das temperaturas usuais de operação de baterias de estado sólido, com perdas de massa mais significativas acima de $200\,^{\circ}$C. Para NLTO/POMA-50, a condutividade elétrica total atingiu aproximadamente $9{,}75 \times 10^{-7}$ S·cm^{-1} à temperatura ambiente. Para LLZO/POMA-15, a condutividade elétrica total atingiu aproximadamente $1{,}89 \times 10^{-7}$ S·cm^{-1} à temperatura ambiente. Em ambos os casos, houve um aumento de cerca de duas ordens de grandeza em relação à amostra puramente cerâmica. Em ambos os compósitos, os tempos de relaxação diminuíram com a adição de POMA, indicando maior mobilidade dos portadores de carga. A condutividade também apresentou comportamento compatível com o modelo de percolação adotado, sugerindo a formação de caminhos condutivos com a incorporação do polímero. Como os experimentos não separaram as contribuições iônica e eletrônica, o aumento observado é atribuído à condutividade elétrica total, sem identificação conclusiva do portador dominante. Os resultados estabelecem correlações entre composição, evolução estrutural e resposta elétrica, e indicam a necessidade de medidas de número de transporte, estabilidade eletroquímica e desempenho em célula para avaliar esses materiais como eletrólitos sólidos.

Palavras-chave: Eletrólitos sólidos, Compósitos cerâmica–polímero, Poli(o-metoxianilina), Titanato de sódio dopado com lítio, LLZO do tipo granada.

ABSTRACT

This thesis investigates the influence of HCl-doped poly(o-methoxyaniline) (POMA) on the structure, morphology, thermal stability, and electrical response of two ceramic–polymer systems: nominally 3 mol% Li-doped sodium titanate (NLTO/POMA) and $Li_{6.95}Mg_{0.15}La_{2.75}Sr_{0.25}Zr_2O_{12}$ (LLZO/POMA). The materials were examined by X-ray diffraction with Rietveld refinement, FTIR spectroscopy, scanning electron microscopy, TG/DTG/DSC, and impedance spectroscopy. In the NLTO/POMA system, polymer addition was accompanied by a relative decrease in crystalline $Na_2Ti_3O_7$ and by the appearance of $H_2Ti_3O_7$ and NaCl at higher POMA contents, consistent with ion-exchange reactions and the chemistry of the protonated polymer. In the LLZO/POMA system, cubic LLZO remained among the major crystalline phases but coexisted with tetragonal LLZO and substantial amounts of Li_2CO_3 and LiOH, revealing surface degradation during processing and ambient exposure. Fourier-transform infrared spectroscopy confirmed the presence of the characteristic vibrational features of the materials in the composites, while thermal analyses showed relative stability of the systems at temperatures above the typical operating conditions of solid-state batteries, with the most significant mass losses occurring above $200\,^{\circ}$C. NLTO/POMA-50 reached a total electrical conductivity of approximately 9.75×10^{-7} S·cm^{-1} at room temperature. LLZO/POMA-15 reached a total electrical conductivity of approximately 1.89×10^{-7} S·cm^{-1} at room temperature. In both cases, an increase of approximately two orders of magnitude was observed compared with the corresponding pure ceramic sample. In both composites, the relaxation times decreased with increasing POMA content, which may be interpreted as an improvement in charge-carrier mobility. In addition, the conductivity behavior showed strong agreement with the adopted percolation model, suggesting that the conductivity enhancement occurs through percolation pathways formed with polymer incorporation. Because the experiments did not separate ionic and electronic contributions, the observed enhancement is assigned to the total electrical conductivity of the composites without conclusively identifying the dominant carrier. The results establish correlations among composition, structural evolution, and electrical response, while showing that transference-number, electrochemical-stability, and full-cell measurements are required before these materials can be assessed as solid electrolytes.

Keywords: Solid-state electrolytes, Ceramic–polymer composites, Poly(o-methoxyaniline), Lithium-doped sodium titanate, Garnet-type LLZO.

LIST OF FIGURES

Figure 1 Schematic representation of a lithium-ion battery during (a) charging and (b) discharging. During charging, Li^+ ions migrate from the cathode to the graphite anode through the liquid electrolyte, while electrons are supplied through the external circuit. During discharging, Li^+ ions migrate from the anode to the cathode, while electrons flow through the external circuit, supplying electrical energy. 28

Figure 2 Schematic representation of solid-electrolyte types and the main challenges associated with their application in solid-state batteries. . . 29

Figure 3 Crystal structures of (a) $Na_2Ti_3O_7$, (b) $Na_2Ti_6O_{13}$, and (c) $NaLiTi_3O_7$. Ti, O, Na, and Li atoms are represented in blue, red, yellow, and green, respectively. 30

Figure 4 Crystal structures: (a) cubic LLZO, (b) tetragonal LLZO. Color code: O (red), Zr (green), La (blue), Li (white). 31

Figure 5 Chemical structures of the conducting polymer and its precursor: (a) polyaniline (PANI); (b) poly(*o*-methoxyaniline) (POMA); and (c) the *o*-anisidine monomer. 32

Figure 6 Schematic representation of protonation and charge transport by polaron migration in POMA. 33

Figure 7 Schematic representation of the connectivity patterns for two-phase composites according to the m–n classification, where m and n represent the dimensional connectivity of each constituent phase. 34

Figure 8 Schematic illustration of the sonochemical synthesis process, showing acoustic cavitation, bubble collapse, and the subsequent nucleation and growth of ceramic particles. 35

Figure 9 Schematic illustration of the high-energy ball milling process. . . . 36

Figure 10 Schematic illustration of the oxidative polymerization process, highlighting the oxidation, coupling, propagation, and protonation stages that lead to the formation of an electrically conductive polymer. 37

Figure 11 Schematic illustration of X-ray powder diffraction (a), the Bragg diffraction condition (b), ICSD reference diffraction pattern of $Na_2Ti_3O_7$ 39

Figure 12 Schematic illustration of the operating principles of SEM and EDS. 42

Figure 13 Schematic representation of the thermal characterization techniques: (a) thermogravimetric analysis (TG), (b) derivative thermogravimetry (DTG), and (c) differential scanning calorimetry (DSC). . 44

Figure 14 Equivalent parallel RC circuit and the corresponding ideal Nyquist plot, illustrating the frequency dependence of the complex impedance. 46

Figure 15 Representative Nyquist plots for different ideal electrical elements and equivalent circuits commonly used in impedance spectroscopy. . . 47

Figure 16 Relationship between the polycrystalline microstructure, the idealized grain-and-grain-boundary model, the equivalent electrical circuit, and the corresponding Nyquist impedance response. 48

Figure 17 Experimental X-ray diffraction patterns of NLTO and NLTO/POMA composites. 62

Figure 18 Crystal structures of the phases identified by Rietveld refinement. . 64

Figure 19 Rietveld refinement profiles of (a) NLTO, (b) NLTO/POMA-10, (c) NLTO/POMA-15, (d) NLTO/POMA-35, and (e) NLTO/POMA-50. (f) Le Bail refinement profile of HCl-doped POMA. 66

Figure 20 SEM micrographs of (a) NLTO, (b) NLTO/POMA-10, (c) NLTO/POMA-15, (d) NLTO/POMA-35, (e) NLTO/POMA-50, and (f) HCl-doped POMA. 71

Figure 21 FTIR spectra of NLTO, NLTO/POMA composites, and POMA. . . 72

Figure 22 Thermogravimetric analysis of NLTO and NLTO/POMA composites: (a) TG curves and (b) DTG curves. 75

Figure 23 DSC thermograms recorded in the high-temperature region for: (a) NLTO, (b) NLTO/POMA-10, (c) NLTO/POMA-15, (d) NLTO/POMA-35, (e) NLTO/POMA-50, and (f) HCl-doped POMA. 77

Figure 24 (a) Nyquist plots of NLTO and NLTO/POMA composites with equivalent-circuit fitting (inset). (b) The real part of the impedance (Z') fitted with the modified Debye model. 80

Figure 25 Frequency dependence of (a) the imaginary part of the impedance (Z''), (b) dielectric loss ($\tan\delta$) for NLTO and NLTO/POMA composites, and (c) AC conductivity as a function of frequency fitted using Jonscher's law. 84

Figure 26 X-ray diffraction patterns of LLZO and LLZO/POMA composites. Miller indices: cubic LLZO (black), tetragonal LLZO (green), Li_2CO_3 (blue), and LiOH (yellow). 88

Figure 27 Crystal structures of (a) cubic LLZO, (b) tetragonal LLZO, (c) Li_2CO_3, and (d) LiOH. Color code: O (red), Zr (green), La (blue), Li (white), and C (black). 90

Figure 28 Rietveld refinements of (a) LLZO, (b) LLZO/POMA-1, (c) LLZO/POMA-5, (d) LLZO/POMA-10, (e) LLZO/POMA-15, and Le Bail refinement of (f) POMA. 92

Figure 29 SEM micrographs of (a) LLZO, (b) LLZO/POMA-1, (c) LLZO/POMA-5, (d) LLZO/POMA-10, (e) LLZO/POMA-15, and (f) POMA. 96

Figure 30 EDS spectra of (a) LLZO, (b) LLZO/POMA-1, (c) LLZO/POMA-5, (d) LLZO/POMA-10, (e) LLZO/POMA-15, and (f) POMA. 97

Figure 31 FTIR spectra of LLZO, LLZO/POMA composites, and POMA. . . 98

Figure 32 Thermogravimetric analysis of LLZO, LLZO/POMA composites, and POMA: (a) TG curves and (b) DTG curves. 100

Figure 33 DSC thermograms for: (a) LLZO, (b) LLZO/POMA-1, (c) LLZO/POMA-5, (d) LLZO/POMA-10, (e) LLZO/POMA-15, and (f) POMA, recorded in the high-temperature region. 101

Figure 34 (a) Nyquist plots of LLZO, LLZO/POMA composites, and POMA with equivalent-circuit fitting (inset). (b) The real part of the impedance (Z') fitted with the modified Debye model. 103

Figure 35 Frequency dependence of (a) the imaginary part of the impedance (Z''), (b) dielectric loss ($\tan\delta$) for LLZO, LLZO/POMA composites, and POMA, and (c) AC conductivity as a function of frequency fitted using Jonscher's law. 107

LIST OF TABLES

Table 1 Comparison of previous studies and the scope of the present work. . 26

Table 2 Typical capacitance ranges associated with different electrical processes in impedance spectroscopy. 48

Table 3 Dielectric relaxation models and asymptotic behavior of the imaginary part of the complex permittivity. 51

Table 4 Refined lattice parameters of the crystalline phases identified in the NLTO/POMA composites. Samples are identified as follows: P10 = NLTO/POMA-10; P15 = NLTO/POMA-15; P35 = NLTO/POMA-35; and P50 = NLTO/POMA-50. 68

Table 5 Phase fractions and Rietveld refinement parameters for the NLTO/POMA composites, using the sample notation defined in Table 4. 68

Table 6 Average bond lengths (Å) for the crystalline titanate phases identified in the samples. 70

Table 7 Ti–O bond lengths, force constants, and local vibrational modes calculated using the local harmonic vibrational model for the Ti site with index 4 in the $Na_2Ti_3O_7$ phase. 74

Table 8 Equivalent-circuit parameters and goodness-of-fit indicators for the NLTO/POMA samples. 81

Table 9 Electrical conductivities derived from the equivalent-circuit fitting of the NLTO/POMA samples. 81

Table 10 Kramers–Kronig validation, information criteria, and residuals obtained from the comparison of alternative equivalent-circuit models for the NLTO/POMA samples, where 1A denotes the one-arc model, 2A the two-arc model, AC the arc + CPE tail model, and AW the arc + finite-length Warburg model. 82

Table 11 2×ZARC fit parameters from $Z'(f)$: for each sample the smaller resistance is labeled R_1 (with its corresponding τ_1 and n_1). Units: R in Ω, τ in s. Numbers in parentheses indicate the uncertainty in the last digit(s) of the mantissa. 83

Table 12 Jonscher fitting parameters for the NLTO/POMA system: σ_{DC}, A, and s. 86

Table 13 Refined lattice parameters of the crystalline phases identified in the LLZO/POMA composites. Samples are identified as follows: P1 = LLZO/POMA–1; P5 = LLZO/POMA–5; P10 = LLZO/POMA–10; and P15 = LLZO/POMA–15. 93

Table 14 Phase fractions and Rietveld refinement parameters for the LLZO/POMA composites, using the sample notation defined in Table 13. 94

Table 15 Average Li–O, La–O, and Zr–O bond lengths for the cubic phase of $Li_7La_3Zr_2O_{12}$, by VESTA from CIF files from Rietveld refinement of the XRD data. 96

Table 16 Equivalent-circuit parameters and goodness-of-fit indicators for the LLZO/POMA samples. 104

Table 17 Electrical conductivities derived from the equivalent-circuit fitting of the LLZO/POMA samples. 105

Table 18 Kramers–Kronig validation, information criteria, and residuals obtained from the comparison of alternative equivalent-circuit models for the LLZO/POMA samples, where 1A denotes the one-arc model, 2A the two-arc model, AC the arc + CPE tail model, and AW the arc + finite-length Warburg model. 106

Table 19 2×ZARC fit parameters from $Z'(f)$: for each sample the smaller resistance is labeled R_1 (with its corresponding τ_1 and n_1). Units: R in Ω, τ in s. Numbers in parentheses indicate the uncertainty in the last digit(s) of the mantissa. 106

Table 20 Jonscher fitting parameters for the LLZO/POMA system: σ_{DC}, A, and s. 109

Table 21 Experimental and GEM-calculated electrical conductivities for the NLTO/POMA and LLZO/POMA systems. 112

LIST OF ABBREVIATIONS AND ACRONYMS

AC	Alternating Current
AIC	Akaike Information Criterion
APS	Ammonium Persulfate
ASE	Atomic Simulation Environment
ATR	Attenuated Total Reflectance
BIC	Bayesian Information Criterion
BSE	Backscattered Electrons
CAPES	Coordenação de Aperfeiçoamento de Pessoal de Nível Superior (Brazilian Federal Agency for Support and Evaluation of Graduate Education)
CIF	Crystallographic Information File
CIS	Complex Impedance Spectroscopy
CNPq	Conselho Nacional de Desenvolvimento Científico e Tecnológico (National Council for Scientific and Technological Development)
COD	Crystallography Open Database
CPE	Constant Phase Element
DC	Direct Current
DRT	Distribution of Relaxation Times
DRX	X-ray Diffraction (Difração de Raios X)
DSC	Differential Scanning Calorimetry
DTG	Derivative Thermogravimetry
EDS	Energy-Dispersive X-ray Spectroscopy
EIS	Electrochemical Impedance Spectroscopy
FAPEAM	Fundação de Amparo à Pesquisa do Estado do Amazonas (Amazonas State Research Foundation)

FT	Faculdade de Tecnologia (Faculty of Technology)
FTIR	Fourier-Transform Infrared Spectroscopy
GEM	General Effective Medium
HF	High-Frequency
ICDD	International Centre for Diffraction Data
ICE	Instituto de Ciências Exatas (Institute of Exact Sciences)
ICSD	Inorganic Crystal Structure Database
LabSiNap	Laboratório de Sínteses de Nanoestruturas Aplicadas (Laboratory of Synthesis of Applied Nanostructures)
LabYM	Laboratório Yvonne Mascarenhas (Yvonne Mascarenhas Laboratory)
LATP	Lithium Aluminum Titanium Phosphate
LF	Low-Frequency
LFQM	Laboratório de Ensaios Físico-Químicos (Physicochemical Testing Laboratory)
LISICON	LIthium Super Ionic CONductor
LLZO	Lithium Lanthanum Zirconium Oxide ($Li_7La_3Zr_2O_{12}$)
LPMAT	Laboratório de Processamento de Materiais Tecnológicos (Technological Materials Processing Laboratory)
MEV	Scanning Electron Microscopy (Microscopia Eletrônica de Varredura)
NiCd	Nickel-Cadmium
NiMH	Nickel-Metal Hydride
Lin-KK	Linear Kramers–Kronig
NLLS	Nonlinear Least Squares
NLTO	Lithium-Doped Sodium Titanate
NTO	Sodium Titanate
OPD	Optical Path Difference
PANI	Polyaniline

PEO	Poly(ethylene oxide)
POMA	Poly(o-methoxyaniline)
PPGFIS	Programa de Pós-Graduação em Física (Graduate Program in Physics)
PVA	Poly(vinyl alcohol)
PVDF	Poly(vinylidene fluoride)
PVDF-HFP	Poly(vinylidene fluoride-co-hexafluoropropylene)
SE / SED	Secondary Electrons / Secondary Electron Detector
SEM	Scanning Electron Microscopy
SDD	Silicon Drift Detector
SSE	Solid-State Electrolyte
TG	Thermogravimetric Analysis
UFAM	Universidade Federal do Amazonas (Federal University of Amazonas)
UFRPE	Universidade Federal Rural de Pernambuco (Federal Rural University of Pernambuco)
VESTA	Visualization for Electronic and Structural Analysis
WRSS	Weighted Residual Sum of Squares
XRD	X-ray Diffraction
ZARC	Cole-Cole Equivalent Circuit Element (Z-Arc)

CONTENTS

1 Introduction **20**

1.1 Objectives 24

1.1.1 General Objective 24

1.1.2 Specific Objectives 24

2 Literature Review **25**

2.1 State of the Art 25

2.2 Theoretical Background 27

2.2.1 Solid-State Batteries 27

2.2.2 Sodium Titanates 29

2.2.3 Lithium Lanthanum Zirconium Oxide (LLZO) 31

2.2.4 Poly(o-methoxyaniline) (POMA) 32

2.2.5 Composites 34

2.2.6 Synthesis Techniques 35

2.2.6.1 Sonochemical Synthesis 35

2.2.6.2 High-energy ball milling 36

2.2.6.3 Oxidative Polymerization 37

2.2.7 Characterization Techniques 38

2.2.7.1 Structural, Morphological, and Optical Characterization 38

2.2.7.2 Thermal Characterization 43

2.2.7.3 Electrical Characterization 44

3 Materials and Methods **52**

3.1 Sodium Titanate-Based Materials 52
3.1.1 Synthesis of Lithium-Doped Sodium Titanate 52
3.1.2 Synthesis of Poly(*o*-methoxyaniline) (POMA) 53
3.1.3 Preparation of NLTO/POMA Composites 54
3.1.4 Characterization 54
3.2 LLZO-Based Materials 59
3.2.1 Synthesis of Doped LLZO 59
3.2.2 Preparation of LLZO/POMA Composites 60
3.2.3 Characterization 60

4 Results and Discussion **62**

4.1 Structural and Electrical Characterization of NLTO/POMA Composites 62
4.1.1 POMA-Induced Structural and Phase Evolution 62
4.1.2 POMA-Induced Morphological Evolution 71
4.1.3 Vibrational Modes and Chemical Bonding 72
4.1.4 Thermal Behavior and Stability 75
4.1.5 Electrical Response and Relaxation Processes 79
4.2 Structural and Electrical Characterization of Mg/Sr-Doped LLZO/POMA Composites 87
4.2.1 Crystal-Phase Evolution upon POMA Incorporation 87
4.2.2 Morphological Evolution upon POMA Incorporation 96
4.2.3 Vibrational Modes and Chemical Bonding 98
4.2.4 Thermal Behavior and Stability 99
4.2.5 Electrical Response and Relaxation Processes 102
4.3 Comparative Analysis of POMA-Induced Effects in NLTO- and LLZO-Based Composites 110

5 Final Considerations **113**

5.1 Conclusions 113

5.2 Suggestions for Future Work 114

References **115**

Annex A – Published Article — NLTO Composition Selection **128**

Annex B – Published Article — NLTO: Lithium Doping and Organic-Phase Effects **143**

Annex C – Published Article — LLZO/POMA Composite System **160**

Annex D – Published Article — Complementary Study on LLZO/POMA Composites **178**

1 INTRODUCTION

The global energy scenario has become an increasing concern in recent decades. Approximately 80% of the world's energy demand is still supplied by fossil fuels, contributing to the continuous rise in atmospheric CO_2 emissions. In 2020, the global average atmospheric CO_2 concentration reached 412.5 ppm, corresponding to an increase of approximately 50% compared with the pre-industrial period. The transportation sector accounts for nearly 21% of global CO_2 emissions, with approximately 12% originating from road vehicles (ORSETTI *et al.*, 2022). In this context, the transition toward renewable energy sources has become increasingly urgent, not only to mitigate greenhouse gas emissions but also to reduce the dependence on fossil fuels, whose costs have been strongly influenced by recent geopolitical instabilities. Energy storage technologies play a key role in this transition, since the widespread adoption of electric vehicles relies on the development of batteries capable of providing competitive performance, safety, and cost-effectiveness (LIU *et al.*, 2024). Therefore, the development of materials that enable safer, more efficient, economically viable, and environmentally sustainable energy storage systems has become one of the major challenges in materials science and electrochemical energy storage research.

Lithium-ion batteries represent a major advancement in energy storage technology, following earlier developments such as the lead–acid battery introduced by the French physicist Gaston Planté in 1859 (KURZWEIL, 2010). However, commercial lithium-ion batteries employ organic liquid electrolytes, which are highly flammable and volatile, posing significant safety concerns due to the risk of leakage and explosion (SUN; KANG; CUI, 2023). These limitations have motivated the development of all-solid-state batteries, in which the liquid electrolyte is replaced by a solid electrolyte, thereby minimizing the risk of electrolyte leakage (XU *et al.*, 2023). In addition to their improved safety, both inorganic and polymeric solid-state batteries have attracted considerable attention because of their high energy density and electrochemical stability,

making them promising candidates for next-generation energy storage systems (TRAN *et al.*, 2023).

In this context, sodium titanates, $Na_2Ti_nO_{2n+1}$, have attracted considerable attention as promising ceramic electrolytes for solid-state battery applications. Titanium-based compounds are abundant in nature and exhibit low toxicity, making them attractive from both economic and environmental perspectives (CHOI *et al.*, 2022; CHEN *et al.*, 2024). Despite these advantages, the ionic conductivity of sodium titanates remains limited by the relatively low mobility of Na^+ ions. In contrast, Li^+ ions exhibit higher diffusivity because of their smaller ionic radius (approximately 76 pm) compared with that of Na^+ ions (approximately 102 pm), resulting in improved ionic conductivity (MELO *et al.*, 2023).

Several strategies have been proposed to overcome this limitation, including doping and incorporating conductive species. For example, sodium trititanate has been doped with ions such as Nb^{5+} and F^- to improve its electrical properties (CHOI *et al.*, 2022). The electrical conductivity of $Na_2Ti_3O_7$ and $Na_2Ti_6O_{13}$ has been reported to be on the order of 10^{-6} S·cm^{-1} (SILVA *et al.*, 2023). More recently, lithium doping has emerged as a promising alternative, increasing the conductivity of these compounds to the order of 10^{-5} S·cm^{-1} with the addition of only 5% lithium (MELO *et al.*, 2023). Similar strategies have also been applied to other ceramic electrolytes, including lithium aluminum titanium phosphate ($Li_{1.3}Al_{0.3}Ti_{1.7}(PO_4)_3$, LATP) and superionic lithium conductors belonging to the LISICON (LIthium Super Ionic CONductor) family (MIARA *et al.*, 2013; ALTAYARAN, 2020). In these materials, doping can modify the structure by promoting the formation of vacancies, creating preferential pathways for ionic migration, and increasing the concentration of mobile charge carriers (Li^+).

In addition to sodium titanates, Lithium lanthanum zirconate ($Li_7La_3Zr_2O_{12}$, LLZO) has been extensively investigated as one of the most promising ceramic solid electrolytes for all-solid-state batteries due to its high ionic conductivity and excellent chemical stability toward metallic lithium (MURUGAN *et al.*, 2007; ZHANG *et al.*, 2014). Since the pioneering work of Murugan *et al.* (2007), which demonstrated fast Li^+ transport in LLZO, considerable efforts have been devoted to understanding the influence of synthesis methods, dopant chemistry, and defect engineering on its structural and electrochemical properties.

Among the different crystalline forms of LLZO, the cubic garnet phase is of partic-

ular interest because it exhibits ionic conductivities several orders of magnitude higher than those of the tetragonal phase (MURUGAN *et al.*, 2007; AWAKA *et al.*, 2009). However, challenges such as lithium volatilization during sintering, limited densification, and phase instability continue to hinder its large-scale application, motivating the development of optimized processing routes and suitable doping strategies (AWAKA *et al.*, 2009; WOOD *et al.*, 2021).

Different dopants have been investigated to stabilize the cubic phase and improve the overall performance of LLZO. Among these, Mg and Sr have attracted considerable attention because they promote structural stabilization and enhance the material's electrochemical performance (GEIGER *et al.*, 2011; SACCOCCIO *et al.*, 2017; HWANG; ABRHA, 2020).

In addition to ceramic electrolytes, conducting polymers have attracted considerable interest as materials for solid-state batteries. Compared with purely ceramic electrolytes, these materials generally exhibit lower interfacial resistance, lower density, and greater mechanical flexibility, while also allowing relatively simple synthesis and processing. Furthermore, they preserve the main safety advantages associated with solid electrolytes, such as the absence of electrolyte leakage and reduced flammability, making them promising candidates for the development of ceramic–polymer composite electrolytes (LEI *et al.*, 2023).

Among the different conducting polymers, poly(*o*-methoxyaniline) (POMA), an *o*-methoxy derivative of polyaniline (PANI), has attracted particular attention because of its relatively high electrical conductivity, with reported values on the order of 10^{-2} S·cm^{-1} (BIONDO *et al.*, 2020). Its electrical conductivity originates from the conjugated polymer backbone, in which protonation promotes the formation of polarons responsible for charge transport.

Ceramic and polymeric materials each exhibit characteristic advantages and limitations when employed as solid electrolytes. Consequently, ceramic–polymer composites have attracted increasing attention because they combine the mechanical and thermal stability of ceramic electrolytes with the flexibility, ease of processing, and improved interfacial contact provided by polymeric materials. As a result, these composites have emerged as promising candidates for the development of advanced solid-state electrolytes.

The electrical performance of ceramic–polymer composites depends strongly on

the characteristics of both phases and, particularly, on the interactions established at the ceramic–polymer interface. In many systems, the incorporation of polymers into ceramic electrolytes may reduce the overall conductivity owing to the lower ionic conductivity of the polymeric phase (GHORBANZADE *et al.*, 2023). Conversely, the addition of ceramic fillers to polymer matrices has frequently been associated with enhanced ionic conductivity by promoting more favorable ion-transport pathways and improving the structural organization of the composite (LECHARTIER *et al.*, 2022).

Among conducting polymers, poly(*o*-methoxyaniline) (POMA) has attracted interest as a matrix for ceramic composites because, besides its good processability, its electrical properties may contribute to improving the overall performance of composite electrolytes. In LLZO-based and sodium titanate-based composites, interactions at the ceramic–polymer interface may modify the local charge distribution and transport pathways, while the conducting polymer phase can provide additional pathways for charge transport. These combined effects can influence the overall electrical conductivity of the composite (TRAN *et al.*, 2023; MILERIO *et al.*, 2025; SILVA *et al.*, 2023).

Motivated by the challenges in developing advanced solid-state electrolytes, this thesis investigates two ceramic–polymer systems. The first consists of ceramic–polymer composites prepared from sonochemically synthesized nominally lithium-doped sodium titanate (3 mol% Li), with different POMA contents, in order to investigate the influence of the polymer phase on the structural, morphological, thermal, and electrical properties of the composites. The lithium content was selected based on the composition that exhibited the most favorable electrical performance in a previous study by Silva *et al.* (2026), reproduced in Annex A.

The second part of this thesis investigates Mg/Sr co-doped LLZO and its ceramic–polymer composites with systematically varied POMA contents (1, 5, 10, and 15 wt%). Particular emphasis is placed on establishing correlations between composition, crystal structure, thermal stability, microstructure, and electrical response through a comprehensive experimental approach. Structural analyses based on Rietveld refinement, bond-length and polyhedral-distortion calculations, thermal characterization by TG/DTG/DSC, and electrical analyses combining equivalent-circuit modeling and Jonscher's universal power law were employed to provide a detailed understanding of the mechanisms governing the electrical behavior of these composites.

By integrating two distinct ceramic electrolyte systems with conducting-polymer

composites, this thesis provides a broader understanding of the relationships between composition, structure, and electrical properties in ceramic–polymer composites within the context of solid-state electrolyte research.

1.1 Objectives

1.1.1 General Objective

Prepare and investigate Li-doped sodium titanate/POMA and Mg/Sr-codoped LLZO/POMA composites, establishing relationships among composition, crystalline phase evolution, microstructure, thermal stability, and room-temperature electrical response, as a preliminary assessment of their suitability for solid-electrolyte applications.

1.1.2 Specific Objectives

(i) Synthesize nominally Li-doped NLTO and Mg/Sr-codoped LLZO, documenting their nominal compositions, processing conditions, and crystalline phases formed.

(ii) Prepare composite series with controlled POMA weight fractions and verify the reproducibility of the processing routes.

(iii) Evaluate the crystalline-phase evolution, polymer-related amorphous contribution, morphology, particle-size distribution, and thermal stability of the composites.

(iv) Model the impedance spectra, evaluate the robustness of the equivalent-circuit models, and correlate the electrical response with the structural and morphological characteristics.

(v) Determine the total electrical conductivity and critically compare the two composite systems.

2 LITERATURE REVIEW

2.1 State of the Art

Ceramic materials and ceramic–polymer composites have been extensively studied, particularly with regard to doping processes and their influence on electrical and structural properties. In this context, the present work investigates the effects of lithium doping in sodium titanate and the addition of POMA to the doped material, as well as the effects of incorporating this polymer into LLZO. To contextualize the advances in this field, it is relevant to review the existing literature, highlighting previous studies on doping and ceramic–polymer composites.

For example, Melo *et al.* (2023) investigated the lithium doping of sodium titanate using the hydrothermal synthesis method. Three crystalline phases were identified: $Na_2Ti_3O_7$, $Na_2Ti_6O_{13}$, and $NaLiTi_3O_7$. The content of the main phase, $Na_2Ti_3O_7$, decreased from 85.81% in the undoped sample to 66.03% in the sample containing 1% lithium. The highest electrical conductivity was obtained for the sample with 5% lithium, reaching values on the order of 10^{-5} S·cm^{-1}.

Silva *et al.* (2023) investigated a sodium titanate composite ($Na_2Ti_3O_7/Na_2Ti_6O_{13}$) combined with POMA (poly(o-methoxyaniline)). In this study, a ceramic material containing approximately 50% of each crystalline phase was obtained using the sonochemical synthesis method. The ceramic material was incorporated into a polymer matrix at proportions of 0%, 10%, 15%, and 35% $Na_2Ti_3O_{7/}Na_2Ti_6O_{13}$. A significant increase in resistivity was observed, from the order of 10^2 Ω for the pure POMA sample to 10^4 Ω for the sample containing 35% ceramic material.

Costa *et al.* (2022) investigated ceramic–polymer composites based on a $Na_2Ti_3O_7/Na_2Ti_6O_{13}$ ceramic matrix combined with POMA at concentrations of 0%, 1%, 10%, 15%, 35%, and 50%. In addition to varying the polymer content, the influence of temperature was also investigated over the range from 298 K to 368 K, in

increments of 10 K. The results showed that the resistivity of the composites ranged from $10^5\ \Omega \cdot \text{cm}$ to $10^8\ \Omega \cdot \text{cm}$, depending on the composition and temperature.

Xu *et al.* (2023) successfully synthesized cubic-phase LLZO via a solid-state reaction. In this case, complex impedance spectroscopy revealed an ionic conductivity on the order of 10^{-4} S·cm^{-1}.

In addition, Seo *et al.* (2020) synthesized Mg- and Sr-doped LLZO with different dopant concentrations according to the general formula $Li_{7-(2x+y)}Mg_xLa_{3-y}Sr_yZr_2O_{12}$. The composition $Li_{6.95}Mg_{0.15}La_{2.75}Sr_{0.25}Zr_2O_{12}$ exhibited the highest ionic conductivity (1.4×10^{-3} S·cm^{-1}), as well as the most effective stabilization of the cubic LLZO phase.

The same composition was employed by Milério *et al.* (2025) to prepare composites with poly(*o*-methoxyaniline) (POMA), with POMA contents of 1, 5, 20, and 50% added to the ceramic matrix. Among the composites, the sample containing 20% POMA exhibited a bulk conductivity on the order of 10^{-5} S·cm^{-1}.

Table 1: Comparison of previous studies and the scope of the present work.

Study	Ceramic system	Doping	POMA	Main distinction
Melo *et al.* (2023)	Sodium titanate	Li	No	Hydrothermal synthesis; Li-doping investigation
Silva *et al.* (2023)	$Na_2Ti_3O_7/Na_2Ti_6O_{13}$	No	Yes	Ceramic dispersed in a POMA matrix
Costa *et al.* (2022)	$Na_2Ti_3O_7/Na_2Ti_6O_{13}$	No	Yes	Temperature-dependent electrical response
Seo *et al.* (2020)	LLZO	Mg/Sr	No	Optimization of Mg/Sr codoping
Milério *et al.* (2025)	LLZO	Mg/Sr	Yes	LLZO/POMA composites with 1–50 wt.% POMA
Present work	**Sodium titanate**	**Li**	**Yes**	**Li-doped titanate/POMA composites**
Present work	**LLZO**	**Mg/Sr**	**Yes**	**Different POMA range and extended electrical/structural analysis**

Table 1 presents a comparison between previous studies and the present work. Sodium titanate has already been investigated independently for both lithium doping and POMA incorporation. However, no studies report the preparation of composites based on lithium-doped sodium titanate and POMA. For the Mg/Sr-codoped LLZO/POMA system, this work explores a different range of POMA contents. It extends the electrical analysis by applying Jonscher's power law and evaluating relaxation processes using the modified Debye model. In addition, a critical comparison between the two systems is performed to evaluate the influence of POMA incorporation on the structure of the ceramic matrices and on their respective electrical behavior.

2.2 Theoretical Background

2.2.1 Solid-State Batteries

In the history of battery development, the lead–acid battery, invented by Gaston Planté in 1860 (LINDEN, 1995), represents a significant milestone. It became notable for its ability to deliver high electrical currents, an essential characteristic for the automotive industry. Its continued widespread use is attributed to factors such as low cost, proven reliability, and high recyclability (LINDEN, 1995). Despite the emergence of newer technologies, the simplicity and effectiveness of lead-acid batteries have ensured their continued relevance in the automotive market.

In 1899, Swedish engineer Waldemar Jungner developed the nickel–cadmium (NiCd) battery (CHANG *et al.*, 2016). This technology represented a more efficient and durable alternative to the lead–acid batteries available at the time, becoming particularly useful for portable electronic devices due to its higher energy capacity and resistance to repeated charge-discharge cycles (AKTAŞ; KIRÇIÇEK, 2021).

As an evolution of nickel–cadmium (NiCd) batteries, nickel–metal hydride (NiMH) batteries, developed in the 1980s, offer significantly higher energy storage capacity while eliminating the use of cadmium, a toxic metal. Owing to these advantages, NiMH batteries gradually replaced NiCd batteries in portable electronic devices and became widely used in hybrid vehicles (YOUNG; YASUOKA, 2016; LINDEN, 1995; OVSHINSKY; FETCENKO; ROSS, 1993).

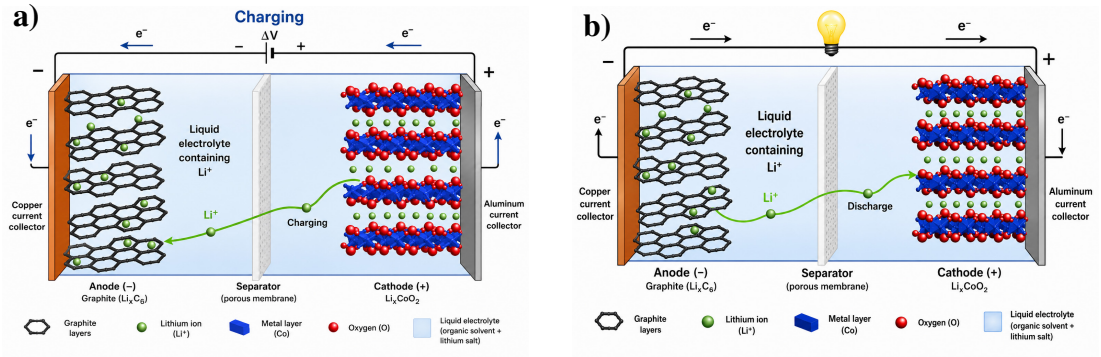
The 2019 Nobel Prize in Chemistry laureates, Stanley Whittingham, John B. Goodenough, and Akira Yoshino, were responsible for the development of lithium-ion (Li-ion) batteries. In 1970, Stanley Whittingham developed a battery using a titanium disulfide cathode and a metallic lithium anode (WHITTINGHAM, 1976). In 1980, John B. Goodenough doubled the battery voltage by using lithium-ion-intercalated cobalt oxide as the cathode material (HUANG, 2022). Subsequently, in 1985, Akira Yoshino developed the first commercially viable lithium-ion battery by integrating safer and more durable materials (YOSHINO, 2012).

This technology is widely used in modern electronic devices due to its several advantages over previous technologies, such as higher energy storage capacity, reduced size, and the absence of toxic components. The evolution of lithium-ion batteries has revolutionized energy storage, enabling the development of portable devices, electric

vehicles, and renewable energy systems.

However, commercial lithium-ion batteries present several issues associated with the use of liquid electrolytes composed of lithium salts dissolved in carbon-based organic solvents (LI *et al.*, 2021), together with a separator, as illustrated in Figure 1.

Figure 1: Schematic representation of a lithium-ion battery during (a) charging and (b) discharging. During charging, Li^+ ions migrate from the cathode to the graphite anode through the liquid electrolyte, while electrons are supplied through the external circuit. During discharging, Li^+ ions migrate from the anode to the cathode, while electrons flow through the external circuit, supplying electrical energy.



Source: Prepared by the author with graphical assistance from ChatGPT (OpenAI) (2026).

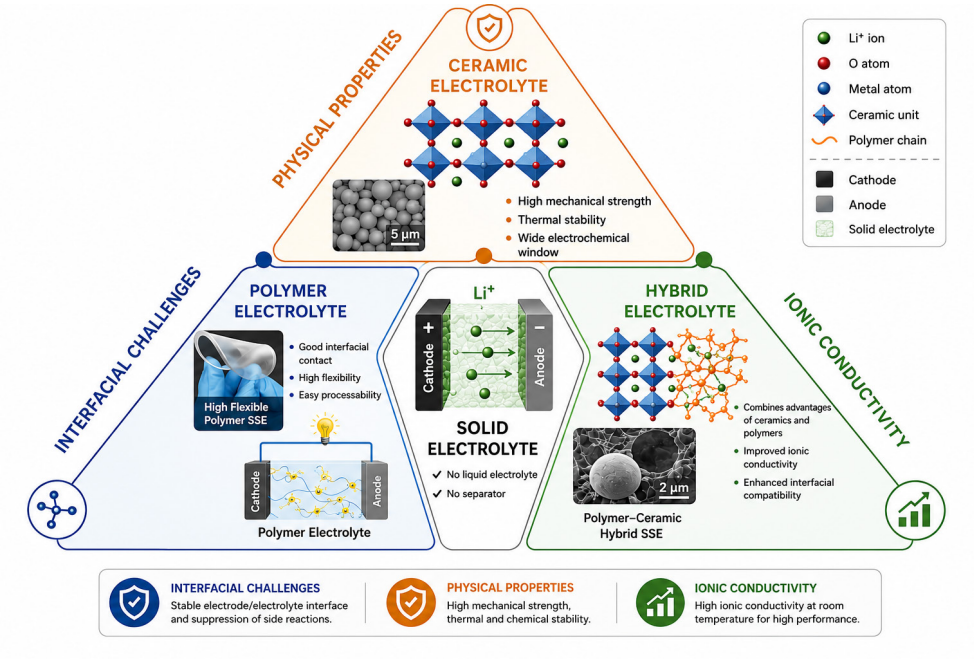
This configuration may compromise battery safety, as there is a risk of explosion and leakage of toxic materials (MADRID *et al.*, 2024), which can be harmful upon contact with the skin (LI *et al.*, 2021). These risks become more evident in cases of separator rupture, which may result in a short circuit.

Concerns regarding safety, together with the narrow operating temperature range of liquid-electrolyte lithium-ion batteries and their inability to prevent lithium dendrite formation (LI *et al.*, 2021; LUO *et al.*, 2024), highlight the need for research into technologies capable of overcoming these limitations. In this context, solid-state batteries have emerged as a promising research field.

Solid-state batteries eliminate the need for a separator, since they enable ionic conduction while preventing electronic conduction, as schematically illustrated in Figure 1, owing to the structure of the materials employed in this type of device. These materials generally include ceramics, polymers, or composites combining both. Research in this

field focuses on overcoming several challenges, including increasing the ionic conductivity of materials at room temperature, improving interfacial stability and mechanical properties, and optimizing battery design (LI *et al.*, 2021), as schematically illustrated in Figure 2.

Figure 2: Schematic representation of solid-electrolyte types and the main challenges associated with their application in solid-state batteries.



Source: Prepared by the author with graphical assistance from ChatGPT (OpenAI) (2026).

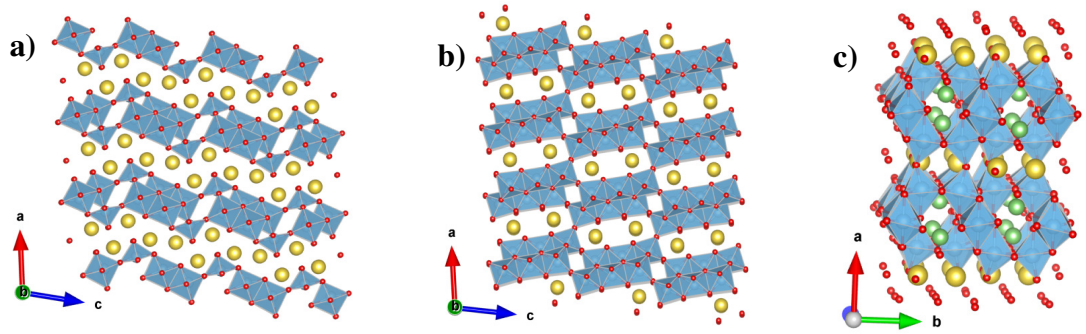
In summary, solid-state batteries represent a promising alternative, offering enhanced user safety due to their chemical stability and potential for higher energy density. The scientific community still faces the challenge of overcoming barriers to large-scale commercial production of these batteries, even as demand for safer, more efficient energy storage solutions is already evident.

2.2.2 Sodium Titanates

Sodium titanates are mainly found in two crystalline forms: sodium trititanate ($Na_2Ti_3O_7$) and sodium hexatitanate ($Na_2Ti_6O_{13}$). $Na_2Ti_3O_7$ has a layered structure composed of TiO_6 octahedra interconnected along a crystallographic axis. In this structure, Na^+ ions are intercalated between the titanium oxide layers (DONG *et al.*, 2022),

as shown in Figure 3a.

Figure 3: Crystal structures of (a) $Na_2Ti_3O_7$, (b) $Na_2Ti_6O_{13}$, and (c) $NaLiTi_3O_7$. Ti, O, Na, and Li atoms are represented in blue, red, yellow, and green, respectively.



Source: Prepared by the author using VESTA (2026).

On the other hand, $Na_2Ti_6O_{13}$ exhibits a more complex three-dimensional structure, in which TiO_6 octahedra form tunnels along the crystal lattice. Sodium ions are accommodated within these tunnels (DONG *et al.*, 2022), as illustrated in Figure 3b.

The structural configurations of $Na_2Ti_3O_7$ and $Na_2Ti_6O_{13}$ enable efficient Na^+ ionic conduction. In $Na_2Ti_3O_7$, the ions are transported through its layered structure, whereas in $Na_2Ti_6O_{13}$, conduction occurs through the tunnels formed by TiO_6 octahedra. In addition to ionic conduction, these materials exhibit excellent thermal stability, with melting points above $1000\ ^\circ C$, significantly higher than the operating temperature range of commercial batteries, which typically ranges from 20 to $40\ ^\circ C$ (ORTIZ *et al.*, 2024).

Additionally, the high chemical stability of these materials is crucial for the durability and safety of electrochemical devices. These characteristics make sodium titanates promising candidates for solid-state battery applications. Researchers have already extensively investigated these materials as electrode materials (LIBICH *et al.*, 2020). Melo *et al.* (2023) proposed Li-doped sodium trititanate as a possible solid-state electrolyte due to the increase in total electrical conductivity with Li addition; however, the authors emphasized the need for further studies to confirm its applicability in this context. The continued development of materials with these properties may lead to significant advances in the efficiency and safety of next-generation batteries.

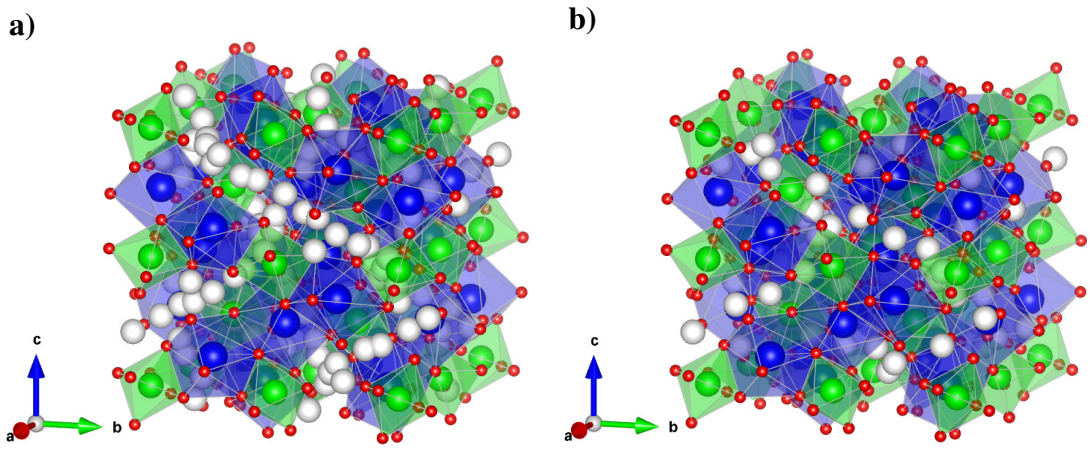
An effective strategy for improving the conductivity of ceramic materials is doping with lithium ions. In the case of sodium titanates, the partial substitution of Na^+

ions by Li^+ ions aims to exploit the higher diffusivity of Li^+, owing to its smaller ionic radius (SHIH; AGUADERO; SKINNER, 2018). This substitution facilitates ion mobility within the crystal structure, thereby enhancing ionic transport efficiency. Li^+ doping in $Na_2Ti_3O_7$ favors the formation of a new phase, $NaLiTi_3O_7$, whose structure is illustrated in Figure 3c. Although $NaLiTi_3O_7$ has been investigated mainly as an electrode material for lithium- and sodium-ion batteries (VADIVAZHAGAN; JAYAN; NALLATHAMBY, 2022), its application as a solid electrolyte remains largely unexplored.

2.2.3 Lithium Lanthanum Zirconium Oxide (LLZO)

Lithium lanthanum zirconate (LLZO, $Li_7La_3Zr_2O_{12}$) is a ceramic material known for its garnet-type structure, which exhibits a high density of ions that favors ionic conductivity (MILERIO *et al.*, 2025). In this structure, lithium ions occupy specific interstitial sites, facilitating ionic transport through the crystal lattice (QU *et al.*, 2025).

Figure 4: Crystal structures: (a) cubic LLZO, (b) tetragonal LLZO. Color code: O (red), Zr (green), La (blue), Li (white).



Source: Prepared by the author using VESTA (2026).

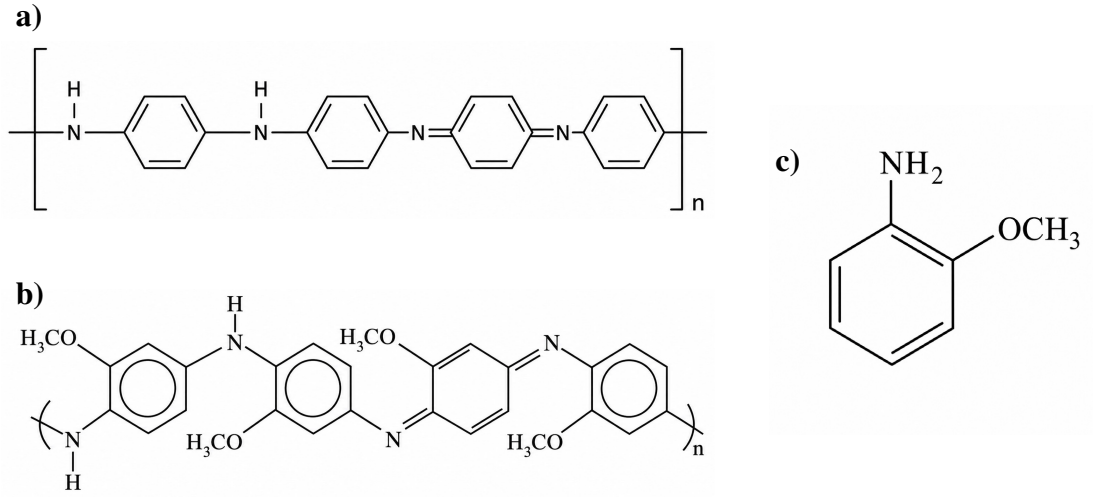
LLZO can exist in two distinct crystalline phases, as shown in Figure 4: the cubic phase, belonging to the $Ia\bar{3}d$ space group, and the tetragonal phase, associated with the $I4_1/acd$ space group (KALITA; ENDO; NISHI, 2023). Among these, the cubic phase stands out due to its higher ionic conductivity, ranging from 10^{-6} to 10^{-3} S·cm^{-1} (PUENTE *et al.*, 2021; EL-SHINAWI *et al.*, 2024), making it the most suitable phase

for applications in energy storage devices, such as solid-state lithium-ion batteries.

In addition to its high ionic conductivity, LLZO stands out for its remarkable thermal stability, withstanding temperatures of approximately 1000 °C without undergoing significant degradation. This characteristic is particularly important for high-temperature sintering processes and for maintaining structural stability under extreme operating conditions. Furthermore, LLZO exhibits excellent chemical stability, minimizing undesirable reactions with electrode materials, such as metallic lithium, which is crucial for the durability and performance of solid-state batteries (JANEK; ZEIER, 2023; YANG *et al.*, 2022; CHU *et al.*, 2024). Additionally, LLZO has been extensively studied as a solid-state electrolyte, with reported ionic conductivity values on the order of 10^{-3} S cm^{-1} (SAZVAR *et al.*, 2025). Despite these promising results, challenges remain, including electrolyte–electrode interfacial resistance and surface degradation due to the material's reactivity. These combined properties make LLZO one of the most promising solid electrolytes for the development of high-energy-density and long-life energy storage devices.

2.2.4 Poly(o-methoxyaniline) (POMA)

Figure 5: Chemical structures of the conducting polymer and its precursor: (a) polyaniline (PANI); (b) poly(*o*-methoxyaniline) (POMA); and (c) the *o*-anisidine monomer.

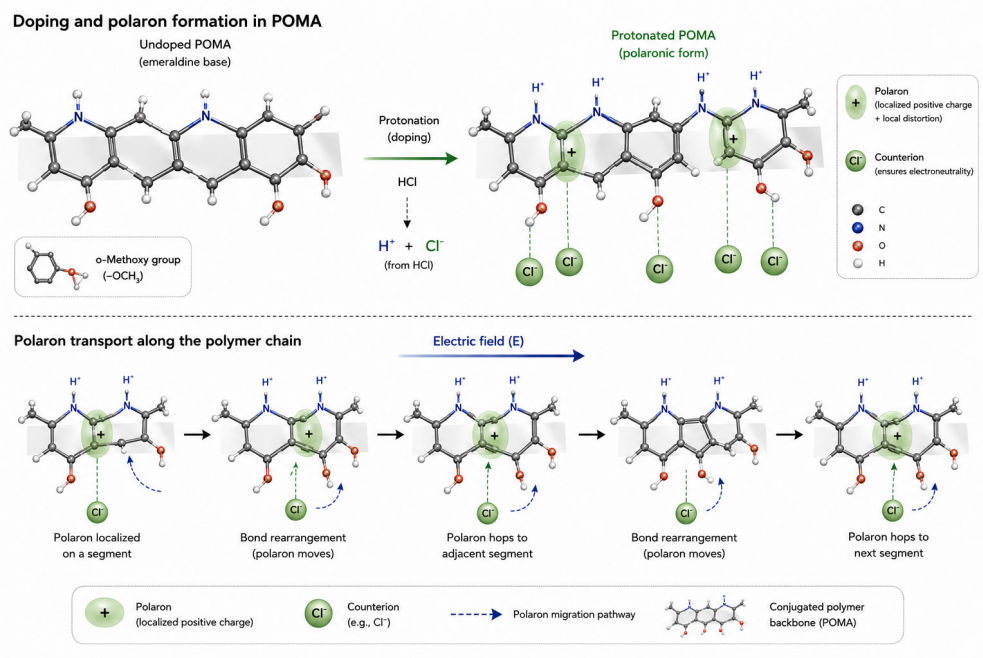


Source: Galiani *et al.* (2007).

Poly(o-methoxyaniline) (POMA) (Figure 5b) is a polymer derived from polyaniline (PANI) (Figure 5a), distinguished by its higher solubility and excellent electrical

properties. Like PANI, the molecular structure of POMA consists of benzene rings linked by amine (−NH−) groups and quinoid rings containing imine (−N=) groups (SILVA *et al.*, 2023). The main structural difference between POMA and PANI lies in the presence of a methoxy ($-OCH_3$) (Figure 5c) group at the ortho position of the aromatic ring in POMA (SILVA *et al.*, 2023), as illustrated in Figure 4c. This structural modification provides POMA with distinct physical and chemical characteristics, including improved processability and tunable electrical properties.

Figure 6: Schematic representation of protonation and charge transport by polaron migration in POMA.



Source: Prepared by the author with graphical assistance from ChatGPT (OpenAI) (2026).

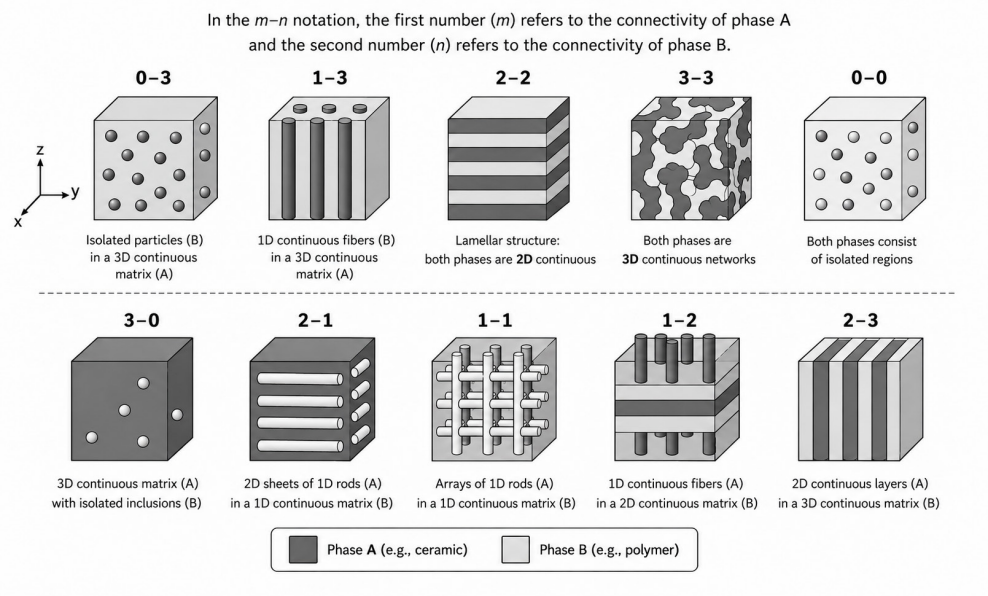
Poly(*o*-methoxyaniline) (POMA) has been widely investigated for electrical applications due to its conductive properties, which can be significantly enhanced through doping processes. Biondo *et al.* (2020) demonstrated that doping POMA with hydrochloric acid (HCl) can increase its electrical conductivity to values on the order of 10^{-1} S/cm, highlighting its potential for applications in electronic devices.

The electrical conductivity of POMA originates from its conjugated polymer backbone, in which protonation during the doping process promotes the formation of polarons, which are quasiparticles consisting of a localized charge coupled to a local dis-

tortion of the polymer chain. These quasiparticles act as the primary charge carriers, while electroneutrality is maintained by counterions incorporated during protonation. Under an external electric field, polarons migrate through the conjugated chains by successive rearrangements of single and double bonds, thereby enabling electrical conduction through the polymer (Figure 6) (BIONDO *et al.*, 2020; PALETI *et al.*, 2024). These electrical properties have motivated the incorporation of POMA into ceramic–polymer composites, including LLZO-based systems investigated for solid-state electrolyte applications (MILERIO *et al.*, 2025).

2.2.5 Composites

Figure 7: Schematic representation of the connectivity patterns for two-phase composites according to the m–n classification, where m and n represent the dimensional connectivity of each constituent phase.



Source: Adapted from Newnham, Skinner e Cross (1978).

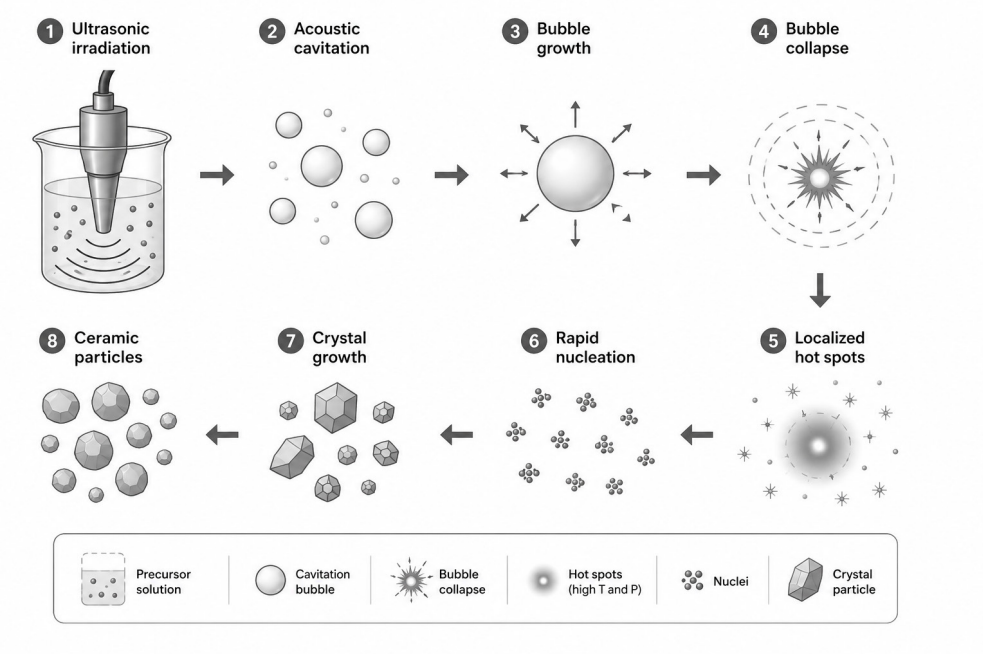
A composite can be understood as a microscopically heterogeneous system composed of two or more materials with distinct physical and/or chemical characteristics, separated by identifiable interfaces (CALLISTER JR.; RETHWISCH, 2014). A composite's physical response depends on its constituent components' characteristics, as well as on interfacial interactions, phase connectivity, and percolation phenomena, which can affect the material's electrical, dielectric, thermal, and mechanical properties.

Composite materials can be classified according to different criteria, including the spatial arrangement and connectivity of their constituent phases. In this context, Newnham, Skinner e Cross (1978) introduced a classification system based on the spatial connectivity between the constituent phases of a composite. This classification uses the indices m and n, which range from 0 to 3 and indicate the number of dimensions in which each phase is continuously connected. In this scheme, 0 indicates a phase consisting of isolated particles dispersed within the other phase. The index 1 represents one-dimensional connectivity, such as a filament or fiber, whereas 2 indicates two-dimensional connectivity, such as a layer. Finally, 3 indicates that the phase is continuously connected in three dimensions.

2.2.6 Synthesis Techniques

2.2.6.1 Sonochemical Synthesis

Figure 8: Schematic illustration of the sonochemical synthesis process, showing acoustic cavitation, bubble collapse, and the subsequent nucleation and growth of ceramic particles.

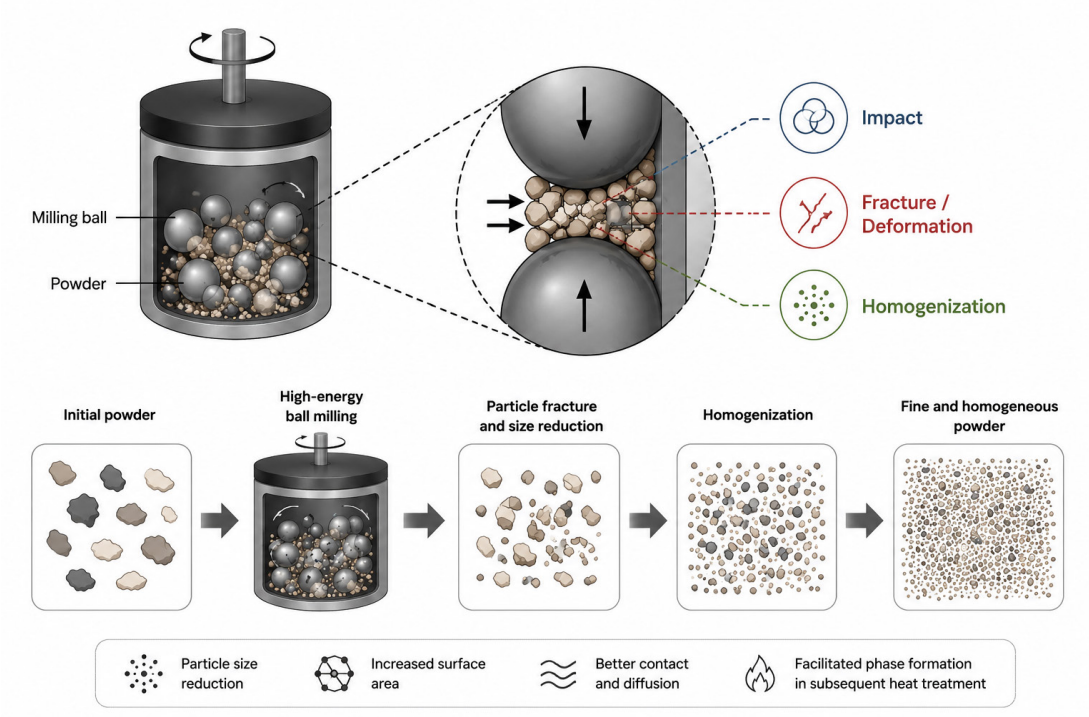


Source: Prepared by the author with graphical assistance from ChatGPT (OpenAI) (2026).

Sonochemical synthesis is based on the application of ultrasonic irradiation to dispersions or solutions, as illustrated in Figure 8.The irradiation promotes the formation of acoustic cavitation bubbles, whose rapid growth and collapse generate localized regions of high temperatures and pressures (on the order of 10^4 K and 10^3 atm) over extremely short time intervals (MATYSZCZAK *et al.*, 2024). These conditions promote intense energy transfer, accelerating reaction kinetics and enabling the synthesis of materials under experimental conditions that require lower energy consumption and shorter processing times when compared with other synthesis routes (TRINH *et al.*, 2025).Among the advantages of sonochemical synthesis over other synthesis routes are smaller particle size, morphology control through the adjustment of operating parameters, improved crystallinity, reduced nanoparticle agglomeration, enhanced product properties, room–temperature synthesis, and rapid, low-cost processing (MATYSZCZAK *et al.*, 2024)

2.2.6.2 High-energy ball milling

Figure 9: Schematic illustration of the high-energy ball milling process.

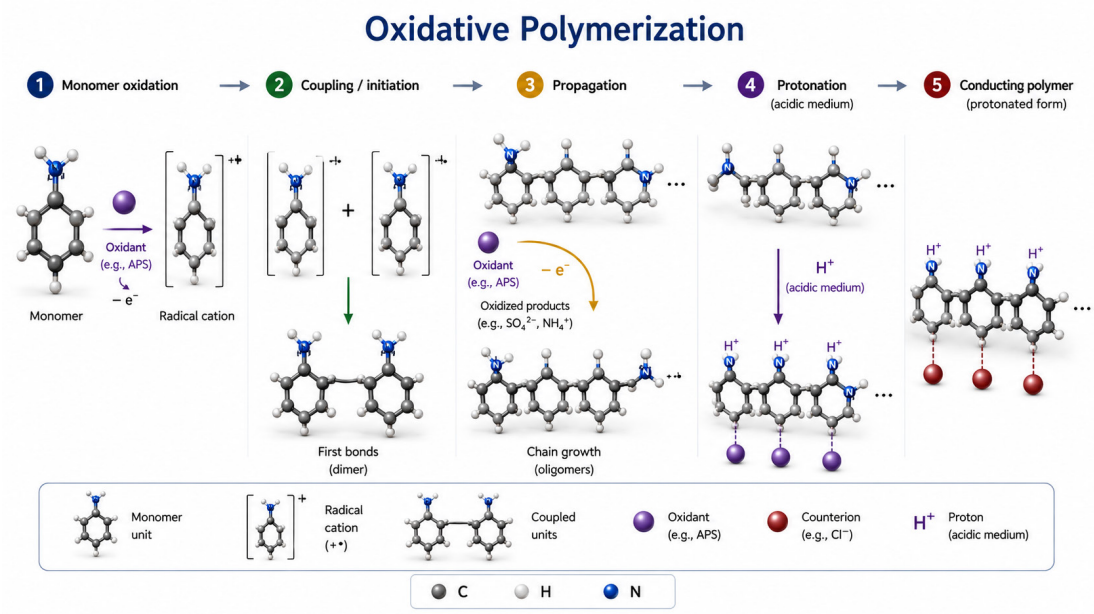


Source: Prepared by the author with graphical assistance from ChatGPT (OpenAI) (2026).

High-energy ball milling-assisted solid-state reaction is based on the transfer of mechanical energy from repeated impacts between the milling balls and the material particles inside the milling container, as well as from impacts experienced by particles trapped between the milling balls and the container walls, as shown in Figure 9. These effects promote shear-induced fracture, plastic deformation, and particle-size reduction, while also achieving a high degree of powder homogenization. As a result, the specific surface area and the contact between reactants are increased (FROTA, 2026), favoring diffusion processes and phase formation during subsequent heat treatments (ZHANG; YING, 2001).

2.2.6.3 Oxidative Polymerization

Figure 10: Schematic illustration of the oxidative polymerization process, highlighting the oxidation, coupling, propagation, and protonation stages that lead to the formation of an electrically conductive polymer.



Source: Prepared by the author with graphical assistance from ChatGPT (OpenAI) (2026).

Polymerization is the chemical process through which monomer molecules react to form high-molecular-weight macromolecules by the successive formation of covalent bonds. Depending on the reaction mechanism, this process may occur through either chain-growth or step-growth polymerization. In chain-growth polymerization,

polymer chains are formed by the successive addition of monomer units to active centers generated during the initiation stage, followed by the propagation and termination stages.

The structure, molecular weight, and final properties of the resulting polymer depend on factors such as the polymerization mechanism, reaction conditions, the type of initiator, and the reaction medium. In the case of intrinsically conducting polymers, oxidative polymerization is one of the most widely employed synthesis methods (STEJSKAL; GILBERT, 2002). In this process, an oxidizing agent removes electrons from the monomer molecules, generating radical cations that subsequently undergo coupling reactions, thereby initiating polymer chain growth. Successive oxidation and coupling steps promote chain propagation, while protonation in an acidic medium stabilizes the polymer backbone in its electrically conductive form (STEJSKAL; GILBERT, 2002; BEYGISANGCHIN *et al.*, 2024). This method is widely used because it enables polymer synthesis under relatively mild experimental conditions while providing good control over the structure and properties of the resulting material.

2.2.7 Characterization Techniques

2.2.7.1 Structural, Morphological, and Optical Characterization

The structural and morphological characterization was performed using X-ray diffraction (XRD) to identify the crystalline phases, scanning electron microscopy (SEM) to examine the surface morphology, energy-dispersive X-ray spectroscopy (EDS) to determine the elemental composition, and Fourier-transform infrared spectroscopy (FTIR) to investigate the chemical bonds and interactions among the components of the composites.

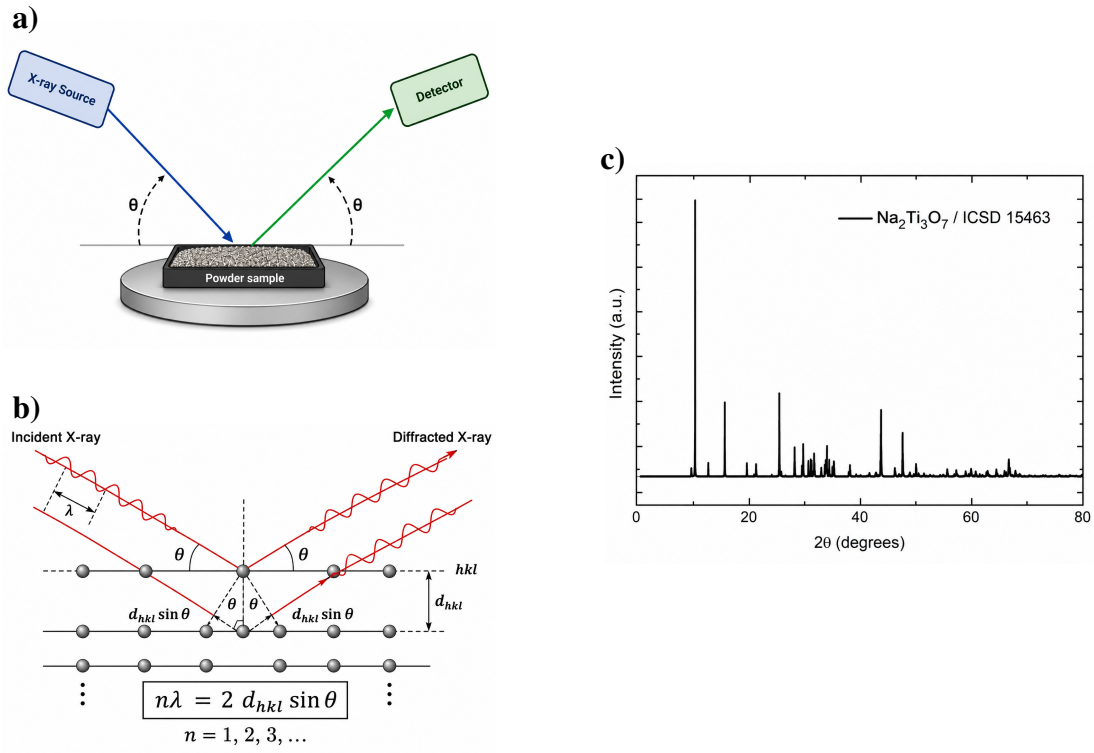
X-ray diffraction is an effective technique for identifying crystalline phases. The method consists of irradiating a powdered sample with an X-ray beam and detecting the diffracted rays using a detector, as illustrated in Figure 11a. The condition for constructive diffraction is given by Bragg's law (Equation 2.1) (BUNACIU; UDRIŞTIOIU; ABOUL-ENEIN, 2015):

$$n\lambda = 2d_{hkl}\sin\theta \tag{2.1}$$

where n is the diffraction order, λ is the wavelength of the incident X-ray radiation, d_{hkl}

is the interplanar spacing of the crystallographic plane identified by the Miller indices (hkl), and θ is the Bragg angle.

Figure 11: Schematic illustration of X-ray powder diffraction (a), the Bragg diffraction condition (b), ICSD reference diffraction pattern of $Na_2Ti_3O_7$



Source: Galiani *et al.* (2007).

The diffraction condition can also be expressed in reciprocal space in terms of the magnitude of the scattering vector, given by Equation 2.2 (SIVIA, 2011).

$$q = \frac{4\pi}{\lambda}\sin\theta \tag{2.2}$$

Similarly, in reciprocal space, the reciprocal lattice vector associated with the crystallographic plane (hkl) is given by Equation 2.3 (ALS-NIELSEN; MCMORROW, 2011).

$$|\mathbf{G}_{hkl}| = \frac{2\pi}{d_{hkl}} \tag{2.3}$$

Thus, the diffraction condition is satisfied when the relationship given in Equa-

tion 2.4 is fulfilled.

$$q = |\mathbf{G}_{hkl}|. \tag{2.4}$$

For cubic crystal systems, for example, the interplanar spacing can be calculated from the lattice parameter according to Equation 2.5 (ALS-NIELSEN; MCMORROW, 2011):

$$d_{hkl} = \frac{a}{\sqrt{h^2 + k^2 + l^2}} \tag{2.5}$$

where a is the lattice parameter and h, k, and l are the Miller indices. For crystal systems with other symmetries, the interplanar spacing is determined using the corresponding expressions for each crystal system.

When the Bragg condition is satisfied, the diffractometer records the diffracted intensity as a function of the diffraction angle (2θ) (GREGORY, 1957), producing a diffraction pattern such as those shown in Figure 11c. The intensity of each diffraction peak is proportional to the square of the corresponding structure factor, as given by Equation 2.6 (ALS-NIELSEN; MCMORROW, 2011):

$$I_{hkl} \propto |F_{hkl}|^2 \tag{2.6}$$

where F_{hkl} is the corresponding structure factor.

The resulting diffraction pattern can be analyzed to identify crystalline phases by comparison with reference patterns available in crystallographic databases, such as the International Center for Diffraction Data (ICDD). A more comprehensive structural analysis can be performed through Rietveld refinement using dedicated software packages, such as GSAS-II or FullProf. This approach enables determination of the weight percentages of the crystalline phases in the sample, as well as the lattice parameters of their corresponding unit cells. The Rietveld refinement is based on minimizing the residual function expressed by Equation 2.7 (RIETVELD, 1969; YOUNG, 1993):

$$S = \sum_i w_i \left(y_i^{\text{obs}} - y_i^{\text{calc}}\right)^2 \tag{2.7}$$

where y_i^{obs} and y_i^{calc} are the observed and calculated intensities, respectively, at point i of the diffraction pattern, and w_i is the statistical weighting factor.

In addition, several statistical parameters are used to quantify the agreement between the experimental and calculated diffraction profiles, thereby providing a measure of the refinement quality. One of the most widely used is the weighted profile residual (R_{wp}), defined by Equation 2.8 (DINNEBIER; LEINEWEBER; EVANS, 2019):

$$R_{wp} = \left[\frac{\sum_i w_i \left(y_i^{\text{obs}} - y_i^{\text{calc}} \right)^2}{\sum_i w_i \left(y_i^{\text{obs}} \right)^2} \right]^{1/2} \times 100\% \tag{2.8}$$

Equation 2.9 (DINNEBIER; LEINEWEBER; EVANS, 2019) defines another important statistical parameter, the expected profile residual (R_{exp}).

$$R_{exp} = \left[\frac{N - P + C}{\sum_i w_i \left(y_i^{\text{obs}} \right)^2} \right]^{1/2} \times 100\% \tag{2.9}$$

where N is the number of experimental observations, P is the number of refined parameters, and C is the number of constraints imposed during the refinement.

The goodness-of-fit parameter (χ^2) can be calculated from the values of R_{wp} and R_{exp} using Equation 2.10 (DINNEBIER; LEINEWEBER; EVANS, 2019).

$$\chi^2 = \left(\frac{R_{wp}}{R_{exp}} \right)^2 \tag{2.10}$$

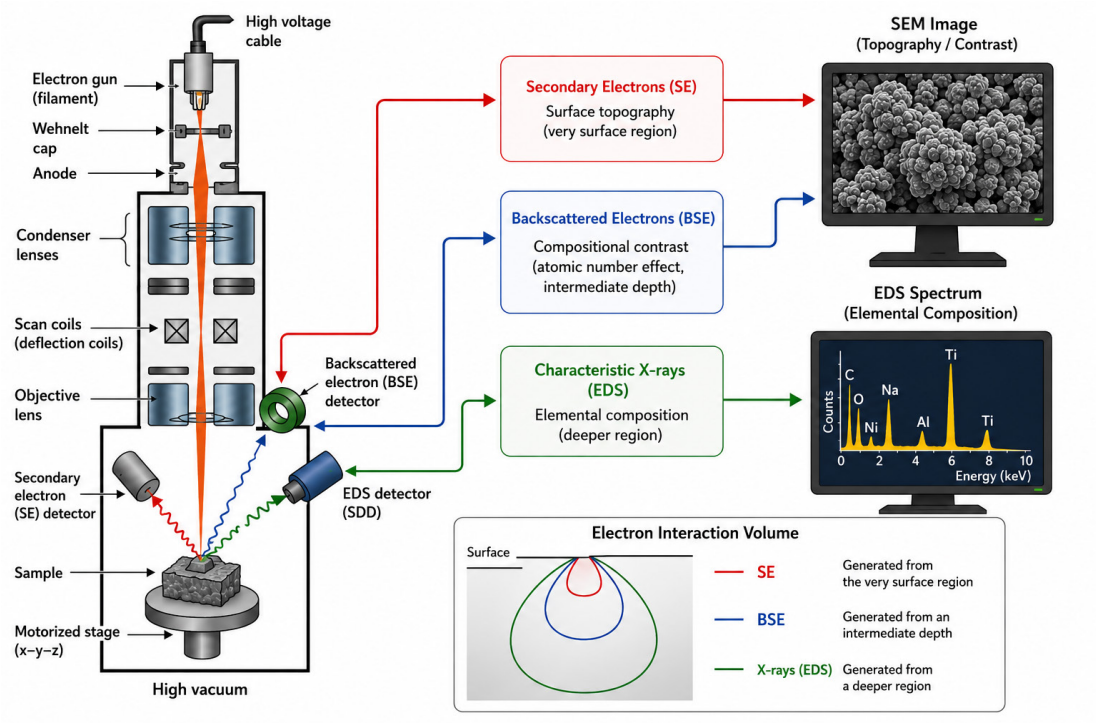
The value of χ^2 provides a measure of the agreement between the calculated and experimental diffraction profiles. Values close to unity indicate a good fit between the calculated and observed data, whereas higher values suggest that the refinement can be further improved.

Another important characterization technique is scanning electron microscopy (SEM). SEM operates by scanning a focused electron beam across the surface of a sample, promoting interactions between the incident electrons and the atoms of the material. These interactions generate several signals, primarily secondary and backscattered electrons (EGERTON *et al.*, 2005). The detected signals are used to produce high-resolution images, enabling the observation of surface morphology and microstructural features at the nanometer scale (EGERTON *et al.*, 2005).

SEM provides information on the morphology and surface features of materials, including their roughness, porosity, and particle size. In addition, it enables the identification of microstructural defects and provides compositional contrast arising from

the presence of different constituents in composites or polymer blends. Furthermore, SEM is frequently coupled with energy-dispersive X-ray spectroscopy (EDS) to determine the elemental composition of materials. This technique is based on detecting characteristic X-rays emitted when atoms in the sample, ionized by the incident electron beam, undergo electronic transitions in which electrons from higher-energy shells fill vacancies in inner shells. Since the energy of the characteristic X-rays emitted by each chemical element is unique, the resulting spectrum enables qualitative and semi-quantitative analyses of the material composition (GOLDSTEIN *et al.*, 2018).

Figure 12: Schematic illustration of the operating principles of SEM and EDS.



Source: Prepared by the author with graphical assistance from ChatGPT (OpenAI) (2026).

On the other hand, Fourier transform infrared spectroscopy (FTIR) is a technique that measures the absorption of infrared radiation by a sample, which is directly related to the vibrational modes of the chemical bonds present in the material (FERRER-ROCA *et al.*, 2024). In an FTIR spectrometer, the detector initially records an interferogram as a function of the optical path difference (OPD). This interferogram is mathematically transformed into an infrared spectrum by means of the Fourier transform, yielding the absorbance (or transmittance) as a function of the wavenumber (GRIFFITHS, 1983).

The Fourier transform is expressed by Equation 2.11:

$$F(\tilde{\nu}) = \int_{-\infty}^{\infty} I(\delta)\, e^{-i2\pi\tilde{\nu}\delta}\, d\delta \tag{2.11}$$

where $F(\tilde{\nu})$ is the infrared spectrum in the wavenumber domain, $I(\delta)$ is the measured interferogram, δ is the optical path difference (OPD), $\tilde{\nu}$ is the wavenumber (cm^{-1}), and $e^{-i2\pi\tilde{\nu}\delta}$ is the complex exponential kernel of the Fourier transform Griffiths (1983).

Each vibrational mode is associated with a characteristic frequency. In a simplified model, a chemical bond between two atoms can be approximated as a system of two masses connected by a spring. Under the harmonic oscillator approximation, the vibrational frequency is given by Equation 2.12 (GRIFFITHS, 1983):

$$\nu = \frac{1}{2\pi}\sqrt{\frac{k}{\mu}} \tag{2.12}$$

where ν is the vibrational frequency, k is the bond force constant, and μ is the reduced mass of the two-atom system, defined as

$$\mu = \frac{m_1 m_2}{m_1 + m_2}, \tag{2.13}$$

where m_1 and m_2 are the masses of the two bonded atoms.

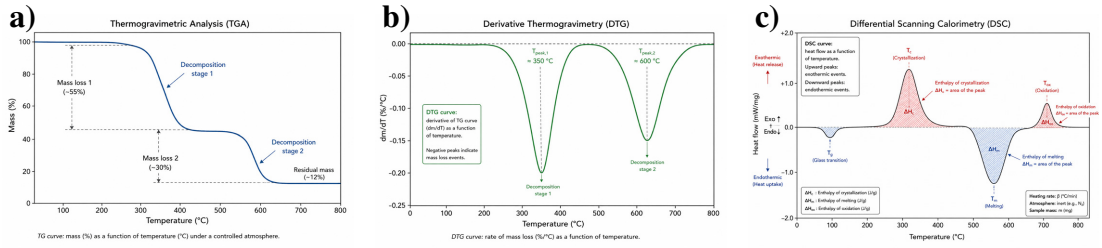
Therefore, each chemical bond exhibits characteristic vibrational modes at well-defined frequencies, commonly expressed as wavenumbers. The FTIR spectrum consists of absorption bands at characteristic wavenumbers, enabling the identification of specific chemical bonds and the characterization of the sample's chemical composition (GONG; CHEN; WU, 2024).

2.2.7.2 Thermal Characterization

Thermal characterization plays a fundamental role in the study of materials intended for solid-state battery applications, since thermal stability is a key requirement for the safe and reliable operation of these devices. Thermogravimetric analysis (TG) is employed to evaluate the mass loss of a sample as a function of temperature, as illustrated in Figure 13a, whereas derivative thermogravimetry (DTG) (Figure 13b) represents the first derivative of the TG curve with respect to temperature, highlighting the rate of mass loss and facilitating the identification of individual thermal decomposition

events. This technique is particularly useful for investigating ceramic–polymer composites because polymers generally exhibit lower thermal stability than ceramic materials (WUNDERLICH, 2005). Consequently, TG/DTG can be used to estimate the polymer content and to assess whether the composite exhibits adequate thermal stability for battery operating conditions.

Figure 13: Schematic representation of the thermal characterization techniques: (a) thermogravimetric analysis (TG), (b) derivative thermogravimetry (DTG), and (c) differential scanning calorimetry (DSC).



Source: Prepared by the author with graphical assistance from ChatGPT (OpenAI) (2026).

Another important thermal characterization technique is differential scanning calorimetry (DSC), which is used to investigate the thermal transitions of materials, such as glass transition, crystallization, and melting. This information is essential for determining the temperature range over which the composites retain the physical properties required for their intended application. DSC measures the heat flow associated with physical or chemical changes in the sample as a function of temperature, as illustrated in Figure 13c.

2.2.7.3 Electrical Characterization

Complex impedance spectroscopy (CIS) is a characterization technique widely used to investigate the electrical properties of materials (ZHELTIKOV, 2007). The technique consists of applying a small alternating voltage across the sample while varying the excitation frequency over a broad range. The resulting alternating current is measured, allowing the complex impedance to be determined according to Equation 2.14:

$$Z(\omega) = \frac{V(\omega)}{I(\omega)} \tag{2.14}$$

where $Z(\omega)$ is the complex impedance, $V(\omega)$ is the applied alternating voltage, $I(\omega)$ is the resulting alternating current, and ω is the angular frequency.

Since impedance is a complex quantity, it can also be expressed in the form given by Equation 2.15:

$$Z(\omega) = Z'(\omega) + jZ''(\omega) \tag{2.15}$$

where $Z'(\omega)$ and $Z''(\omega)$ are the real and imaginary components of the complex impedance, respectively, and $j = \sqrt{-1}$ is the imaginary unit.

The real component of the impedance is associated with the resistive response of the material, whereas the imaginary component is related to energy storage processes, which are typically capacitive or, less frequently, inductive in nature. For an ideal capacitor, the impedance is given by

$$Z_C(\omega) = \frac{1}{j\omega C} = -\frac{j}{\omega C}, \tag{2.16}$$

where C is the capacitance.

For a resistor and a capacitor connected in series, the total impedance is expressed as

$$Z_{\mathrm{s}}(\omega) = R + \frac{1}{j\omega C}, \tag{2.17}$$

whereas, for a parallel RC circuit, the total admittance is given by

$$\frac{1}{Z_{\mathrm{p}}(\omega)} = \frac{1}{R} + j\omega C, \tag{2.18}$$

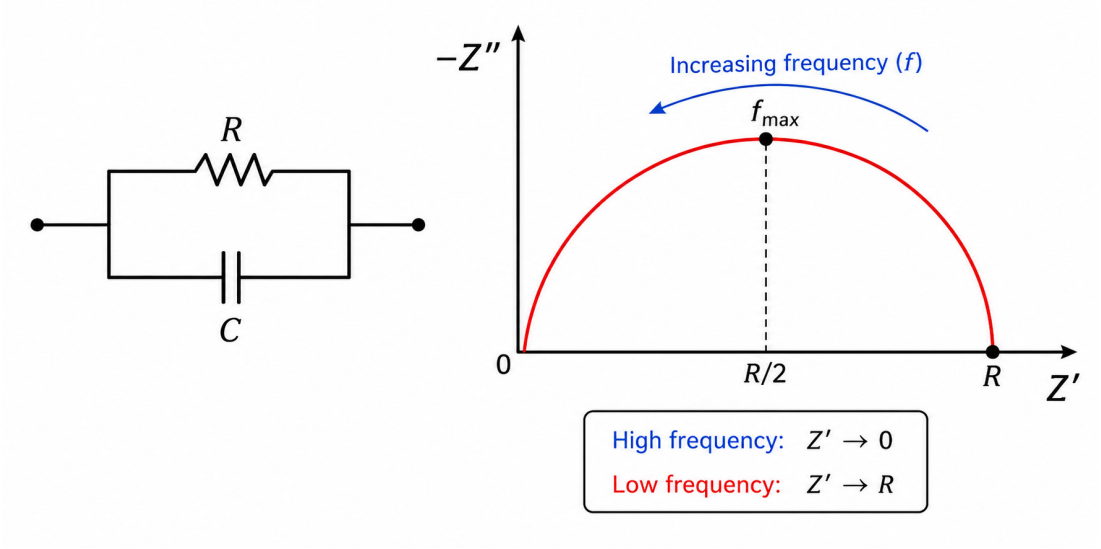
or, equivalently,

$$Z_{\mathrm{p}}(\omega) = \frac{R}{1 + j\omega RC}. \tag{2.19}$$

The impedance measurement provides the real, Z', and imaginary, Z'', components of the impedance over a range of frequencies. The plot of $-Z''$ versus Z', commonly referred to as the Nyquist plot, enables identification of different electrical processes in the material using equivalent circuit models.

In Figure 14, the arrow above the Nyquist plot indicates the direction of increasing frequency. Accordingly, the region where Z' approaches zero corresponds to the high-frequency limit, whereas the region where Z' approaches R corresponds to the low-frequency limit for the equivalent parallel RC circuit. This behavior is well described by the equivalent circuit because, as the frequency increases, the impedance of the capacitive branch decreases, causing an increasing fraction of the current to flow through the capacitor. Consequently, the total impedance decreases, as can be verified from Equation 2.19.

Figure 14: Equivalent parallel RC circuit and the corresponding ideal Nyquist plot, illustrating the frequency dependence of the complex impedance.



Source: Prepared by the author with graphical assistance from ChatGPT (OpenAI) (2026).

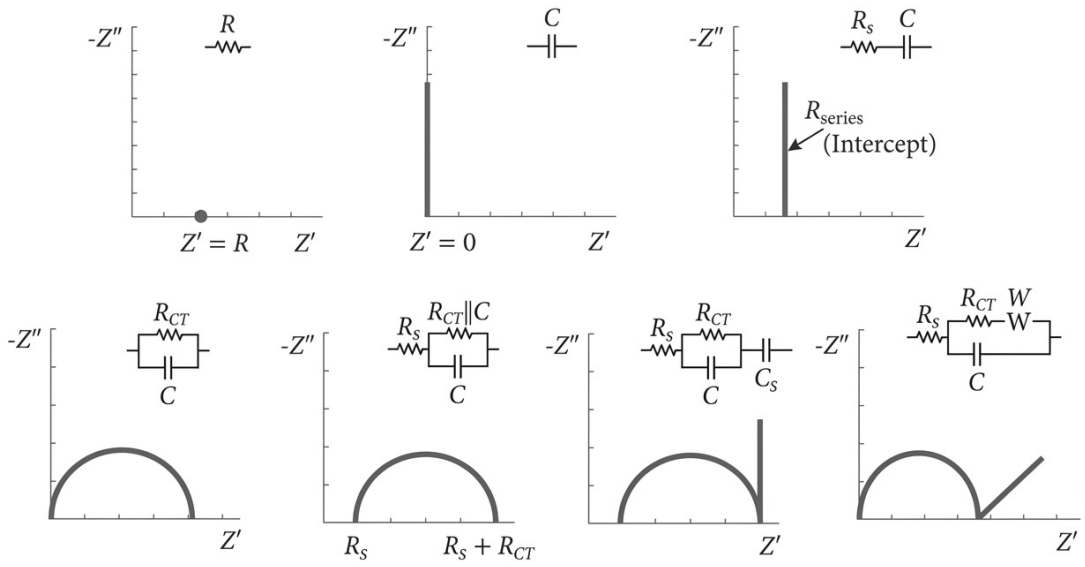
Conversely, at low frequencies, the impedance of the capacitor becomes very large, causing the resistive branch to dominate the electrical response. As the excitation frequency decreases, the applied alternating voltage increasingly resembles a direct current (DC) signal. Consequently, the resistance R obtained from the low-frequency intercept corresponds to the DC electrical resistance of the sample. The DC electrical conductivity can therefore be calculated using Equation 2.20:

$$\sigma_{\mathrm{DC}} = \frac{e}{R\,A} \tag{2.20}$$

where σ is the DC electrical conductivity, e is the thickness of the pellet, A is its cross-

sectional area, and R is the electrical resistance. It should be noted that the behavior illustrated in Figure 14 represents an idealized case (SILVA *et al.*, 2024). In practice, considerably more complex impedance responses may be observed, particularly for composite materials, as illustrated in Figure 15.

Figure 15: Representative Nyquist plots for different ideal electrical elements and equivalent circuits commonly used in impedance spectroscopy.



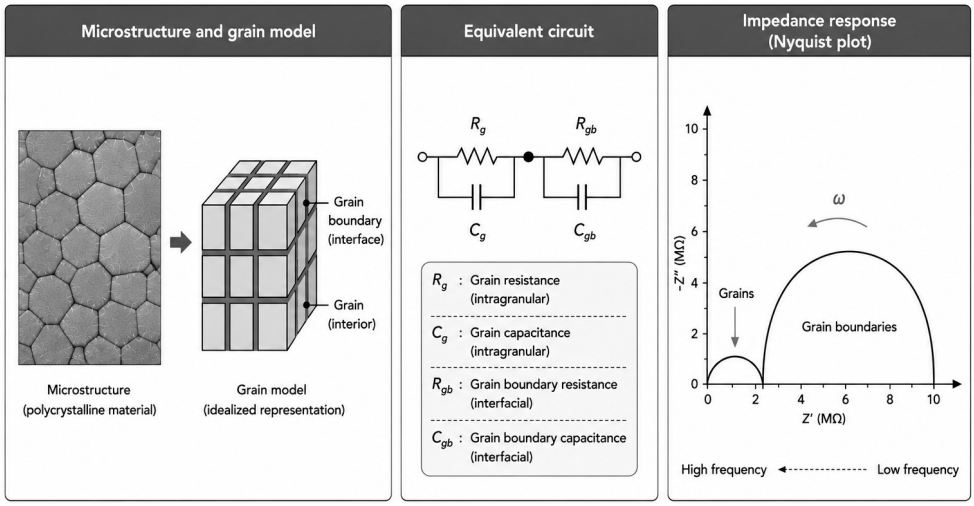
Source: Prepared by the author with graphical assistance from ChatGPT (OpenAI) (2026).

It is important to emphasize the correspondence between the equivalent circuit model and the material's microstructure. A representative example is the grain-and-grain-boundary model. This model is commonly applied to polycrystalline materials, whose microstructure consists of relatively homogeneous grains surrounded by regions of different electrical properties known as grain boundaries, as illustrated in Figure 16.

The equivalent-circuit model presented in Figure 16 is frequently employed in the literature to describe grain and grain boundary contributions in ceramic materials. However, this interpretation should not be generalized, particularly for unsintered pellet samples or ceramic–polymer composites, in which different electrical processes may contribute to the impedance response. In such systems, the low-frequency branch is generally associated with interfacial phenomena, such as the electrode–electrolyte interface and/or the interface between the ceramic and polymer phases. Therefore, a more careful interpretation of the equivalent circuit and the physical processes associ-

ated with each branch requires analyzing the characteristic capacitances, which provide an additional criterion for identifying the electrical processes involved, as shown in Table 2.

Figure 16: Relationship between the polycrystalline microstructure, the idealized grain-and-grain-boundary model, the equivalent electrical circuit, and the corresponding Nyquist impedance response.



Source: Prepared by the author with graphical assistance from ChatGPT (OpenAI) (2026).

Table 2: Typical capacitance ranges associated with different electrical processes in impedance spectroscopy.

Capacitance (F)	**Typical process**
10^{-12}–10^{-11}	Bulk / grain
$\sim 10^{-11}$	Second phase
10^{-11}–10^{-8}	Grain boundary
10^{-10}–10^{-9}	Bulk ferroelectric
10^{-9}–10^{-7}	Surface layer
10^{-7}–10^{-5}	Sample–electrode interface / Double layer / Surface charge
$\sim 10^{-4}$	Electrochemical reactions / Surface layer at electrode / Adsorption

Source: Adapted from Zhang, Pu e Chen (2023).

In addition to software based on the Distribution of Relaxation Times (DRT) anal-

ysis, equivalent electrical circuits can be obtained by fitting impedance spectra with the modified Debye model. In this framework, each relaxation process is represented by a parallel resistor–constant phase element association, $(R \parallel \text{CPE})$, connected in series with a resistance R_s. For a system comprising two relaxation processes, the real part of the impedance is given by Equation 2.21 (NAHIR, 2005).

$$Z'(\omega) = R_s + \sum_{k=1}^{2} \frac{R_k \left[1 + (\omega\tau_k)^{n_k} \cos\left(\frac{n_k\pi}{2}\right)\right]}{1 + 2(\omega\tau_k)^{n_k} \cos\left(\frac{n_k\pi}{2}\right) + (\omega\tau_k)^{2n_k}}. \tag{2.21}$$

where $Z'(\omega)$ is the real part of the complex impedance, R_s is the series resistance, R_k is the resistance associated with the k-th relaxation process, τ_k is its characteristic relaxation time, n_k is the constant-phase exponent associated with that process ($0 < n_k \leq 1$), and $\omega = 2\pi f$ is the angular frequency, with f denoting the frequency. When $n_k = 1$, the ideal Debye response is recovered.

The constant phase element (CPE) is characterized by Q and n, with admittance given by $Y_{\text{CPE}}(\omega) = Q(j\omega)^n$. For the $R \parallel$ CPE circuit branch, the characteristic time satisfies $\tau = (RQ)^{1/n}$. When $n = 1$, the model reduces to the pure Debye case $(R \parallel C)$, in which $\tau = RC$. For $n \neq 1$, however, the CPE parameter Q cannot be directly interpreted as a capacitance. Therefore, an effective capacitance was calculated for each $R \parallel$ CPE branch according to Equation 2.22 (GOLDSBERRY *et al.*, 2024).

$$C_{\text{eff}} = Q^{1/n} R^{(1-n)/n}, \tag{2.22}$$

where R is the resistance associated with the corresponding $R \parallel$ CPE branch. This relation also reduces to $C_{\text{eff}} = Q = C$ when $n = 1$.

Therefore, complex impedance spectroscopy is of paramount importance for determining the electrical properties of a material, such as its electronic or ionic conductivity (ALJARRAH; SALMAN, 2021), as well as its dielectric properties. These dielectric characteristics can be analyzed using a different formalism, namely the frequency dependence of the complex permittivity, as described by Equation 2.23 (HAKIKI; LIN; LIN, 2024).

$$\varepsilon^*(\omega) = \frac{1}{j\omega C_0 Z^*(\omega)} \tag{2.23}$$

where C_0 is the geometric capacitance, previously defined as $C_0 = \varepsilon_0 A/d$.

In addition, impedance spectroscopy data can be analyzed using other formalisms,

such as the admittance formalism, Y, described by Equations 2.24 and 2.25, as proposed by Bauerle (1969). Another widely used approach is the electric modulus formalism, M^*, which is defined as the reciprocal of the complex permittivity, as expressed by Equations 2.26 and 2.27.

$$Y(\omega) = \frac{1}{Z(\omega)} = \frac{1}{Z'(\omega) + jZ''(\omega)} \tag{2.24}$$

$$Y(\omega) = G(\omega) + jB(\omega) \tag{2.25}$$

where $G(\omega)$ is the conductance, corresponding to the real part of $Y(\omega)$, and $B(\omega)$ is the susceptance, corresponding to its imaginary part.

$$M^*(\omega) = \frac{1}{\varepsilon^*(\omega)} \tag{2.26}$$

$$M^*(\omega) = M'(\omega) + jM''(\omega) \tag{2.27}$$

where $M'(\omega)$ and $M''(\omega)$ are the real and imaginary components of the complex electric modulus, respectively.

In addition to these formalisms, several models are used to fit the dielectric response curves of materials. Table 3 presents some of these models.

In Table 3, ε_s is the static permittivity of the material, ω is the angular frequency, τ is the characteristic relaxation time, α is a dimensionless parameter of the Cole–Cole model ($0 < \alpha < 1$), β is a dimensionless parameter ($0 < \beta < 1$) used in the Davidson–Cole model, ω_p is the characteristic relaxation (or peak) frequency, and m and n are dimensionless parameters of the Jonscher–Dissado–Hill model that describe the dispersion of the dielectric relaxation process.

Within the complex permittivity formalism, the AC electrical conductivity (σ_{AC}) can be derived from the imaginary part of the complex permittivity, as expressed by Equation 2.28 (BARSOUKOV; MACDONALD, 2005).

$$\sigma_{AC} = \omega\varepsilon_0\varepsilon'' \tag{2.28}$$

where ω is the angular frequency, ε_0 is the vacuum permittivity, and ε'' is the imaginary

part of the complex permittivity, also known as the dielectric loss factor.

Table 3: Dielectric relaxation models and asymptotic behavior of the imaginary part of the complex permittivity.

Models	$\varepsilon^*(\omega)$	$\varepsilon''(\omega) \propto$
Debye	$\frac{\varepsilon_s}{1+j\omega\tau}$	$\omega^{-1},\ \omega \ll \omega_p$ $\omega^{-1},\ \omega \gg \omega_p$
Cole–Cole	$\frac{\varepsilon_s}{1+(j\omega\tau)^{1-\alpha}}$ $0 < \alpha < 1$	$\omega^{1-\alpha},\ \omega \ll \omega_p$ $\omega^{-(1-\alpha)},\ \omega \gg \omega_p$
Davidson–Cole	$\frac{\varepsilon_s}{(1+j\omega\tau)^{\beta}}$ $0 < \beta < 1$	$\omega^{-1},\ \omega \ll \omega_p$ $\omega^{-\beta},\ \omega \gg \omega_p$
Havriliak–Negami	$\frac{\varepsilon_s}{[1+(j\omega\tau)^{1-\alpha}]^{\beta}}$ $0 < (\alpha, \beta) < 1$	$\omega^{1-\alpha},\ \omega \ll \omega_p$ $\omega^{-\beta(1-\alpha)},\ \omega \gg \omega_p$
Jonscher–Dissado–Hill	$\propto (j\omega)^m;\ \omega = \omega_p$ $S = m$ or $(-1-n)$ where $0 < (m, n) < 1$ $\propto [1+j\omega\tau]^{-1},$ near ω_p	$\omega^m,\ \omega \ll \omega_p$ $\omega^4,$ near ω_p $\omega^1,$ near ω_p $\omega^{1-n},\ \omega \gg \omega_p$

Source: Adapted from (DELGADO *et al.*, 2003).

Furthermore, the AC electrical conductivity (σ_{AC}) can also be determined from the imaginary part of the complex permittivity using the permittivity formalism, as expressed by Equation 2.28 (BARSOUKOV; MACDONALD, 2005). The frequency dependence of the AC electrical conductivity can be further analyzed using Jonscher's universal power law, described by Equation 2.29.

$$\sigma(\omega) = \sigma_{\text{DC}} + A\omega^s, \qquad 0 < s < 1 \tag{2.29}$$

where $\sigma(\omega)$ is the effective electrical conductivity as a function of the angular frequency ω, σ_{DC} is the direct current (DC) conductivity, A is a pre-exponential factor associated with the dispersive contribution to the conductivity, and s is the dispersion exponent ($0 < s < 1$), whose value is related to the charge transport mechanism and the relaxation processes occurring within the material.

Thus, complex impedance spectroscopy provides a comprehensive set of data that enables a detailed evaluation of the electrical properties of materials.

3 MATERIALS AND METHODS

All synthesis, sample preparation, storage, and characterization procedures were carried out under laboratory ambient atmosphere. Unless otherwise specified, all procedures were performed at room temperature. Thermal treatments and oven-drying steps were conducted at the temperatures described for each experimental procedure, also under ambient atmosphere. Consequently, the powders and pellets were handled and stored under laboratory ambient conditions throughout the experimental work. Powder samples were stored in polypropylene microcentrifuge (Eppendorf) tubes, whereas pellets were stored in unsealed plastic containers. No specific control of the ambient humidity or CO_2 concentration was employed during sample preparation, storage, or characterization, except where a controlled atmosphere is explicitly specified for the experimental technique.

Throughout this work, when uncertainties are reported in parentheses, they refer to the uncertainty in the last digits of the corresponding value; for example, $2.11477(8)$ represents 2.11477 ± 0.00008. The number of reported decimal places was defined according to the precision of the corresponding uncertainty. In fitting and refinement procedures, parameters indicated as *fixed* were held constant at values obtained from preliminary fits, particularly when they exhibited lower uncertainties. This procedure was used to reduce the number of degrees of freedom and parameter correlations during the refinement of the remaining parameters.

3.1 Sodium Titanate-Based Materials

3.1.1 Synthesis of Lithium-Doped Sodium Titanate

The synthesis of lithium-doped sodium titanate (NLTO) was carried out by a sonochemical route adapted from the methodology proposed by Leyet *et al.* (2018), and

Silva *et al.* (2026). Titanium isopropoxide ($C_{12}H_{28}O_4Ti$, Aldrich, $> 97\%$) was used as the titanium precursor, whereas sodium hydroxide (NaOH, Synth, 98%) was employed as the sodium source, and lithium acetate dihydrate ($C_2H_3LiO_2 \cdot 2H_2O$, Sigma-Aldrich, 97%) for lithium doping.

Initially, titanium isopropoxide was dissolved in isopropyl alcohol, while sodium hydroxide and lithium acetate dihydrate were both dissolved in distilled water at a concentration of 1 mol·L^{-1}. The three solutions were then mixed under magnetic stirring until a homogeneous suspension was obtained. Subsequently, the suspension was subjected to sonication for 15 min using an ultrasonic processor operating at 487.5 W (65% of the nominal power).

After the sonochemical treatment, the resulting material was dried in an oven at $100\,^{\circ}$C for 24 h. The dried powders were then calcined in a muffle furnace at $900\,^{\circ}$C for 1 h under air (uncontrolled atmosphere), using a heating rate of $10\,^{\circ}\mathrm{C\,min^{-1}}$, followed by furnace cooling to room–temperature.

The amounts of each reagent were calculated from the nominal overall stoichiometry presented in Equation 3.1. The equation is an idealized representation intended only to establish the reactant molar ratios and does not represent the individual hydrolysis, condensation, and calcination steps involved in the synthesis

$$2\,\mathrm{NaOH} + 3\,\mathrm{C_{12}H_{28}O_4Ti} \longrightarrow \mathrm{Na_2Ti_3O_7} + 3\,\mathrm{C_{12}H_{28}O_2} + \mathrm{H_2O} \tag{3.1}$$

Nominal substitutions of sodium with lithium were performed to obtain the composition $Na_{2-x}Li_xTi_3O_7$, with $x = 0.03$. The selected lithium content was based on the results of a previous study by Silva *et al.* (2026), reproduced in Annex A, in which this composition exhibited the most favorable electrical performance.

3.1.2 Synthesis of Poly(*o*-methoxyaniline) (POMA)

The synthesis of poly(*o*-methoxyaniline) (POMA) was carried out following the procedure reported by Silva *et al.* (2021) and Sanches *et al.* (2011). The residual Cl^- content, the degree of protonation, and the doping state of the polymer after washing to neutral pH were not evaluated in the present study, as these parameters were beyond the scope of this work. Initially, $28\,\mathrm{mL}$ of *o*-anisidine ($CH_3OC_6H_4NH_2$, Sigma-Aldrich, 99%) was dissolved in $300\,\mathrm{mL}$ of $1\,\mathrm{mol\,L^{-1}}$ hydrochloric acid (HCl, Synth, 37%).

Subsequently, a solution containing $11.64\,\mathrm{g}$ of ammonium persulfate ($(NH_4)_2S_2O_8$, Sigma-Aldrich, 98%) dissolved in $200\,\mathrm{mL}$ of $1\,\mathrm{mol\,L^{-1}}$ HCl was added dropwise to the monomer solution under continuous magnetic stirring.

The oxidative polymerization was carried out at room temperature under continuous magnetic stirring for $3\,\mathrm{h}$. The resulting precipitate was collected by vacuum filtration using an oil-free diaphragm pump and thoroughly washed with distilled water until neutral pH was reached, ensuring the removal of residual acid and reaction by-products. Finally, the polymer was dried under vacuum for five days, yielding POMA as a fine powder.

3.1.3 Preparation of NLTO/POMA Composites

The ceramic-polymer composites, designed with a 3–0 connectivity configuration (Figure 7), were prepared by mixing the NLTO ceramic matrix with POMA at polymer contents of 0, 10, 15, 35, and 50 wt%. These compositions correspond to the samples NLTO, NLTO/POMA-10, NLTO/POMA-15, NLTO/POMA-35, and NLTO/POMA-50, respectively. The appropriate amounts of NLTO and POMA were accurately weighed and subsequently dry-mixed in an agate mortar by gentle grinding until a visually homogeneous powder mixture was obtained.

3.1.4 Characterization

X-ray diffraction (XRD) measurements were performed using a PANalytical Empyrean diffractometer operating with Cu K_α radiation ($\lambda = 1.5406$ Å) in Bragg–Brentano geometry at the Laboratory of Synthesis of Applied Nanostructures (LabSiNap), Federal Rural University of Pernambuco (UFRPE), Brazil. The instrument was operated at 40 kV and 40 mA, and diffraction patterns were collected over a 2θ range from 2° to 80° with a step size of 0.0205° using a divergence slit of 0.2°. The total scan time was ≈ 20 min. Rietveld refinements were carried out using the GSAS-II software. The background was modeled using a first-kind Chebyshev polynomial with 12 refined coefficients, while the diffraction peak profiles were described using the Thompson–Cox–Hastings pseudo-Voigt function with the Finger–Cox–Jephcoat asymmetry correction. Preferred orientation was not modeled during the Rietveld refinements. Instrumental profile parameters (U, V, W, X, Y, and SH/L) were kept fixed during the refinement. The refined parameters included the background coefficients, sample dis-

placement, scale factors, lattice parameters, and phase fractions. Refinements were considered converged when successive refinement cycles produced stable agreement indices and negligible variations in the refined parameters.

Fourier-transform infrared (FTIR) spectra were recorded using a Cary 630 spectrometer (Agilent Technologies, USA) equipped with an attenuated total reflectance (ATR) accessory and a zinc selenide (ZnSe) crystal at the Yvonne Mascarenhas Laboratory (LabYM), Federal University of Amazonas (UFAM), Brazil. The spectra were collected over the wavenumber range from $4000\,\mathrm{cm}^{-1}$ to $650\,\mathrm{cm}^{-1}$. During the measurements, the samples were placed in direct contact with the ATR crystal, positioned approximately $1.8\,\mathrm{mm}$ from the prism.

Local harmonic vibrational calculations were performed to assist the interpretation of the FTIR spectra of the $Na_2Ti_3O_7$ phase. The crystallographic structures obtained from the Rietveld refinement were used as input, and the Ti–O local environment was analyzed considering only the nearest oxygen atoms with Ti–O bond lengths shorter than 2.60 Å. The force constants were estimated according to the procedure described in Section 2.2.7.1, and the corresponding local vibrational modes were obtained from the diagonalization of the mass-weighted Hessian matrix. The structural data were processed using the Atomic Simulation Environment (ASE) (LARSEN *et al.*, 2017), and the calculations were performed with custom Python scripts.

Scanning electron microscopy (SEM) analyses were performed using a JEOL JSM-IT500HR microscope equipped with a secondary electron detector (SED) at the Laboratory of Synthesis of Applied Nanostructures (LabSiNap), Federal Rural University of Pernambuco (UFRPE), Brazil. For the NTO and NLTO samples, the measurements were carried out at an accelerating voltage of $5\,\mathrm{kV}$, with a working distance of $13.5\,\mathrm{mm}$ and a magnification of $7000\times$. The acquired micrographs were recorded with a scale bar of $2\,\mu\mathrm{m}$. For the NLTO/POMA composites, the samples were first coated with a $10\,\mathrm{nm}$-thick gold layer to improve surface conductivity. The measurements were then performed at an accelerating voltage of $10\,\mathrm{kV}$, using a working distance ranging from $4.97\,\mathrm{mm}$ to $8.03\,\mathrm{mm}$ and a magnification of $10\,000\times$. The acquired micrographs were recorded with a scale bar of $5\,\mu\mathrm{m}$.

Simultaneous thermogravimetric (TG) and differential scanning calorimetry (DSC) measurements were performed using a TA Instruments SDT Q600 thermal analyzer at the Physicochemical Testing Laboratory (LFQM), Faculty of Technology (FT), Federal

University of Amazonas (UFAM), Brazil. The derivative thermogravimetric (DTG) curves were calculated from the TG data. Approximately $10\,\mathrm{mg}$ of each sample was placed in a $90\,\mu\mathrm{L}$ alumina crucible without a lid. The measurements were carried out under a nitrogen atmosphere (N_2 5.0) with a flow rate of $30\,\mathrm{mL\,min^{-1}}$. The samples were heated from room–temperature to $1100\,^{\circ}\mathrm{C}$ at a heating rate of $10\,^{\circ}\mathrm{C\,min^{-1}}$, followed by an isothermal hold of $10\,\mathrm{min}$.

Complex impedance spectroscopy (EIS) measurements were performed using a Solartron 1260 impedance analyzer at the Laboratory of Technological Materials Processing (LPMAT), Faculty of Technology (FT), Federal University of Amazonas (UFAM), Brazil. The measurements were carried out at room temperature with an excitation voltage of 500 mV over the frequency range from 10 Hz to 1 MHz.The excitation voltage amplitude of 500 mV was selected to improve the signal-to-noise ratio due to the high resistivity of the ceramic and ceramic–polymer samples. Although lower excitation amplitudes are more commonly employed, impedance studies of ceramic materials using Solartron instrumentation have also been reported with this excitation amplitude (NOBRE; LANFREDI, 2003; SILVA *et al.*, 2023). A Solartron 12962A sample holder was employed, featuring two parallel-plate brass electrodes, one fixed and the other adjustable to accommodate the sample thickness. A slight mechanical pressure was applied to ensure good electrical contact. For pellet preparation, the material powder was compacted by uniaxial pressing under a load of 1.5 tons for 2.5 min. No binder was used during pellet preparation. No conductive coating was applied to the samples prior to the measurements. All pellets had a diameter of $10\,\mathrm{mm}$. The pellet thicknesses were $1.55\,\mathrm{mm}$ (NLTO), $1.51\,\mathrm{mm}$ (NLTO/POMA-10), $1.55\,\mathrm{mm}$ (NLTO/POMA-15), $1.75\,\mathrm{mm}$ (NLTO/POMA-35), $2.00\,\mathrm{mm}$ (NLTO/POMA-50), and $1.82\,\mathrm{mm}$ (POMA). The mass of the pellets ranged from $0.188\,\mathrm{g}$ to $0.321\,\mathrm{g}$. Based on the geometrical dimensions, the estimated geometrical densities were $2.579\,\mathrm{g\,cm^{-3}}$ for NLTO, $2.707\,\mathrm{g\,cm^{-3}}$ for NLTO/POMA-10, $2.604\,\mathrm{g\,cm^{-3}}$ for NLTO/POMA-15, $2.197\,\mathrm{g\,cm^{-3}}$ for NLTO/POMA-35, $1.884\,\mathrm{g\,cm^{-3}}$ for NLTO/POMA-50, and $1.315\,\mathrm{g\,cm^{-3}}$ for POMA.

For each composition, at least three representative pellets were prepared and characterized under identical processing and measurement conditions. There was no variation above 5%.

The experimental impedance data were analyzed in Python using the SciPy library. The $Z'(f)$ data were fitted with the curve_fit routine according to the modified Debye

model described in Section 2.2.7.3. The AC conductivity data were fitted using the Jonscher universal power law with the least_squares routine. The experimental datasets were imported from CSV files using the pandas library. The optimized parameters and their respective standard errors were estimated from the covariance matrix returned by the fitting procedures.

In addition, the impedance spectra were fitted to equivalent circuits using ZView software (Scribner Associates, Inc., Southern Pines, NC, USA) by means of complex nonlinear least-squares fitting. Calculated-modulus weighting was employed, and the quality of the fits was assessed from the chi-squared values. A maximum of 100 iterations was allowed, and, when necessary, selected parameters were held fixed to ensure convergence of the fitting procedure. The fitting was performed over the entire measured frequency range.

For the selection of the equivalent-circuit models used for fitting in ZView, the experimental data were processed and different equivalent-circuit models were compared using a routine developed in Python 3.x with the NumPy, pandas, and SciPy libraries. The fits were performed by nonlinear least squares using the curve_fit function, with weighting by the inverse of the impedance modulus, according to Equation 3.2 (ŽIC *et al.*, 2020).

$$w_i = \frac{1}{|Z(\omega_i)|}. \tag{3.2}$$

The consistency of the experimental impedance spectra was evaluated using the linear Kramers–Kronig (Lin-KK) test. In addition, the quality of the fits was assessed from the relative residuals normalized by the impedance modulus, as defined in Equations 3.3 and 3.4 (PEREZ, 2025).

$$\Delta Z'(\omega_i) = \frac{Z'_{\text{exp}}(\omega_i) - Z'_{\text{fit}}(\omega_i)}{|Z_{\text{exp}}(\omega_i)|} \times 100, \tag{3.3}$$

$$\Delta Z''(\omega_i) = \frac{Z''_{\text{exp}}(\omega_i) - Z''_{\text{fit}}(\omega_i)}{|Z_{\text{exp}}(\omega_i)|} \times 100. \tag{3.4}$$

Equivalent-circuit models comprising one arc, two arcs, one arc associated with a CPE tail, and one arc associated with a finite-length Warburg element were compared. The comparison among the competing models was performed using the Akaike information criterion (AIC) and Bayesian information criterion (BIC), according to Equa-

tions 3.5 and 3.6 (BURNHAM; ANDERSON, 2002; AKAIKE, 1974).

$$\text{AIC} = N \ln\left(\frac{\text{WRSS}}{N}\right) + 2k, \tag{3.5}$$

$$\text{BIC} = N \ln\left(\frac{\text{WRSS}}{N}\right) + k \ln N, \tag{3.6}$$

where N represents the number of data points considered in the fitting, k is the number of adjustable parameters, and WRSS is the weighted residual sum of squares. Lower AIC and BIC values were used as statistical criteria for comparing the competing models, together with residual analysis and the physical consistency of the fitted parameters.

The need to include an ohmic series resistance (R_s) in the final equivalent circuits was also quantitatively evaluated. The R_s/R_1 ratio remained below 0.2% for most samples, with a maximum value below 1.2%. Based on the BIC criterion, R_s was therefore omitted from the final circuit topology. This reduced the number of free parameters in the nonlinear least-squares (NLLS) fitting without substantially affecting the resistance associated with the HF process (R_1).

The possible contribution of percolation to the electrical behavior of the composites was evaluated using the General Effective Medium (GEM) model proposed by McLachlan, Blaszkiewicz e Newnham (1990) and Zare e Rhee (2019). This model combines concepts from percolation theory and effective-medium theory and describes the electrical conductivity of a binary composite as a function of the volume fraction of its constituent phases. The GEM model is described by Equation 3.7.

$$\frac{(1-\phi)\left(\sigma_{\text{c}}^{1/t} - \sigma_{\text{m}}^{1/t}\right)}{\sigma_{\text{c}}^{1/t} + A\sigma_{\text{m}}^{1/t}} + \frac{\phi\left(\sigma_{\text{p}}^{1/t} - \sigma_{\text{m}}^{1/t}\right)}{\sigma_{\text{p}}^{1/t} + A\sigma_{\text{m}}^{1/t}} = 0, \tag{3.7}$$

where σ_{c}, σ_{p}, and σ_{m} are the electrical conductivities of the ceramic phase, POMA, and the composite, respectively; ϕ is the POMA volume fraction; t is the critical exponent; and

$$A = \frac{1-\phi_c}{\phi_c}, \tag{3.8}$$

where ϕ_c represents the estimated percolation threshold.

The POMA volume fraction (ϕ) used in the GEM model was calculated from the nominal mass fraction and the densities of the polymer and ceramic phases according to Equation 3.9.

$$\phi = \frac{w_{\text{POMA}}/\rho_{\text{POMA}}}{w_{\text{POMA}}/\rho_{\text{POMA}} + (1-w_{\text{POMA}})/\rho_{\text{ceramic}}}, \tag{3.9}$$

where w_{POMA} is the POMA mass fraction, ρ_{POMA} is the POMA density, and ρ_{ceramic} is the density of the corresponding ceramic matrix. For the LLZO-based system, the effective density of the ceramic matrix was estimated from the phase fractions obtained by Rietveld refinement and the densities of the identified crystalline phases.

In the GEM formalism, ϕ_c represents the critical volume fraction, or percolation threshold, at which the conductive phase is predicted to form a continuous conducting network throughout the composite. The parameter t is the critical exponent describing the evolution of conductivity in the vicinity of the percolation threshold. Unlike ϕ, which was calculated independently for each composition from the nominal POMA content and phase densities, ϕ_c and t were obtained as fitting parameters of the GEM model.

The values of ϕ_c and t were estimated by nonlinear fitting of the GEM model using Python with the NumPy and SciPy libraries. Since the conductivity values span several orders of magnitude, the optimization was performed in logarithmic conductivity space by minimizing the differences between $\log_{10}(\sigma_{\text{exp}})$ and $\log_{10}(\sigma_{\text{GEM}})$ over the investigated compositions.

The quality of the resulting fit was evaluated using the coefficient of determination in logarithmic scale, $R^2_{\log}$, described by Equation 3.10.

$$R^2_{\log} = 1 - \frac{\sum_i \left[\log_{10}(\sigma_{\text{exp},i}) - \log_{10}(\sigma_{\text{GEM},i})\right]^2}{\sum_i \left[\log_{10}(\sigma_{\text{exp},i}) - \overline{\log_{10}(\sigma_{\text{exp}})}\right]^2}, \tag{3.10}$$

where $\sigma_{\text{exp},i}$ and $\sigma_{\text{GEM},i}$ are the experimental and GEM-calculated conductivities for each composition, respectively.

3.2 LLZO-Based Materials

3.2.1 Synthesis of Doped LLZO

The synthesis of doped LLZO was carried out using high-purity commercial reagents: La_2O_3 (Dinâmica, 99.9%), ZrO_2 (Sigma-Aldrich, 99%, 5 µm), Li_2CO_3 (Labsynth, 99%), MgO (Vetec and Sigma-Aldrich, 95%), and $Sr(C_2H_3O_2)_2$ (Vetec, 98%). The precursor amounts were calculated according to the nominal composition

$Li_{6.95}Mg_{0.15}La_{2.75}Sr_{0.25}Zr_2O_{12}$, which has been reported to exhibit high ionic conductivity and relative densities above $90\,\%$ (SAMSON *et al.*, 2019). To compensate for lithium volatilization during the heat treatment, a $12.9\,\%$ excess of Li_2CO_3 was added, corresponding to $0.4\,\mathrm{g}$ per $10\,\mathrm{g}$ of the nominal composition, following the procedure reported by Seo *et al.* (2020).

The precursor powders were homogenized by ball milling for 36 h and subsequently calcined at $1000\,^{\circ}\mathrm{C}$ for 4 h. After calcination, the powders were subjected to a second ball-milling step for 36 h to improve chemical homogeneity and reduce the particle size. To minimize lithium volatilization during calcination, the crucible was sealed with an alumina–PVA paste.

3.2.2 Preparation of LLZO/POMA Composites

The ceramic–polymer composites were prepared by mixing LLZO with 0, 1, 5, 10, and 15 wt% POMA, corresponding to the samples LLZO, LLZO/POMA-1, LLZO/POMA-5, LLZO/POMA-10, and LLZO/POMA-15, respectively. The appropriate amounts of LLZO and POMA were dispersed in distilled water using a proportion of $10\,\mathrm{mL}$ of water per gram of powder mixture. The suspension was subsequently homogenized in an ultrasonic bath for 15 min and then dried in an oven at $40\,^{\circ}\mathrm{C}$ for 24 h, yielding the ceramic–polymer composite powders.

3.2.3 Characterization

X-ray diffraction (XRD) patterns were acquired following the procedure described in Section 3.1.4, except for the 2θ range (5°–80°), the use of a divergence slit of 0.05°, the total acquisition time ($\approx$ 127 min), and the refinement of the instrumental profile parameters U, V, W, and X during the Rietveld analysis.

Fourier-transform infrared (FTIR) and TG/DSC measurements were performed under the same experimental conditions described in Section 3.1.4. For the LLZO/POMA series, the TG/DSC measurements were carried out from room–temperature to $1200\,^{\circ}\mathrm{C}$, while all other experimental parameters remained unchanged.

Scanning electron microscopy (SEM) measurements were performed using a field-emission scanning electron microscope (JSM-IT500HR, JEOL, Japan) equipped with a secondary electron detector at the Laboratory of Synthesis of Applied Nanostructures

(LabSiNap), Federal Rural University of Pernambuco (UFRPE), Brazil. Prior to examination, the samples were coated with a 10 nm-thick gold layer to improve surface conductivity. The measurements were carried out at an accelerating voltage of 5 kV, using a working distance ranging from 4.94 mm to 7.02 mm. The micrographs were acquired at a magnification of 15 000×, with a scale bar of 2 µm.

Electrochemical impedance spectroscopy (EIS) measurements were performed following the procedure described in Section 3.1.4. No conductive coating was applied to the samples prior to the measurements. For pellet preparation, the powder was compacted by uniaxial pressing at a load of 3 tons for 5 min. No binder was used during pellet preparation. All pellets had a diameter of 15 mm. The pellet thicknesses were 1.00 mm for LLZO, LLZO/POMA-1, LLZO/POMA-5, and LLZO/POMA-10, 1.23 mm for LLZO/POMA-15, and 1.97 mm for POMA. The mass of the pellets ranged from 0.292 g to 0.409 g. Based on the geometrical dimensions, the estimated geometrical densities were 2.939 g cm^{-3} for LLZO, 1.771 g cm^{-3} for LLZO/POMA-1, 1.698 g cm^{-3} for LLZO/POMA-5, 1.652 g cm^{-3} for LLZO/POMA-10, 1.353 g cm^{-3} for LLZO/POMA-15, and 1.175 g cm^{-3} for POMA. Following the same protocol described in Section 3.1.4, at least three representative pellets were prepared for each composition and used for the electrical characterization. There was no variation above 5%.

The selection of the equivalent-circuit models, the decision to omit a series resistance, and the evaluation of the conductivity behavior using the General Effective Medium (GEM) percolation model were performed according to the procedures described in Section 3.1.4.

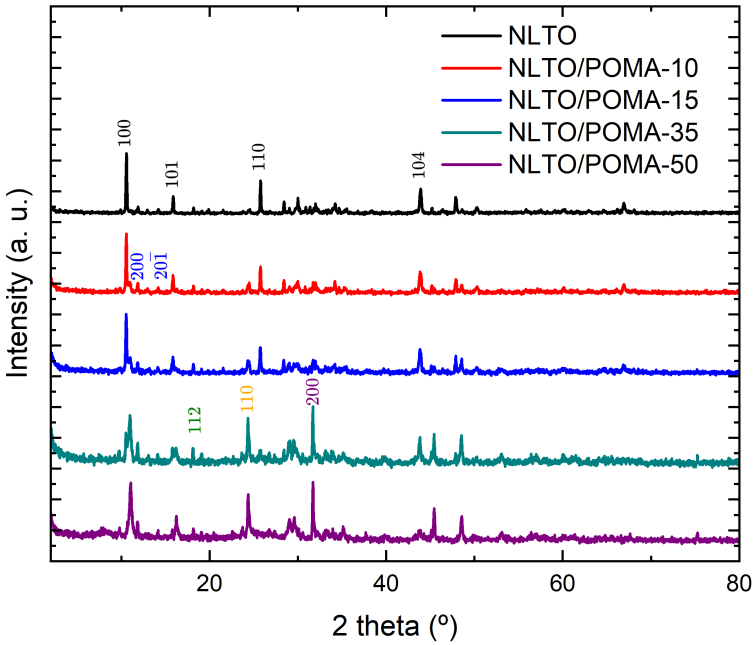
4 RESULTS AND DISCUSSION

4.1 Structural and Electrical Characterization of NLTO/POMA Composites

4.1.1 POMA-Induced Structural and Phase Evolution

Figure 17 presents the experimental X-ray diffraction patterns of the NLTO/POMA composites. The diffraction patterns reveal the evolution of the crystalline phases as a function of the POMA content. To facilitate phase identification, the main diffraction peaks were indexed according to their corresponding Miller indices.

Figure 17: Experimental X-ray diffraction patterns of NLTO and NLTO/POMA composites.



Source: Prepared by the author.

The diffraction patterns indicate that the $Na_2Ti_3O_7$ phase is still the primary crystalline structure of the NLTO, NLTO/POMA-10, and NLTO/POMA-15 samples. This conclusion is corroborated by the strong reflection at $2\theta \approx 10.5°$, which is indexed as (100), corresponding to the most intense diffraction peak of $Na_2Ti_3O_7$ (SILVA *et al.*, 2026; SILVA *et al.*, 2025). For the NLTO/POMA-35 and NLTO/POMA-50 samples, this reflection is significantly diminished, indicating a decrease in the proportion of this phase.

The reflections indexed as (200) ($2\theta \approx 11.8°$) and $(2\ 0\ \bar{1})$ ($2\theta \approx 14.1°$), which are present in all samples, are characteristic of the $Na_2Ti_6O_{13}$ phase (YOUSSRY; MUSSA, 2021). These peaks become progressively more intense with increasing POMA content, particularly for the NLTO/POMA-35 and NLTO/POMA-50 samples, indicating an increase in the proportion of this secondary phase.

The diffraction peak indexed as (112), located at $2\theta \approx 18.1°$, is attributed to the $NaLiTi_3O_7$ phase (YAHYA *et al.*, 2023). This phase results from the incorporation of lithium into the layered structure of $Na_2Ti_3O_7$ during the lithium-doping process and is identified in all investigated compositions, indicating that it remains stable after composite preparation.

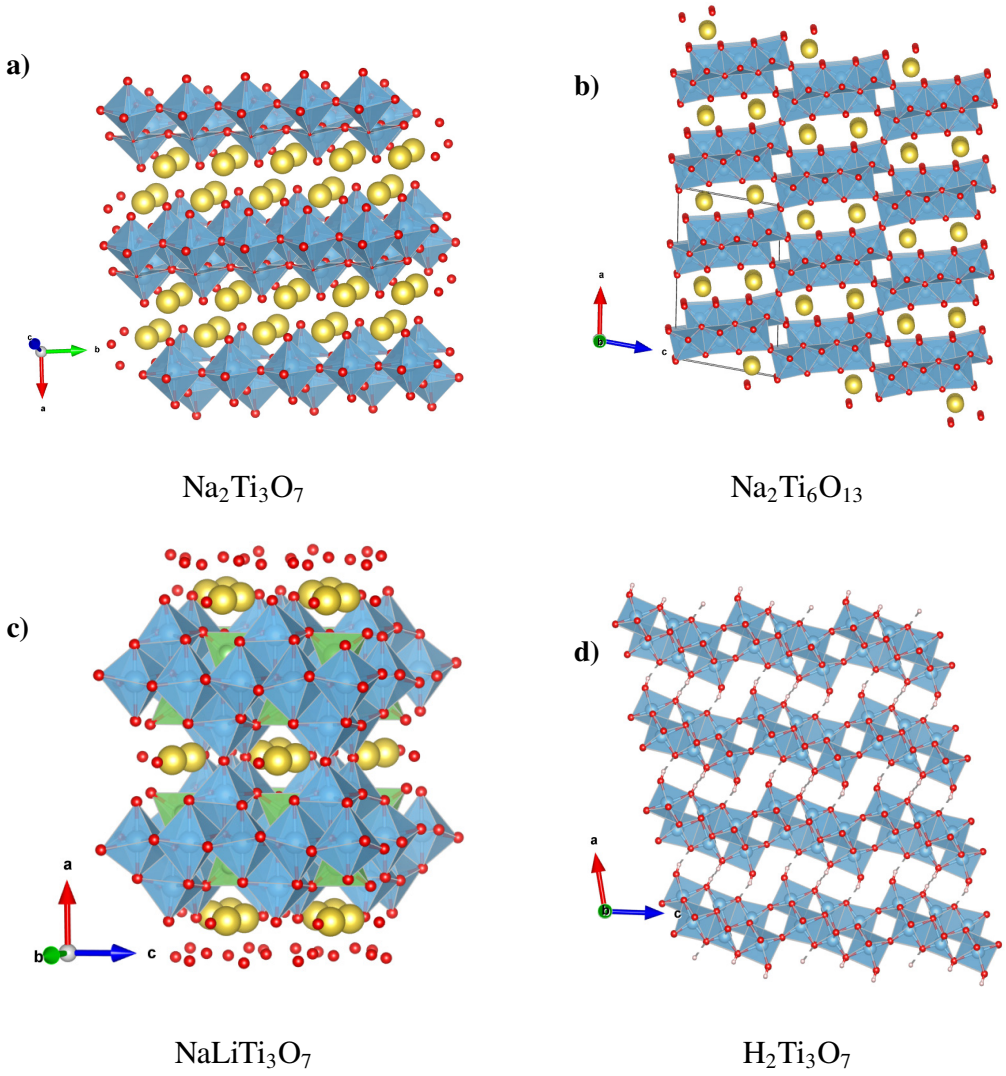
Additional crystalline phases become more evident in the composites containing 35 wt% and 50 wt% POMA. The reflection indexed as (110), located at $2\theta \approx 24.3°$, is assigned to the $H_2Ti_3O_7$ phase (ZÁRATE *et al.*, 2007; CHANG; LIN; CHOU, 2020), while the peak indexed as (200) at $2\theta \approx 31.7°$ corresponds to crystalline NaCl (WANG *et al.*, 2025). The formation of $H_2Ti_3O_7$ is associated with the partial replacement of sodium ions by hydrogen within the layered titanate structure, whereas the presence of NaCl is attributed to the interaction between sodium-containing species from the ceramic phase and hydrochloric acid employed during the synthesis of HCl-doped POMA.

Overall, the progressive reduction of the $Na_2Ti_3O_7$ reflections, accompanied by the increase of the $Na_2Ti_6O_{13}$, $H_2Ti_3O_7$, and NaCl phases, suggests that increasing POMA contents promote chemical interactions at the ceramic–polymer interface. These interactions become more pronounced at higher polymer loadings, leading to partial modifications of the original titanate composition and consequently altering the phase assemblage of the composites.

Figures 18a–d present the crystal structures of the $Na_2Ti_3O_7$, $Na_2Ti_6O_{13}$,

$NaLiTi_3O_7$, and $H_2Ti_3O_7$ phases obtained from the crystallographic data used in the Rietveld refinement. In these representations, the red, blue, yellow, green, and white spheres correspond to O, Ti, Na, Li, and H atoms, respectively.

Figure 18: Crystal structures of the phases identified by Rietveld refinement.



Source: Crystal structures generated in VESTA from the refined crystallographic information files (CIFs).

Among the identified phases, $Na_2Ti_3O_7$ and $H_2Ti_3O_7$ exhibit layered structures formed by TiO_6 octahedra, with the cations located between adjacent layers (TSIAMT-SOURI *et al.*, 2018; PAK *et al.*, 2023; LI *et al.*, 2026; LIU *et al.*, 2023). This structural arrangement facilitates ion-exchange reactions and provides a plausible explanation for the partial transformation of $Na_2Ti_3O_7$ into $H_2Ti_3O_7$ observed in the composites with higher POMA contents.

In contrast, the $Na_2Ti_6O_{13}$ and $NaLiTi_3O_7$ phases possess three-dimensional frameworks composed of interconnected TiO_6 octahedra. In these structures, the alkali ions are accommodated inside tunnels or crystallographic sites within the framework rather than between layers (YANG *et al.*, 2024). This structural characteristic makes ion exchange less favorable and may explain why both phases become progressively more representative as the POMA content increases.

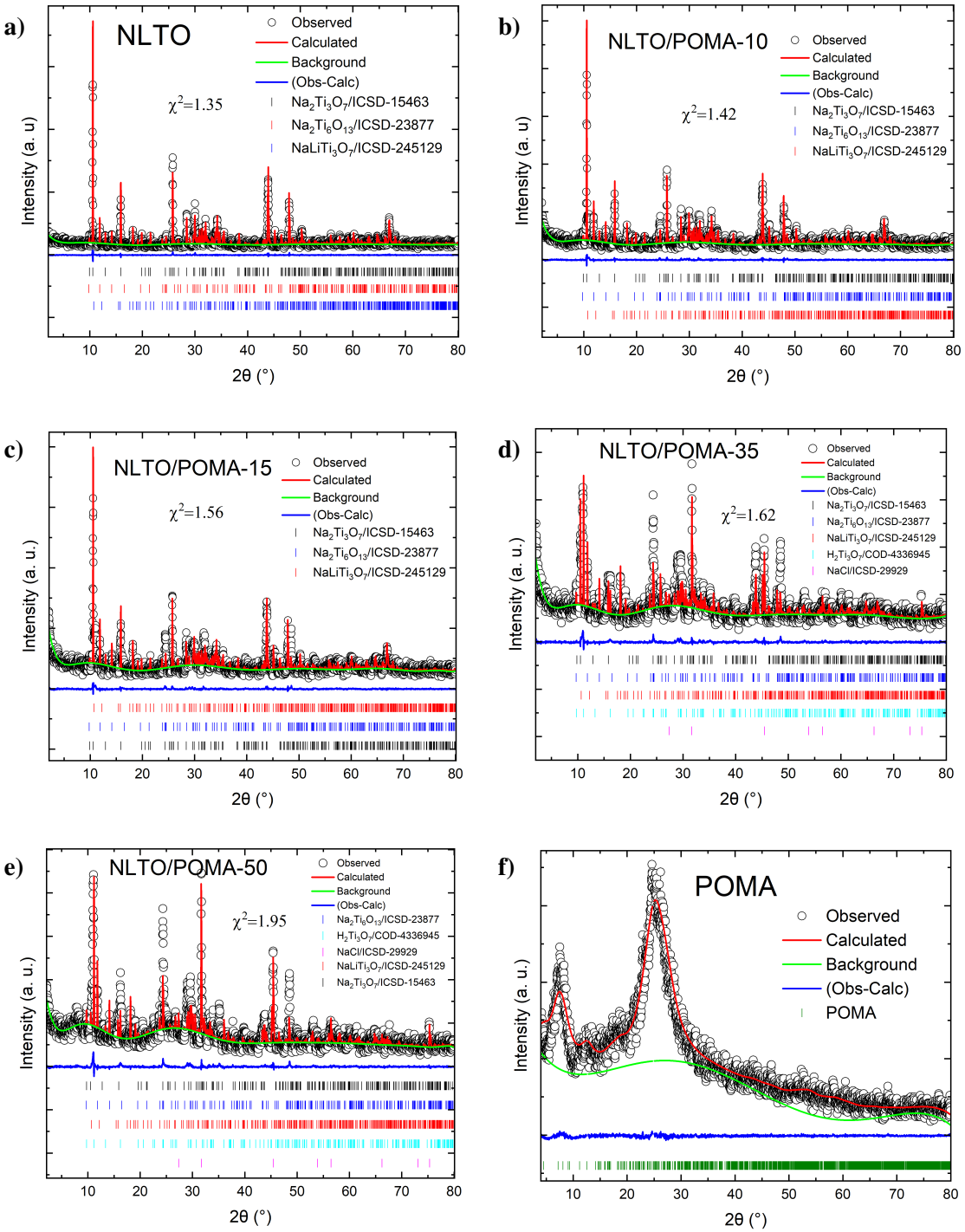
Therefore, the structural representations are consistent with the phase evolution obtained from the Rietveld refinement, indicating that the layered $Na_2Ti_3O_7$ phase is more susceptible to chemical modification during composite preparation, whereas the three-dimensional titanate phases remain comparatively less affected.

Figures 19a–f present the Rietveld refinement profiles of the NLTO and NLTO/POMA samples. The refined lattice parameters and phase fractions are summarized in Tables 4 and 5, respectively. The agreement between the experimental and calculated diffraction patterns is consistent with the crystalline phases previously identified from the experimental X-ray diffraction patterns.

Before discussing the results in detail, it is important to emphasize that Rietveld refinement does not allow quantification of the amorphous fraction corresponding to POMA because of its predominantly amorphous nature, as evidenced by Figure 19f, and because no internal standard was added to the samples prior to the X-ray diffraction measurements. Therefore, all phase weight percentages reported in this work correspond only to the crystalline phases included in the refinement model and are normalized with respect to the total modeled crystalline fraction. Consequently, they should not be interpreted as the absolute composition of the composites. Nevertheless, these phase fractions remain suitable for evaluating the relative evolution of the crystalline phases with increasing POMA addition.

The addition of POMA progressively modifies the phase composition of the composites. The amount of $Na_2Ti_3O_7$ decreases from 79.3 ± 0.7 wt% in the pristine NLTO sample to 72.3 ± 0.9 wt% and 67.5 ± 1.1 wt% for the NLTO/POMA-10 and NLTO/POMA-15 composites, respectively. This reduction becomes considerably more pronounced for the NLTO/POMA-35 and NLTO/POMA-50 samples, where the phase fraction decreases to 25.0 ± 1.1 wt% and 3.7 ± 1.2 wt%, respectively.

Figure 19: Rietveld refinement profiles of (a) NLTO, (b) NLTO/POMA-10, (c) NLTO/POMA-15, (d) NLTO/POMA-35, and (e) NLTO/POMA-50. (f) Le Bail refinement profile of HCl-doped POMA.



Source: Prepared by the author.

Conversely, the Rietveld-refined phase fractions of $Na_2Ti_6O_{13}$ and $NaLiTi_3O_7$

gradually increase with increasing POMA content. The refined phase fraction of $Na_2Ti_6O_{13}$ increases from 9.4 $\pm$ 0.5 wt% in the pristine sample to 21.2 $\pm$ 1.2 wt% in the NLTO/POMA-50 composite, whereas that of $NaLiTi_3O_7$ increases from 11.3 $\pm$ 0.6 wt% to 23.2 $\pm$ 1.4 wt%. It should be noted that these values correspond to normalized crystalline phase fractions obtained by the Rietveld refinement. Therefore, the increase in the refined fractions of $Na_2Ti_6O_{13}$ and $NaLiTi_3O_7$ does not necessarily imply a proportional increase in their absolute amounts. Rather, these values describe changes in their relative contributions to the crystalline fraction, particularly as the fraction of $Na_2Ti_3O_7$ decreases, and additional crystalline phases emerge at higher POMA contents.

Furthermore, the lattice parameters of the identified crystalline phases exhibit slight variations. The $Na_2Ti_3O_7$ phase shows a small increase in the unit-cell volume, from 291.493 (26) Å^3 for the pristine NLTO sample to 292.021 (48) Å^3 for the NLTO/POMA-15 composite. Since POMA macromolecules do not occupy interstitial sites or substitute lattice atoms, this expansion is most likely not the result of polymer incorporation into the crystal lattice. Therefore, these changes are more likely associated with indirect structural effects arising from the interaction between the ceramic particles and HCl-doped POMA, such as changes in the local chemical environment or ion-exchange processes occurring at the particle surface (KOZDRA *et al.*, 2024; LECHARTIER *et al.*, 2022). Although these variations are relatively small, they indicate that the preparation of the composite slightly influences the crystal structure of $Na_2Ti_3O_7$ without changing its crystallographic symmetry. For the $Na_2Ti_6O_{13}$ phase, the unit-cell volume shows only minor variations throughout the composite series, suggesting that its crystal structure is comparatively less affected by the incorporation of POMA.

A significant structural change occurs for the NLTO/POMA-35 and NLTO/POMA-50 samples, where the $H_2Ti_3O_7$ and NaCl phases are identified. The appearance of $H_2Ti_3O_7$ indicates a partial ion-exchange process in which sodium ions are replaced by hydrogen within the layered titanate structure, a mechanism commonly reported for sodium titanates due to their high ion-exchange capability (AN; WANG; WU, 2014; DONG *et al.*, 2024). In addition, the formation of crystalline NaCl is attributed to the interaction between sodium ions released from the titanate structure and chloride ions originating from the hydrochloric acid employed during the synthesis of HCl-doped POMA.

Table 4: Refined lattice parameters of the crystalline phases identified in the NLTO/POMA composites. Samples are identified as follows: P10 = NLTO/POMA-10; P15 = NLTO/POMA-15; P35 = NLTO/POMA-35; and P50 = NLTO/POMA-50.

Phase	**Parameter**	**NLTO**	**P10**	**P15**	**P35**	**P50**
$Na_2Ti_3O_7$	a (Å)	8.569(1)	8.574(2)	8.573(3)	8.554(6)	8.559(42)
	b (Å)	3.800(1)	3.800(1)	3.801(1)	3.795(1)	3.801(4)
	c (Å)	9.136(1)	9.141(2)	9.148(2)	9.147(6)	9.231(43)
	β (°)	101.571(5)	101.540(7)	101.586(9)	101.745(24)	102.514(177)
	V (Å^3)	291.493(26)	291.813(38)	292.021(48)	290.675(100)	293.145(572)
$Na_2Ti_6O_{13}$	a (Å)	15.125(6)	15.124(5)	15.143(6)	15.067(7)	15.095(7)
	b (Å)	3.750(1)	3.753(1)	3.756(1)	3.748(1)	3.748(1)
	c (Å)	9.164(4)	9.178(4)	9.166(5)	9.183(5)	9.167(5)
	β (°)	99.051(21)	99.072(19)	99.130(23)	99.007(24)	98.946(24)
	V (Å^3)	513.261(146)	514.456(144)	514.741(174)	512.146(196)	512.325(206)
$NaLiTi_3O_7$	a (Å)	16.512(4)	16.483(4)	16.523(4)	16.496(4)	16.502(4)
	b (Å)	11.232(3)	11.244(3)	11.240(3)	11.206(3)	11.211(3)
	c (Å)	11.486(3)	11.485(3)	11.498(3)	11.488(3)	11.461(3)
	V (Å^3)	2130.147(521)	2128.636(616)	2135.526(649)	2123.609(673)	2120.394(740)
$H_2Ti_3O_7$	a (Å)	–	–	–	16.177(11)	16.068(11)
	b (Å)	–	–	–	3.752(1)	3.752(1)
	c (Å)	–	–	–	9.214(4)	9.205(4)
	β (°)	–	–	–	101.245(25)	100.999(25)
	V (Å^3)	–	–	–	548.493(202)	544.642(196)
NaCl	a (Å)	–	–	–	5.638(1)	5.637(1)
	V (Å^3)	–	–	–	179.180(55)	179.090(53)

Source: Prepared by the author.

Table 5: Phase fractions and Rietveld refinement parameters for the NLTO/POMA composites, using the sample notation defined in Table 4.

Parameter	**NLTO**	**P10**	**P15**	**P35**	**P50**
$Na_2Ti_3O_7$ (wt%)	79.3 ± 0.7	72.3 ± 0.9	67.5 ± 1.1	25.0 ± 1.1	3.7 ± 1.2
$Na_2Ti_6O_{13}$ (wt%)	9.4 ± 0.5	14.3 ± 0.6	15.3 ± 0.8	17.2 ± 1.0	21.2 ± 1.2
$NaLiTi_3O_7$ (wt%)	11.3 ± 0.6	13.4 ± 0.8	17.2 ± 1.0	21.6 ± 1.1	23.2 ± 1.4
$H_2Ti_3O_7$ (wt%)	–	–	–	19.3 ± 0.8	25.5 ± 1.1
NaCl (wt%)	–	–	–	16.9 ± 0.8	26.5 ± 1.1
χ^2	1.35	1.42	1.56	1.62	1.95
R_{wp} (%)	17.89	18.75	19.68	21.00	22.79
R_{exp} (%)	15.42	15.76	15.74	16.54	16.28

Source: Prepared by the author.

The crystalline structure of HCl-doped POMA was evaluated by the Le Bail refine-

ment method, and the corresponding refinement profile is shown in Figure 19f. The initial lattice parameters reported by Biondo *et al.* (2020) were used as the starting model for the refinement. After refinement, the lattice parameters were determined as $a = 6.0162(222)$ Å, $b = 11.8956(607)$ Å, $c = 18.5249(1345)$ Å, $\alpha = 83.3229(7874)°$, $\beta = 85.5924(2628)°$, and $\gamma = 95.8542(566)°$. The refinement converged with satisfactory agreement indices ($\chi^2 = 1.05$, $R_{wp} = 14.720\%$, and $R_{exp} = 14.37\%$), indicating that the reported crystal structure adequately describes the diffraction profile of the synthesized HCl-doped POMA.

In summary, the Rietveld refinement demonstrates that the incorporation of HCl-doped POMA promotes a progressive modification of the crystalline composition of the NLTO/POMA composites. The crystalline phase most affected was $Na_2Ti_3O_7$, which showed a continuous reduction in its relative phase fraction, together with subtle changes in its lattice parameters. On the other hand, the $Na_2Ti_6O_{13}$ and $NaLiTi_3O_7$ phases showed an increase in wt% with the addition of POMA, whereas their lattice parameters remained practically unchanged. Furthermore, the appearance of the $H_2Ti_3O_7$ and NaCl phases indicates the occurrence of ion-exchange reactions involving the replacement of Na by H, as well as sodium extraction during the preparation of the composites. This type of ion-exchange process has already been reported in the literature (CAMPÉON *et al.*, 2025). At first glance, such protonation may appear unlikely in a dry-mixing process. However, it has been demonstrated that exposure of $Na_2Ti_3O_7$ to humid air promotes the Na^+/H^+ ion exchange (ZARRABEITIA *et al.*, 2016). Furthermore, the TG/DTG and DSC results indicate the presence of adsorbed water in POMA, providing a potential medium for this ion-exchange process. Therefore, the combination of an uncontrolled laboratory atmosphere and the intimate contact established between POMA and the ceramic particles during mortar mixing may have favored the partial protonation of $Na_2Ti_3O_7$ and, consequently, the increase in the crystalline fraction of $H_2Ti_3O_7$ with increasing polymer content. This ion-exchange process releases Na^+ ions, which may subsequently react with residual chloride species originating from the POMA synthesis. This interpretation is consistent with the identification of the NaCl phase by Rietveld refinement. Overall, these results demonstrate that incorporating HCl-doped POMA affects both the phase composition and the structural evolution of the ceramic component.

Table 6 summarizes the average atomic bond lengths of the main crystalline phases identified in the NLTO/POMA composites. These values were obtained using VESTA

(MOMMA; IZUMI, 2011) from the crystallographic information files (CIFs) generated after the Rietveld refinement. Although only slight variations are observed, the average bond lengths follow trends similar to those previously identified for the lattice parameters.

Among the identified phases, $Na_2Ti_3O_7$ exhibits small variations in the average bond lengths. The average Ti–O bond length changes from 1.994(174) Å for pristine NLTO to 1.998(174) Å for the NLTO/POMA-50 composite, whereas the average Na–O bond length changes from 2.651(178) Å to 2.654(180) Å. The NLTO/POMA-35 sample shows a slight decrease in both average bond lengths. However, considering the associated uncertainties, these variations are small and do not indicate a pronounced modification of the local $Na_2Ti_3O_7$ structure.

The small variations in the average bond lengths of the $Na_2Ti_3O_7$ crystalline phase are consistent with the slight variation observed in the refined unit-cell volume. Taken together, these results suggest that the chemical environment created by HCl-doped POMA may influence the local structure of this layered titanate without producing a pronounced change in its crystallographic structure.

In contrast, the $Na_2Ti_6O_{13}$ and $NaLiTi_3O_7$ phases exhibit only minor fluctuations in their average bond lengths, without a clear systematic trend as the POMA content increases. These observations agree with the lattice parameter analysis and indicate that the crystal structures of these phases are comparatively less affected during composite preparation.

Table 6: Average bond lengths (Å) for the crystalline titanate phases identified in the samples.

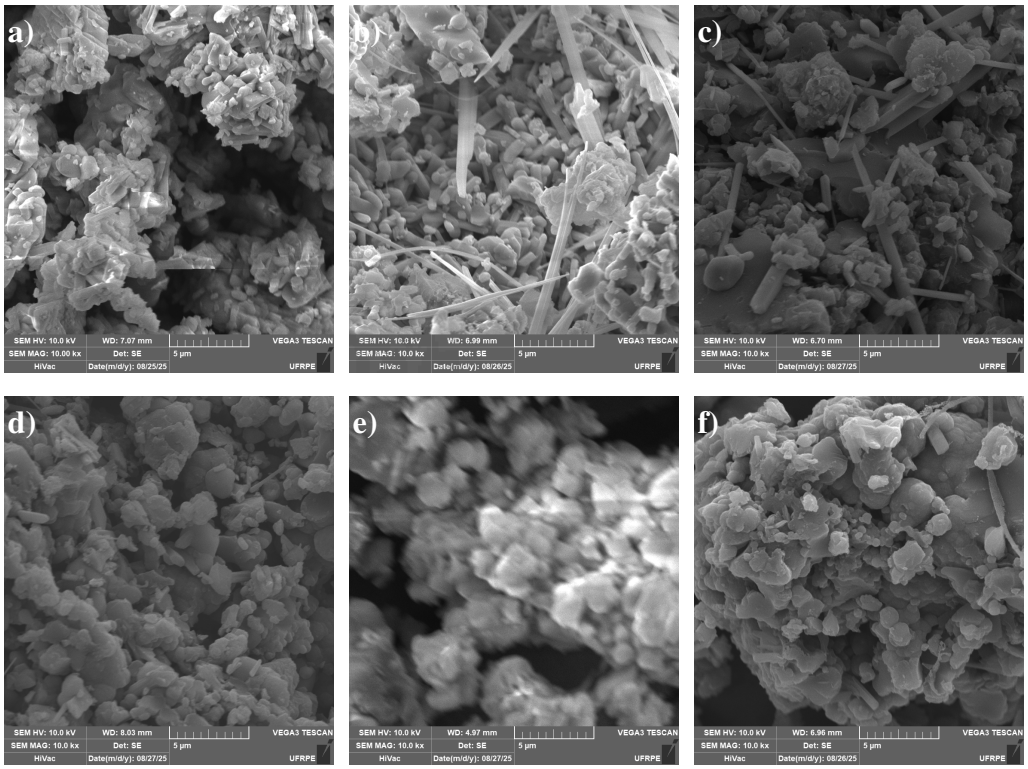
Sample	**$Na_2Ti_3O_7$**		**$Na_2Ti_6O_{13}$**		**$NaLiTi_3O_7$**		
	Ti–O	**Na–O**	**Ti–O**	**Na–O**	**Ti–O**	**Na–O**	**Li–O**
NLTO	1.994(174)	2.651(178)	1.960(96)	2.702(165)	1.977(96)	2.798(180)	2.045(124)
NLTO/POMA-10	1.995(174)	2.652(178)	1.961(96)	2.704(165)	1.977(96)	2.797(179)	2.044(124)
NLTO/POMA-15	1.995(174)	2.653(178)	1.961(96)	2.705(165)	1.979(96)	2.800(180)	2.046(124)
NLTO/POMA-35	1.992(174)	2.648(178)	1.958(96)	2.699(166)	1.975(96)	2.795(181)	2.043(123)
NLTO/POMA-50	1.998(174)	2.654(180)	1.959(96)	2.700(166)	1.974(96)	2.793(179)	2.042(124)

Source: Prepared by the author.

4.1.2 POMA-Induced Morphological Evolution

Figure 20 presents the scanning electron microscopy (SEM) images of the analyzed powder samples. Figure 20a, corresponding to the NLTO sample, shows a morphology predominantly composed of agglomerates of rod- or needle-like particles with irregular sizes, as previously reported by Silva *et al.* (2026) and Melo *et al.* (2023).

Figure 20: SEM micrographs of (a) NLTO, (b) NLTO/POMA-10, (c) NLTO/POMA-15, (d) NLTO/POMA-35, (e) NLTO/POMA-50, and (f) HCl-doped POMA.



Source: Prepared by the author.

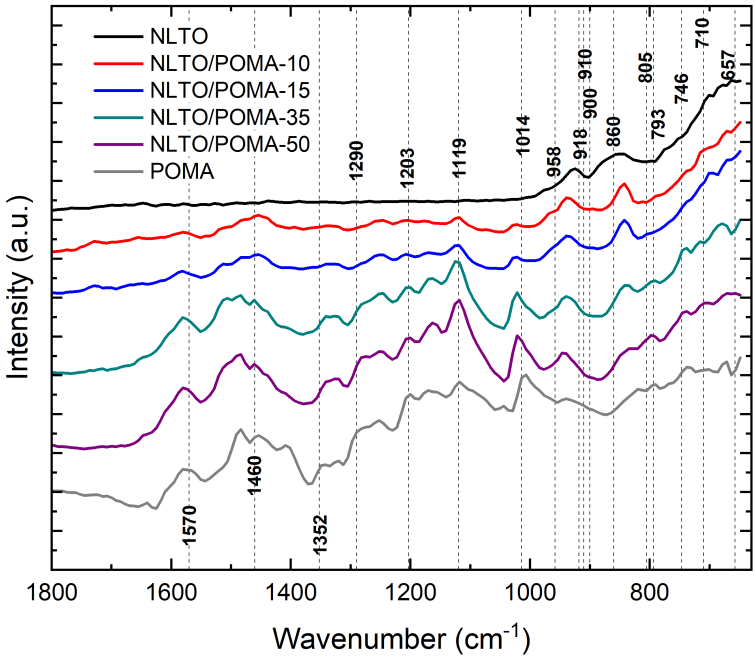
The NLTO/POMA-10 sample retains the characteristic morphology composed of agglomerates of rod- or needle-like particles with irregular sizes, as shown in Figure 20b. Figure 20c, corresponding to the NLTO/POMA-15 sample, exhibits a heterogeneous morphology comprising elongated rod- and needle-like particles together with irregularly shaped agglomerates. Overall, the morphology remains qualitatively similar to that observed for the NLTO/POMA-10 composite.

The NLTO/POMA-35 and NLTO/POMA-50 samples, shown in Figures 20d and 20e, respectively, no longer exhibit the same abundance of rod- and needle-like particles

observed in the samples with lower POMA contents. Instead, a higher degree of particle agglomeration is observed, accompanied by an increased presence of particles with a more rounded morphology. Figure 20f shows that the morphology of HCl-doped POMA, as previously reported in the literature (BIONDO *et al.*, 2020; SILVA *et al.*, 2021; SANCHES *et al.*, 2014a), is characterized by irregular agglomerates typical of polymeric materials.

4.1.3 Vibrational Modes and Chemical Bonding

Figure 21: FTIR spectra of NLTO, NLTO/POMA composites, and POMA.



Source: Prepared by the author.

Figure 21 presents the FTIR spectra of the NLTO, NLTO/POMA composites, and HCl-doped POMA. The spectrum of the NLTO sample, represented by the black curve, is characterized mainly by absorption bands below 1000 cm^{-1}, which are associated with Ti–O, Ti–O–Ti, and Na–O bonds. The bands observed between 650 and 800 cm^{-1} are related to surface phonon modes involving Ti–O and Ti–O–Ti bonds (LIMA *et al.*, 2023; SILVA *et al.*, 2025). The bands between 900 and 918 cm^{-1} are attributed to Ti–O bonds (ALI *et al.*, 2016). The band at 743 cm^{-1} is assigned to the Na–O bond involved in a complex lattice vibration mode (SILVA *et al.*, 2018; SILVA *et al.*, 2025). In addition, the band at 860 cm^{-1} corresponds to the Ti–O–Ti stretching vibration of

the $Na_2Ti_3O_7$ phase, whereas the bands at 891 and 910 cm^{-1} are associated with Ti–O bond vibrations involving oxygen atoms in less-coordinated structural environments (SHIRPOUR; CABANA; DOEFF, 2013; VIANA *et al.*, 2011).

The FTIR spectrum of HCl-doped POMA exhibits the characteristic absorption bands reported for this polymer in the literature. The band around 1460 cm^{-1} is attributed to the C–H deformation of the $-OCH_3$ group (BIONDO *et al.*, 2020; ELGEGREN *et al.*, 2019), whereas the band at 1290 cm^{-1} is associated with C–N stretching (BIONDO *et al.*, 2020; SILVERSTEIN; BASSLER, 1962; NYCZYK *et al.*, 2009). The bands at 793, 1014, 1119, and 1203 cm^{-1} are related to the 1,4-substituted benzene ring structure characteristic of POMA (BIONDO *et al.*, 2020). The band at 746 cm^{-1} is assigned to the out-of-plane deformation of C–H bonds in mono- and 1,2-disubstituted aromatic carbons (SANCHES *et al.*, 2014b). The band at 1255 cm^{-1} corresponds to the stretching vibration of the C–O–C bond (SMITH, 2017). Finally, the band at 1352 cm^{-1} may indicate the presence of residual ammonium persulfate (APS), which was used as the oxidizing agent during the synthesis of POMA (BIONDO *et al.*, 2020).

In addition to the FTIR analysis, the local vibrational modes of the TiO_n environment belonging to the $Na_2Ti_3O_7$ crystalline phase were investigated using a local harmonic vibrational model. For each crystallographic structure, the nearest oxygen atoms surrounding a selected Ti site were considered, including only Ti–O bonds with $r_i \leq 2.60$ Å. The system was modeled as a set of radial Ti–O springs, whose force constants were estimated using a Badger-type relationship,

$$k_i = k_{\text{ref}} \left(\frac{r_{\text{ref}}}{r_i} \right)^3, \tag{4.1}$$

where r_i is the Ti–O bond length, $r_{\text{ref}} = 1.95$ Å, and k_{ref} is the reference force constant (BADGER, 1934; CIOSLOWSKI; LIU; CASTRO, 2000; KURITA; MATSUURA; OHNO, 2004). The latter was obtained from the reference vibrational frequency, $\tilde{\nu}_{\text{ref}} = 891$ cm^{-1}, according to

$$k_{\text{ref}} = (2\pi c \tilde{\nu}_{\text{ref}})^2 \mu_{\text{TiO}}, \tag{4.2}$$

where c is the speed of light and μ_{TiO} (see Section 2.2.7.1) is the reduced mass of the Ti–O bond.

The resulting force constants were used to construct the local Cartesian Hessian,

which was converted into the mass-weighted Hessian according to the normal-mode formalism (LARSEN *et al.*, 2017),

$$\mathbf{H}_w = \mathbf{M}^{-1/2}\mathbf{H}\mathbf{M}^{-1/2} \tag{4.3}$$

whose eigenvalues were used to calculate the local vibrational wavenumbers. The calculated Ti–O bond lengths, force constants, and local vibrational modes are summarized in Table 7.

In addition to the FTIR analysis, the local vibrational modes of the TiO_n environment in the $Na_2Ti_3O_7$ phase were investigated using a local harmonic vibrational model. For each crystallographic structure, the nearest oxygen atoms surrounding a selected Ti site were considered, including only Ti–O bonds with $r_i \leq 2.60$ Å. The corresponding force constants were estimated using a Badger-type relationship (BADGER, 1934; CIOSLOWSKI; LIU; CASTRO, 2000; KURITA; MATSUURA; OHNO, 2004),

Table 7: Ti–O bond lengths, force constants, and local vibrational modes calculated using the local harmonic vibrational model for the Ti site with index 4 in the $Na_2Ti_3O_7$ phase.

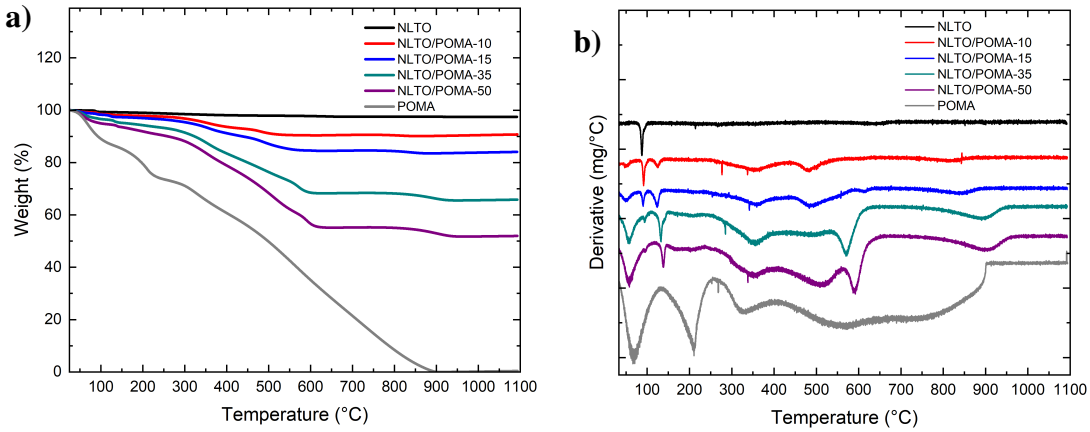
	Ti–O bond lengths r_i (Å)					Force constants k_i (N m^{-1})					Local vibrational modes $\tilde{\nu}_i$ (cm^{-1})				
Sample	r_1	r_2	r_3	r_4	r_5	k_1	k_2	k_3	k_4	k_5	$\tilde{\nu}_1$	$\tilde{\nu}_2$	$\tilde{\nu}_3$	$\tilde{\nu}_4$	$\tilde{\nu}_5$
NLTO	1.827	1.921	1.968	2.109	2.312	682.4	586.6	545.8	443.6	336.5	649.0	717.2	906.6	940.8	1015.1
NLTO/POMA-10	1.828	1.921	1.968	2.110	2.314	680.9	586.5	545.3	443.0	335.8	648.3	716.7	906.5	940.3	1014.1
NLTO/POMA-15	1.828	1.921	1.969	2.110	2.314	680.4	586.2	544.7	442.9	335.5	648.0	716.5	906.3	939.9	1013.7
NLTO/POMA-35	1.825	1.918	1.967	2.106	2.311	684.4	589.3	546.1	445.2	337.2	649.6	718.2	908.6	941.6	1016.5
NLTO/POMA-50	1.827	1.921	1.981	2.112	2.316	682.2	586.5	534.8	441.4	334.8	647.4	713.8	906.2	934.1	1014.3

Source: Prepared by the author.

Despite the simplicity of the local harmonic vibrational model, the calculated vibrational modes are in good agreement with the experimental FTIR spectra. In particular, the experimental bands observed near 657, 710, 900–910, 948, and 1014 cm^{-1} are well reproduced by the calculated modes listed in Table 7, with differences of only a few wavenumbers. Similar behavior is observed for the NLTO/POMA composites, which exhibit only small variations in both the calculated vibrational modes and the corresponding force constants. These results support the assignment of the experimental absorption bands to Ti–O vibrations of the $Na_2Ti_3O_7$ phase and indicate that the incorporation of HCl-doped POMA produces only subtle modifications in the local environment of the ceramic structure.

4.1.4 Thermal Behavior and Stability

Figure 22: Thermogravimetric analysis of NLTO and NLTO/POMA composites: (a) TG curves and (b) DTG curves.



Source: Prepared by the author.

Figure 22a shows the TG curves of NLTO, NLTO/POMA composites, and HCl-doped POMA. A progressive mass loss is observed for all samples as the temperature increases. The NLTO sample exhibits high thermal stability, with only 3.5% mass loss at 1100 °C. Among the composites, NLTO/POMA-10 exhibits the lowest mass variation, retaining approximately 90.7% of its initial mass at this temperature, whereas NLTO/POMA-50 retains about 52% of its initial mass. The HCl-doped POMA sample undergoes almost complete thermal decomposition at approximately 890 °C.

These results indicate that increasing the POMA content progressively reduces the overall thermal stability of the composites. Nevertheless, the major mass-loss events occur only at temperatures above approximately 300 °C, which is considerably higher than the typical operating temperature range of solid-state batteries (20–40 °C) (ORTIZ *et al.*, 2024). Therefore, the reduction in thermal stability is not expected to compromise the applicability of these materials as solid-state battery electrolytes.

The DTG curves shown in Figure 22b correspond to the first derivative of the TG curves and allow the identification of the main thermal events associated with the degradation of the samples. The NLTO sample exhibits a single peak at approximately 85.5 °C, which is attributed to the evaporation of adsorbed water and residual precursor species.

The composite samples exhibit additional thermal events as a consequence of the

presence of POMA. The first peak, observed between approximately 91 °C and 125 °C, is associated with the release of adsorbed moisture and residual organic species remaining from the synthesis. At higher temperatures, two pronounced mass-loss events are observed in all composites, with peaks near 355 °C and 482 °C. The first is associated with the main thermal degradation stage of the POMA phase (ALVES *et al.*, 2010), whereas the second is attributed to the decomposition and structural reorganization of carbonaceous residues formed during the primary degradation process.

In addition to the events discussed above, two peaks located near 570 °C and 900 °C become significantly more pronounced in the NLTO/POMA-35 and NLTO/POMA-50 samples, indicating the appearance of additional degradation processes at higher POMA contents.

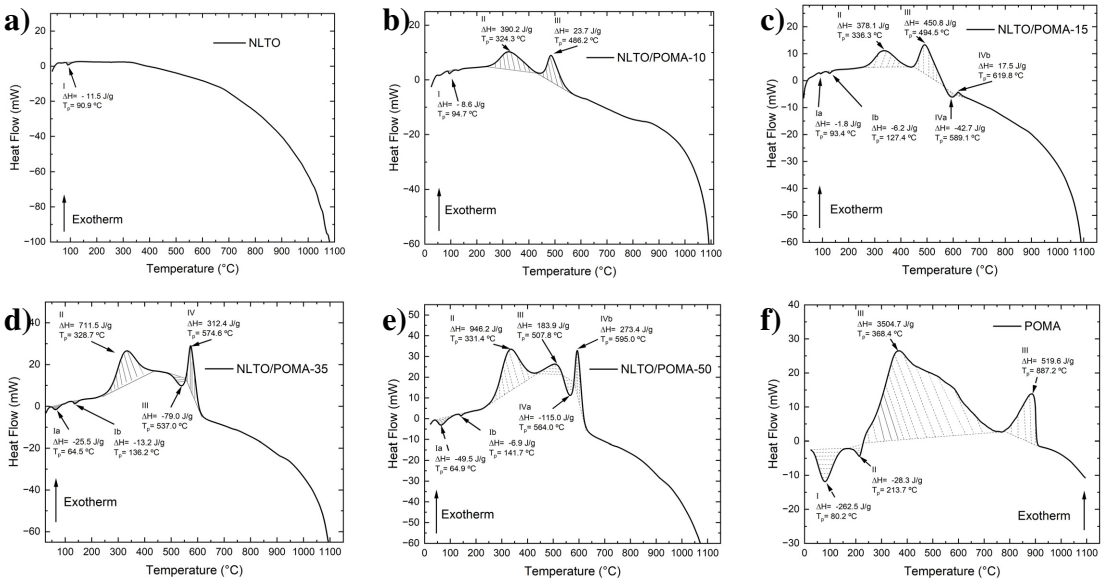
The DTG curve of HCl-doped POMA also exhibits several characteristic thermal events. A pronounced peak is observed near 68 °C and is attributed to the loss of adsorbed water and residual solvents from the synthesis process. The peaks located around 210 °C and 330 °C are associated with the thermal degradation of POMA, initiated by the cleavage of OCH_3 side groups. A further peak near 555 °C is likely related to the thermal decomposition and structural reorganization of carbonaceous residues, whereas the event observed above 700 °C corresponds to the final degradation stage of the polymer.

Although some of these degradation events are also observed in the composite samples, the peaks near 570 °C and, particularly, around 900 °C become considerably more intense only in composites with higher POMA content. These events are therefore attributed to the degradation of carbonaceous species formed during the reorganization and decomposition processes occurring in the early stages of POMA degradation. The event near 900 °C is likely associated with the decomposition of more condensed and thermally stable carbonaceous structures. Their much lower intensity in the pure POMA sample suggests that these species are stabilized by interactions between the polymeric phase and the sodium titanate matrix, giving rise to degradation products with enhanced thermal stability.

Figure 23 shows the DSC thermograms of NLTO, the NLTO/POMA composites, and HCl-doped POMA. Consistent with the DTG analysis, the DSC curves reveal a series of endothermic and exothermic events associated with moisture removal, degradation of the polymeric phase, and the decomposition and reorganization of carbona-

ceous species formed during thermal degradation. The thermal events observed for each sample are discussed according to their characteristic temperature ranges.

Figure 23: DSC thermograms recorded in the high-temperature region for: (a) NLTO, (b) NLTO/POMA-10, (c) NLTO/POMA-15, (d) NLTO/POMA-35, (e) NLTO/POMA-50, and (f) HCl-doped POMA.



Source: Prepared by the author.

The low-temperature region, extending from approximately 80 °C to 140 °C, is characterized by endothermic processes associated with the removal of physically adsorbed species. The NLTO sample exhibits a single peak at approximately 90.9 °C, corresponding to the thermal event previously identified in the DTG curve and attributed to the evaporation of adsorbed water and residual precursor species.

A similar endothermic event is observed in all composite samples. For NLTO/POMA-10, this process begins at approximately 86 °C, ends near 120 °C, and exhibits a peak at 94.7 °C. As the POMA content increases, an additional endothermic peak emerges between approximately 120 °C and 141 °C, becoming evident from the NLTO/POMA-15 sample onward. Given the temperature range at which these events occur, they are attributed to the evaporation of adsorbed water and residual solvents from the synthesis process.

The HCl-doped POMA sample exhibits two endothermic events in this temperature range, with peaks at approximately 80 °C and 213 °C. The first is associated with the loss of moisture and volatile species, whereas the second is likely related to the initial

dedoping of POMA (SILVA *et al.*, 2022), the removal of weakly bound organic species, and/or the structural reorganization of the polymer chains.

The second major thermal event, observed between approximately 250 °C and 420 °C, corresponds to the main degradation stage of the POMA phase. This endothermic process is observed in all composite samples and is centered at approximately 324.3 °C for the NLTO/POMA-10 sample. The corresponding peak is consistent with the principal degradation event previously identified in the DTG curves.

A progressive increase in the enthalpy associated with this process is observed as the POMA content increases. The enthalpy rises from 390.2 J/g for NLTO/POMA-10 to 946.2 J/g for NLTO/POMA-50, reaching 3507.7 J/g for the HCl-doped POMA sample. This behavior is expected, since the energy required for the degradation process is directly related to the amount of polymer present in the material.

However, the enthalpy obtained for the HCl-doped POMA sample should be interpreted with caution. In this sample, a broad exothermic region is observed over the temperature range of approximately 230–745 °C. This broad thermal feature most likely results from the superposition of different processes, including POMA pyrolysis, carbonization, and structural reorganization. Consequently, the high integrated enthalpy reflects the cumulative contribution of multiple overlapping thermal events. Furthermore, the shape of the DSC curve makes it difficult to define a baseline that allows the unambiguous separation of each process. The enthalpy values were obtained by integrating the area enclosed between the DSC curve and the baseline defined for each thermal event. The sensitivity of the integration procedure was assessed by independently varying the integration limits by ±5 °C. This analysis resulted in typical variations of 1–5% in the calculated enthalpy values, indicating good reproducibility of the adopted integration procedure.

The third thermal event is observed between approximately 440 °C and 550 °C in all composite samples, although its intensity increases with increasing POMA content. This exothermic process corresponds to the second major degradation stage identified in the DTG curves and is attributed to the decomposition and/or reorganization of carbonaceous residues formed during the initial stages of POMA degradation.

Additional exothermic events are observed between approximately 580 °C and 600 °C in the composites containing higher POMA contents. These thermal processes become evident from the NLTO/POMA-15 sample onward and remain present, with

slight variations in peak temperature, in the NLTO/POMA-35 and NLTO/POMA-50 samples. Furthermore, the enthalpy associated with these events increases progressively as the polymer content in the ceramic matrix increases.

These thermal events are absent in the composite containing the lowest polymer content and are considerably less pronounced in the HCl-doped POMA sample. This behavior suggests that they are associated with the thermal decomposition, carbonization, and structural reorganization of carbonaceous species stabilized by interfacial interactions between the polymeric phase and the sodium titanate matrix. The higher thermal stability of these species suggests that the ceramic phase may influence the degradation pathway of POMA. However, the chemical nature of the resulting carbonaceous residues cannot be established solely from the present thermal analyses and would require complementary characterization techniques, which are beyond the scope of this work.

Overall, the thermal analyses demonstrate that increasing the POMA content progressively reduces the thermal stability of the composites while introducing additional degradation and structural reorganization processes associated with the polymeric phase. The combined TG, DTG, and DSC results indicate that interfacial interactions between POMA and the sodium titanate matrix modify the degradation pathway of the polymer, leading to the formation of thermally stable carbonaceous species in the composites with higher polymer contents. Despite these changes, the principal degradation events occur at temperatures well above the typical operating range of solid-state batteries. Therefore, from a thermal-decomposition standpoint, the reduced thermal stability does not compromise the potential of these composites for solid-state electrolyte applications. However, the assessment of the thermal suitability of a solid electrolyte cannot be based solely on the absence of significant mass loss. It also requires the evaluation of additional factors, such as electrochemical stability, gas evolution, and the thermal stability of the protonated state of POMA. These aspects are beyond the scope of the thermal analyses performed in the present work but represent important directions for future investigations.

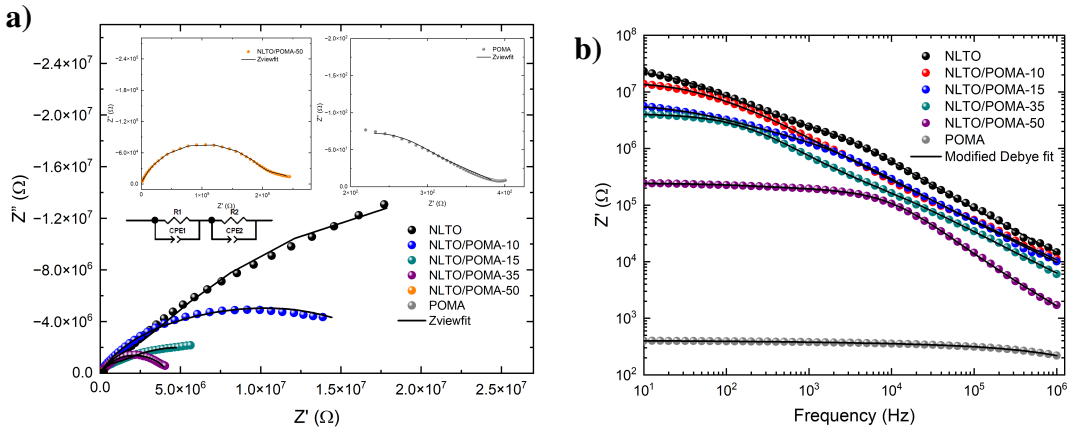
4.1.5 Electrical Response and Relaxation Processes

Figure 24a shows the Nyquist plots (Z'' versus Z') obtained by complex impedance spectroscopy for the NLTO, NLTO/POMA composites, and pure POMA samples. The

largest semicircle (black) corresponds to the NLTO sample (lithium-doped sodium titanate) without POMA, whereas the red, blue, green, and purple curves correspond to the NLTO/POMA-10, NLTO/POMA-15, NLTO/POMA-35, and NLTO/POMA-50 composites, respectively. The smallest semicircle (gray) represents pure POMA. As the POMA content increases, the diameter of the semicircles progressively decreases, indicating a reduction in the electrical resistance of the pellets.

Because non-blocking electrodes were employed, the present impedance measurements do not allow separation of the ionic and electronic contributions to the measured conductivity. Consequently, the following discussion focuses on changes in the overall charge-transport behavior rather than on a specific transport mechanism.

Figure 24: (a) Nyquist plots of NLTO and NLTO/POMA composites with equivalent-circuit fitting (inset). (b) The real part of the impedance (Z') fitted with the modified Debye model.



Source: Prepared by the author.

The inset of Figure 24a presents the equivalent circuit adopted to describe the electrical response of the samples. The resistor R_1 and the constant phase element (CPE1) are connected in parallel, which describes the electrical response of the high-frequency (HF) process. Likewise, the resistor R_2 and the constant phase element (CPE2) model the response of the low-frequency (LF) interfacial process. The CPE is included to account for the non-ideal capacitive behavior commonly observed in electrochemical systems (ZHAO *et al.*, 2022a; SCHALENBACH *et al.*, 2021; XIAO *et al.*, 2024; GHARBI *et al.*, 2025). From a physical perspective, the high-frequency (HF) processes, represented by the $R_1 \parallel \text{CPE}_1$ branch, can be interpreted as an effective response arising from the superposition of electrical contributions from different crystalline regions and

the polymeric phase associated with faster relaxation processes. In contrast, the low-frequency (LF) processes may reflect slower phenomena involving interfaces, electrode interactions, and polarization.

Table 8 summarizes the equivalent-circuit parameters obtained from the ZView fitting, while Table 9 presents the conductivities associated with the HF and LF processes (σ_1 and σ_2, respectively), as well as the total conductivity of the NLTO/POMA samples. The conductivity values were calculated according to Equation 2.20, described in Section 2.2.7.3. The effective capacitances were calculated using Equation 2.22, also presented in Section 2.2.7.3. Overall, total resistance (R_1+R_2) decreases with increasing POMA content, indicating that incorporating the conducting polymer facilitates charge transport throughout the material.

Table 8: Equivalent-circuit parameters and goodness-of-fit indicators for the NLTO/POMA samples.

Sample	R_1 (Ω)	$C_{\text{eff},1}$ (F)	R_2 (Ω)	$C_{\text{eff},2}$ (F)	χ^2	**Sum of squares**
NLTO	1.75×10^{6} (17)	3.15×10^{-11} (20)	4.71×10^{7} (22)	2.78×10^{-10} (16)	3.69×10^{-3}	9.60×10^{-2}
NLTO/POMA-10	6.93×10^{6} (44)	1.29×10^{-10} (11)	1.32×10^{7} (13)	6.76×10^{-10} (98)	1.03×10^{-3}	2.69×10^{-2}
NLTO/POMA-15	1.54×10^{6} (10)	6.59×10^{-11} (30)	6.27×10^{6} (19)	6.92×10^{-10} (67)	1.45×10^{-3}	3.77×10^{-2}
NLTO/POMA-35	1.16×10^{5} (9)	9.45×10^{-11} (44)	4.21×10^{6} (3)	1.97×10^{-10} (4)	5.06×10^{-4}	1.32×10^{-2}
NLTO/POMA-50	1.98×10^{5} (2)	7.44×10^{-11} (8)	6.33×10^{4} (12)	2.66×10^{-8} (34)	7.82×10^{-4}	2.03×10^{-2}
POMA	1.88×10^{2} (8)	6.88×10^{-10} (100)	2.27×10^{2} (8)	4.61×10^{-10} (217)	2.53×10^{-4}	6.58×10^{-3}

Source: Prepared by the author.

Table 9: Electrical conductivities derived from the equivalent-circuit fitting of the NLTO/POMA samples.

Sample	σ_1 (S·cm^{-1})	σ_2 (S·cm^{-1})	σ_{total} (S·cm^{-1})
NLTO	1.13×10^{-7} (11)	4.19×10^{-9} (20)	4.04×10^{-9} (18)
NLTO/POMA-10	2.77×10^{-8} (18)	1.46×10^{-8} (14)	9.57×10^{-9} (63)
NLTO/POMA-15	1.28×10^{-7} (8)	3.15×10^{-8} (9)	2.53×10^{-8} (7)
NLTO/POMA-35	1.91×10^{-6} (14)	5.30×10^{-8} (4)	5.15×10^{-8} (4)
NLTO/POMA-50	1.29×10^{-6} (1)	4.02×10^{-6} (8)	9.75×10^{-7} (9)
POMA	1.23×10^{-3} (6)	1.02×10^{-3} (4)	5.59×10^{-4} (16)

Source: Prepared by the author.

The quality of the equivalent-circuit fits performed in ZView was assessed using the chi-squared (χ^2) parameter and the sum of squared residuals. For all samples, the obtained χ^2 values ranged from 2.529×10^{-4} to 3.693×10^{-3}, while the sum of squared residuals ranged from 6.5754×10^{-3} to 9.6018×10^{-2}. These values, together with the visual agreement between the experimental impedance spectra and the fitted curves, support the use of the adopted equivalent-circuit model to describe the experimental data.

The incorporation of POMA leads to a progressive increase in total conductivity, with σ_{total} increasing by approximately two orders of magnitude, from 4.04×10^{-9} to 9.75×10^{-7} S·cm^{-1} for the NLTO and NLTO/POMA-50 samples, respectively. The conductivities associated with the HF and LF processes, σ_1 and σ_2, respectively, also show an overall tendency to increase with increasing POMA content, although some deviations from a monotonic behavior are observed. These variations do not alter the overall trend observed for σ_{total}.

Table 10: Kramers–Kronig validation, information criteria, and residuals obtained from the comparison of alternative equivalent-circuit models for the NLTO/POMA samples, where 1A denotes the one-arc model, 2A the two-arc model, AC the arc + CPE tail model, and AW the arc + finite-length Warburg model.

Sample	KK error (%)	Model favored by AIC/BIC	AIC_{1A}	AIC_{2A}	AIC_{AC}	AIC_{AW}	BIC_{1A}	BIC_{2A}	BIC_{AC}	BIC_{AW}	Residuals Z'/Z'' (%)
NLTO	8.53	Arc + Warburg	-286.01	-284.41	-285.52	**-408.08**	-278.45	-269.28	-270.39	**-390.43**	8.53 / 6.90
NLTO/POMA-10	7.28	Two arcs	-451.43	**-501.45**	-432.92	-497.07	-443.62	**-485.82**	-417.29	-478.83	7.28 / 5.31
NLTO/POMA-15	2.61	Two arcs	-376.46	**-616.35**	-544.45	-539.52	-368.65	**-600.72**	-528.82	-521.29	2.61 / 4.47
NLTO/POMA-35	9.58	Two arcs	-279.66	**-455.39**	-264.13	-216.55	-271.85	**-439.76**	-248.50	-198.31	9.58 / 7.11
NLTO/POMA-50	12.91	Two arcs	-363.96	**-376.55**	-326.57	-345.20	-356.15	**-360.92**	-310.94	-326.96	12.91 / 7.49
POMA	0.22	Two arcs	-887.93	**-1109.82**	-979.01	-1053.19	-880.12	**-1094.19**	-963.38	-1034.96	0.22 / 0.42

Source: Prepared by the author.

The suitability of the proposed equivalent-circuit models was quantitatively evaluated using the Akaike information criterion (AIC) and Bayesian information criterion (BIC), together with residual analysis and the Kramers–Kronig consistency test (BOUKAMP, 1995; ORAZEM; TRIBOLLET, 2008), as summarized in Table 10. For the NLTO/POMA composites, the information criteria favored the two-arc model, $(R_1 \parallel CPE_1)(R_2 \parallel CPE_2)$, for all compositions analyzed. For pristine NLTO, although the model consisting of one arc associated with a finite-length Warburg element (W_s) yielded lower AIC and BIC values, the two-arc model was retained as a common representation for the entire series. This choice preserves the comparability of the HF

and LF processes across the different compositions and is further supported by the consistency in magnitude between the conductivity values derived from the two-arc equivalent-circuit model and those independently obtained from the Jonscher analysis, without implying that the adopted model corresponds to the individual statistical minimum for every sample. Most samples exhibited mean residuals below 10%, while the largest deviations were predominantly observed at the limits of the frequency range (BOUKAMP, 1995; ORAZEM; TRIBOLLET, 2008).

Figure 24b shows the frequency dependence of the real component of the impedance (Z'). At very low frequencies, the impedance of the NLTO sample approaches $2.3 \times 10^7\ \Omega$, whereas the NLTO/POMA-50 sample exhibits values on the order of $10^5\ \Omega$. These values agree in magnitude with the total resistance obtained from the equivalent-circuit fitting performed in ZView (Table 8), confirming the progressive reduction in electrical resistance with increasing POMA content.

To further analyze the frequency dependence of the real impedance, the experimental data were fitted using the modified Debye model, presented in Section 2.2.7.3, according to Equation 2.21 (NAHIR, 2005).

Table 11: 2×ZARC fit parameters from $Z'(f)$: for each sample the smaller resistance is labeled R_1 (with its corresponding τ_1 and n_1). Units: R in Ω, τ in s. Numbers in parentheses indicate the uncertainty in the last digit(s) of the mantissa.

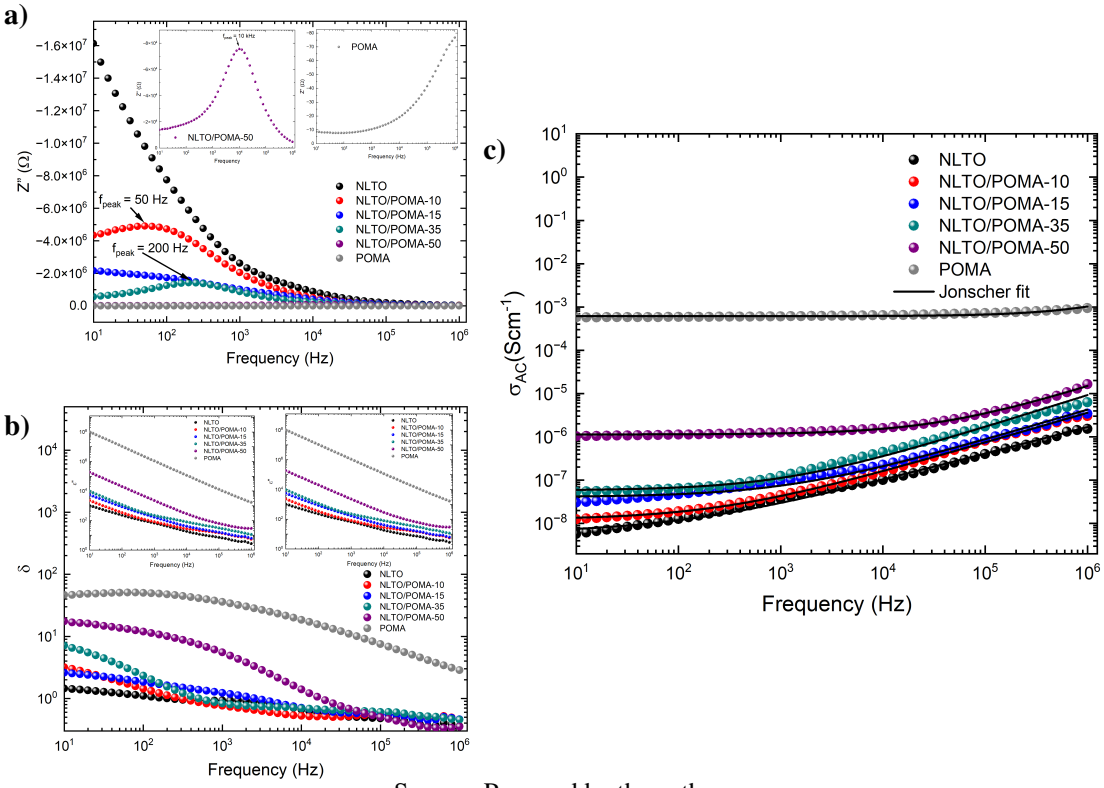
Sample	R_1 (Ω)	τ_1 (s)	n_1	R_2 (Ω)	τ_2 (s)	n_2
NLTO	1.60×10^6 (6)	4.43×10^{-5} (fixed)	0.78(1)	2.57×10^7 (12)	4.44×10^{-3} (4)	0.71(1)
NLTO/POMA-10	6.52×10^6 (34)	3.75×10^{-3} (fixed)	0.85 (fixed)	8.45×10^6 (15)	9.50×10^{-4} (fixed)	0.69(1)
NLTO/POMA-15	1.32×10^6 (5)	8.90×10^{-5} (fixed)	0.72(1)	4.96×10^6 (21)	2.56×10^{-3} (25)	0.67(2)
NLTO/POMA-35	1.25×10^5 (6)	1.10×10^{-5} (fixed)	0.67(1)	4.07×10^6 (5)	7.90×10^{-4} (2)	0.75(1)
NLTO/POMA-50	4.87×10^4 (28)	7.43×10^{-4} (fixed)	0.71 (fixed)	1.95×10^5 (17)	1.40×10^{-5} (2)	0.81(1)
POMA	1.57×10^2 (1)	8.86×10^{-7} (fixed)	0.27(1)	2.53×10^2 (1)	8.03×10^{-8} (1)	0.62(1)

Source: Prepared by the author.

The fitting parameters associated with the two relaxation processes ($R \parallel$ CPE) are listed in Table 11. These parameters are consistent with the equivalent-circuit analysis obtained from the ZView fitting (Table 8), reinforcing the interpretation of the electrical response in terms of the HF contribution and the interfacial LF contribution. To stabilize the fitting procedure, all parameters were initially allowed to vary freely. Subsequently, the parameters exhibiting lower uncertainties were fixed at the values obtained from the preliminary fit, reducing parameter correlations during the refine-

ment of the remaining parameters. This procedure improves the numerical stability of the fitting but does not, by itself, guarantee the uniqueness of the obtained parameter set, since different combinations of correlated parameters may provide comparably good descriptions of the experimental data. Nevertheless, the consistency between the parameters obtained from the relaxation analysis and those derived from the equivalent-circuit fitting provides additional support for the physical plausibility of the obtained solution.

Figure 25: Frequency dependence of (a) the imaginary part of the impedance (Z''), (b) dielectric loss (tan δ) for NLTO and NLTO/POMA composites, and (c) AC conductivity as a function of frequency fitted using Jonscher's law.



Source: Prepared by the author.

Figure 25a shows the frequency dependence of the imaginary component of the impedance (Z''). The relaxation time can be determined from the peak frequency of each curve according to $\tau = 1/(2\pi f_{\text{peak}})$ (MACDONALD *et al.*, 2018). Since the relaxation time is inversely proportional to the peak frequency, shorter relaxation times indicate faster electrical relaxation and/or enhanced charge-carrier dynamics within the material.

For the NLTO/POMA-10 sample, the peak occurs at approximately 50 Hz, corre-

sponding to a relaxation time of 3.18×10^{-3} s. For the NLTO/POMA-15 sample, the peak shifts to approximately 200 Hz, resulting in a relaxation time of 7.96×10^{-4} s. This trend becomes even more pronounced for the NLTO/POMA-50 sample, whose peak frequency is approximately 10 kHz, corresponding to a relaxation time of 1.59×10^{-5} s. The progressive decrease in relaxation time indicates a faster electrical response as POMA content increases. Thus, relaxation time reflects the characteristic timescale of charge-carrier and polarization responses to the applied electric field. In this case, the peaks reflect the sample's overall electrical behavior, involving contributions from the ceramic and polymeric regions and their interfaces, rather than specific, isolated processes. Therefore, the relaxation time associated with the Z'' peak as a function of frequency cannot be unambiguously assigned to a single microscopic transport mechanism.

The dielectric response associated with these relaxation processes can be further analyzed through the complex permittivity, introduced in Section 2.2.7.3 and defined by Equation 2.23 (BARSOUKOV; MACDONALD, 2005).

Figure 25b shows the frequency dependence of the dielectric loss factor ($\tan\delta$). At low frequencies, the POMA sample exhibits the highest dielectric loss, with values close to 46, followed by the NLTO/POMA-50 composite, with values around 17. This behavior reflects the more dissipative nature of these samples and is associated with greater contributions from electrical conduction and interfacial polarization, particularly Maxwell–Wagner–Sillars polarization (MEENA; DHAKA, 2024; HOTA *et al.*, 2025).

The remaining samples exhibit $\tan\delta$ values below 10 and show an overall tendency toward increasing dielectric losses with increasing POMA content, except for the NLTO/POMA-10 and NLTO/POMA-15 samples, which deviate from this trend. The NLTO sample exhibits a dielectric loss factor of approximately 1.4, indicating lower dielectric losses, although it also presents the lowest electrical conductivity.

At high frequencies, all composite samples exhibit very low and similar $\tan\delta$ values, indicating that dipoles and charge carriers are no longer able to follow the rapid oscillation of the applied electric field.

Figure 25c shows the frequency dependence of the AC electrical conductivity of the NLTO/POMA composites. The conductivity was calculated from the dielectric response according to the procedure described in Section 2.2.7.3 using Equation 2.28

(MUKHERJEE *et al.*, 2014; JONSCHER, 1999).

The experimental conductivity curves were fitted using the Jonscher universal power law introduced in Section 2.2.7.3 (Equation 2.29) (IBRAHIM *et al.*, 2025). The fitting parameters are summarized in Table 12.

The fitted parameters summarized in Table 12 show that the total DC conductivity (including HF and LF interfacial contributions) increases with increasing POMA content, rising by approximately three orders of magnitude, from $6.14(52) \times 10^{-9}$ S·cm^{-1} for the NLTO sample to $1.14(1) \times 10^{-6}$ S·cm^{-1} for the NLTO/POMA-50 composite. In addition, the Jonscher exponent s increases from 0.617 for the NLTO sample to 0.766 for the NLTO/POMA-50 composite. Within the Jonscher formalism, the exponent s characterizes the frequency-dependent dispersive contribution to the conductivity. Therefore, the observed increase in s indicates a systematic change in the frequency dependence of the electrical response with increasing POMA content. However, since the measurements were performed at a single temperature, the variation in s is interpreted here descriptively, without assigning it to a specific microscopic charge-transport mechanism.

Table 12: Jonscher fitting parameters for the NLTO/POMA system: σ_{DC}, A, and s.

Sample	σ_{DC} (S·cm^{-1})	A	s
NLTO	6.14×10^{-9}(52)	1.08×10^{-10}(fixed)	0.617(2)
NLTO/POMA-10	1.23×10^{-8}(3)	7.50×10^{-11}(fixed)	0.688(1)
NLTO/POMA-15	4.08×10^{-8}(18)	7.66×10^{-11}(fixed)	0.697(3)
NLTO/POMA-35	5.81×10^{-8}(27)	8.29×10^{-11}(fixed)	0.742(3)
NLTO/POMA-50	1.14×10^{-6}(1)	8.50×10^{-11}(fixed)	0.766(1)
POMA	$6.15(5) \times 10^{-4}$	5.33×10^{-10}(fixed)	0.866(4)

Source: Prepared by the author.

Previous studies have reported the synthesis and electrical characterization of undoped sodium titanate/POMA composites. Silva *et al.* (2023) reported a conductivity of 5.8×10^{-5} S·cm^{-1} for a composite containing 35% by mass of undoped sodium titanate. Likewise, Silva *et al.* (2021) obtained a conductivity on the order of 10^{-6} S·cm^{-1} for a sodium titanate composite containing 50% POMA. Although direct comparisons are limited by differences in the ceramic composition and processing conditions, the NLTO/POMA-50 composite developed in the present work exhibits a total conductiv-

ity on the order of 10^{-7} S·cm^{-1}, comparable to values reported for similar ceramic–polymer composites. Furthermore, σ_1 reaches the order of 10^{-6} S·cm^{-1}, indicating that the incorporation of POMA enhances charge-transport within the HF process.

Overall, the electrical characterization indicates that incorporating POMA promotes more favorable charge-transport pathways in the NLTO-based composites, resulting in higher conductivity and a less dispersive electrical response. Since carrier-selective electrodes were not employed, it is not possible to determine whether the measured conductivity is predominantly ionic or electronic. Considering that HCl-doped POMA is an electronically conducting polymer, part of the conductivity enhancement may also arise from electronic transport through the polymeric phase. Although increased electronic conductivity is undesirable for a solid electrolyte, incorporating POMA may still offer advantages by modifying ceramic–polymer interfaces and charge-transport pathways and, because the polymeric phase is more compliant, potentially improving physical contact at the electrolyte–electrode interface. However, the present measurements cannot establish whether these effects effectively enhance ionic transport or reduce electrolyte–electrode interfacial resistance. This distinction should be investigated in future studies using ionic- or electronic-blocking electrodes.

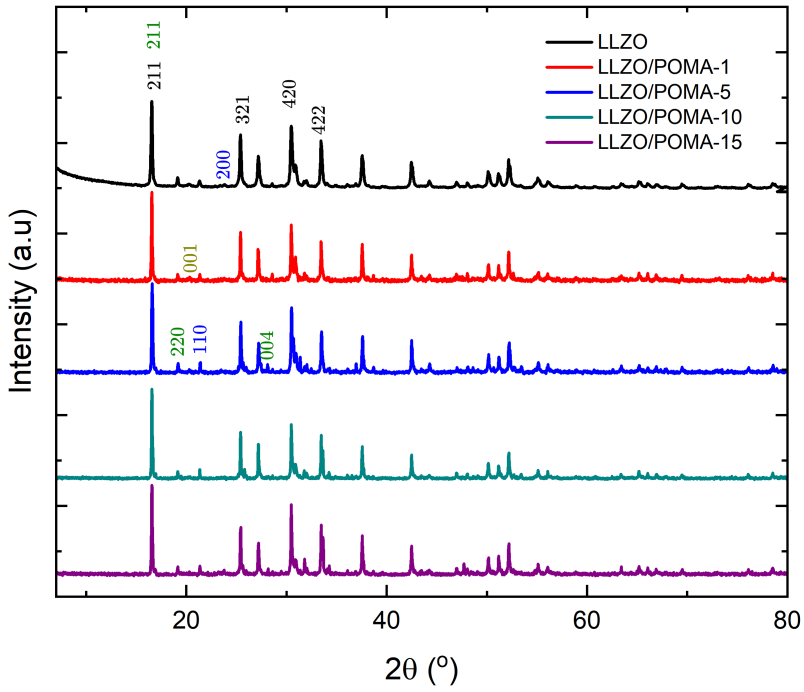
4.2 Structural and Electrical Characterization of Mg/Sr-Doped LLZO/POMA Composites

4.2.1 Crystal-Phase Evolution upon POMA Incorporation

Figure 26 presents the experimental X-ray diffraction patterns of the LLZO and LLZO/POMA composites. The black curve corresponds to unmodified LLZO, while the red, blue, dark yellow, and purple curves represent the composites containing 1, 5, 10, and 15 wt% POMA, respectively.

The main diffraction peaks were indexed using Miller indices to facilitate phase identification and to evaluate the structural evolution of the composites with increasing POMA content. The first intense reflection, located at $2\theta \approx 16.6°$, corresponds to the (211) plane of $Li_7La_3Zr_2O_{12}$, which is common to both the cubic and tetragonal polymorphs (KIM *et al.*, 2023). The persistence of this reflection with high intensity in all samples indicates that the garnet structure is preserved after the incorporation of POMA.

Figure 26: X-ray diffraction patterns of LLZO and LLZO/POMA composites. Miller indices: cubic LLZO (black), tetragonal LLZO (green), Li_2CO_3 (blue), and LiOH (yellow).



Source: Prepared by the author.

Reflections indexed as (220) ($2\theta \approx 19.1°$) and (004) ($2\theta \approx 28.1°$), highlighted in green in the LLZO/POMA-5 diffractogram, are characteristic of the tetragonal phase of LLZO. The presence of these reflections in all samples indicates that a small fraction of the tetragonal phase is retained throughout the composite series, a behavior frequently reported for garnet electrolytes synthesized under similar conditions (RAJU *et al.*, 2021; RANGASAMY *et al.*, 2013).

Additional reflections at $2\theta \approx 21.4°$ and 23.9°, indexed as (110) and (200), respectively, are assigned to Li_2CO_3. Their presence in all samples agrees with previous reports describing the spontaneous formation of lithium carbonate on LLZO surfaces after exposure to atmospheric CO_2 and moisture (MOHAMMADI *et al.*, 2023; SAHAL *et al.*, 2024; HAN *et al.*, 2024; YI *et al.*, 2023).

Likewise, the reflection at $2\theta \approx 20.3°$, indexed as (001), is attributed to LiOH. This phase is formed by the reaction of LLZO with water, as described by Equation (4.4)

(HAN *et al.*, 2024).

$$Li_7La_3Zr_2O_{12} + xH_2O \longrightarrow Li_{7-x}H_xLa_3Zr_2O_{12} + xLiOH \tag{4.4}$$

Subsequently, the lithium hydroxide formed on the surface reacts with atmospheric CO_2, producing Li_2CO_3, as described by Equation (4.5) (HAN *et al.*, 2024).

$$LiOH + \frac{1}{2}CO_2 \longrightarrow \frac{1}{2}Li_2CO_3 + \frac{1}{2}H_2O \tag{4.5}$$

Therefore, the appearance of LiOH and Li_2CO_3 in the diffraction patterns is attributed to the well-known surface reactivity of LLZO toward ambient humidity and CO_2, which accounts for the presence of these secondary phases. This process has been reported in the literature primarily as a result of the surface reactivity of LLZO involving Li^+/H^+ exchange (ZHANG *et al.*, 2024), rather than as a complete decomposition of the garnet structure. Thus, La and Zr remain within the LLZO framework, and the formation of LiOH does not necessarily imply the formation of additional La- or Zr-containing crystalline phases. The remaining reflections are consistent with the crystalline phases included in the Rietveld refinement, with no additional crystalline phases identified within the resolution of the XRD measurements.

Figures 27a–d present the crystal structures of the phases identified by X-ray diffraction. The structural models were generated using VESTA (MOMMA; IZUMI, 2011) from crystallographic information files (CIFs) obtained from experimental databases.

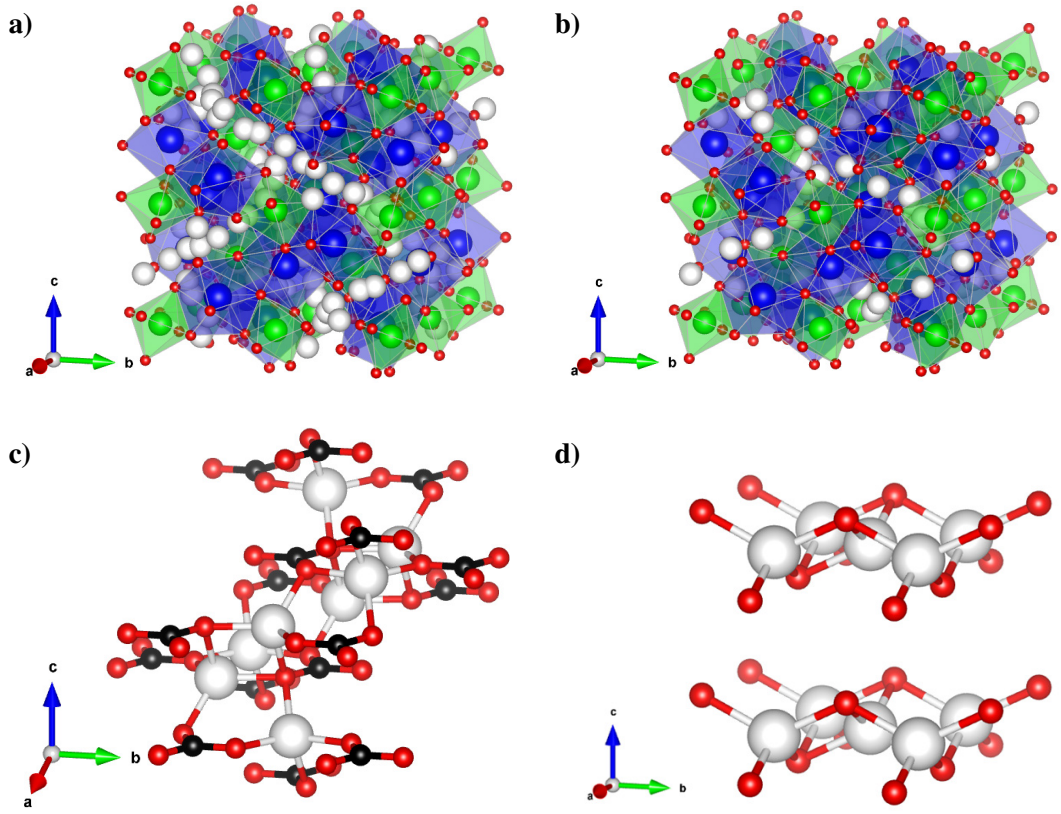
Figure 27a shows the cubic phase of $Li_7La_3Zr_2O_{12}$. One of its main structural characteristics is the large number of lithium ions occupying partially filled interstitial sites. Combined with the high degree of disorder in the lithium sublattice, this structural arrangement provides numerous pathways for lithium-ion migration, resulting in the high ionic conductivity characteristic of the cubic garnet phase (ZHAO *et al.*, 2022b; HIROSE *et al.*, 2018).

Figure 27b shows the tetragonal phase of $Li_7La_3Zr_2O_{12}$. In contrast to the cubic phase, the lithium sublattice is more ordered, with lithium ions occupying well-defined crystallographic sites (ZHAO *et al.*, 2022b; HIROSE *et al.*, 2018). Although this ordered arrangement increases the structural stability of the material, it reduces the number of available pathways for lithium-ion migration. Consequently, the tetragonal phase

exhibits significantly lower ionic conductivity than its cubic counterpart.

According to Raju *et al.* (2021), the cubic phase contains a considerably larger number of vacant lithium sites than the tetragonal phase. In the cubic garnet structure, lithium ions occupy only two crystallographic sites, 24d and 96h, where the number indicates the multiplicity of the site and the letter identifies its crystallographic symmetry (EGGESTAD; SELBACH; WILLIAMSON, 2024; PUENTE *et al.*, 2021). Consequently, the cubic unit cell provides 120 available lithium sites, although only 56 are occupied by lithium ions. The large number of vacant sites facilitates lithium-ion migration through the crystal lattice, which is one of the main factors responsible for the high ionic conductivity of the cubic phase.

Figure 27: Crystal structures of (a) cubic LLZO, (b) tetragonal LLZO, (c) Li_2CO_3, and (d) LiOH. Color code: O (red), Zr (green), La (blue), Li (white), and C (black).



Source: Prepared by the author using VESTA (2026).

In the tetragonal phase, lithium ions occupy three crystallographic sites, 8a, 16f, and 32g (EGGESTAD; SELBACH; WILLIAMSON, 2024; PUENTE *et al.*, 2021), providing a total of 56 lithium sites, which corresponds to the number of lithium ions in

the unit cell. Consequently, the lithium sublattice is highly ordered, with little or no intrinsic vacancy concentration available to support lithium-ion migration. In addition, the migration pathways between neighboring lithium sites are longer than those in the cubic phase (ZHAO *et al.*, 2022b), increasing the activation barrier for ionic transport. As a result, the tetragonal phase exhibits substantially lower ionic conductivity than the cubic phase.

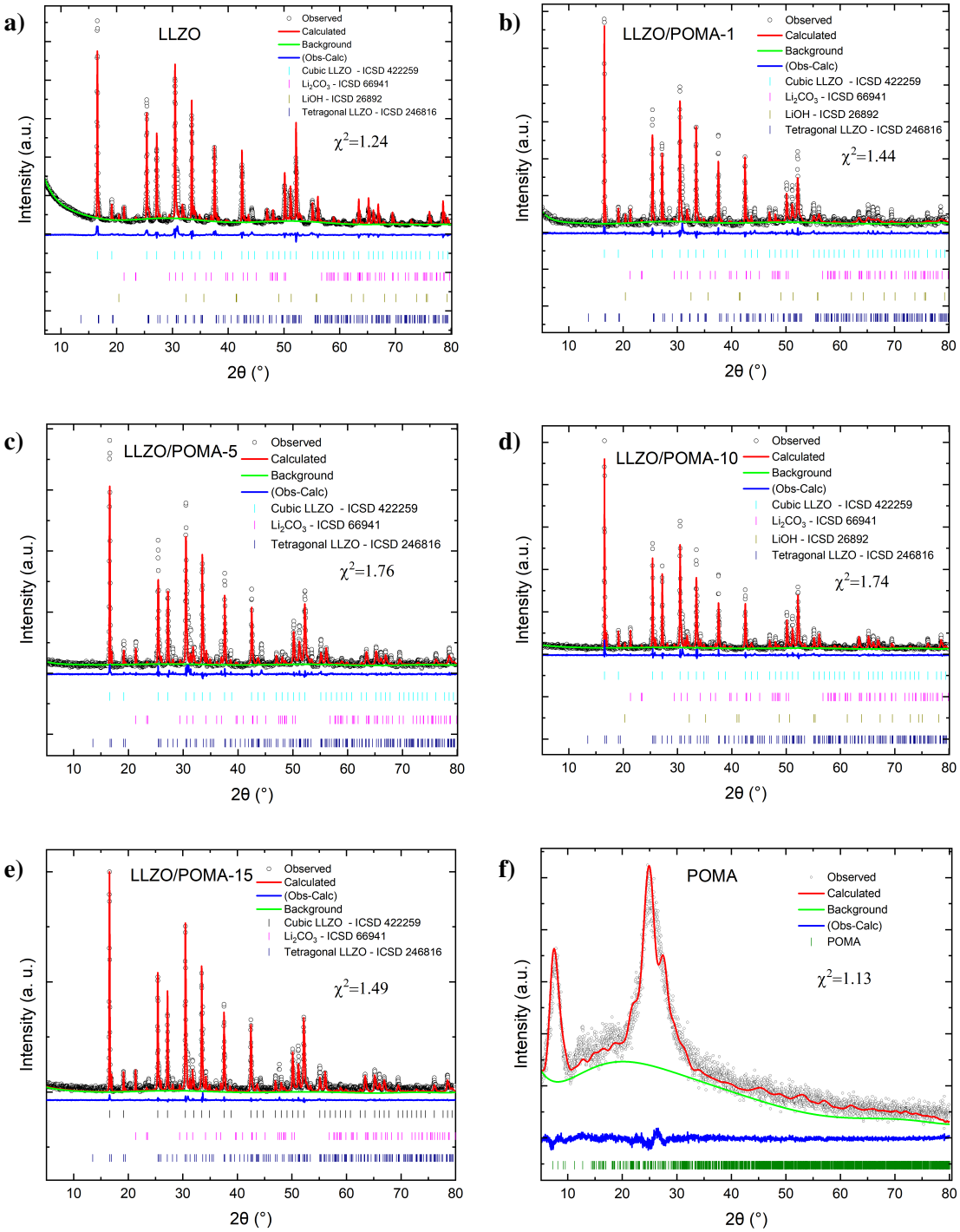
The structures of Li_2CO_3 and LiOH are shown in Figures 27c and 27d, respectively. As discussed previously, these phases are formed on the LLZO surface through reactions with atmospheric moisture and carbon dioxide. Their presence is undesirable because both compounds exhibit low lithium-ion conductivity and reduce interfacial stability between LLZO and lithium metal, thereby increasing interfacial resistance and degrading the electrolyte's electrochemical performance (GHORBANZADE; LÓPEZ-ARANGUREN; AMO, 2024).

Figures 28a–f present the Rietveld refinement results for LLZO and the LLZO/POMA composites, while Figure 28f corresponds to the Le Bail refinement of POMA. The refinements suggest that the cubic phase of $Li_7La_3Zr_2O_{12}$ is the predominant crystalline phase in all samples. In addition, a minor tetragonal fraction is identified throughout the composite series. The secondary phase Li_2CO_3 is also detected in all samples, whereas LiOH is absent only in the LLZO/POMA-5 and LLZO/POMA-15 composites. As previously discussed in Section 4.1, the phase weight fractions reported in this work correspond to the modeled crystalline phases and are normalized with respect to the total modeled crystalline fraction, rather than representing the absolute composition of the composites.

For the pristine LLZO sample, the Rietveld refinement indicates that the cubic phase of $Li_7La_3Zr_2O_{12}$ (space group $I\bar{3}d$) is the major crystalline phase, corresponding to 53.6 $\pm$ 1.0 wt%, followed by the tetragonal phase (space group $I4_1/acd$) with 17.2 $\pm$ 0.5 wt%. The refinement also suggests the presence of the secondary phases Li_2CO_3 (25.5 $\pm$ 1.1 wt%) and LiOH (3.7 $\pm$ 0.7 wt%). The refined lattice parameters, phase fractions, and refinement parameters are summarized in Tables 13 and 14. Compared with pristine LLZO, the LLZO/POMA-1 composite exhibits an increase in the cubic phase of $Li_7La_3Zr_2O_{12}$ (58.1 $\pm$ 1.2 wt%), accompanied by a decrease in the tetragonal fraction. Slight increases are also observed in the amounts of Li_2CO_3 (27.7 $\pm$ 1.3 wt%) and LiOH (5.0 $\pm$ 0.8 wt%). In addition, the lattice parameter of the cubic phase increases slightly, with *a* change from 13.1023(6) Å to 13.109(1) Å, correspond-

ing to an increase in the unit-cell volume from 2249.3(3) Å^3 to 2252.6(5) Å^3.

Figure 28: Rietveld refinements of (a) LLZO, (b) LLZO/POMA-1, (c) LLZO/POMA-5, (d) LLZO/POMA-10, (e) LLZO/POMA-15, and Le Bail refinement of (f) POMA.



Source: Prepared by the author.

Although POMA can interact with the LLZO surface, polymer macromolecules are

generally too large to occupy interstitial sites or substitute lattice atoms, as commonly observed in ceramic–polymer composites (LECHARTIER *et al.*, 2022; GHORBANZADE *et al.*, 2023; KOZDRA *et al.*, 2024). Therefore, the observed structural changes are more likely associated with indirect interfacial effects than with modifications of the LLZO crystal structure itself.

Table 13: Refined lattice parameters of the crystalline phases identified in the LLZO/POMA composites. Samples are identified as follows: P1 = LLZO/POMA–1; P5 = LLZO/POMA–5; P10 = LLZO/POMA–10; and P15 = LLZO/POMA–15.

Phase	**Parameter**	**LLZO**	**P1**	**P5**	**P10**	**P15**
Cubic LLZO	a (Å)	13.102(1)	13.109(1)	13.111(1)	13.109(1)	13.108(1)
	V (Å^3)	2249.3(3)	2252.6(5)	2253.5(6)	2252.7(4)	2252.4(2)
Tetragonal LLZO	a (Å)	13.056(2)	13.034(4)	13.117(3)	13.120(3)	13.120(3)
	c (Å)	12.852(2)	12.889(5)	12.698(3)	12.680(3)	12.681(3)
	V (Å^3)	2190.6(5)	2190.0(10)	2185.0(10)	2182.6(8)	2182.8(9)
Li_2CO_3	a (Å)	8.340(30)	8.350(40)	8.370(40)	8.350(30)	8.360(30)
	b (Å)	4.971(2)	4.973(3)	4.972(2)	4.973(2)	4.969(2)
	c (Å)	6.160(20)	6.180(20)	6.180(20)	6.180(10)	6.180(20)
	β (°)	114.170(50)	114.470(70)	114.450(60)	114.430(50)	114.450(50)
	V (Å^3)	233.0(1)	233.6(1)	234.2(2)	234.0(1)	233.8(1)
LiOH	a (Å)	3.560(3)	3.564(5)	–	3.604(8)	–
	c (Å)	4.354(3)	4.346(2)	–	4.369(3)	–
	V (Å^3)	55.2(1)	55.2(2)	–	56.7(3)	–

Source: Prepared by the author.

Compared with pristine LLZO, the LLZO/POMA-5 sample exhibits a similar fraction of the cubic $Li_7La_3Zr_2O_{12}$ phase, while the tetragonal fraction remains lower than that of the pristine material, although the reduction is less pronounced than in LLZO/POMA-1. This partial increase relative to LLZO/POMA-1 indicates that the tetragonal phase fraction does not evolve monotonically with increasing POMA content. A marked increase in the Li_2CO_3 content is observed, from 25.5 $\pm$ 1.1 wt% to 33.2 $\pm$ 1.2 wt%, whereas no LiOH phase is detected by the refinement. This result is consistent with a more advanced surface degradation process, in which LiOH formed during the initial stages reacts with atmospheric CO_2 to produce Li_2CO_3. The higher Li_2CO_3 content also indicates a greater consumption of lithium species at the LLZO surface, which may contribute to limiting any further increase in the relative fraction of the cubic phase.

The LLZO/POMA-5 sample also exhibits the largest expansion of the cubic unit

cell, with the lattice volume increasing from 2249.3(3) $Å^3$ for pristine LLZO to 2253.5(6) $Å^3$. In contrast, the tetragonal phase shows a reduction in lattice volume relative to the pristine material. Similar variations are observed for the LLZO/POMA-10 and LLZO/POMA-15 composites. Overall, the observed variations are relatively small and suggest that the incorporation of POMA does not significantly modify the crystal structure of the LLZO phases.

Table 14: Phase fractions and Rietveld refinement parameters for the LLZO/POMA composites, using the sample notation defined in Table 13.

Parameter	**LLZO**	**P1**	**P5**	**P10**	**P15**
Cubic LLZO (wt%)	53.6 ± 1.0	58.1 ± 1.2	53.6 ± 1.0	53.2 ± 1.0	55.3 ± 1.0
Tetragonal LLZO (wt%)	17.2 ± 0.5	9.2 ± 0.5	13.2 ± 0.6	12.6 ± 0.6	12.8 ± 0.6
Li_2CO_3 (wt%)	25.5 ± 1.1	27.7 ± 1.3	33.2 ± 1.2	31.2 ± 1.1	31.9 ± 1.2
LiOH (wt%)	3.7 ± 0.7	5.0 ± 0.8	–	3.0 ± 0.6	–
χ^2	1.24	1.44	1.76	1.74	1.49
R_{wp} (%)	15.96	19.83	20.16	19.66	18.94
R_{exp} (%)	14.32	16.53	15.20	14.90	15.52

Source: Prepared by the author.

The LLZO/POMA-10 and LLZO/POMA-15 samples exhibit similar weight fractions of the cubic (∼53 wt%) and tetragonal (∼13 wt%) phases, as well as comparable amounts of Li_2CO_3 (∼31 wt%). The only notable difference between these two compositions is the absence of LiOH in LLZO/POMA-15. Their lattice parameters also remain nearly unchanged, indicating that the structural changes associated with POMA addition become nearly constant for concentrations above 10 wt%.

Given that the POMA employed in this study was synthesized in its HCl-doped (POMA-Cl) form, chloride ions may influence the system's early evolution by modifying local charge compensation or interfacial electrostatics. However, the convergence of phase fractions and lattice parameters for POMA contents above 5–10 wt% suggests that the LLZO/POMA interface reaches a structurally stable regime, beyond which additional polymer or counterions no longer produce significant crystallographic changes.

Figure 28f presents the Le Bail refinement of the POMA sample. The initial lattice parameters, taken from Biondo *et al.* (2020), were $a = 6.0233$ Å, $b = 11.9863$ Å, $c = 18.9307$ Å, $\alpha = 83.1724°$, $\beta = 84.1401°$, and $\gamma = 88.8810°$. After refinement, the lattice parameters converged to $a = 6.10326(35)$ Å, $b = 12.2273(115)$ Å, $c = 18.6559(251)$ Å, $\alpha = 83.1112(138)°$, $\beta = 95.1501(365)°$, and $\gamma = 95.1501(88)°$.

The refinement yielded satisfactory agreement indices, with $\chi^2 = 1.13$, $R_{wp} = 12.98\%$, and $R_{exp} = 12.21\%$.

Another important observation is the systematic increase in Li_2CO_3 content up to the LLZO/POMA–5 sample (25.50 $\pm$ 1.11% for LLZO, 27.72 $\pm$ 1.29% for LLZO/POMA–1, and 33.20 $\pm$ 1.15% for LLZO/POMA–5). From LLZO/POMA–10 onward, the Li_2CO_3 fraction stabilizes at approximately 30 wt%. This behavior suggests that the initial incorporation of POMA increases the degradation reactions of LLZO. Beyond approximately 10 wt% POMA, however, no further significant increase in the Li_2CO_3 content is observed.

In contrast, the LiOH content does not exhibit a monotonic trend with increasing POMA concentration. Since LiOH readily reacts with atmospheric CO_2 to form Li_2CO_3, small amounts generated during the initial stages of surface degradation may no longer be detected in the final Rietveld refinements. Consequently, variations in the relative amounts of Li_2CO_3 and LiOH are more likely associated with surface degradation phenomena than with intrinsic modifications of the LLZO bulk structure. Therefore, the structural evolution of the composites is more appropriately evaluated using the relative fractions of the cubic and tetragonal $Li_7La_3Zr_2O_{12}$ phases, along with their lattice parameters and bond-length variations, which provide additional structural information about the refined garnet framework.

Table 15 summarizes the average atomic bond lengths of the predominant crystalline phase, cubic $Li_7La_3Zr_2O_{12}$, calculated using VESTA (MOMMA; IZUMI, 2011) from the CIF files obtained through Rietveld refinement of the XRD data. Upon POMA incorporation, slight variations in the local coordination environment are observed. Up to the LLZO/POMA-5 composition, the average Li–O, La–O, and Zr–O bond lengths exhibit a small increase, consistent with the slight expansion of the cubic unit cell discussed previously. For higher POMA contents (LLZO/POMA-10 and LLZO/POMA-15), the average bond lengths remain nearly unchanged or decrease slightly, suggesting that the structural response of the garnet lattice becomes nearly constant as the polymer concentration increases.

Despite the cubic LLZO phase remaining the predominant crystalline phase in all compositions, the aqueous route adopted for the preparation of the ceramic–polymer composites presents an inherent limitation due to the well-known reactivity of LLZO toward water. Although no significant structural degradation of the cubic phase was

observed under the adopted processing conditions, the possibility of surface reactions cannot be completely ruled out. Therefore, future studies should investigate the structural and electrical properties of LLZO/POMA composites prepared by dry-mixing routes, enabling a direct comparison with the aqueous processing method employed in the present work.

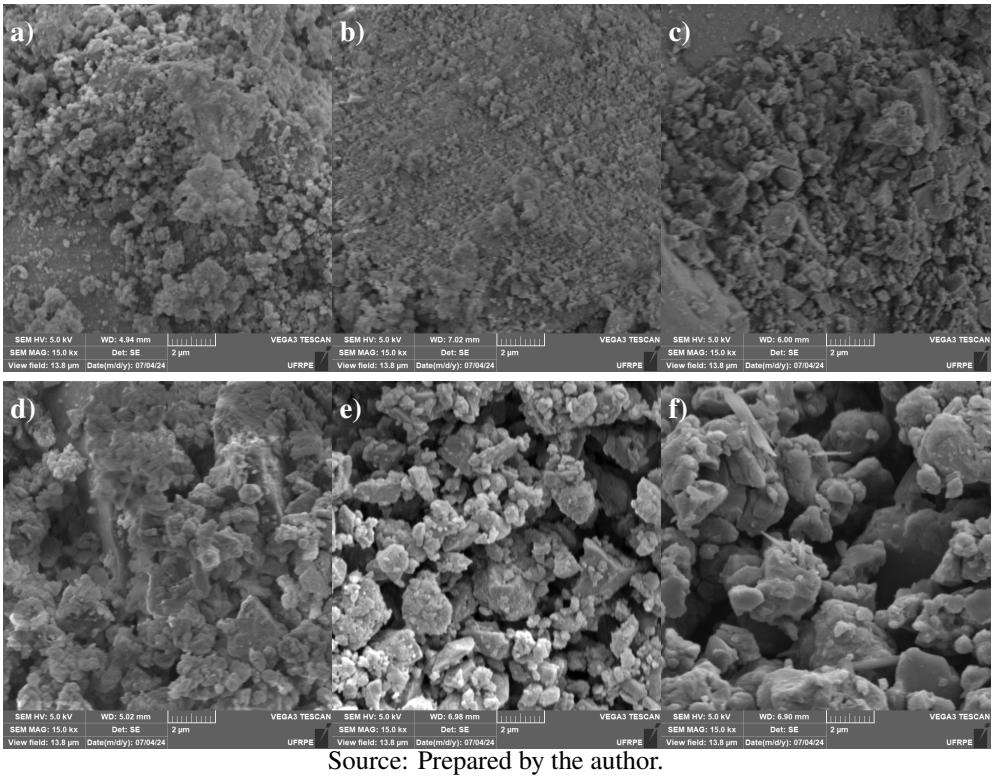
Table 15: Average Li–O, La–O, and Zr–O bond lengths for the cubic phase of $Li_7La_3Zr_2O_{12}$, by VESTA from CIF files from Rietveld refinement of the XRD data.

Sample	La-O (Å)	Zr-O (Å)	Li1-O (Å)	Li2-O (Å)
LLZO	2.57821 (3)	2.12895 (3)	1.92446 (3)	2.11280 (3)
LLZO/POMA-1	2.58065 (9)	2.13093 (7)	1.92625 (8)	2.11477 (8)
LLZO/POMA-5	2.58095 (11)	2.13122 (7)	1.92652 (9)	2.11506 (9)
LLZO/POMA-10	2.58063 (6)	2.13095 (6)	1.92627 (6)	2.11478 (7)
LLZO/POMA-15	2.58054 (3)	2.13087 (3)	1.92619 (3)	2.11470 (3)

Source: Prepared by the author.

4.2.2 Morphological Evolution upon POMA Incorporation

Figure 29: SEM micrographs of (a) LLZO, (b) LLZO/POMA-1, (c) LLZO/POMA-5, (d) LLZO/POMA-10, (e) LLZO/POMA-15, and (f) POMA.



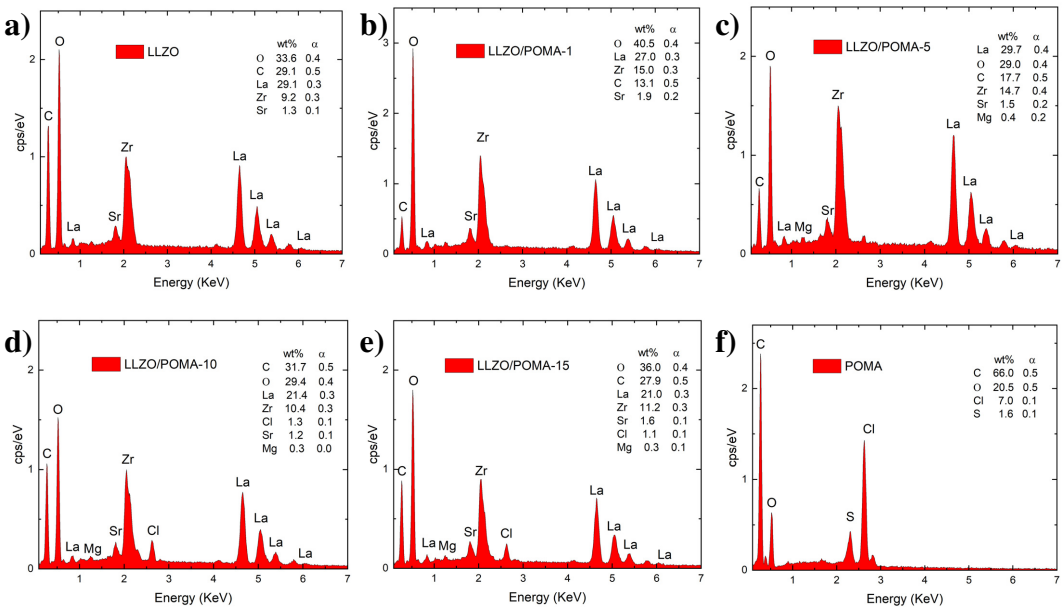
Source: Prepared by the author.

Figures 29–30 present the SEM micrographs and EDS spectra of the analyzed powder samples. Figure 29a shows the pristine LLZO sample, which exhibits a heterogeneous morphology characterized by particles with markedly different sizes and irregular shapes. Compared with pristine LLZO, the LLZO/POMA-1 composite sample (Figure 29b) exhibits a more homogeneous appearance. The addition of 1 wt% POMA may have contributed to this morphology by promoting greater cohesion between ceramic particles.

Figure 29c shows the LLZO/POMA-5 composite. Compared with the previous compositions, the particles appear more dispersed, with larger interparticle spaces, resulting in a more porous microstructure. The morphology changes further with the LLZO/POMA-10 sample (Figure 29d), which exhibits a more irregular microstructure resembling that of polymeric materials. A similar tendency is observed for the LLZO/POMA-15 composite (Figure 29e). In this sample, the voids between particles become even more evident.

Finally, the POMA sample (Figure 29f) exhibits the irregular agglomerated morphology commonly reported for this polymer (BIONDO *et al.*, 2020; SILVA *et al.*, 2021; SANCHES *et al.*, 2014a).

Figure 30: EDS spectra of (a) LLZO, (b) LLZO/POMA-1, (c) LLZO/POMA-5, (d) LLZO/POMA-10, (e) LLZO/POMA-15, and (f) POMA.

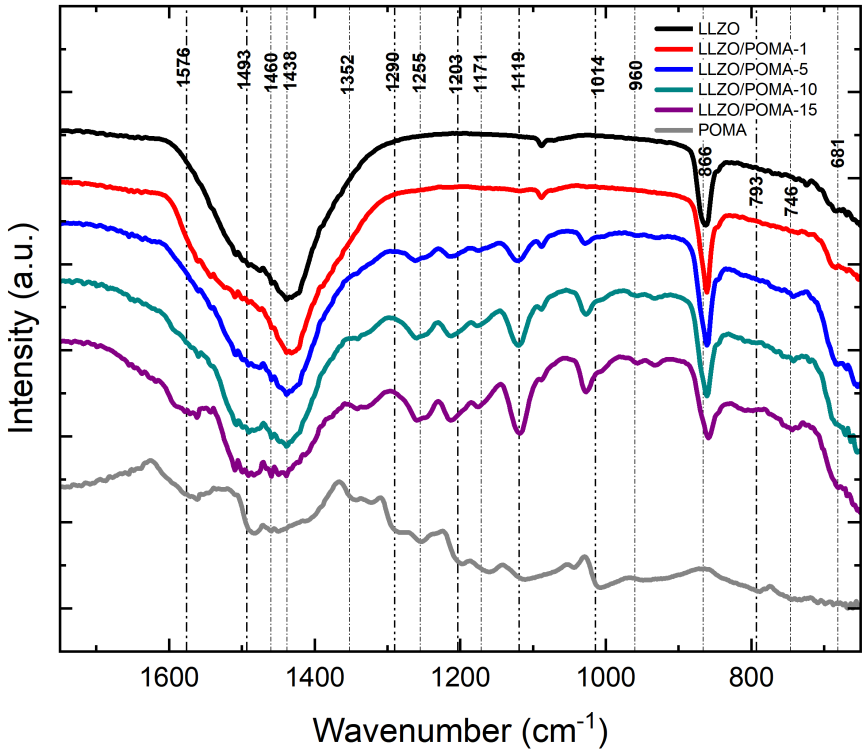


Source: Prepared by the author.

Figures 30a–f present the EDS spectra of the analyzed samples. The detected elements are consistent with the expected composition of the ceramic–polymer systems. In addition to La, Zr, and O, the spectra reveal the presence of Mg and Sr, which originate from the doping of the LLZO structure. Chlorine is associated with the hydrochloric acid used during the synthesis and doping of POMA, whereas sulfur originates from the ammonium persulfate employed as the oxidizing agent during the polymerization process.

4.2.3 Vibrational Modes and Chemical Bonding

Figure 31: FTIR spectra of LLZO, LLZO/POMA composites, and POMA.



Source: Prepared by the author.

Figure 31 presents the Fourier-transform infrared (FTIR) spectra of all analyzed samples. Several absorption bands characteristic of POMA can be identified. The band at 1460 cm^{-1} is attributed to the C–H deformation of the $-OCH_3$ group (BIONDO *et al.*, 2020; ELGEGREN *et al.*, 2019). The band at 1290 cm^{-1} corresponds to C–N stretching vibrations (BIONDO *et al.*, 2020; SILVERSTEIN; BASSLER, 1962; NYCZYK *et al.*, 2009), whereas the bands between 1203 and 793 cm^{-1} are associated

with the 1,4-substituted benzene ring, one of the structural units of POMA (BIONDO *et al.*, 2020). In addition, the band at 1255 cm^{-1} is assigned to C–O–C stretching vibrations (SMITH, 2017), while the band at 746 cm^{-1} is attributed to the out-of-plane C–H deformation of mono- and 1,2-disubstituted aromatic rings (SANCHES *et al.*, 2014a).

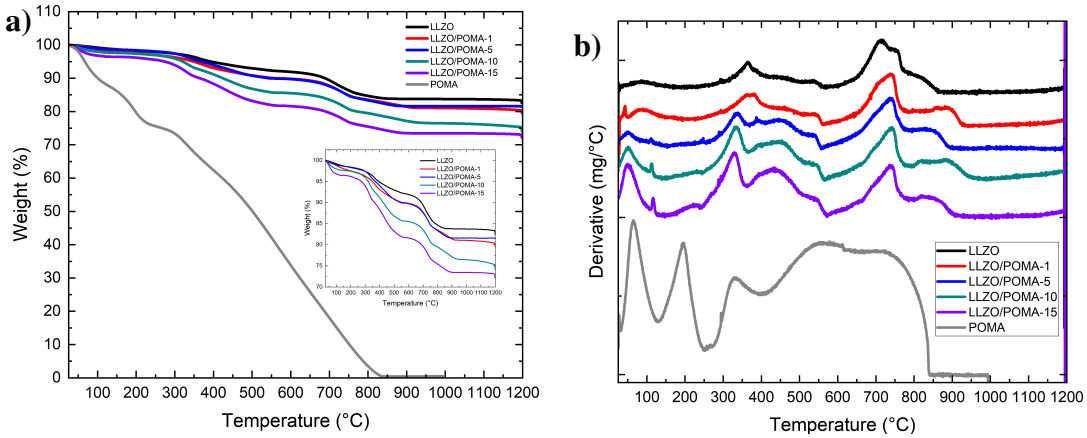
The band at 1352 cm^{-1} may be related to residual ammonium persulfate (APS) (BIONDO *et al.*, 2020), the oxidizing agent employed during POMA synthesis. This interpretation is consistent with the sulfur detected by EDS in the POMA sample (Figure 30f). According to Aote e Deshpande (2024), the bands at 688 and 681 cm^{-1} are assigned to Zr–O and La–O vibrations, respectively, supporting the formation of the LLZO phase. Furthermore, the band at 1438 cm^{-1} is associated with the asymmetric stretching vibration of the carbonate (CO_3^{2-}) group, corroborating the presence of Li_2CO_3 previously identified by XRD.

4.2.4 Thermal Behavior and Stability

Figure 32 presents the thermogravimetric (TG) and derivative thermogravimetric (DTG) curves of the analyzed samples. The TG curves (Figure 32a) show a progressive mass loss with increasing temperature. The pristine LLZO sample exhibits the lowest mass variation, retaining approximately 83% of its initial mass at 1200 °C, whereas the LLZO/POMA-15 composite shows the highest mass loss, retaining about 73% of its initial mass. The difference of approximately 10 wt% between pristine LLZO and LLZO/POMA-15 indicates that increasing the POMA content reduces the thermal stability of the composites. However, the residual mass remains considerably higher than expected from the nominal polymer content, suggesting that part of the polymer undergoes pyrolysis, leading to the formation of thermally stable carbonaceous residues rather than being completely volatilized. In contrast, the POMA sample undergoes a much more pronounced mass loss, with the decomposition occurring predominantly at intermediate temperatures, after which no significant additional mass variation is observed up to 1200 °C.

In the composite samples, the first major DTG peak progressively shifts toward lower temperatures as POMA content increases. For instance, in the LLZO/POMA–15 sample, the peak occurs at approximately 329 °C, indicating that the primary degradation process begins earlier in the presence of POMA.

Figure 32: Thermogravimetric analysis of LLZO, LLZO/POMA composites, and POMA: (a) TG curves and (b) DTG curves.



Source: Prepared by the author.

In addition, a low-temperature DTG feature (approximately 40–80 °C) becomes progressively more pronounced with increasing POMA content. This event is attributed to the release of physically adsorbed water and residual solvent associated with the polymeric phase. The enhanced mass loss in this temperature range is consistent with the higher amounts of LiOH and Li_2CO_3 identified by XRD, since moisture promotes surface reactions on LLZO that lead to the formation of these secondary phases. The greater intensity of this event in the composites suggests that incorporating POMA increases the material's susceptibility to moisture adsorption, thereby contributing to the observed low-temperature mass loss.

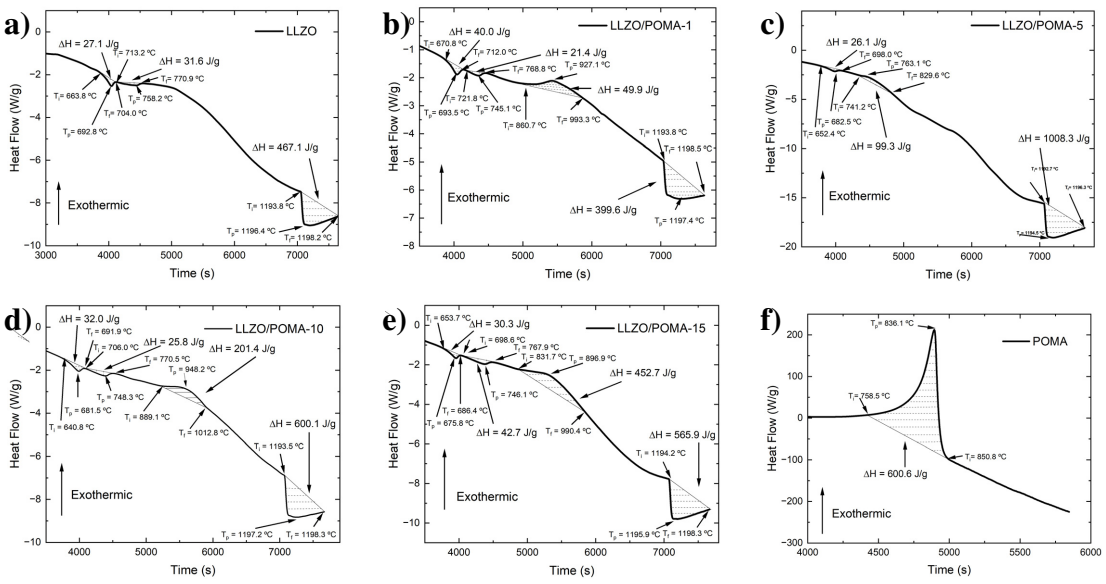
In all composite samples, a pronounced DTG peak is observed at approximately 743 °C. Unlike the low-temperature degradation events, this peak exhibits little variation with increasing POMA content. This behavior is consistent with the TG curves (Figure 32a), which indicate that approximately 90 wt% of the initial POMA mass has already decomposed by this temperature. Therefore, this high-temperature event is predominantly associated with the ceramic component of the composites.

The gray DTG curve in Figure 32b corresponds to the POMA sample. A pronounced peak is observed at approximately 63 °C, indicating a high mass-loss rate in this temperature range, which is attributed to the evaporation of physically adsorbed water and residual solvent. The peaks centered near 200 and 300 °C are associated with the thermal degradation of the polymer, beginning with the cleavage of the methoxy ($-OCH_3$) side groups (GAŁKA; KOWALONEK; KACZMAREK, 2014). At higher

temperatures (approximately 500–800 °C), additional degradation events are observed and are attributed to the decomposition of the remaining carbonaceous residues formed during the earlier stages of polymer degradation (GAŁKA; KOWALONEK; KACZMAREK, 2014), completing the thermal decomposition of POMA.

Figures 33a–f present the DSC thermograms of the analyzed samples. The enthalpy values were calculated as described in Section 4.1. Using the same integration procedure, typical variations of 1–5% were obtained for the calculated enthalpy values. For the pristine LLZO sample (Figure 33a), three endothermic events are observed, centered at approximately 692.8, 758.2, and 1196.4 °C. The first event extends from 663.8 to 704.0 °C, the second from 713.2 to 770.9 °C, and the third from 1193.8 to 1198.2 °C. The first two endothermic events are attributed to the tetragonal-to-cubic phase transition, which occurs upon heating as internal stresses within the LLZO crystal lattice are progressively relieved (LARRAZ; ORERA; SANJUÁN, 2013). The high-temperature endothermic event has also been reported for LLZO-based materials (MATSUI *et al.*, 2014), although its origin remains under discussion in the literature.

Figure 33: DSC thermograms for: (a) LLZO, (b) LLZO/POMA-1, (c) LLZO/POMA-5, (d) LLZO/POMA-10, (e) LLZO/POMA-15, and (f) POMA, recorded in the high-temperature region.



Source: Prepared by the author.

In addition to the endothermic events observed for pristine LLZO, all composite samples exhibit an exothermic peak between approximately 763 and 948 °C. This fea-

ture is attributed to the final stage of POMA thermal decomposition (BERNAL *et al.*, 2002). A similar exothermic peak is also observed for the pristine POMA sample (Figure 33f), centered at approximately 836.1 °C, supporting this assignment.

In summary, the incorporation of POMA shifts the onset of the main degradation events to lower temperatures, reflecting the lower thermal stability of the polymeric phase. Nevertheless, from the standpoint of thermal decomposition, this behavior does not compromise the potential application of these composites as solid-state electrolytes, since all samples exhibit negligible mass loss up to approximately 300 °C, well above the typical operating temperature of solid-state batteries (20–40 °C) (ORTIZ *et al.*, 2024). However, as discussed in Section 4.1, assessing their suitability from a thermal perspective also requires evaluating additional factors beyond mass loss, which were outside the scope of the present study. Furthermore, the thermal analysis is consistent with the structural and spectroscopic results, indicating that incorporating POMA increases the composites' susceptibility to moisture uptake during preparation and handling. This behavior favors the initial formation of LiOH, which subsequently reacts with atmospheric CO_2 to form Li_2CO_3, as described by Eq. (4.5). The observation that the Li_2CO_3 content reaches a plateau at approximately 30 wt% for POMA contents above 10 wt% suggests that, at higher polymer loadings, the polymer matrix progressively covers the LLZO particles, thereby limiting further surface reactions with the surrounding atmosphere. The enthalpy values were calculated as described in Section 4.1.

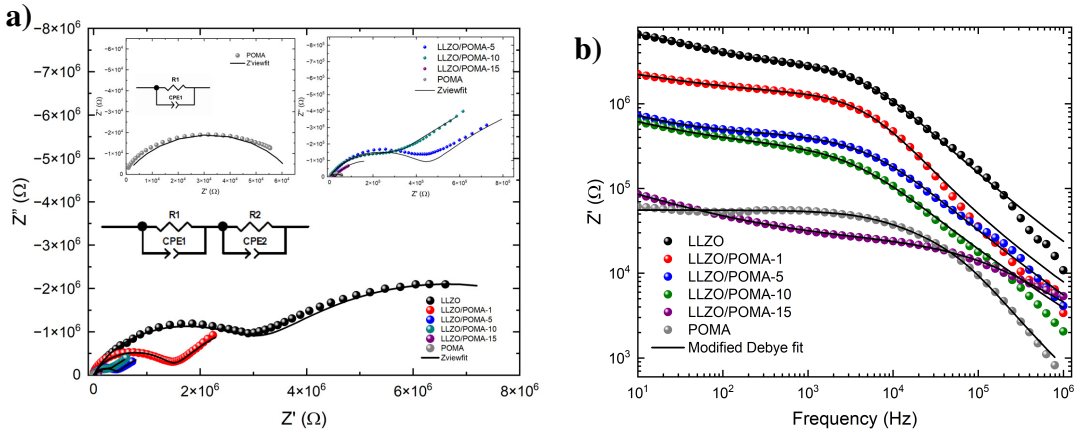
4.2.5 Electrical Response and Relaxation Processes

Figure 34a presents the Nyquist (Z'' versus Z') plots obtained from complex impedance spectroscopy. The largest semicircle, shown in black, corresponds to the pristine LLZO sample. The LLZO/POMA-1, LLZO/POMA-5, LLZO/POMA-10, and LLZO/POMA-15 composites are represented by the red, blue, green, and purple curves, respectively, whereas the smallest semicircle (gray) corresponds to the pristine POMA sample. A progressive reduction in the semicircle diameter is observed as POMA content increases, indicating a decrease in the electrical resistance of the composites.

As discussed in Section 4.1, the experimental methodology employed in this work does not allow separation of the ionic and electronic contributions to the measured electrical conductivity. Therefore, the discussion presented in this section refers to

the overall charge-transport behavior without attributing the observed variations to a specific transport mechanism.

Figure 34: (a) Nyquist plots of LLZO, LLZO/POMA composites, and POMA with equivalent-circuit fitting (inset). (b) The real part of the impedance (Z') fitted with the modified Debye model.



Source: Prepared by the author.

The equivalent circuit shown in the inset of Figure 34a was used to describe the electrical response of both pristine LLZO and the LLZO/POMA composites. The resistor R_1 and the constant phase element (CPE1) are connected in parallel and represent the electrical response of the HF process. The resistor R_2 and the constant phase element (CPE2) describe the response of the interfacial LF process. The CPE is employed instead of an ideal capacitor to account for the non-ideal capacitive behavior associated with a distribution of relaxation times, as evidenced by the depressed semicircular arcs observed in the Nyquist plots (ZHAO *et al.*, 2022a; SCHALENBACH *et al.*, 2021; XIAO *et al.*, 2024). This equivalent circuit was selected because the impedance spectra exhibit two partially overlapping depressed semicircles, indicating the presence of two distinct electrical processes. Similar equivalent-circuit models have been successfully applied to ceramic-based solid electrolytes and related composite systems (COSTA *et al.*, 2022). As discussed in Section 4.1.5, the $R_1 \parallel \text{CPE}_1$ branch can be interpreted as an effective response arising from the superposition of contributions from the different crystalline phases and the polymeric phase. In turn, the $R_2 \parallel \text{CPE}_2$ branch may be associated with slower processes involving interfaces, electrode interactions, and polarization effects.

Figure 34b presents the real component of the impedance (Z') as a function of

frequency. At low frequencies, Z' approaches approximately $6.6 \times 10^6\ \Omega$ for pristine LLZO, whereas a value on the order of $10^4\ \Omega$ is obtained for the LLZO/POMA-15 composite. These values are consistent with the low-frequency resistances determined from the equivalent-circuit fitting using ZView, confirming the progressive reduction in electrical resistance with increasing POMA content. To further analyze the relaxation processes, the experimental $Z'(\omega)$ spectra were fitted using the modified Debye model introduced in Section 2.2.7.3, according to Eq. (2.21).

Table 16 summarizes the equivalent-circuit parameters obtained from the ZView fitting, and Table 17 presents conductivities calculated according to Equation 2.20 described in Section 2.2.7.3. The effective capacitances were calculated using Equation 2.22, described in Section 2.2.7.3. Both R_1, associated with the effective high-frequency response, and R_2, associated with slower low-frequency processes, decrease progressively with increasing POMA content. There is only a minor deviation from this trend between the LLZO/POMA-5 and LLZO/POMA-10 samples, due to a slight increase in R_1 (from $4.40 \times 10^5\ \Omega$ to $4.71 \times 10^5\ \Omega$). The conductivities corresponding to the HF (σ_1) and LF (σ_2) processes, as well as the total conductivity, exhibit an overall increasing trend with increasing POMA content. An exception is observed between the LLZO/POMA–5 and LLZO/POMA–10 samples, for which the conductivity values are very similar, with a slight decrease in σ_1 and σ_{total}. For example, σ_1 increases by approximately two orders of magnitude, from 1.89×10^{-8} S·cm^{-1} for pristine LLZO to 2.48×10^{-6} S·cm^{-1} for LLZO/POMA-15. For all samples, the ZView fitting yielded χ^2 values on the order of 10^{-3} to 10^{-2}, supporting the use of the adopted equivalent-circuit model to describe the experimental impedance spectra.

Table 16: Equivalent-circuit parameters and goodness-of-fit indicators for the LLZO/POMA samples.

Sample	R_1 **(Ω)**	$C_{\text{eff},1}$ **(F)**	R_2 **(Ω)**	$C_{\text{eff},2}$ **(F)**	χ^2	**Sum of squares**
LLZO	2.99×10^6 (8)	9.61×10^{-12} (23)	7.40×10^6 (74)	1.70×10^{-9} (22)	3.21×10^{-3}	8.35×10^{-2}
LLZO/POMA–1	1.49×10^6 (2)	2.20×10^{-11} (5)	4.99×10^6 (10)	2.07×10^{-8} (9)	1.44×10^{-3}	3.76×10^{-2}
LLZO/POMA–5	4.40×10^5 (10)	5.96×10^{-11} (49)	2.07×10^6 (4)	6.39×10^{-8} (35)	4.11×10^{-3}	9.04×10^{-2}
LLZO/POMA–10	4.71×10^5 (31)	1.90×10^{-10} (7)	2.06×10^6 (22)	3.80×10^{-8} (94)	6.45×10^{-3}	4.33×10^{-2}
LLZO/POMA–15	2.81×10^4 (17)	7.54×10^{-11} (145)	3.39×10^5 (22)	1.12×10^{-7} (15)	3.23×10^{-2}	8.41×10^{-1}
POMA	6.38×10^4 (31)	1.81×10^{-10} (14)	—	—	1.00×10^{-2}	2.01×10^{-1}

Source: Prepared by the author.

The suitability of the equivalent-circuit models was evaluated following the same procedure described in Section 4.1. For the LLZO/POMA composite series, the two-arc model, $(R_1 \parallel CPE_1)(R_2 \parallel CPE_2)$, was favored by the statistical criteria for most compositions. However, LLZO/POMA–1 and LLZO/POMA–15 yielded lower information-criterion values for the arc + CPE tail and arc + finite-length Warburg (W_s) models, respectively. For pristine POMA, the one-arc model exhibited the best statistical adequacy, consistent with the single electrical process clearly observed in its impedance spectrum.

Despite the differences observed for some compositions, the two-arc model was retained for the LLZO/POMA composites to preserve a common representation of the HF and LF processes and to enable a systematic comparison of the fitted parameters across the series. For the POMA sample, the one-arc model was adopted based on its clear statistical preference according to both the AIC and BIC criteria. This choice is further supported by the consistency in magnitude between the conductivity values derived from the two-arc equivalent-circuit model and those independently obtained from the Jonscher analysis.

Table 17: Electrical conductivities derived from the equivalent-circuit fitting of the LLZO/POMA samples.

Sample	σ_1 (S·cm^{-1})	σ_2 (S·cm^{-1})	σ_{total} (S·cm^{-1})
LLZO	1.89×10^{-8} (5)	7.65×10^{-9} (76)	5.45×10^{-9} (39)
LLZO/POMA–1	3.81×10^{-8} (4)	1.13×10^{-8} (2)	8.74×10^{-9} (13)
LLZO/POMA–5	1.29×10^{-7} (3)	2.74×10^{-8} (5)	2.26×10^{-8} (4)
LLZO/POMA–10	1.20×10^{-7} (8)	2.75×10^{-8} (30)	2.24×10^{-8} (20)
LLZO/POMA–15	2.48×10^{-6} (15)	2.05×10^{-7} (13)	1.89×10^{-7} (11)
POMA	1.75×10^{-6} (9)	—	1.75×10^{-6} (9)

Source: Prepared by the author.

Most samples exhibited mean residuals below 10%. The largest residuals, ranging from 10% to 15%, were predominantly observed at the limits of the frequency range, where instrumental and electrode-polarization effects may become more significant. The consistency of the impedance spectra was additionally evaluated using the Kramers–Kronig test (ORAZEM; TRIBOLLET, 2008).

Table 18: Kramers–Kronig validation, information criteria, and residuals obtained from the comparison of alternative equivalent-circuit models for the LLZO/POMA samples, where 1A denotes the one-arc model, 2A the two-arc model, AC the arc + CPE tail model, and AW the arc + finite-length Warburg model.

Sample	**KK error (%)**	**Model favored by AIC/BIC**	**AIC$_{1A}$**	**AIC$_{2A}$**	**AIC$_{AC}$**	**AIC$_{AW}$**	**BIC$_{1A}$**	**BIC$_{2A}$**	**BIC$_{AC}$**	**BIC$_{AW}$**	**Residuals Z'/Z'' (%)**
LLZO	5.29	Two arcs	-335.67	**-531.33**	-245.34	-249.40	-327.79	**-515.58**	-229.59	-231.02	5.29 / 4.43
LLZO/POMA–1	15.01	Arc + CPE tail	-320.93	-311.98	**-352.52**	-290.91	-313.05	-296.23	**-336.77**	-272.54	15.01 / 11.05
LLZO/POMA–5	7.42	Two arcs	-257.74	**-454.83**	-257.17	-305.93	-249.86	**-439.08**	-241.42	-287.56	7.42 / 7.61
LLZO/POMA–10	4.00	Two arcs	-518.58	**-934.34**	-512.80	-499.82	-508.81	**-914.80**	-493.26	-477.02	4.00 / 7.25
LLZO/POMA–15	4.80	Arc + Warburg	-354.11	-446.51	-446.46	**-457.90**	-346.23	-430.76	-430.71	**-439.53**	4.80 / 11.00
POMA	6.69	One arc	**-318.25**	-287.04	-210.51	-106.64	**-311.68**	-273.90	-197.37	-91.32	6.69 / 6.66

Source: Prepared by the author.

The parameters obtained from fitting the experimental $Z'(\omega)$ spectra with the modified Debye model are summarized in Table 19. The series resistance was fixed at $R_s = 0$, consistent with the values obtained from the equivalent-circuit fitting performed using ZView. The resistance values obtained from the two approaches show good agreement: the fitted R_1 values are comparable to those listed in Table 16, whereas the R_2 values agree at least within the same order of magnitude. Overall, the consistency between the equivalent-circuit and modified Debye analyses supports the assignment of the two relaxation processes to HF and LF contributions and suggests the progressive reduction in the electrical resistance with increasing POMA content. The same procedure described in Section 4.1 was adopted, with selected parameters fixed to improve fitting stability.

Table 19: 2×ZARC fit parameters from $Z'(f)$: for each sample the smaller resistance is labeled R_1 (with its corresponding τ_1 and n_1). Units: R in Ω, τ in s. Numbers in parentheses indicate the uncertainty in the last digit(s) of the mantissa.

Sample	R_1 (Ω)	τ_1 (s)	n_1	R_2 (Ω)	τ_2 (s)	n_2
LLZO	2.92×10^6 (3)	2.82×10^{-5} (4)	0.77(1)	5.92×10^6 (19)	8.72×10^{-3} (5)	0.64(1)
LLZO/POMA–1	1.31×10^6 (1)	2.83×10^{-5} (4)	0.83 (fixed)	2.27×10^6 (18)	3.06×10^{-2} (67)	0.52 (fixed)
LLZO/POMA–5	4.39×10^5 (0)	2.40×10^{-5} (2)	0.72 (fixed)	1.25×10^6 (17)	7.33×10^{-2} (17)	0.62 (fixed)
LLZO/POMA–10	3.05×10^5 (0)	3.63×10^{-5} (6)	0.72 (fixed)	1.51×10^6 (1)	1.73×10^{-1} (fixed)	0.49 (fixed)
LLZO/POMA–15	2.32×10^4 (0)	1.23×10^{-6} (3)	0.61 (fixed)	3.49×10^5 (30)	3.83×10^{-1} (86)	0.43 (fixed)
POMA	2.01×10^4 (18)	2.53×10^{-6} (34)	0.88 (fixed)	3.57×10^4 (19)	1.48×10^{-5} (fixed)	0.79 (fixed)

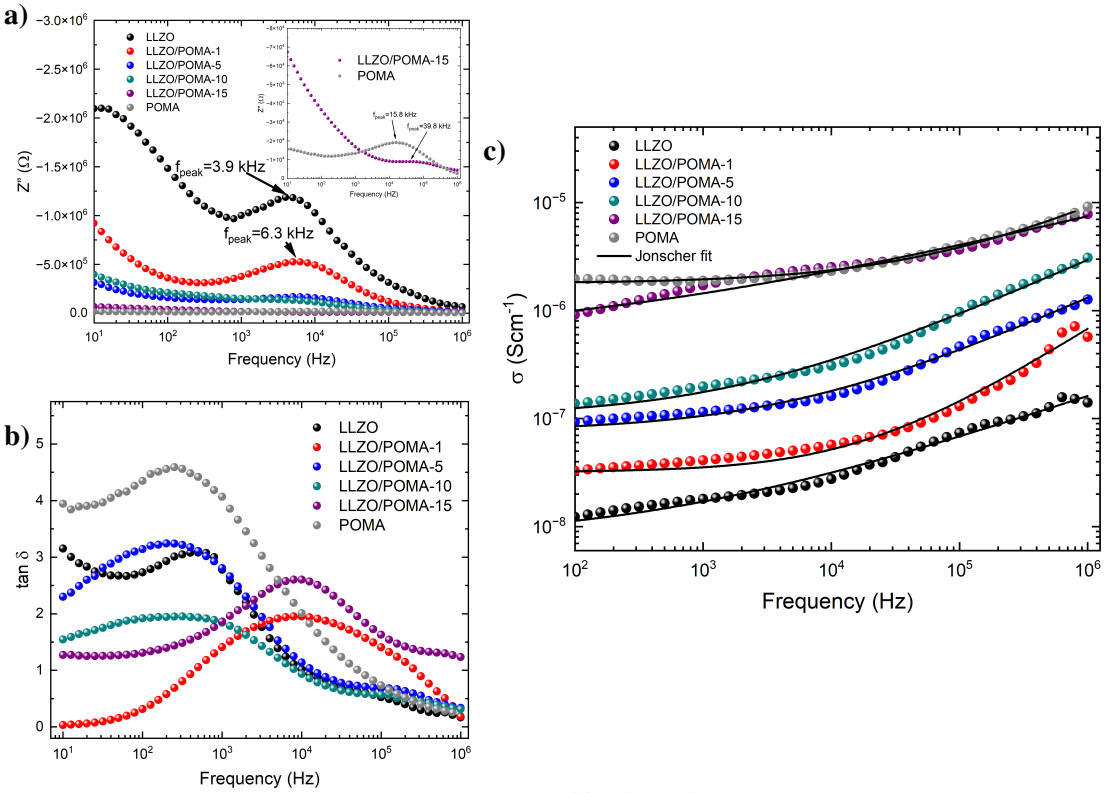
Source: Prepared by the author.

Figure 35a presents the imaginary component of the impedance (Z'') as a function

of frequency. As discussed in Section 4.1, the peak frequency is directly related to the characteristic relaxation time of the charge carriers. A progressive shift of the Z'' maximum toward higher frequencies is observed with increasing POMA content, indicating shorter relaxation times.

For pristine LLZO, the relaxation peak is centered at approximately 3.9 kHz, whereas it shifts to 6.3 kHz for the LLZO/POMA-1 composite and reaches 39.8 kHz for LLZO/POMA-15. These frequencies correspond to progressively shorter relaxation times, indicating faster electrical relaxation as the POMA content increases. This behavior is consistent with the impedance analyses discussed above, indicating that incorporating POMA facilitates charge-transport by reducing the resistance in HF and LF regions.

Figure 35: Frequency dependence of (a) the imaginary part of the impedance (Z''), (b) dielectric loss ($\tan\delta$) for LLZO, LLZO/POMA composites, and POMA, and (c) AC conductivity as a function of frequency fitted using Jonscher's law.



Source: Prepared by the author.

Complex impedance spectroscopy also provides access to the dielectric response of the material through the complex permittivity formalism discussed in Section 2.2.7.3. Based on this approach, the dielectric behavior of the LLZO/POMA composites was

evaluated as a function of frequency.

Figure 35b presents the dielectric loss factor ($\tan\delta$) as a function of frequency. As discussed in Section 4.1, $\tan\delta$ provides information on dielectric relaxation and energy dissipation in the material. Its frequency-dependent behavior changes with POMA incorporation, particularly in the low-frequency region, where, except for the LLZO/POMA-5 sample, the composites exhibit lower $\tan\delta$ values than pristine LLZO. Since $\tan\delta = \varepsilon''/\varepsilon'$, these lower values indicate a smaller relative contribution of dielectric losses to the dielectric response.

Figure 35c shows the frequency dependence of the AC conductivity. A progressive increase in conductivity is observed with increasing POMA content. At high frequencies, the conductivity increases from 1.41×10^{-7} S·cm^{-1} for pristine LLZO to 7.47×10^{-6} S·cm^{-1} for LLZO/POMA-15, while pristine POMA exhibits a conductivity of 8.30×10^{-6} S·cm^{-1}. The experimental conductivity spectra were fitted using the Jonscher model presented in Section 2.2.7.3. The resulting parameters are summarized in Table 20.

The fitted parameters indicate a clear increase in the total DC conductivity, including both HF and interfacial LF contributions, with increasing POMA content. Overall, the DC conductivity increases by approximately two orders of magnitude, from $7.58(46) \times 10^{-9}$ S·cm^{-1} for pristine LLZO to $5.44(99) \times 10^{-7}$ S·cm^{-1} for the LLZO/POMA-15 composite.

Another relevant result presented in Table 20 is the systematic reduction of the Jonscher exponent s, from 0.756 for LLZO/POMA-1 to 0.295 for LLZO/POMA-15. Within the Jonscher formalism, the exponent s characterizes the frequency-dependent dispersive contribution to the conductivity. Therefore, the progressive decrease in s indicates a systematic change in the frequency dependence of the electrical response with increasing POMA content.

Such variation may reflect changes in the distribution of relaxation processes and in the electrical heterogeneity of the ceramic–polymer system. However, the microscopic origin of this behavior cannot be unambiguously established from the s values obtained at a single temperature. Therefore, the observed trend is interpreted here primarily as evidence that POMA incorporation progressively modifies the dispersive electrical response of the composites, concomitantly with the observed increase in DC conductivity.

Table 20: Jonscher fitting parameters for the LLZO/POMA system: σ_{DC}, A, and s.

Sample	σ_{DC} (S·cm^{-1})	A	s
LLZO	$7.58 \times 10^{-9}(46)$	$2.76 \times 10^{-10}(53)$	$0.404(11)$
LLZO/POMA–1	$3.19 \times 10^{-8}(14)$	$4.67 \times 10^{-12}(fixed)$	$0.756(11)$
LLZO/POMA–5	$7.63 \times 10^{-8}(26)$	$2.73 \times 10^{-10}(65)$	$0.538(14)$
LLZO/POMA–10	$1.04 \times 10^{-7}(5)$	$6.89 \times 10^{-10}(fixed)$	$0.532(15)$
LLZO/POMA–15	$5.44 \times 10^{-7}(99)$	$6.82 \times 10^{-8}(fixed)$	$0.295(16)$
POMA	$1.78 \times 10^{-6}(2)$	$1.33 \times 10^{-9}(25)$	$0.551(13)$

Source: Prepared by the author.

To place the present results in context, previous studies have reported LLZO-based composites incorporating different polymer matrices. For instance, a PVDF/LLZO composite engineered with a three-dimensional interconnected LLZO architecture exhibited an ionic conductivity of 1.51×10^{-4} S·cm^{-1} (WU *et al.*, 2020), whereas the same study reported a conductivity of 7.5×10^{-5} S·cm^{-1} for PVDF/LLZO composites containing LLZO as discrete particles. For LLZO/PEO systems with 20 wt% polymer, conductivities on the order of 10^{-5} S·cm^{-1} have been reported (GHORBANZADE *et al.*, 2023). Composites incorporating Al-doped LLZO nanofibers in a PVDF-HFP matrix reached 3.26×10^{-4} S·cm^{-1} (HAN *et al.*, 2025), and a similar value (2.9×10^{-4} S·cm^{-1}) has been reported for LLZO/PAN composites (ZHAO *et al.*, 2025). Overall, LLZO/polymer composites typically exhibit ionic conductivities in the 10^{-5}–10^{-4} S·cm^{-1} range.

The conductivity values reported for LLZO/polymer composites in the literature therefore provide a useful context for evaluating the electrical response of the present system. The LLZO/POMA-15 composite exhibited a high-frequency conductivity (σ_1) of 2.48 $\times$ 10^{-6} S·cm^{-1}, which is of a comparable order of magnitude to the lower conductivity values reported for some LLZO/polymer composites. However, this comparison is limited to the magnitude of the electrical response, since the values reported in the literature correspond predominantly to ionic conductivity, whereas the ionic and electronic contributions to σ_1 could not be separated in the present study.

Furthermore, the samples obtained in this work contained significant crystalline fractions of Li_2CO_3 and, to a lesser extent, LiOH, in addition to the presence of the tetragonal LLZO phase. These secondary phases are well known to significantly in-

fluence the electrical response of the material by increasing the material resistance and interfacial effects, which tend to reduce the total electrical conductivity compared with samples composed predominantly of high-purity cubic LLZO (COUNIHAN *et al.*, 2025). The presence of these phases may also modify the system's capacitive response, shifting the capacitance from a regime characteristic of grain and grain boundary processes to one dominated by interfacial processes, which are typically associated with higher capacitance values due to interfacial polarization effects (Table 2). Nevertheless, these limitations do not compromise the main objective of the present work, which is to evaluate the influence of POMA on the structural and electrical properties of ceramic–polymer composites. Since all compositions were prepared from the same LLZO batch using the same experimental procedure, the influence of these secondary phases is expected to be similar for all samples. Therefore, the differences observed among the compositions can be primarily attributed to the incorporation of POMA.

Because non-blocking electrodes were employed, the present measurements do not allow an unambiguous separation of ionic and electronic contributions to the overall DC conductivity. Such a distinction would require complementary measurements, such as DC polarization using ion-blocking electrodes or transference-number experiments. Nevertheless, cubic LLZO is widely recognized as a predominantly lithium-ion conductor (RAJU *et al.*, 2021; JUNG *et al.*, 2022; QU *et al.*, 2025; MILERIO *et al.*, 2025). On the other hand, HCl-doped POMA is an electronically conducting polymer whose charge transport occurs through polarons and bipolarons. Therefore, although the observed conductivity enhancement may result from changes in the charge-transport pathways within the LLZO/POMA composite induced by the polymeric phase, HCl-doped POMA is an electronically conducting polymer. Consequently, an increased electronic contribution to the total conductivity cannot be ruled out, and the relative contributions of ionic and electronic transport remain to be established by carrier-selective measurements.

4.3 Comparative Analysis of POMA-Induced Effects in NLTO- and LLZO-Based Composites

The incorporation of POMA into the two ceramic matrices investigated in this work produced distinct effects. In the NLTO/POMA system, the presence of species associated with the acid doping of POMA favors protonation and Na^+/H^+ ion-exchange

processes within the layered structure of $Na_2Ti_3O_7$, accompanied by the formation of $H_2Ti_3O_7$ and NaCl. In the LLZO/POMA system, on the other hand, POMA incorporation did not compromise the predominance of the cubic LLZO phase among the identified crystalline phases. However, processing in an aqueous medium favored H^+/Li^+ exchange processes associated with the reactivity of LLZO with water and the formation of LiOH and Li_2CO_3. Thus, the structural effects of POMA incorporation differ between the two systems. In the NLTO/POMA composites, more pronounced bulk phase transformations occur at higher POMA contents, whereas the LLZO/POMA composites largely preserve the garnet structure of the cubic LLZO phase among the crystalline phases, despite the surface degradation associated with the reactivity of LLZO in aqueous media.

Despite these distinct chemical changes, both systems exhibited an increase in electrical conductivity with POMA incorporation. In the case of NLTO, previous studies have indicated that Na^+/H^+ exchange does not necessarily compromise the material's electrochemical properties. Considering the structural and electrical results together, the conductivity enhancement observed in the composites may be associated with a combination of improved interparticle contact, the contribution of the conductive polymer phase, the formation of percolation pathways, and interfacial polarization phenomena. Therefore, the observed increase in electrical conductivity should not be interpreted, by itself, as evidence of enhanced Li^+ mobility within LLZO or increased ionic mobility within the sodium titanate phases.

Table 21 summarizes the experimental conductivities and the corresponding values calculated using the GEM model described in Section 3.1.4. The model was applied to evaluate whether the observed evolution of electrical conductivity is consistent with a percolation mechanism. Overall, the model reproduces the evolution of the electrical conductivity in both composite systems.

Good agreement can be observed between the experimental conductivity values and those calculated using the GEM model. In addition, the $R^2_{\log}$ values, used to evaluate the overall quality of the model fit, were 0.993 and 0.962 for the NLTO/POMA and LLZO/POMA systems, respectively, indicating that the model adequately describes the evolution of conductivity in both systems. Therefore, the experimental behavior of the total conductivity is consistent with a percolation mechanism, suggesting that the progressive formation of conductive pathways associated with the polymeric phase plays a relevant role in the conductivity enhancement of the composites.

Table 21: Experimental and GEM-calculated electrical conductivities for the NLTO/POMA and LLZO/POMA systems.

NLTO/POMA			**LLZO/POMA**		
Sample	σ_{exp} (**S·cm^{-1}**)	σ_{GEM} (**S·cm^{-1}**)	**Sample**	σ_{exp} (**S·cm^{-1}**)	σ_{GEM} (**S·cm^{-1}**)
NLTO	4.04×10^{-9} (18)	4.04×10^{-9} (18)	LLZO	5.45×10^{-9} (39)	5.45×10^{-9} (39)
NLTO/POMA-10	9.57×10^{-9} (63)	8.45×10^{-9} (21)	LLZO/POMA-1	8.74×10^{-9} (13)	6.06×10^{-9} (36)
NLTO/POMA-15	2.53×10^{-8} (7)	1.24×10^{-8} (2)	LLZO/POMA-5	2.26×10^{-8} (4)	1.01×10^{-8} (19)
NLTO/POMA-35	5.15×10^{-8} (4)	7.67×10^{-8} (26)	LLZO/POMA-10	2.24×10^{-8} (20)	3.11×10^{-8} (62)
NLTO/POMA-50	9.75×10^{-7} (9)	9.17×10^{-7} (13)	LLZO/POMA-15	1.89×10^{-7} (11)	1.62×10^{-7} (19)
POMA	5.59×10^{-4} (16)	5.59×10^{-4} (16)	POMA	1.75×10^{-6} (9)	1.75×10^{-6} (9)
$\phi_c = 0.786 \pm 0.004$ $t = 1.99 \pm 0.07$ $R^2_{\log} = 0.993$			$\phi_c = 0.283 \pm 0.029$ $t \approx 1.0$ $R^2_{\log} = 0.962$		

Source: Prepared by the author.

Regarding the POMA conductivity values used in the GEM analysis, the values differ between the NLTO/POMA and LLZO/POMA systems. Although synthesized using the same procedure, the samples correspond to independent batches prepared at different times and to pellets processed under different conditions, resulting in different densities. Moreover, parameters such as the degree of protonation, which directly affects charge-carrier concentration and electrical conductivity, were not controlled. Therefore, these values represent the conductivity of the respective POMA samples used in each system rather than repeated measurements of the same sample.

Considering that electrical conduction in HCl-doped POMA occurs predominantly through electronic transport mediated by polarons, these results suggest an increasing contribution of electronic conduction as the POMA fraction increases. However, the GEM model and the impedance measurements employed in this work cannot, by themselves, quantitatively distinguish the ionic and electronic contributions to the total conductivity. Complementary techniques would therefore be required to determine these contributions and to establish an optimal composition that balances high ionic conductivity, low electronic conductivity, chemical stability, density, and mechanical integrity, while maintaining suitable interfacial properties at the electrodes. Thus, although the results obtained demonstrate the potential of these composites and reveal relevant trends in electrical transport, the set of techniques and characterizations employed in this work is not sufficient to definitively establish their applicability as electrolytes in electrochemical devices.

5 FINAL CONSIDERATIONS

5.1 Conclusions

The results demonstrate that POMA incorporation modifies the structural evolution and reduces the apparent electrical resistance of the NLTO/POMA and LLZO/POMA systems. In NLTO/POMA, high polymer contents are associated with a relative decrease in $Na_2Ti_3O_7$ and the formation of $H_2Ti_3O_7$ and NaCl, consistent with reactions involving protonated POMA. In LLZO/POMA, the cubic phase remains among the major crystalline phases, although the significant presence of Li_2CO_3, tetragonal LLZO, and LiOH indicates limitations related to phase purity and degradation during processing.

In addition to the structural and electrical analyses, spectroscopic and thermal characterizations provided complementary information on both systems. Spectroscopic analyses identified vibrational features associated with the ceramic phases and POMA in the composites. Thermal analysis, in turn, showed that both systems exhibit relative thermal stability above the typical operating conditions of solid-state batteries, with the most significant mass losses occurring only above 200 °C.

In addition, both the NLTO/POMA and LLZO/POMA systems exhibited an increase in total electrical conductivity of approximately two orders of magnitude, accompanied by a decrease in relaxation times with increasing POMA content. Together, these results indicate that POMA incorporation promotes a faster electrical response and modifies the charge-transport processes in both ceramic–polymer systems. The highest conductivity values were obtained for NLTO/POMA-50 and LLZO/POMA-15 within their respective compositional series. Moreover, the electrical behavior of both systems was consistent with the adopted percolation model, suggesting that the conduc-

tivity enhancement is associated with the progressive formation of conductive pathways as the polymer content increases.

In summary, the addition of POMA decreases the resistances associated with the high- and low-frequency processes. However, since HCl-doped POMA exhibits electronic conduction and the measurements performed in this work do not distinguish between charge carriers, the obtained values should be interpreted as total electrical conductivity. Therefore, the results establish relationships among composition, phase evolution, microstructure, and electrical response, but do not yet demonstrate that the composites behave as predominantly ionic electrolytes. Further validation requires transport-number measurements, electrochemical stability evaluation, temperature-dependent measurements, and cell testing.

5.2 Suggestions for Future Work

To further advance this research by addressing aspects beyond the scope of the present work and by improving the formulations developed, the following suggestions for future work are proposed:

a) Perform impedance spectroscopy measurements over a wide temperature range to enable the application of conduction models and the determination of activation energies. Such analyses may provide further insight into the charge-transport mechanisms and help distinguish the ionic and electronic contributions to the overall electrical conductivity of the ceramic–polymer composites.

b) Investigate the electrical response of the composites using ion-blocking electrodes in combination with DC polarization or transference-number measurements. These experiments would allow a quantitative estimation of the ionic and electronic conductivity components, providing a more comprehensive understanding of the transport properties of the investigated systems.

c) Prepare LLZO/POMA composites using a dry route under a controlled atmosphere to investigate the influence of POMA on the ceramic matrix under conditions that minimize LLZO reactivity.

d) Evaluate the potential application of NLTO/POMA and LLZO/POMA composites as solid-state electrolytes through electrochemical cycling tests in coin cells.

REFERENCES

AKAIKE, H. A new look at the statistical model identification. **IEEE transactions on automatic control**, Ieee, v. 19, n. 6, p. 716–723, 1974.

AKTAŞ, A.; KIRÇIÇEK, Y. Solar hybrid systems and energy storage systems. **Solar hybrid systems**, Elsevier Amsterdam, The Netherlands, p. 87–125, 2021.

ALI, S. *et al.* Crystal structure and photocatalytic properties of titanate nanotubes prepared by chemical processing and subsequent annealing. **Journal of Materials Science**, Springer, v. 51, p. 7322–7335, 2016.

ALJARRAH, M.; SALMAN, F. A simple analysis of impedance spectroscopy. **Journal of The Institution of Engineers (India): Series D**, Springer, v. 102, p. 237–242, 2021.

ALS-NIELSEN, J.; MCMORROW, D. **Elements of Modern X-ray Physics**. 2. ed. Chichester, UK: John Wiley & Sons, 2011. ISBN 978-0-470-97395-0.

ALTAYARAN, F. A. **The Effects of Doping on the Lithium Ionic Conductivity of LLZO Solid-State Electrolyte**. Dissertação (Mestrado) — North Dakota State University, 2020.

ALVES, W. F. *et al.* Thermo-analyses of polyaniline and its derivatives. **Thermochimica Acta**, Elsevier, v. 502, n. 1-2, p. 43–46, 2010.

AN, Y.; WANG, D.; WU, C. Ion-exchange between $Na_2Ti_3O_7$ and $H_2Ti_3O_7$ nanosheets at different ph levels: An experimental and first-principles study. **Physica E: Low-dimensional Systems and Nanostructures**, Elsevier, v. 60, p. 210–213, 2014.

AOTE, M.; DESHPANDE, A. Study of ge-doped garnet type $Li_7La_3Zr_2O_{12}$ as solid electrolyte for li-ion battery application. **Journal of Materials Science: Materials in Electronics**, Springer, v. 35, n. 8, p. 586, 2024.

AWAKA, J. *et al.* Synthesis and structure analysis of tetragonal $Li_7La_3Zr_2O_{12}$ with the garnet-related type structure. **Journal of solid state chemistry**, Elsevier, v. 182, n. 8, p. 2046–2052, 2009.

BADGER, R. M. A relation between internuclear distances and bond force constants. **The Journal of Chemical Physics**, American Institute of Physics, v. 2, n. 3, p. 128–131, 1934.

BARSOUKOV, E.; MACDONALD, J. R. **Impedance Spectroscopy: Theory, Experiment, and Applications**. 2nd. ed. Hoboken, NJ: John Wiley & Sons, Inc., 2005. ISBN 0471647497.

BAUERLE, J. Study of solid electrolyte polarization by a complex admittance method. **Journal of Physics and Chemistry of Solids**, Elsevier, v. 30, n. 12, p. 2657–2670, 1969.

BERNAL, C. *et al.* Influence of some experimental parameters on the results of differential scanning calorimetry-dsc. **Química Nova**, SciELO Brasil, v. 25, p. 849–855, 2002.

BEYGISANGCHIN, M. *et al.* Recent progress in polyaniline and its composites; synthesis, properties, and applications. **European Polymer Journal**, Elsevier, v. 210, p. 112948, 2024.

BIONDO, M. M. *et al.* Chemically synthesized poly (o-methoxyaniline): Influence of counterions on the structural and electrical properties. **Journal of Molecular Structure**, Elsevier, v. 1205, p. 127588, 2020.

BOUKAMP, B. A. A linear kronig-kramers transform test for immittance data validation. **Journal of the electrochemical society**, The Electrochemical Society, Inc., v. 142, n. 6, p. 1885–1894, 1995.

BUNACIU, A. A.; UDRIŞTIOIU, E. G.; ABOUL-ENEIN, H. Y. X-ray diffraction: instrumentation and applications. **Critical reviews in analytical chemistry**, Taylor & Francis, v. 45, n. 4, p. 289–299, 2015.

BURNHAM, K. P.; ANDERSON, D. R. **Model Selection and Multimodel Inference: A Practical Information-Theoretic Approach**. 2nd. ed. New York: Springer-Verlag, 2002.

CALLISTER JR., W. D.; RETHWISCH, D. G. **Materials Science and Engineering: An Introduction**. 9. ed. [S.l.]: John Wiley & Sons, 2014.

CAMPÉON, B. D. *et al.* Mechanistic study on moisture exposure of ti-based layered oxides for sodium storage applications. **Journal of Materials Chemistry A**, The Royal Society of Chemistry, v. 13, n. 3, p. 2187–2197, 2025.

CHANG, S. *et al.* Reviews on the us patents regarding nickel/metal hydride batteries. **Batteries**, MDPI, v. 2, n. 2, p. 10, 2016.

CHANG, Y.-C.; LIN, J.-C.; CHOU, C.-M. $H_2Ti_3O_7$ nanowires as a high-performance photocatalytic and surface-enhanced raman scattering substrate. **Journal of Photochemistry and Photobiology A: Chemistry**, Elsevier, v. 400, p. 112666, 2020.

CHEN, F. *et al.* The chance of sodium titanate anode for the practical sodium-ion batteries. **Chinese Journal of Chemical Engineering**, Elsevier, v. 72, p. 226–244, 2024.

CHOI, Y.-S. *et al.* Intrinsic defects and their role in the phase transition of na-ion anode $Na_2Ti_3O_7$. **ACS Applied Energy Materials**, ACS Publications, v. 6, n. 1, p. 484–495, 2022.

CHU, J. *et al.* Optimization strategies for key interfaces of llzo-based solid-state lithium metal batteries. **Materials Chemistry Frontiers**, Royal Society of Chemistry, v. 8, n. 9, p. 2109–2134, 2024.

CIOSLOWSKI, J.; LIU, G.; CASTRO, R. A. M. Badger's rule revisited. **Chemical Physics Letters**, Elsevier, v. 331, n. 5-6, p. 497–501, 2000.

COSTA, S. D. S. *et al.* Temperature dependence of the electrical properties of $Na_2Ti_3O_7$/$Na_2Ti_6O_{13}$/poma composites. **Molecules**, MDPI, v. 27, n. 18, p. 5756, 2022.

COUNIHAN, M. J. *et al.* Improved interfacial li-ion transport in composite polymer electrolytes via surface modification of llzo. **Energy Materials**, Open Access with Excellence, v. 5, n. 3, 2025.

DELGADO, A. *et al.* An elementary picture of dielectric spectroscopy in solids: Physical basis. **Journal of chemical education**, ACS Publications, v. 80, n. 9, p. 1062, 2003.

DINNEBIER, R. E.; LEINEWEBER, A.; EVANS, J. S. O. **Rietveld Refinement: Practical Powder Diffraction Pattern Analysis Using TOPAS**. Berlin/Boston: Walter de Gruyter, 2019. ISBN 978-3-11-045621-9.

DONG, J. *et al.* Review and prospects on the low-voltage $Na_2Ti_3O_7$ anode materials for sodium-ion batteries. **Journal of Energy Chemistry**, Elsevier, v. 88, p. 446–460, 2024.

DONG, S. *et al.* Titanates for sodium-ion storage. **Nano Today**, Elsevier, v. 42, p. 101349, 2022.

EGERTON, R. F. *et al.* **Physical principles of electron microscopy**. [S.l.]: Springer, 2005. v. 56.

EGGESTAD, K.; SELBACH, S. M.; WILLIAMSON, B. A. Doping implications of li solid state electrolyte $Li_7La_3Zr_2O_{12}$. **Journal of Materials Chemistry A**, Royal Society of Chemistry, v. 12, n. 26, p. 15666–15675, 2024.

EL-SHINAWI, H. *et al.* Stabilization of the cubic, fast-ion conducting phase of li 7 la 3 sn 2 o 12 garnet by gallium doping. **RSC advances**, Royal Society of Chemistry, v. 14, n. 11, p. 7557–7563, 2024.

ELGEGREN, M. *et al.* Ultrasound-assisted encapsulation of sacha inchi (plukenetia volubilis linneo.) oil in alginate-chitosan nanoparticles. **Polymers**, MDPI, v. 11, n. 8, p. 1245, 2019.

FERRER-ROCA, C. *et al.* Fourier transform infrared investigation of dielectric and lattice dynamical properties of cualo 2 delafossite under high pressure. **Physical Review B**, APS, v. 110, n. 10, p. 104312, 2024.

FROTA, H. Contact dynamics in ball mills with ellipsoidal, spherical and cylindrical shapes. **Powder Technology**, Elsevier, p. 122573, 2026.

GALIANI, P. D. *et al.* Compósitos de borracha natural com polianilina. **Polímeros**, SciELO Brasil, v. 17, p. 93–97, 2007.

GAŁKA, P.; KOWALONEK, J.; KACZMAREK, H. Thermogravimetric analysis of thermal stability of poly (methyl methacrylate) films modified with photoinitiators. **Journal of Thermal Analysis and Calorimetry**, Springer, v. 115, p. 1387–1394, 2014.

GEIGER, C. A. *et al.* Crystal chemistry and stability of "$Li_7La_3Zr_2O_{12}$" garnet: a fast lithium-ion conductor. **Inorganic chemistry**, ACS Publications, v. 50, n. 3, p. 1089–1097, 2011.

GHARBI, I. *et al.* Comprehensive study of the structural, microstructural, and electrical properties of $RbZnPO_4$: insights into conduction mechanisms and the olpt models. **Materials Advances**, Royal Society of Chemistry, v. 6, n. 18, p. 6358–6369, 2025.

GHORBANZADE, P. *et al.* Influence of the llzo–peo interface on the micro-and macro-scale properties of composite polymer electrolytes for solid-state batteries. **Materials Today Energy**, Elsevier, v. 38, p. 101448, 2023.

GHORBANZADE, P.; LÓPEZ-ARANGUREN, P.; AMO, J. M. López del. A vision for llzo carbonate formation: Perspectives on surface treatment approaches and characterization techniques. **ChemElectroChem**, Wiley Online Library, v. 11, n. 11, p. e202400136, 2024.

GOLDSBERRY, R. *et al.* Effect of temperature on passive film characteristics of lpbf (laser powder-bed fusion) processing on uns-s31603. **Materials**, MDPI, v. 17, n. 14, p. 3420, 2024.

GOLDSTEIN, J. I. *et al.* **Scanning Electron Microscopy and X-Ray Microanalysis**. 4th. ed. New York: Springer, 2018. ISBN 978-1-4939-6674-5.

GONG, Y.; CHEN, X.; WU, W. Application of fourier transform infrared (ftir) spectroscopy in sample preparation: Material characterization and mechanism investigation. **Advances in Sample Preparation**, Elsevier, v. 11, p. 100122, 2024.

GREGORY, N. Elements of x-ray diffraction. **Journal of the American Chemical Society**, ACS Publications, v. 79, n. 7, p. 1773–1774, 1957.

GRIFFITHS, P. R. Fourier transform infrared spectrometry. **Science**, American Association for the Advancement of Science, v. 222, n. 4621, p. 297–302, 1983.

HAKIKI, F.; LIN, W.-T.; LIN, C.-P. Broadband complex dielectric permittivity: Combined impedance spectroscopy and time domain reflectometry. **Measurement**, Elsevier, v. 235, p. 114993, 2024.

HAN, J.-Y. *et al.* Electrospun 1d al-llzo incorporated pvdf-hfp composite electrolyte with fast Li^+ pathway derived from highway-traction effect for high performance lithium metal batteries. **Chemical Engineering Journal**, Elsevier, v. 505, p. 159627, 2025.

HAN, S. *et al.* Recent advances in solving Li_2CO_3 problems in garnet-based solid-state battery: A systematic review (2020–2023). **Journal of Energy Chemistry**, Elsevier, v. 90, p. 58–76, 2024.

HIROSE, E. *et al.* Structural stability of the li-ion conductor $Li_7La_3Zr_2O_{12}$ investigated by high-pressure in-situ x-ray diffraction and raman spectroscopy. **Materials Research Bulletin**, Elsevier, v. 107, p. 361–365, 2018.

HOTA, S. S. *et al.* Dielectric characteristics and energy storage capabilities of pvdf-based composite incorporating 2d gnp nanofiller. **Results in Engineering**, Elsevier, v. 26, p. 105593, 2025.

HUANG, Y. The discovery of cathode materials for lithium-ion batteries from the view of interdisciplinarity. **Interdisciplinary Materials**, Wiley Online Library, v. 1, n. 3, p. 323–329, 2022.

HWANG, B.-J.; ABRHA, L. H. Cubic garnet solid electrolyte with superior air stability. In: THE ELECTROCHEMICAL SOCIETY, INC. **Electrochemical Society Meeting Abstracts prime2020**. [S.l.], 2020. p. 494–494.

IBRAHIM, S. *et al.* Ac conductivity, dielectric and thermal properties of hybrid composite: bagasse cellulose carbon nanofibers composite. **Indian Journal of Physics**, Springer, v. 99, n. 2, p. 535–550, 2025.

JANEK, J.; ZEIER, W. G. Challenges in speeding up solid-state battery development. **Nature Energy**, Nature Publishing Group, v. 8, n. 3, p. 230–240, 2023.

JONSCHER, A. K. Dielectric relaxation in solids. **Journal of Physics D: Applied Physics**, v. 32, n. 14, p. R57–R70, 1999.

JUNG, S.-K. *et al.* Unlocking the hidden chemical space in cubic-phase garnet solid electrolyte for efficient quasi-all-solid-state lithium batteries. **Nature Communications**, Nature Publishing Group UK London, v. 13, n. 1, p. 7638, 2022.

KALITA, G.; ENDO, T.; NISHI, T. Recent development on low temperature synthesis of cubic-phase llzo electrolyte particles for application in all-solid-state batteries. **Journal of Alloys and Compounds**, Elsevier, v. 969, p. 172282, 2023.

KIM, J. W. *et al.* Enhanced li-ion conductivity of $Li_7La_3Zr_2O_{12}$ by simultaneous substitution of aluminum and niobium using a modified sol–gel method. **Battery Energy**, Wiley Online Library, v. 2, n. 2, p. 20220024, 2023.

KOZDRA, M. *et al.* The sensitive aspects of modelling polymer–ceramic composite solid-state electrolytes using molecular dynamics simulations. **Physical Chemistry Chemical Physics**, Royal Society of Chemistry, v. 26, n. 7, p. 6216–6227, 2024.

KURITA, E.; MATSUURA, H.; OHNO, K. Relationship between force constants and bond lengths for cx (x= c, si, ge, n, p, as, o, s, se, f, cl and br) single and multiple bonds: Formulation of badger's rule for universal use. **Spectrochimica Acta Part A: Molecular and Biomolecular Spectroscopy**, Elsevier, v. 60, n. 13, p. 3013–3023, 2004.

KURZWEIL, P. Gaston planté and his invention of the lead–acid battery—the genesis of the first practical rechargeable battery. **Journal of Power Sources**, Elsevier, v. 195, n. 14, p. 4424–4434, 2010.

LARRAZ, G.; ORERA, A.; SANJUÁN, M. Cubic phases of garnet-type $Li_7La_3Zr_2O_{12}$: the role of hydration. **Journal of Materials Chemistry A**, Royal Society of Chemistry, v. 1, n. 37, p. 11419–11428, 2013.

LARSEN, A. H. *et al.* The atomic simulation environment—a python library for working with atoms. **Journal of Physics: Condensed Matter**, IOP Publishing, v. 29, n. 27, p. 273002, 2017.

LECHARTIER, M. *et al.* Single-ion polymer/llzo hybrid electrolytes with high lithium conductivity. **Materials Advances**, Royal Society of Chemistry, v. 3, n. 2, p. 1139–1151, 2022.

LEI, M. *et al.* Polymer electrolytes reinforced by 2d fluorinated filler for all-solid-state li-fe-f conversion-type lithium metal batteries. **Nano Research**, Springer, v. 16, n. 6, p. 8469–8477, 2023.

LEYET, Y. *et al.* Synthesis of $Na_2Ti_3O_7$ nanoparticles by sonochemical method for solid state electrolyte applications. **Journal of Solid State Electrochemistry**, Springer, v. 22, p. 1315–1319, 2018.

LI, C. *et al.* An advance review of solid-state battery: Challenges, progress and prospects. **Sustainable Materials and Technologies**, Elsevier, v. 29, p. e00297, 2021.

LI, F. *et al.* Intergrowth of layered $Na_2Ti_3O_7$ and tunnel na2ti7o15 forming a high-performance anode for sodium-ion batteries. **Journal of Energy Chemistry**, Elsevier, v. 118, p. 211–222, 2026.

LIBICH, J. *et al.* Sodium-ion batteries: Electrochemical properties of sodium titanate as negative electrode. **Journal of Energy Storage**, Elsevier, v. 27, p. 101150, 2020.

LIMA, C. D. de A. *et al.* Synthesis, characterization, and thermal stability study of sodium and sodium–aluminum titanate nanotubes. **Solid State Sciences**, Elsevier, v. 138, p. 107134, 2023.

LINDEN, D. Handbook of batteries. In: **Fuel and energy abstracts**. [S.l.: s.n.], 1995. v. 4, n. 36, p. 265.

LIU, T. *et al.* Structure, properties, preparation, and application of layered titanates. **Inorganic Chemistry**, ACS Publications, v. 63, n. 1, p. 1–26, 2023.

LIU, Z. *et al.* Low-cost iron trichloride cathode for all-solid-state lithium-ion batteries. **Nature Sustainability**, Nature Publishing Group UK London, p. 1–9, 2024.

LUO, Y. *et al.* Safety concerns in solid-state lithium batteries: from materials to devices. **Energy & Environmental Science**, Royal Society of Chemistry, v. 17, n. 20, p. 7543–7565, 2024.

MACDONALD, J. R. *et al.* **Impedance spectroscopy: theory, experiment, and applications**. [S.l.]: John Wiley & Sons, 2018.

MADRID, J. C. M. *et al.* Impact of TiO_2 at the grain boundaries in lithium lanthanum titanate solid electrolytes. **ACS Applied Energy Materials**, ACS Publications, v. 7, n. 19, p. 8342–8355, 2024.

MATSUI, M. *et al.* Phase stability of a garnet-type lithium ion conductor $Li_7La_3Zr_2O_{12}$. **Dalton Transactions**, Royal Society of Chemistry, v. 43, n. 3, p. 1019–1024, 2014.

MATYSZCZAK, G. *et al.* Sonochemical synthesis of low-dimensional nanostructures and their applications—a review. **Materials**, MDPI, v. 17, n. 22, p. 5488, 2024.

MCLACHLAN, D. S.; BLASZKIEWICZ, M.; NEWNHAM, R. E. Electrical resistivity of composites. **Journal of the American Ceramic Society**, Wiley Online Library, v. 73, n. 8, p. 2187–2203, 1990.

MEENA, R.; DHAKA, R. S. Structural properties, dielectric relaxation, and impedance spectroscopy of nasicon type $Na_{3+x}Zr_{2-x}Pr_xSi_2PO_{12}$ ceramics. **Journal of the American Ceramic Society**, Wiley Online Library, v. 107, n. 12, p. 8378–8395, 2024.

MELO, A. *et al.* Synthesis microwave-assisted: fast method to obtain lithium-doped sodium titanate. **Journal of Materials Science: Materials in Electronics**, Springer, v. 34, n. 6, p. 537, 2023.

MIARA, L. J. *et al.* Effect of rb and ta doping on the ionic conductivity and stability of the garnet $li_7(la_{3-x}rb_x)(zr_{2-y}ta_y)o_{12}$ ($0 \leq x \leq 0.375, 0 \leq y \leq 1$) superionic conductor: A first principles investigation. **Chemistry of Materials**, ACS Publications, v. 25, n. 15, p. 3048–3055, 2013.

MILERIO, J. V. G. *et al.* Tuning ionic conductivity and thermal stability in poma-enriched llzo composites for next-generation lithium-ion batteries. **The Journal of Physical Chemistry C**, ACS Publications, v. 129, n. 19, p. 9127–9139, 2025.

MOHAMMADI, S. *et al.* Surface modification and chemical stability of garnet llzo solid electrolyte by zno coating through a facile and practical method. **Materials Chemistry and Physics**, Elsevier, v. 308, p. 128235, 2023.

MOMMA, K.; IZUMI, F. Vesta 3 for three-dimensional visualization of crystal, volumetric and morphology data. **Applied Crystallography**, International Union of Crystallography, v. 44, n. 6, p. 1272–1276, 2011.

MUKHERJEE, R. *et al.* Structural and electrical transport properties of a rare earth double perovskite oxide: Ba_2ErNbO_6. **Journal of Rare Earths**, Elsevier, v. 32, n. 4, p. 334–342, 2014.

MURUGAN, R. *et al.* Fast lithium ion conduction in garnet-type $Li_7La_3Zr_2O_{12}$. **ANGEWANDTE CHEMIE-INTERNATIONAL EDITION IN ENGLISH-**, John Wiley & Sons, Ltd, v. 46, n. 41, p. 7778, 2007.

NAHIR, T. M. **Impedance Spectroscopy: Theory, Experiment, and Applications (Book Review)**. [S.l.: s.n.], 2005. Review of the book edited by E. Barsoukov and J. R. Macdonald. ISBN 0471647497.

NEWNHAM, R.; SKINNER, D.; CROSS, L. Connectivity and piezoelectric-pyroelectric composites. **Materials research bulletin**, Elsevier, v. 13, n. 5, p. 525–536, 1978.

NOBRE, M. A. d. L.; LANFREDI, S. Electrical characterization by impedance spectroscopy of zn7sb2o12 ceramic. **Materials Research**, SciELO Brasil, v. 6, n. 2, p. 151–156, 2003.

NYCZYK, A. *et al.* Nanocomposites of polyaniline, its derivatives and platinum prepared using aqueous pt sol. **Synthetic metals**, Elsevier, v. 159, n. 7-8, p. 561–567, 2009.

ORAZEM, M. E.; TRIBOLLET, B. **Electrochemical Impedance Spectroscopy**. Hoboken, NJ: John Wiley & Sons, 2008. (The Electrochemical Society Series). ISBN 978-0-470-04140-6.

ORSETTI, N. G. *et al.* The transcendental role of lithium zirconates in the development of modern energy technologies. **Ceramics International**, Elsevier, v. 48, n. 7, p. 8930–8959, 2022.

ORTIZ, Y. *et al.* Recent advances in thermal management strategies for lithium-ion batteries: A comprehensive review. **Batteries**, MDPI, v. 10, n. 3, p. 83, 2024.

OVSHINSKY, S. R.; FETCENKO, M. A.; ROSS, J. A nickel metal hydride battery for electric vehicles. **Science**, American Association for the Advancement of Science, v. 260, n. 5105, p. 176–181, 1993.

PAK, Y.-C. *et al.* Defect formation and ambivalent effects on electrochemical performance in layered sodium titanate $Na_2Ti_3O_7$. **Physical Chemistry Chemical Physics**, Royal Society of Chemistry, v. 25, n. 4, p. 3420–3431, 2023.

PALETI, S. H. K. *et al.* Impact of doping on the mechanical properties of conjugated polymers. **Chemical Society Reviews**, Royal Society of Chemistry, v. 53, n. 4, p. 1702–1729, 2024.

PEREZ, F. A. N. Analytical–computational integration of equivalent circuit modeling, hybrid optimization, and statistical validation for electrochemical impedance spectroscopy. **Electrochem**, MDPI, v. 6, n. 4, p. 35, 2025.

PUENTE, P. G. *et al.* Garnet-type solid electrolyte: Advances of ionic transport performance and its application in all-solid-state batteries. **Journal of Advanced Ceramics**, Springer, p. 1–40, 2021.

QU, J. *et al.* Preparation and electrochemical characteristics of the co-doped $Li_7La_3Zr_2O_{12}$ solid electrolyte with $Fe_3{}^+$ and $Bi_3{}^+$. **Molecules**, MDPI, v. 30, n. 9, p. 2028, 2025.

RAJU, M. M. *et al.* Crystal structure and preparation of $Li_7La_3Zr_2O_{12}$ (llzo) solid-state electrolyte and doping impacts on the conductivity: An overview. **Electrochem**, MDPI, v. 2, n. 3, p. 390–414, 2021.

RANGASAMY, E. *et al.* The effect of 24c-site (a) cation substitution on the tetragonal–cubic phase transition in $Li_{7-x}La_{3-x}A_xZr_2O_{12}$ garnet-based ceramic electrolyte. **Journal of Power Sources**, Elsevier, v. 230, p. 261–266, 2013.

RIETVELD, H. M. A profile refinement method for nuclear and magnetic structures. **Applied Crystallography**, International Union of Crystallography, v. 2, n. 2, p. 65–71, 1969.

SACCOCCIO, M. *et al.* Low-temperature pulsed laser deposition of garnet $Li_{6.4}La_3Zr_{1.4}Ta_{0.6}O_{12}$ films as all-solid-state lithium battery electrolytes. **Journal of Power Sources**, v. 365, p. 43–52, 2017.

SAHAL, M. *et al.* Surface reduction of Li_2CO_3 on llzto solid-state electrolyte via scalable open-air plasma treatment. **Batteries**, MDPI, v. 10, n. 7, p. 249, 2024.

SAMSON, A. J. *et al.* A bird's-eye view of li-stuffed garnet-type $Li_7La_3Zr_2O_{12}$ ceramic electrolytes for advanced all-solid-state li batteries. **Energy & Environmental Science**, Royal Society of Chemistry, v. 12, n. 10, p. 2957–2975, 2019.

SANCHES, E. *et al.* Structural characterization of emeraldine-salt polyaniline/gold nanoparticles complexes. **Journal of Nanomaterials**, Wiley Online Library, v. 2011, n. 1, p. 697071, 2011.

SANCHES, E. A. *et al.* Characterization of poly (o-methoxyaniline) emeraldine-base form obtained at different time neutralization. **Journal of Molecular Structure**, Elsevier, v. 1063, p. 336–340, 2014.

SANCHES, E. A. *et al.* Nanostructured polyaniline emeraldine-base form (eb-pani): a structural investigation for different neutralization times. **Journal of Molecular Structure**, Elsevier, v. 1074, p. 732–737, 2014.

SAZVAR, A. *et al.* Review of advances and challenges in Li7La3Zr2O12 solid electrolytes: From processing to performance. **Journal of Power Sources**, Elsevier B.V., v. 657, p. 238150, 2025.

SCHALENBACH, M. *et al.* Double layer capacitances analysed with impedance spectroscopy and cyclic voltammetry: Validity and limits of the constant phase element parameterization. **Physical Chemistry Chemical Physics**, Royal Society of Chemistry, v. 23, n. 37, p. 21097–21105, 2021.

SEO, J.-H. *et al.* Broad temperature dependence, high conductivity, and structure-property relations of cold sintering of llzo-based composite electrolytes. **Journal of the European Ceramic Society**, Elsevier, v. 40, n. 15, p. 6241–6248, 2020.

SHIH, D. P.; AGUADERO, A.; SKINNER, S. J. Improvement of ionic conductivity in a-site lithium doped sodium bismuth titanate. **Solid State Ionics**, Elsevier, v. 317, p. 32–38, 2018.

SHIRPOUR, M.; CABANA, J.; DOEFF, M. New materials based on a layered sodium titanate for dual electrochemical na and li intercalation systems. **Energy & Environmental Science**, Royal Society of Chemistry, v. 6, n. 8, p. 2538–2547, 2013.

SILVA, F. L. R. *et al.* Polarized raman, ftir, and dft study of $Na_2Ti_3O_7$ microcrystals. **Journal of Raman Spectroscopy**, Wiley Online Library, v. 49, n. 3, p. 538–548, 2018.

SILVA, G. M. da *et al.* A review of impedance spectroscopy technique: Applications, modelling, and case study of relative humidity sensors development. **Applied Sciences**, MDPI, v. 14, n. 13, p. 5754, 2024.

SILVA, J. B. da *et al.* Synergistic effects of lithium doping and organic phases on the electrical and dielectric properties of sodium titanate solid-state electrolytes. **Solid State Sciences**, Elsevier, p. 108036, 2025.

SILVA, J. B. da *et al.* Tuning electrical conductivity in lithium-doped sodium titanate via sonochemical synthesis. **Materials Science and Engineering: B**, Elsevier, v. 323, p. 118836, 2026.

SILVA, J. D. *et al.* Structure and electrical properties of the composite $Na_2Ti_3O_7$/$Na_2Ti_6O_{13}$/poma: A study of the effect of adding poma. **Journal of Alloys and Compounds**, Elsevier, v. 867, p. 159025, 2021.

SILVA, J. da *et al.* Poly (o-methoxyaniline) modified by the biphasic ceramic system $Na_2Ti_3O_7$/$Na_2Ti_6O_{13}$. **Journal of Inorganic and Organometallic Polymers and Materials**, Springer, v. 33, n. 5, p. 1381–1387, 2023.

SILVA, J. M. S. da *et al.* Poly (o-methoxyaniline) chain degradation based on a heat treatment (ht) process: Combined experimental and theoretical evaluation. **Molecules**, MDPI, v. 27, n. 12, p. 3693, 2022.

SILVERSTEIN, R. M.; BASSLER, G. C. Spectrometric identification of organic compounds. **Journal of Chemical Education**, ACS Publications, v. 39, n. 11, p. 546, 1962.

SIVIA, D. S. The basics of x-ray and neutron scattering. In: **Elementary Scattering Theory: For X-ray and Neutron Users**. [S.l.]: Oxford University Press, 2011.

SMITH, B. The CO bond iii: Ethers by a knockout. **Spectroscopy**, MJH Life Sciences, v. 32, n. 5, p. 22–26, 2017.

STEJSKAL, J.; GILBERT, R. Polyaniline. preparation of a conducting polymer (iupac technical report). **Pure and applied chemistry**, De Gruyter, v. 74, n. 5, p. 857–867, 2002.

SUN, H.; KANG, S.; CUI, L. Prospects of llzo type solid electrolyte: from material design to battery application. **Chemical Engineering Journal**, Elsevier, v. 454, p. 140375, 2023.

TRAN, H. K. *et al.* Sandwich-structured composite polymer electrolyte based on pvdf-hfp/ppc/al-doped llzo for high-voltage solid-state lithium batteries. **ACS Applied Energy Materials**, ACS Publications, v. 6, n. 3, p. 1475–1487, 2023.

TRINH, Q. T. *et al.* Sonochemistry and sonocatalysis: current progress, existing limitations, and future opportunities in green and sustainable chemistry. **Green Chemistry**, Royal Society of Chemistry, v. 27, p. 4926–4958, 2025.

TSIAMTSOURI, M. A. *et al.* Exfoliation of layered na-ion anode material $Na_2Ti_3O_7$ for enhanced capacity and cyclability. **Chemistry of Materials**, ACS Publications, v. 30, n. 5, p. 1505–1516, 2018.

VADIVAZHAGAN, M.; JAYAN, R.; NALLATHAMBY, K. Exploration of naliti3o7 decorated with biocarbon as anode material for lithium and sodium ion batteries. **Energy & Fuels**, ACS Publications, v. 36, n. 2, p. 1081–1090, 2022.

VIANA, B. C. *et al.* Alkali metal intercalated titanate nanotubes: a vibrational spectroscopy study. **Vibrational Spectroscopy**, Elsevier, v. 55, n. 2, p. 183–187, 2011.

WANG, C. *et al.* Combined frozen crystallization and stepwise decompression evaporation for Na_2SO_4/NaCl separation from mixed salts. **Recycling**, MDPI, v. 10, n. 3, p. 106, 2025.

WHITTINGHAM, M. S. Electrical energy storage and intercalation chemistry. **Science**, American Association for the Advancement of Science, v. 192, n. 4244, p. 1126–1127, 1976.

WOOD, M. *et al.* Exploring the relationship between solvent-assisted ball milling, particle size, and sintering temperature in garnet-type solid electrolytes. **Journal of Power Sources**, Elsevier, v. 484, p. 229252, 2021.

WU, M. *et al.* 3d coral-like llzo/pvdf composite electrolytes with enhanced ionic conductivity and mechanical flexibility for solid-state lithium batteries. **ACS Applied Materials & Interfaces**, ACS Publications, v. 12, n. 47, p. 52652–52659, 2020.

WUNDERLICH, B. **Thermal analysis of polymeric materials**. [S.l.]: Springer Science & Business Media, 2005.

XIAO, Y. *et al.* Electrochemical impedance spectroscopy-based characterization and modeling of lithium-ion batteries based on frequency selection. **Batteries**, MDPI, v. 11, n. 1, p. 11, 2024.

XU, Z. *et al.* Co-doping strategy enhanced the ionic conductivity and excellent lithium stability of garnet-type $Li_7La_3Zr_2O_{12}$ electrolyte in all solid-state lithium batteries. **Journal of Materiomics**, Elsevier, v. 9, n. 4, p. 651–660, 2023.

YAHYA, I. N. D. *et al.* Characteristics of sodium lithium titanate synthesized at different solid-state reaction temperature for lithium-ion battery anode. **Journal of Materials Exploration and Findings**, v. 2, n. 3, p. 3, 2023.

YANG, G. *et al.* An in situ-formed high lithiophilic solid lubricant interface layer for garnet-based solid-state lithium metal batteries. **Electrochimica Acta**, Elsevier, v. 407, p. 139767, 2022.

YANG, P. *et al.* Ni_2^+-doped $Na_2Ti_6O_{13}$ nanotubes to enhance the electrochemical performance of sodium ion batteries. **Journal of Electroanalytical Chemistry**, Elsevier, v. 954, p. 118051, 2024.

YI, X. *et al.* Duality of Li_2CO_3 in solid-state batteries. **Transactions of Tianjin University**, Springer, v. 29, n. 1, p. 73–87, 2023.

YOSHINO, A. The birth of the lithium-ion battery. **Angewandte Chemie International Edition**, Wiley Online Library, v. 51, n. 24, p. 5798–5800, 2012.

YOUNG, K.-h.; YASUOKA, S. Capacity degradation mechanisms in nickel/metal hydride batteries. **Batteries**, MDPI, v. 2, n. 1, p. 3, 2016.

YOUNG, R. A. **The rietveld method**. [S.l.]: International union of crystallography, 1993. v. 5.

YOUSSRY, M.; MUSSA, A. Controllable synthesis of sodium titanates using facile ball milling method. **Ceramics International**, Elsevier, v. 47, n. 10, p. 14021–14032, 2021.

ZÁRATE, R. *et al.* Chemical composition and phase identification of sodium titanate nanostructures grown from titania by hydrothermal processing. **Journal of Physics and Chemistry of Solids**, Elsevier, v. 68, n. 4, p. 628–637, 2007.

ZARE, Y.; RHEE, K. Y. Simplification and development of mclachlan model for electrical conductivity of polymer carbon nanotubes nanocomposites assuming the networking of interphase regions. **Composites Part B: Engineering**, Elsevier, v. 156, p. 64–71, 2019.

ZARRABEITIA, M. *et al.* Towards environmentally friendly na-ion batteries: Moisture and water stability of na2ti3o7. **Journal of Power Sources**, Elsevier, v. 324, p. 378–387, 2016.

ZHANG, D.; YING, D. Solid state reactions in nanometer scaled diffusion couples prepared using high energy ball milling. **Materials Science and Engineering: A**, Elsevier, v. 301, n. 1, p. 90–96, 2001.

ZHANG, L.; PU, Y.; CHEN, M. Complex impedance spectroscopy for capacitive energy-storage ceramics: a review and prospects. **Materials Today Chemistry**, Elsevier, v. 28, p. 101353, 2023.

ZHANG, N. *et al.* Dynamical evolution of CO_2 and H_2O on garnet electrolyte elucidated by ambient pressure x-ray spectroscopies. **Nature Communications**, Nature Publishing Group UK London, v. 15, n. 1, p. 2777, 2024.

ZHANG, Y. *et al.* Field assisted sintering of dense al-substituted cubic phase $Li_7La_3Zr_2O_{12}$ solid electrolytes. **Journal of Power Sources**, Elsevier, v. 268, p. 960–964, 2014.

ZHAO, L. *et al.* A comparative study of equivalent circuit models for electro-chemical impedance spectroscopy analysis of proton exchange membrane fuel cells. **Energies**, MDPI, v. 15, n. 1, p. 386, 2022.

ZHAO, L. *et al.* Constructing low-impedance $Li_7La_3Zr_2O_{12}$-based composite cathode interface for all-solid-state lithium batteries. **Small Structures**, Wiley Online Library, v. 3, n. 12, p. 2200200, 2022.

ZHAO, X. *et al.* Addressing the interface issues of all-solid-state lithium batteries by ultra-thin composite solid-state electrolyte combined with the integrated preparation technology. **InfoMat**, Wiley Online Library, p. e70012, 2025.

ZHELTIKOV, A. **Impedance Spectroscopy: Theory, Experiment, and Applications Second Edition. Evgenij Barsoukov and J. Ross Macdonald (eds). John Wiley & Sons, Inc., Hoboken, New Jersey, 2005, pp. 595**. [S.l.]: Wiley Online Library, 2007.

ŽIC, M. *et al.* Solving cnls problems using levenberg-marquardt algorithm: A new fitting strategy combining limits and a symbolic jacobian matrix. **Journal of Electroanalytical Chemistry**, Elsevier, v. 866, p. 114171, 2020.

ANNEX A – PUBLISHED ARTICLE — NLTO COMPOSITION SELECTION

This annex presents the published article containing the investigation from which the NLTO composition used in the NLTO/POMA composites was selected.

Materials Science and Engineering B 323 (2026) 118836

Contents lists available at ScienceDirect

Materials Science & Engineering B

journal homepage: www.elsevier.com/locate/mseb

Tuning electrical conductivity in lithium-doped sodium titanate via sonochemical synthesis

Jardson Braz da Silva [a,b], Juliana Pereira da Silva [b], Rodrigo Lavareda dos Santos [b], Salomão dos Santos Costa [a,b], Francisco Xavier Nobre [c], Monica Tirado [d], Angsula Ghosh [a], Lianet Aguilera Domínguez [b], Yurimiler Leyet Ruiz [b,*]

[a] Departamento de Física de Materiais, Instituto de Ciências Exatas, Universidade Federal do Amazonas (UFAM), Manaus, AM, Brazil
[b] Laboratório de Processamento de Materiais Tecnológicos, Departamento de Engenharia de Materiais, Universidade Federal do Amazonas (UFAM), Manaus, AM, Brazil
[c] Instituto Federal de Educação, Ciência e Tecnologia do Amazonas, Manaus, AM 69020-120, Brazil
[d] Universidad Nacional de Tucumán (UNT), Facultad de Ciencias Exactas y Tecnología (FACET) and Instituto de Física del Noroeste Argentino: INFINOA (UNT-CONICET), Avenida Independencia, 1800 4000, Tucumán, Argentina

ARTICLE INFO

Keywords:
Lithium-doped sodium Titanate
Sonochemical synthesis
Electrical properties

ABSTRACT

Recent advancements in energy storage technologies and the development of efficient materials for next-generation batteries and catalysts have drawn much attention. To mitigate the intrinsically low ionic conductivity of sodium titanates ($Na_2Ti_nO_{2n+1}$), which arises from the lower diffusivity of Na^+ ions, we present a detailed study of the structural and electrical properties of lithium- doped sodium titanate ($Na_{2-x}Li_xTi_3O_7$) samples synthesized using sonochemistry for the first time. The samples were characterized using various models and experimental techniques, including X-ray diffraction with Rietveld refinement, Scanning Electron Microscopy, Fourier Transform Infrared Spectroscopy, Ultraviolet-Visible Spectroscopy, and Complex Impedance Spectroscopy. In all samples, the $Na_2Ti_3O_7$ phase was identified as the primary phase, with $Na_2Ti_6O_{13}$ as a secondary phase. However, in the samples with 2 % and 3 % lithium-ion addition, a third phase, $NaLiTi_3O_7$, was also observed within the crystalline structure. DFT calculations also supported the study to understand the effect of Li substitution on the samples. Scanning electron microscopy reveals elongated particles and shows increased agglomeration upon lithium addition. In infrared spectroscopy, bands below 1000 cm^{-1} predominate, characteristic of Ti—O and Ti-O-Ti vibrational modes, along with a band at 876 cm^{-1} attributed to the Na—O bond. The UV–Vis technique shows a decrease in the energy gap from 3.75 eV in the sample without lithium addition to 2.66 eV in the sample with 3 % Li^+. Complex impedance spectroscopy, in turn, showed a reduction in resistivity by two orders of magnitude for the sample with the highest lithium addition compared to the undoped sample. The DFT analysis showed consistency with the lattice parameters observed through X-ray diffraction, as well as a decrease in the band gap due to the addition of lithium, confirming the trend observed in the UV–Vis measurements. The findings confirm the viability of the synthesis method in producing the desired crystalline phases and demonstrate a significant enhancement in the electrical properties.

1. Introduction

Lithium-ion batteries mark a major advancement in energy storage, evolving from earlier innovations like the lead–acid battery developed by French physicist Gaston Plante in 1859 [1]. However, the liquid electrolyte used in commercial lithium-ion batteries is highly flammable and volatile, posing a significant risk of explosion [2]. This issue could be addressed through the development of solid-state batteries, which eliminate the risk of electrolyte leakage [3]. Moreover, apart from the concern over the high electrochemical stability, solid-state batteries—both inorganic and polymeric—are characterized by a high energy density, a key focus of extensive research [4].

In this context, sodium titanates, $Na_2Ti_nO_{2n+1}$, have attracted significant attention for their potential use in solid-state batteries. Titanium-based materials are not only abundant in nature, potentially reducing costs, but also exhibit low toxicity, which is thereby favorable

* Corresponding author.
E-mail address: yurileyet@yahoo.es (Y.L. Ruiz).

https://doi.org/10.1016/j.mseb.2025.118836
Received 12 May 2025; Received in revised form 9 September 2025; Accepted 23 September 2025
Available online 7 October 2025
0921-5107/© 2025 Elsevier B.V. All rights are reserved, including those for text and data mining, AI training, and similar technologies.

for both economic and ecological viability [5,6]. However, Li^+ ions provide higher conductivity than Na^+ ions due to the greater diffusivity of lithium ions, attributed to their smaller radius (approximately 76 pm) compared to that of the sodium ions (approximately 102 pm) [7]. To address this challenge, many researchers have doped sodium trititanate with conductive matrices, such as Nb^{5+} and F^- [5]. The electrical conductivity for $Na_2Ti_3O_7$ and $Na_2Ti_6O_{13}$ has been reported to be in the range of 10^{-6} S/cm [8]. Moreover, a recent study reported that doping these compounds with Li^+ increased their conductivity to the order of 10^{-5} S/cm with the addition of only 5 % lithium [7].

Moreover, several studies have addressed the influence of doping on enhancing the ionic conductivity of materials designed for use as solid electrolytes, such as lithium lanthanum zirconium garnet ($Li_7La_3Zr_2O_{12}$, LLZO), lithium aluminum titanium phosphate ($Li_{1.3}Al_{0.3}Ti_{1.7}(PO_4)_3$, LATP), and superionic lithium conductors of the LISICON (LIthium Super Ionic CONductor) type [9–11]. This is because doping can modify the structure of the material, promoting the formation of vacancies, the creation of preferential pathways for ionic migration, and the increase in the concentration of mobile charge carriers (Li^+ ions).

Although several studies have synthesized sodium titanate using a sonochemical route [8,12,13], none of these works investigate the structural and electrical modifications resulting from doping with lithium ions or any other type of dopant. On the other hand, lithium-doped sodium titanate has been synthesized using various other methods [7,14,15]. Recently, a study by [7] revealed a rapid method for synthesizing this material using microwave-assisted hydrothermal techniques. To the best of our knowledge, nonetheless, there are no reports in the literature on the synthesis of this lithium-doped system via a sonochemical route.

The ultrasonic irradiation employed in sonochemical synthesis induces the formation of acoustic cavitations, which generate extreme localized temperatures and pressures [16]. The generation of this cavitation occurs over extremely short time intervals and at a microscopic scale, promoting rapid nucleation and efficient precursor dispersion, which in turn accelerates the reaction kinetics [17]. As a result, both synthesis time and energy consumption are significantly reduced. Moreover, sonochemical synthesis allows for greater control over particle size and morphology, which favors the formation of specific crystalline phases and can even enhance the material's conductivity, since a more uniform morphology tends to reduce contrasts between grains and grain boundaries within the sample. Another relevant advantage is that the sonochemical method minimizes the need for prolonged thermal treatments or high-pressure systems to form the desired crystalline phases.

In this work, we propose the use of the sonochemistry method to synthesize pure sodium titanate, as well as stoichiometrically lithium-doped variants (Li = 0 %, 1 %, 2 %, and 3 %). Additionally, a comprehensive structural and electrical characterization combining experimental techniques and computational calculations was performed to reveal the key changes in this system.

2. Experimental methods

2.1. Synthesis and characterization

The synthesis of both pure sodium titanate, $Na_2Ti_nO_{2n+1}$, and lithium-doped samples, $Na_{2-x}Li_xTi_3O_7$, was performed following the methodology described by [12]. The titanium isopropoxide ($C_{12}H_{28}O_4Ti$) (Aldrich, > 97 %) was diluted in isopropyl alcohol and mixed with sodium hydroxide, NaOH (Synth, 98 %), diluted in distilled water at a one molar concentration, on a magnetic stirrer until homogenized. The mixture was then subjected to sonication for 15 min at a power of 487.5 W (65 %). Subsequently, the samples were dried in an oven for 24 h at 100 °C. A heat treatment was performed in a muffle furnace at 900 °C for one hour under air (uncontrolled atmosphere), with a heating rate of 10 °C min^{-1} and furnace-cooling to room temperature. The quantities of each component were calculated according to the stoichiometric equation given by:

$$2\,NaOH + 3\,C_{12}H_{28}O_4Ti \rightarrow Na_2Ti_3O_7 + 3\,C_{12}H_{28}O_2 + H_2O \quad (1)$$

The lithium-doped sodium titanate samples were prepared following the same stoichiometry as the pure samples but with lithium substitution to form $Na_{2-x}Li_xTi_3O_7$. Lithium acetate dihydrate ($C_2H_3LiO_2 \cdot 2H_2O$, Sigma-Aldrich, 97 %) was used as the lithium source. Different molar percentages of sodium were replaced with lithium ions. In this case, 'x' represents the lithium concentrations used (0.0, 0.01, 0.02, and 0.03) for the samples NTO, NLTO-1 %, NLTO-2 %, and NLTO-3 %, respectively.

X-ray diffraction (XRD) measurements were conducted using a Panalytical Empyrean diffractometer equipped with copper (Cu) and molybdenum (Mo) radiation sources. The instrument was configured with Cu K_α radiation (λ = 1.5406 Å) and operated in Bragg-Brentano geometry. Data collection was carried out over a 2θ range from 5° to 80°.

Scanning Electron Microscopy (SEM) measurements were performed using a JEOL JSM IT500 HR microscope equipped with a Secondary Electron Detector (SED). The acceleration voltage was set to 5 kV, the working distance (WD) was 13.5 mm, the magnification was 7000×, and the scale bar was 2 μm.

The FTIR measurements were carried out using a Fourier Transform Infrared Spectrometer, Cary 630 (Agilent Technologies, USA). The scans were performed over a spectral range of 4000 to 650 cm^{-1} using Attenuated Total Reflectance (ATR) with a zinc selenide (ZnSe) crystal by horizontally positioning the sample close to a prism (d = 1.8 mm).

The UV–Vis measurements were carried out using a UV–Vis Spectrophotometer (model Evolution 220-Thermo Scientific, with double beam and fiber optic probe). The measurement was performed in the wavelength range of 190 to 1100 nm. The data were used to determine the band gap energy of each sample.

The complex impedance measurements were carried out using a Solartron 1260 impedance analyzer, operating at an excitation voltage of 500 mV, at room temperature, over a frequency range from 10 Hz to 1 MHz. Before the measurements, both surfaces of the pellets were coated with conductive silver paint to ensure good electrical contact, then dried at 120 °C for 60 min. The samples were sintered at 900 °C for 1 h and had a diameter of 10 mm and thicknesses of 1.39 mm (NTO), 1.41 mm (NLTO-1 %), 1.40 mm (NLTO-2 %), and 1.34 mm (NLTO-3 %).

2.2. Calculation details

First-principles calculations based on the density functional method using the Quantum Espresso package [18] were performed to investigate the three phases ($Na_2Ti_3O_7$, $Na_2Ti_6O_{13}$, and $NaLiTi_3O_7$) obtained in this work due to Li doping. Ultrasoft pseudopotentials were utilized with a generalized gradient approximation for the Perdew-Burke-Ernzerhof exchange-correlation energy functionals [19]. The convergence was performed with a kinetic energy cut-off of 0.4 keV and a charge-density cut-off of 4 keV. The structures of all three phases were obtained from the experimental analysis of the structures. Brillouin-zone sampling of the supercells was performed using a Monkhorst-Pack k-point grid mesh [20], as follows: $Na_2Ti_3O_7$–4 × 8 × 4 (24 atoms), $Na_2Ti_6O_{13}$–8 × 8 × 8 (21 atoms), $NaLiTi_3O_7$–8 × 8 × 8 (96 atoms). The structural and electronic properties of the three phases were calculated using structures obtained from the experimental measurements and also with the geometries of all the systems, which were completely relaxed without any constraint. The convergence thresholds were considered to be 10^{-2} eV/Å for the total force and 10^{-3} eV for the total energy. The graphic representation of the cells was performed using Xcrysden [21].

3. Results and discussion

3.1. Structural and electronic characterization

Fig. 1a displays the X-ray diffraction patterns of all the samples: NTO

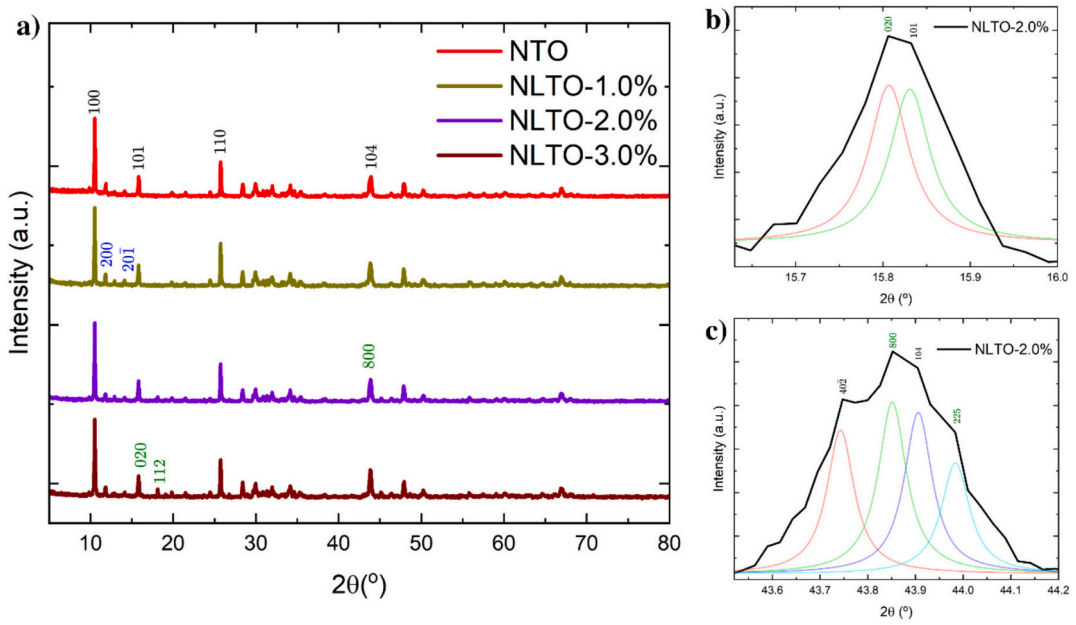


Fig. 1. X-ray Diffraction (XRD) patterns of all powder samples: NTO (red line), NLTO-1 % (yellow line), NLTO- 2 % (violet line), and NLTO-3 % (maroon line). (b) Deconvolution of the 2θ region from 15.6° to 16. (For interpretation of the references to colour in this figure legend, the reader is referred to the web version of this article.)

(red line), NLTO-1 % (yellow line), NLTO-2 % (violet line), and NLTO-3 % (maroon line). Some planes were highlighted using Miller indices to illustrate the behavior of the samples, demonstrating the crystalline phases as the lithium content increased. The first peak observed around 10° corresponds to the most intense peak of the $Na_2Ti_3O_7$ phase, associated with the (100) Miller index. This fact indicates a strong presence of the sodium trititanate phase in all samples [22,23].

The Miller indices (200) and (20$\bar{1}$), highlighted in the yellow curve

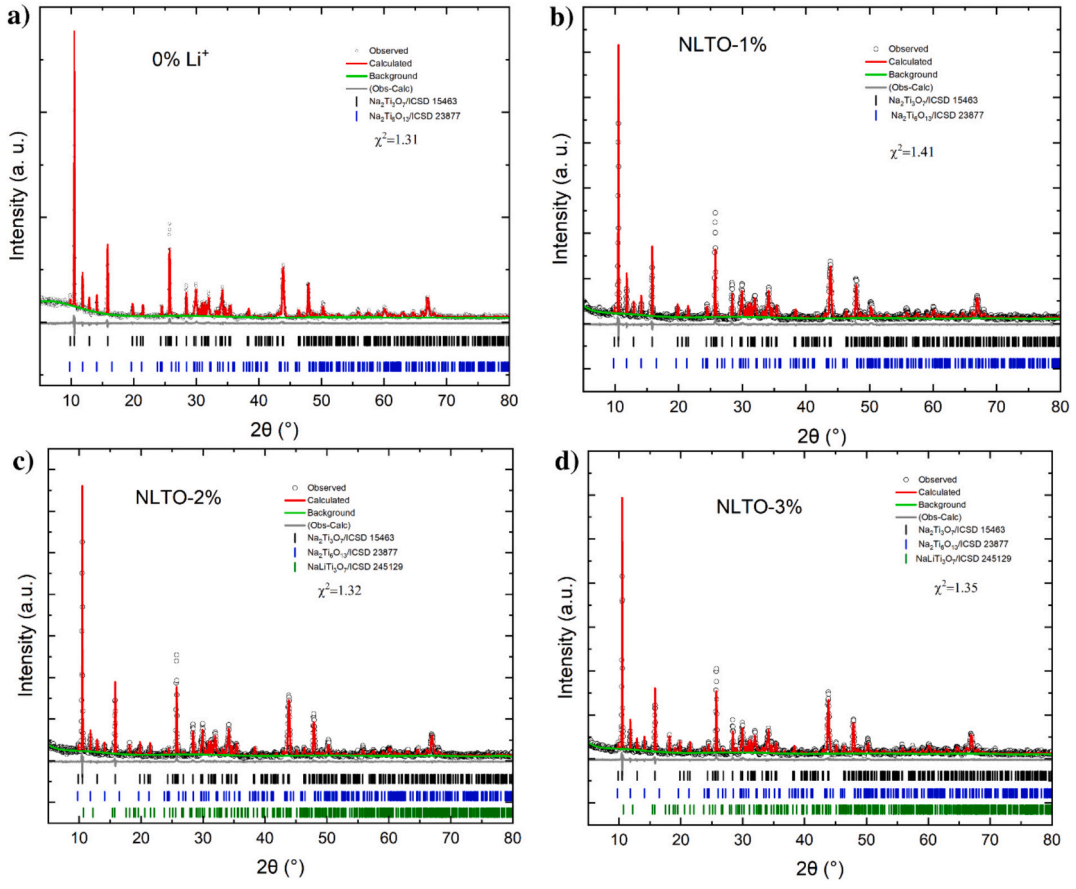


Fig. 2. Rietveld refinement plots for the (a) NTO, (b) NLTO-1 %, (c) NLTO-2 %, and (d) NLTO-3 % samples.

(NLTO-1 %), correspond to the $Na_2Ti_6O_{13}$ crystalline phase [23–25]. These peaks are present in all samples, indicating their presence as a secondary phase, which has been reported in the literature [12,26–28]. Moreover, the Miller index, identified as (112), corresponds to a new crystalline phase, $NaLiTi_3O_7$. The intensity of this peak increases with the addition of lithium, suggesting an enhanced formation of the $NaLiTi_3O_7$ phase. A similar trend is observed for the peak associated with the (800) indices, which also corresponds to the $NaLiTi_3O_7$ crystalline phase [29]. Fig. 1a appears to show more than one Miller index corresponding to the same 2θ value in two regions, around 15.8° and 43.8°. However, Fig. 1b and c reveal, with appropriate scale adjustment and peak deconvolution, that multiple peaks are indeed present in these regions, each associated with a different reflection plane and, consequently, different Miller indices. The magnified view in Fig. 1c even allows the identification of two additional peaks not labeled in Fig. 1a: the $(40\bar{2})$ peak, corresponding to $Na_2Ti_3O_7$, and the (225) peak, corresponding to $NaLiTi_3O_7$.

Fig. 2 presents the Rietveld refinement plots for all samples. The analysis revealed the existence of two monoclinic phases in the NTO sample. Sodium trititanate, $Na_2Ti_3O_7$, with space group $P2_1/m$ (ICSD 15463), has lattice parameters $a = 8.576$ Å, $b = 3.796$ Å, $c = 9.130$ Å, and $\beta = 101.581°$, as shown in Table 2. Additionally, sodium hexatitanate, $Na_2Ti_6O_{13}$, with space group $C2/m$ (ICSD 23877), presents lattice parameters $a = 15.121$ Å, $b = 3.746$ Å, $c = 9.161$ Å, and $\beta = 99.078°$, as described in Table 2. The analysis also indicated that the major phase is $Na_2Ti_3O_7$, representing 87.27 ± 0.36 %, while $Na_2Ti_6O_{13}$ constitutes 12.73 ± 0.36 %, as shown in Table 1.

In turn, the NTO-1 % sample exhibits similar behavior, with the same two crystalline phases and lattice parameters very close to those of the NTO sample, as shown in Table 2. There is a slight increase in the amount of the secondary phase ($Na_2Ti_6O_{13}$), which in this sample is 13.73 ± 0.38 %, while the main phase appears with 86.27 ± 0.38 %, as shown in Table 1. The structural effect due to lithium addition becomes evident in the NLTO-2 % sample, with the appearance of the crystalline phase $NaLiTi_3O_7$, with space group *Cmcm*, and lattice parameters $a = 16.501$ Å, $b = 11.235$ Å, $c = 11.480$ Å, as shown in Table 2. In this sample, the new phase appears at 6.25 ± 0.38 %, while the secondary phase ($Na_2Ti_6O_{13}$) accounts for 7.6 ± 0.31 %, and the main phase ($Na_2Ti_3O_7$) accounts for 86.15 ± 0.31 %. In the NLTO-3 % sample, the $NaLiTi_3O_7$ phase increased considerably (10.61 ± 0.42 %), while the $Na_2Ti_3O_7$ phase decreased to 78.91 ± 0.50 %, and the $Na_2Ti_6O_{13}$ phase appeared at 10.48 ± 0.42 %.

Table 2 shows that there is no significant change in the lattice parameters of the existing phases. The appearance of the third crystalline phase ($NaLiTi_3O_7$) in the NLTO-2 % and NLTO- 3 % samples is likely related to the solubility limit of lithium doping in the other phases, $Na_2Ti_3O_7$ and $Na_2Ti_6O_{13}$. This phenomenon occurs because the lithium ions replace the sodium ions.

The synthesis route used in this work has been demonstrated to be quite viable, as a previous study reported a 50 % proportion of trititanate and hexatitanate phases [8], and another study, utilizing the microwave technique, achieved an 85.81 % composition of trititanate and 14.19 % hexatitanate [7]. In this study, the NTO sample achieved a purity of approximately 87.3 %. The high purity of the crystalline phase was maintained in the other samples (above 86 %) up to the NLTO-2 % sample. In the NLTO-3 % sample, however, there was a significant decrease in the crystalline phase of $Na_2Ti_3O_7$, which is due to the substantial increase in the $NaLiTi_3O_7$ phase.

Table 1
Structural parameters and phase percentages for samples with different concentrations of Li^+.

% Li^+	% $Na_2Ti_3O_7$	% $Na_2Ti_6O_{13}$	% $NaLiTi_3O_7$	χ^2	RWP (%)	Rexp (%)
0.0	87.27 ± 0.36	12.73 ± 0.36	0	1.31	16.68	14.57
1.0	86.27 ± 0.38	13.73 ± 0.38	0	1.41	18.31	15.42
2.0	86.15 ± 0.45	7.60 ± 0.31	6.25 ± 0.37	1.32	17.45	15.19
3.0	78.91 ± 0.50	10.48 ± 0.35	10.61 ± 0.42	1.35	17.83	15.35

Table 2
Lattice parameters resulting from the Rietveld refinement of all Samples.

Sample	Parameter	0 % Li^+	1 % Li^+	2 % Li^+	3 % Li^+
$Na_2Ti_3O_7$	**a (Å)**	8.575 (2)	8.577 (3)	8.574 (2)	8.571 (3)
	b (Å)	3.796 (1)	3.796 (1)	3.796 (1)	3.797 (1)
	c (Å)	9.130 (2)	9.131 (2)	9.132 (2)	9.133 (2)
	V ($Å^3$)	291.14 (5)	291.29 (5)	291.23 (5)	291.16 (5)
	β (°)	101.581 (8)	101.569 (9)	101.572 (8)	101.574 (9)
	ρ (g/cm^3)	3.441	3.440	3.440	3.441
$Na_2Ti_6O_{13}$	**a (Å)**	15.121 (8)	15.143 (8)	15.150 (11)	15.128 (9)
	b (Å)	3.746 (1)	3.746 (1)	3.748 (1)	3.746 (1)
	c (Å)	9.161 (5)	9.153 (5)	9.150 (8)	9.154 (7)
	V ($Å^3$)	512.5 (2)	512.7 (2)	513.0 (3)	512.2 (3)
	β (°)	99.08 (3)	99.12 (3)	99.14 (4)	99.08 (3)
	ρ (g/cm^3)	3.509	3.506	3.505	3.510
$NaLiTi_3O_7$	**a (Å)**			16.50 (1)	16.51 (1)
	b (Å)			11.235 (7)	11.240 (4)
	c (Å)			11.480 (5)	11.491 (4)
	V ($Å^3$)			2128 (1)	2132 (1)
	ρ (g/cm^3)			3.566	3.560

Fig. 3 shows the structures visualized from different orientations to highlight the internal atomic organization. The red spheres represent oxygen atoms, the blue spheres represent titanium atoms, the yellow spheres represent sodium atoms, and the green spheres represent lithium atoms. The structures correspond to the following compounds: (a) $Na_2Ti_3O_7$, (b) $Na_2Ti_6O_{13}$, and (c) $NaLiTi_3O_7$.

Lithium is incorporated into the samples through both interstitial occupation and the substitution of Na^+ ions with Li^+ ions. This mechanism can be verified by analyzing the sample with a 1 % lithium addition, in which the crystalline phase $NaLiTi_3O_7$ was not detected. However, the results indicate lithium incorporation into the structure, as evidenced by a decrease in the band gap for the NLTO-1 % sample compared to the undoped NTO sample, as shown in Fig. 6 and discussed theoretically in Section 3.2. Since there is no crystalline evidence for Na^+ substitution by Li^+ in this sample, it is reasonable to infer that the lithium ions, introduced via lithium acetate, were accommodated in interstitial sites. In the NLTO-2 % sample, the $NaLiTi_3O_7$ crystalline phase emerges with a fraction of 6.25 ± 0.37 %, and in the NLTO-3 % sample, this fraction increases to 10.61 ± 0.42 %. These results suggest a possible saturation of interstitial sites, leading to a progressive formation of the $NaLiTi_3O_7$ phase. Therefore, in these two samples, it is likely that lithium is incorporated both interstitially and through substitution.

Fig. 4 shows the SEM images for samples with 0 %, 1 %, 2 %, and 3 % lithium. These images of sodium titanate predominantly display rod-like or needle-like particles, with sizes ranging between 1 and 2 μm (Fig. 4). This pattern has been previously reported in other studies on sodium titanate [30], including samples doped with lithium [7]. The images generally show similar morphologies, with particles of comparable size and shape. The particles appear relatively smooth, indicating a material with few imperfections. Moreover, no cracks or porosity were observed in any of the samples. However, for the samples with 2 % and 3 % lithium ions, the presence of smaller grains and slightly different shapes is evident. This variation can be attributed to the increased lithium content in the samples [7].

Fig. 5a displays the FTIR spectra of sodium titanate samples doped with different concentrations of lithium (0 %, 1 %, 2 % and 3 %). Infrared spectroscopy indicates the presence of bands below 1000 cm^{-1}, which correspond to Ti-O-Ti stretching and Ti—O vibrations, supporting the structural characteristics of the synthesized material. The absorption band related to sodium titanate was identified in all samples: the

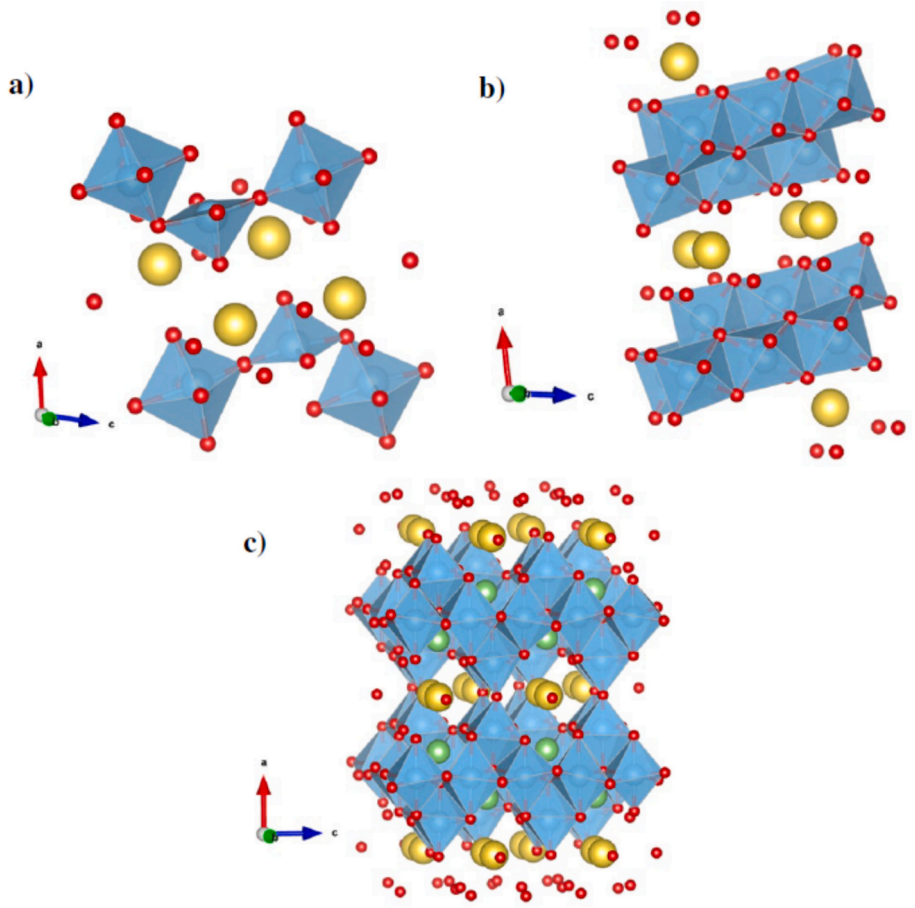


Fig. 3. Structural representations of the observed crystalline phases: (a) $Na_2Ti_3O_7$; (b) $Na_2Ti_6O_{13}$; (c) $NaLiTi_3O_7$. Blue polyhedra: TiO_6 octahedra (Ti in blue at the centers); red spheres: O; yellow spheres: Na; green spheres: Li. (For interpretation of the references to colour in this figure legend, the reader is referred to the web version of this article.)

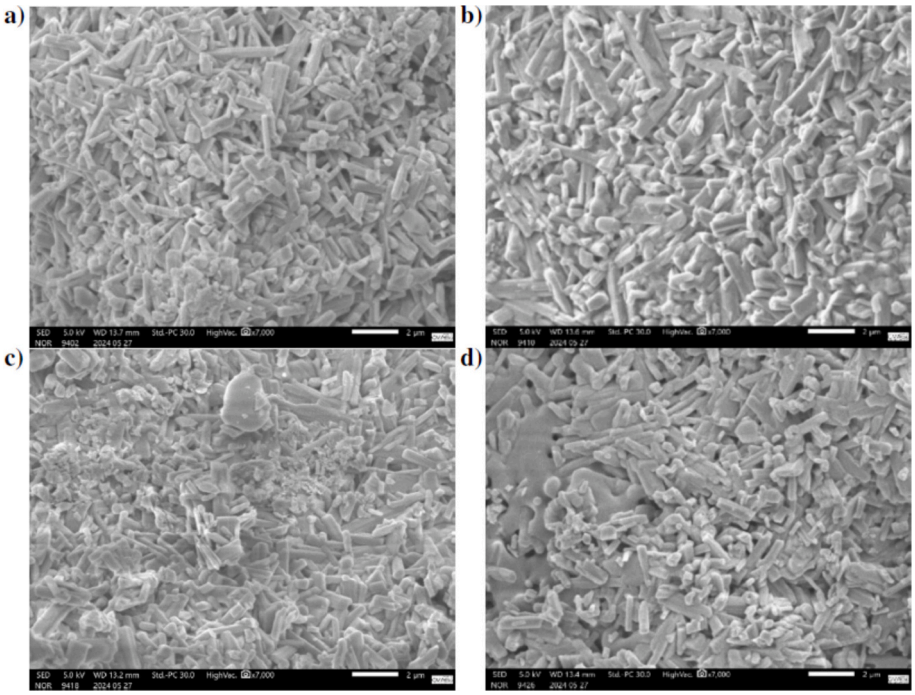


Fig. 4. Scanning Electron Microscopy images for powder NTO, NLTO-1 %, NLTO-2 %, and NLTO-3 % samples.

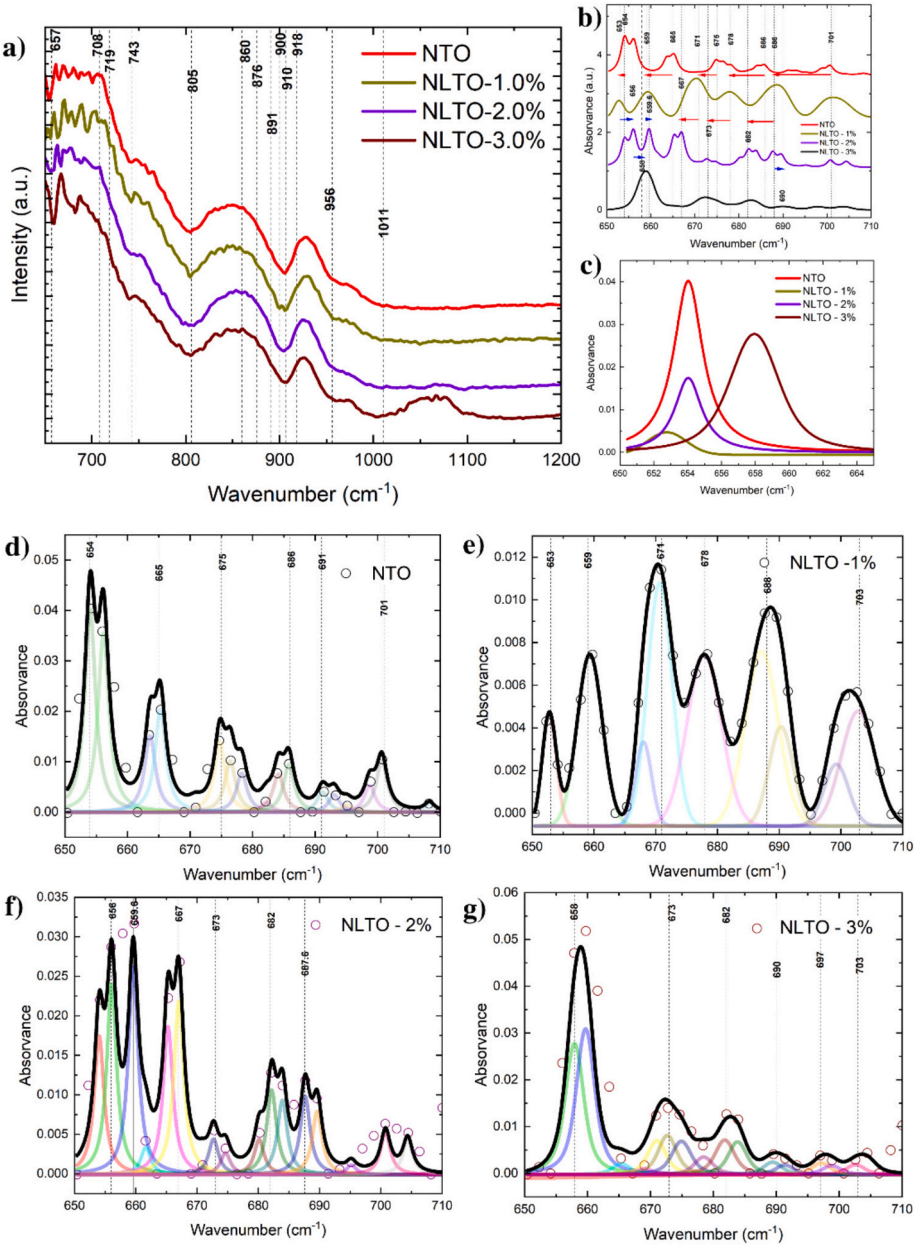


Fig. 5. (a) FTIR spectra of all samples. (b) Detailed visualization of red and blue shifts in FTIR peaks. Evolution of the main peak near 655 cm^{-1} as a function of Li content. (c) Evolution of the main peak near 655 cm^{-1} as a function of Li content. (d–g) Deconvolution of the 650–710 cm^{-1} region for each composition. (For interpretation of the references to colour in this figure legend, the reader is referred to the web version of this article.)

vibration region between 400 and 800 cm^{-1} could be attributed to Ti—O and Ti-O-Ti bond vibrations [31], whereas the bands in the range of 900 to 918 cm^{-1} are associated with Ti—O vibrations [32]. Moreover, the band 860 cm^{-1} can be attributed to the stretching of the O–Ti–O bond in $Na_2Ti_3O_7$. The bands at 891 cm^{-1} and 910 cm^{-1} can be associated with the Ti—O bond vibrations involving less coordinated oxygen atoms that might interact directly with sodium ions [32–34]. Additionally, the peaks observed at 743 cm^{-1} and 876 cm^{-1} have been reported in the literature as corresponding to the Na—O bond vibration [34,35].

Figs. 5d-g show the deconvolution of the FTIR spectra between 650 and 710 cm^{-1}, highlighting the most significant changes in the spectral pattern due to lithium addition. These changes occur due to the influence of lithium on the vibrational modes. In the NLTO-1 % sample, a decrease in the amplitude of the absorbance peaks is observed, indicating an interference of lithium in the structure. In this sample, a slight redshift of the first peak can be observed, which is due to the higher vibrational energy of the bonds in this region due to the presence of lithium.

The 2 % lithium sample shows a reduction in bands and an increase in band overlap, which becomes more pronounced in the sample with 3 % lithium. This fact could indicate the emergence of a new crystalline phase and a change in the sample's morphology. The broadening of the peaks may also indicate the emergence of new phases.

Fig. 5c shows the first peaks of each sample. A decrease in the absorbance intensity can be seen in samples up to the 2 % lithium sample, followed by an increase in the 3 % sample. The changes in the absorbance intensity are related to the variation in the concentration of the bonds corresponding to that band [36]. This observation demonstrates that lithium alters the structures, leading to a decrease in the concentration of Ti—O and Ti–O–Ti bonds. This intensity increases again for the 3 % sample.

The bandwidths also undergo a noticeable change. The sample

without lithium has a full width at half maximum (FWHM) of 2.097 cm^{-1}, whereas upon lithium incorporation the FWHM values become 2.711 cm^{-1}, 1.940 cm^{-1}, and 3.507 cm^{-1} for the samples with 1 %, 2 %, and 3 % lithium, respectively. The increase in peak width may indicate more complex vibrational interactions. For the sample with 2 % lithium, despite the reduced width, the deconvolution reveals the coexistence of multiple vibrational modes in the same region, suggesting the formation of new bonds and the onset of a modified structure. This overall trend of peak broadening is also evident in the 3 % lithium sample. Additionally, in Fig. 7, the overlap of several bands is clearly visible, further supporting the possible emergence of a new crystalline phase, in agreement with the X-ray diffraction results.

Fig. 5b shows the band shifts resulting from lithium addition. The red arrows pointing to the left indicate shifts to lower wavenumbers (redshifts), corresponding to lower bond energies between atoms. Conversely, the blue arrows pointing to the right indicate shifts to higher wavenumbers (blueshifts), which are associated with increased bond energy. The first row of arrows, below the red curve (referring to the NTO sample), shows only redshifts — for instance, the shift from 654 cm^{-1} to 653 cm^{-1} — indicating that the initial addition of 1 % lithium reduces the bond energy in Ti—O and Ti–O–Ti. This redshift behavior, previously reported in the literature for low lithium addition [37], likely occurs due to lithium interfering with these structures, creating a sort of competition with titanium atoms. Below the yellow curve, corresponding to the NLTO- 1 sample, the second row of arrows can be observed. In addition to redshifts, blueshifts appear in the first two peaks, suggesting an increase in the bond energy of Ti—O. Blueshifts are also observed in the third row of arrows, under the violet curve (NLTO-2 % sample), such as from 656 to 658 cm^{-1} and from 688 to 690 cm^{-1}, indicating a further increase in bond energy with the increase of lithium content from 2 % to 3 %. This behavior is most likely associated with the formation of the $NaLiTi_3O_7$ phase, which exhibits an orthorhombic crystalline structure, in contrast to the monoclinic structures of $Na_2Ti_3O_7$ and $Na_2Ti_6O_{13}$. This structural transition may enhance the overall stability of the system, thereby strengthening the atomic bonds.

Furthermore, since the vibration of Ti—O bonds is influenced by the surrounding atoms, the substitution of Na^+ by Li^+ significantly reduces the effective mass of the system. When considering chemical bonds as coupled harmonic oscillators, this mass reduction leads to an increase in the vibrational frequency, as described by Eq. 2 [38].

$$\tilde{\nu} = \frac{1}{2\pi c}\sqrt{\frac{k}{\mu}} \tag{2}$$

where: $\tilde{\nu}$ is the vibrational frequency expressed in wavenumbers (cm^{-1}), c is the speed of light in vacuum, k is the force constant of the bond (N/m), μ is the reduced mass of the system, defined as:

$$\mu = \frac{m_1 m_2}{m_1 + m_2} \tag{3}$$

where m_1 and m_2 are the atomic masses of the two atoms involved in the bond.

The simplified model described by Eqs. (2) and (3) was applied through Partial Hessian *V*ibrational Analysis (PHVA) of the Ti—O coordination polyhedron in the $Na_2Ti_3O_7$ crystalline phase, using the CIF structures as input. For the same Ti site in all samples, the nearest oxygen neighbors within $r \leq 2.60$ Å were considered. A harmonic 3 *N* Hessian was assembled from radial springs along each Ti—O bond, with force constants $k_i = k_{ref}\,(r_{ref}/r_i)^3$ [39–41]. The reference constant was defined as $k_{ref} = (2\pi c\tilde{\nu}_{ref})^2\,\mu_{TiO}$, using $r_{ref} = 1.95$ Å, $\tilde{\nu}_{ref} = 891$ cm^{-1}, and the Ti—O reduced mass (average isotopic masses). mass-weighted Hessian was diagonalized to obtain local vibrational frequencies $\tilde{\nu}$ (cm^{-1}). All calculations were performed using the Atomic Simulation Environment (ASE) [42] together with in-house Python scripts.

Table 3 summarizes the results of the Partial Hessian Vibrational Analysis (PHVA) for a representative Ti site. As expected, the computed local vibrational modes do not match the experimental bands exactly, because in this simplified model the Ti—O polyhedron is treated in isolation and lattice coupling is neglected. Nevertheless, the agreement is reasonable. For example, the calculated mode around 649 cm^{-1} corresponds closely to the FTIR band near 650 cm^{-1}, while the FTIR feature at ~719 cm^{-1} is reproduced by the calculated values of 716–717 cm^{-1}. Similarly, the experimental regions near 910, 958, and 1011 cm^{-1} have counterparts in the PHVA results at approximately 908, 940, and 1015 cm^{-1}.

It is worth noting, however, that the calculated frequencies remain essentially unchanged with increasing Li content. This invariance highlights a limitation of the local PHVA model, which does not capture subtle distortions of the Ti—O environment or long-range structural effects induced by dopant incorporation. The choice of reference bond length (1.95 Å) and reference frequency (891 cm^{-1}) ensures consistent internal scaling but at the same time constrains the sensitivity of the model. Overall, while PHVA effectively reproduces the main vibrational trends of the Ti—O coordination, it should be considered a qualitative approach rather than a quantitative predictor of frequency shifts upon doping.

Fig. 6 displays the band gap determination of sodium titanate samples doped with 0 %, 1 %, 2 %, and 3 % lithium using the Tauc Plot technique through the extrapolation of the linear region of the curve. The Tauc Plot method is based on the following relation:

$$(\alpha h\nu)^2 = A\left(h\nu - {}_g\right) \tag{4}$$

with α being the absorption coefficient, h is Planck's constant, ν is the frequency of light, A is a constant, and E_g is the band gap energy.

To determine the band gap, $(\alpha h\nu)^2$ is plotted as a function of $h\nu$ (photon energy). The extrapolation of the linear part of the curve to the energy axis $h\nu$ gives the value of E_g [23,43]. In Fig. 6, it is observed that the band gap decreases with increasing lithium concentration in sodium titanate samples. The highest band gap value is 3.75 eV for the undoped sample, which is consistent with values reported in the literature [5]. The lowest value is 2.66 eV for the sample doped with 3 % lithium. The errors in determining the band gap values were less than 5 % in all cases. The decrease in the band gap observed in the sequence suggests the effectiveness of the doping technique, as the direct relationship between band gap narrowing and doping has been extensively reported in the literature [44,45].

Although the band gap is directly related to the electronic conductivity, several additional factors are important when considering doping in ceramic materials. Firstly, lithium ions can increase the charge carrier density, occupy interstitial sites, or substitute larger ions (such as sodium, in this work). They may also create vacancies to maintain the electrical neutrality of the material and distort the crystal structure,

Table 3
Ti—O bond lengths and local modes (PHVA) for Ti with five neighbors ($r \leq 2.60$ Å).

% Li^+	Ti–O bond lengths r_i (Å)					Local vibrational modes $\tilde{\nu}_i$ (cm^{-1})				
	r_1	r_2	r_3	r_4	r_5	$\tilde{\nu}_1$	$\tilde{\nu}_2$	$\tilde{\nu}_3$	$\tilde{\nu}_4$	$\tilde{\nu}_5$
0.0	1.826	1.919	1.969	2.110	2.311	649.5	716.6	908.1	940.1	1015.9
1.0	1.826	1.919	1.969	2.110	2.311	649.3	716.4	907.9	939.9	1015.6
2.0	1.826	1.919	1.968	2.110	2.311	649.3	716.7	907.9	940.2	1015.6
3.0	1.826	1.919	1.968	2.109	2.311	649.3	717.0	907.9	940.6	1015.6

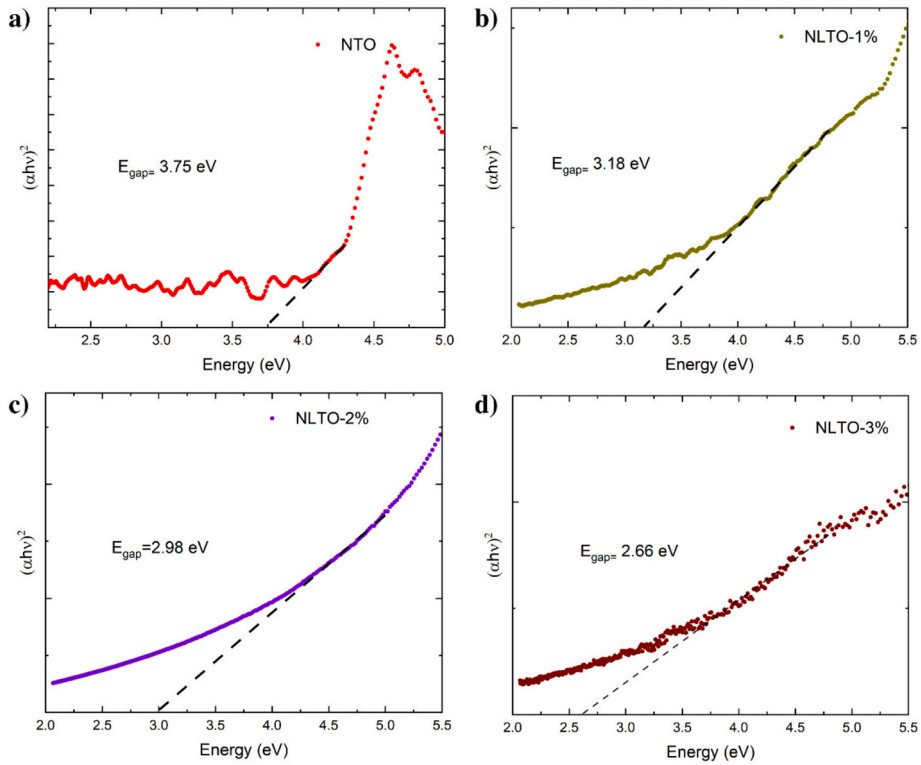


Fig. 6. Band Gap by UV–Vis of sodium titanate powder NTO, NLTO-1 %, NLTO-2 %, and NLTO-3 % samples.

generating new pathways for ion diffusion. Therefore, though there is no direct relationship between the band gap and ionic conductivity, the variation in the band gap may serve, in some materials, as an indicator of improved ionic conductivity. Experimental results showing this relationship between band gap and ionic conductivity have already been reported in the literature [44,46–48].

Fig. 7a shows the Cole-Cole plots of the complex impedance spectroscopy measurements. The largest semicircle, with red points, refers to the sample without lithium addition. The yellow semicircle refers to the sample with a 1 % lithium addition. The violet curve corresponds to the sample with a 2 % lithium addition. The smallest curve, in maroon, corresponds to the measurement of the sample with 3 % addition of Li. The graph shows a decrease in the semicircles formed by Z"(Ω) with the addition of lithium, which indicates that the total electrical resistance of the pellets decreases with lithium addition, with values of 3.63×10^6 Ω, 5.64×10^5 Ω, 9.35×10^4 Ω, and 7.33×10^4 Ω for the NTO, NLTO-1 %, NLTO-2 %, and NLTO-3 % samples, respectively.

The circuit shown in the graph of Fig. 7a represents the equivalent circuit that fitted the Cole-Cole curves for all samples. This circuit models the behavior of both the grains and the grain boundaries in the material. The elements R1 and C1 form a parallel RC circuit, representing the electrical response of the grains, the predominant part of the sample. On the other hand, the elements R2 and CPE1 form another parallel RC circuit, which models the behavior of the regions between the grains, i.e., the grain boundaries. The CPE1, or Constant Phase Element, is used instead of an ideal capacitor to better fit the impedance response of the grain boundaries, reflecting a non-ideal capacitive behavior [49–52].

For a more precise analysis, it is essential to investigate the electrical conductivity, as this is an inherent characteristic of the material. The dimensions of the pellets were considered, as the conductivity is given by Eq. 5 [46,53]:

$$\sigma = \frac{e}{R_b \cdot A} \tag{5}$$

where σ is the electrical conductivity of the material, R_b is the bulk resistance (also referred to as grain resistance, corresponding to the high-frequency semicircle in Cole–Cole plots), A is the cross-sectional

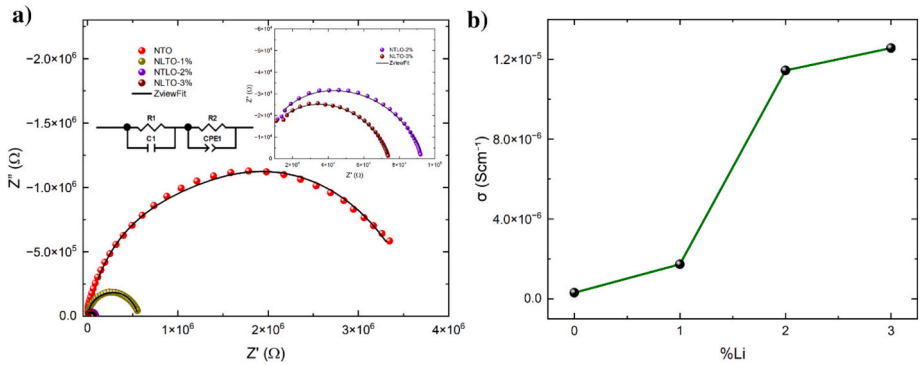


Fig. 7. (a) Cole-Cole plot of Impedance Spectroscopy for sodium titanate samples with varying lithium doping. (b) Conductivity vs. %Li.

area of the pellet, and *e* is the thickness of the pellet.

The resistance used for determining electrical conductivity was obtained by fitting the Cole-Cole plots (Fig. 7a) for each sample. This fitting was performed using the ZView software, which allows for identifying the point where the bulk impedance curve intercepts the Z' axis (R1 of the equivalent circuit). The bulk resistance values (R_1) were 5.80×10^5 Ω, 1.04×10^5 Ω, 1.56×10^4 Ω, and 1.36×10^4 Ω for the NTO, NLTO-1 %, NLTO-2 %, and NLTO-3 % samples, respectively. Therefore, these results were used to analyze the behavior of electrical conductivity, as shown in the graphs of Fig. 7b.

The electrical conductivity (Fig. 7b) increased by two orders of magnitude from the NTO sample to the NLTO-3 % sample (from 10^{-7} Scm^{-1} to 10^{-5} Scm^{-1}). The highest value obtained is for the NLTO-3 % sample, with a value of 1.26×10^{-5} Scm^{-1}. The electrical conductivity within these orders of magnitude has already been reported in the literature for undoped sodium titanate samples [54–56] and a doped sample with 5 % lithium using the microwave synthesis method [7].

Several factors contribute to the increase in conductivity upon the addition of lithium. Firstly, the emergence of the crystalline phase $NaLiTi_3O_7$ in the samples with 2 % and 3 % lithium introduces a material whose structure facilitates the movement of lithium ions due to its tunnel-like conformation [57]. Furthermore, UV–Vis measurements demonstrated the effectiveness of lithium- doping through the reduction of the band gap as the lithium content increases. This behavior indicates that, even before the formation of the new crystalline phase ($NaLiTi_3O_7$), lithium ions were already occupying interstitial sites in the $Na_2Ti_3O_7$ and $Na_2Ti_6O_{13}$ structures. This interstitial occupation suggests an increase in the ionic density in the lithium-doped samples, which is further supported by the data presented in Fig. 9. Therefore, the creation of new conduction pathways combined with the increase in charge carrier density explains the enhancement in conductivity observed in the complex impedance spectroscopy analysis, corroborating the findings obtained through the other experimental techniques.

The curves in Fig. 8 show the behavior of the impedance components as a function of the logarithm of the frequency, as well as the relaxation time behavior with varying lithium concentrations. The red, yellow, violet, and brown curves represent the NTO, NLTO-1 %, NLTO-2 %, and NLTO-3 % samples, respectively. The first curve (Fig. 8a) shows that the value of the real component increases as the frequency decreases. At very low frequencies, the NTO sample shows a value slightly below 4×10^6 Ω, while for the NLTO-3 % sample, this impedance is lower than 8×10^4 Ω. These approximate values of the real component of the impedance are consistent with those calculated through the Zview fit (3.63×10^6 Ω and 7.33×10^4 Ω, respectively). At high frequencies, the values converge to a very low resistance, which is expected since, at high frequencies, the capacitors of the equivalent circuit act as a short circuit.

Additionally, Fig. 8b illustrates the behavior of the imaginary impedance (Z''). The imaginary contribution tends towards zero at low frequencies, as expected, since the real impedance predominates in this region [58]. At high frequencies, Z'' also tends to very low values because the capacitor behaves like a short circuit, and the imaginary component approaches zero. Important information that can be extracted from this graph is the peak frequency (f_{peak}), as it allows the calculation of the relaxation time (τ), given by Eq. 6 [59].

$$\tau = \frac{1}{2\pi f_{peak}} \tag{6}$$

The graph in Fig. 8c shows that the relaxation time decreases with the addition of lithium (from 6.34×10^{-5} s in the NTO sample to 7.98×10^{-7} s in the NLTO-3 % sample). This result is significant because it indicates an increase in ionic conductivity, as the relaxation time refers to the duration required by the system to return to its initial state after being subjected to an electric field. In other words, τ is related to the ease of ion movement in the system [59]. Mathematically, this behavior is represented by Eq. 7.

$$\tau = \frac{\varepsilon_0 \varepsilon'}{\sigma_{DC}} \tag{7}$$

where τ is the relaxation time, ε_0 is the vacuum permittivity (8.854×10^{-12} F/m), and ε' is the real part of the material's permittivity, σ_{DC} is the DC conductivity of the material.

Fig. 9a shows the variation of volumetric charge density with

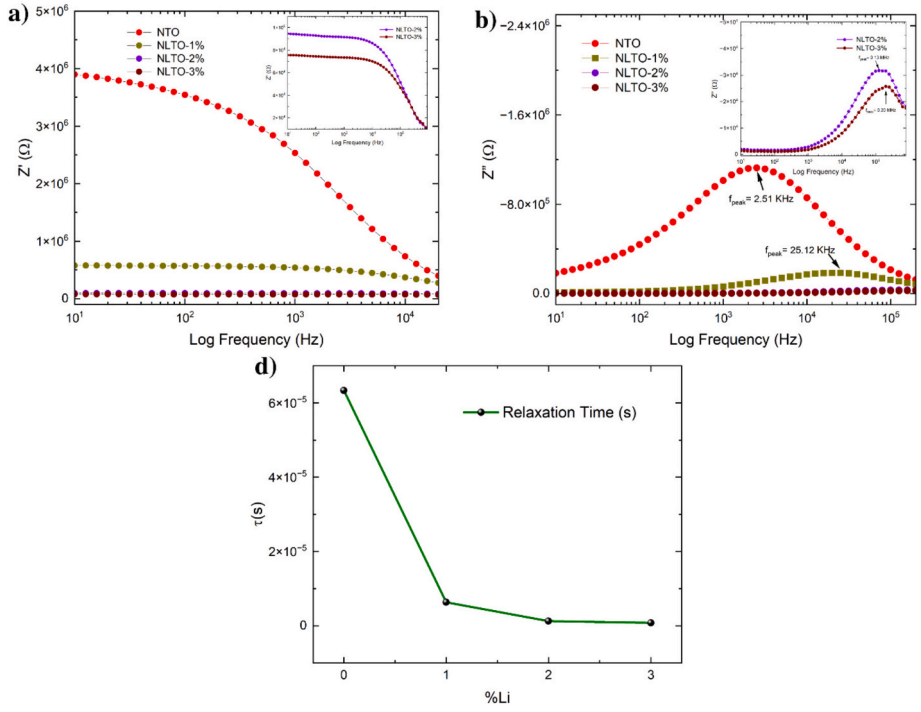


Fig. 8. Plots of Impedance Spectroscopy for sodium titanate samples with varying levels of lithium doping: (a) Real Impedance (Z') vs. Log Frequency, (b) Imaginary Impedance (Z'') vs. Log Frequency, (c) Relaxation time vs. %Li.

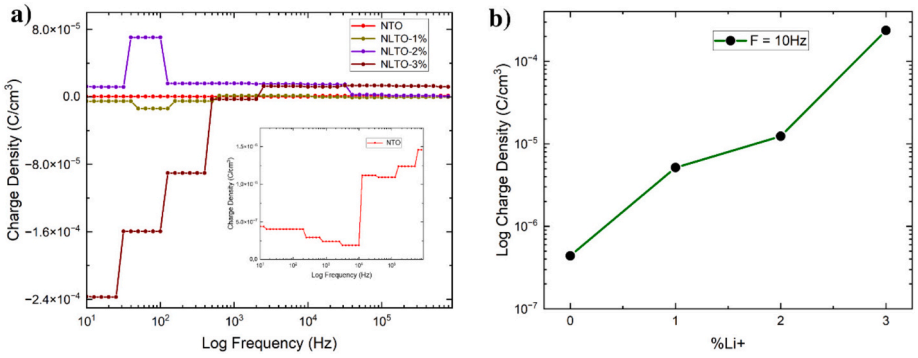


Fig. 9. Plots of Impedance Spectroscopy for sodium titanate samples with varying levels of lithium doping:

frequency. It can be observed that with the increase in lithium concentration, the amplitudes of the curves also increase, indicating a greater difference in density between high and low frequencies. Moreover, at low frequencies, an increase in charge density with increasing lithium concentration is evident. For the sample without lithium, this value is around 10^{-7}C/cm^3; whereas, for the sample with 1 % Li^+ addition, the volumetric charge density ranges between 10^{-5} and 10^{-6}C/cm^3. In case of the sample with 2 % Li^+ addition, the volumetric charge density is around 10^{-5}C/cm^3; and for the sample with 3 % Li^+ addition, the volumetric charge density is around 10^{-4}C/cm^3.

(a) Charge Density vs Log Frequency and (b) Logarithmic Plot of Charge Density at 10 Hz vs. Lithium Doping Percentage.

This dependency becomes more evident when the frequency is held constant, allowing the variation in volumetric charge density to be observed as the percentage of lithium addition changes. Fig. 9b shows the above relation at the lowest frequency used in the measurement, 10 Hz.

The data from complex impedance spectroscopy measurements also enables the analysis of the dielectric properties of the material. The electric permittivity ε can be expressed as [29]:

$$\varepsilon^* = \frac{1}{j\omega C_0 Z^*} \tag{8}$$

where $\omega = 2\pi f$ is the angular frequency, and C_0 is the geometric capacitance without the dielectric material, given by:

$$C_0 = \frac{\varepsilon_0 A}{d} \tag{9}$$

where ε_0 is the permittivity of free space (8.854×10^{-12} F/m), A is the area of the sample, and d is the thickness of the sample.

Separating the real (ε') and imaginary (ε'') parts results in [29]:

$$\varepsilon' = \frac{Z''}{\omega C_0 \left(Z'^2 + Z''^2\right)} \tag{10}$$

and

$$\varepsilon'' = \frac{Z'}{\omega C_0 \left(Z'^2 + Z''^2\right)} \tag{11}$$

ε' vs Log Frequency and Log ε' vs Log Frequency.

Eqs. 10 and 11 were used to calculate the two components of the complex permittivity for each frequency of all the samples, and the values are presented in Fig. 10. Fig. 10a (10b) shows the variation of the real (imaginary) permittivity (ε') with frequency. In both cases, an increase in the magnitude is observed with the addition of lithium. Permittivity is given by:

$$\varepsilon = \varepsilon_r \cdot \varepsilon_0 \tag{12}$$

where ε_r is known as the dielectric constant of the material.

The dielectric constant (ε_r) represents a material's ability to store electrical energy. Therefore, it can be understood that the addition of lithium results in sodium titanate samples improving their energy storage capacity, making them more suitable for use in solid-state electrolytes.

Finally, impedance spectroscopy is a widely employed technique to investigate the transport properties of solid materials, providing important insights into their electrical behavior. However, for a precise differentiation between ionic and electronic conductivity, it is necessary to conduct measurements under blocking conditions that selectively inhibit one type of carrier. In this study, impedance measurements were performed without such selective blocking, resulting in the evaluation of the total electrical response of the material. Although the impedance spectroscopy measurements in this study were performed without selective blocking electrodes— thus reflecting the total electrical response

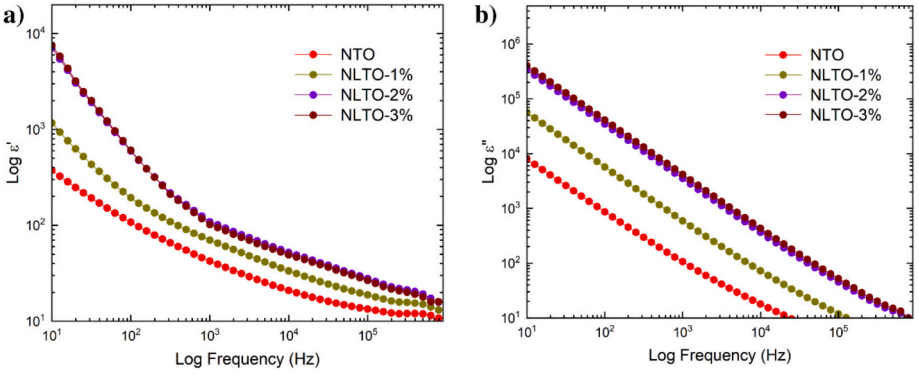


Fig. 10. Plots of Impedance Spectroscopy for sodium titanate samples with varying levels of lithium doping: Log.

of the system—several experimental observations support the predominance of ionic conductivity. This conclusion is supported by the absence of interfacial charge-transfer features or Warburg-type diffusion tails in the Cole–Cole plots, as well as by the formation of the $NaLiTi_3O_7$ phase in samples with higher lithium content. This phase exhibits a tunnel-type structure favorable to Li^+ ion mobility, as reported in the literature [57]. Moreover, sodium titanates, along with other Na^+-based materials [60], have been reported in the literature as predominantly ionic conductors, particularly $Na_2Ti_3O_7$ due to its layered structure [22,61,62]. Therefore, despite the limitations inherent to the current experimental setup, the observed increase in conductivity upon lithium doping is primarily attributed to ionic transport. Nevertheless, to unambiguously determine the predominant type of charge carrier, future studies should make impedance measurements under controlled conditions using blocking electrodes. This technique will allow the quantitative separation of ionic and electronic contributions, thereby providing more robust support for the optimization of these materials in solid-state energy systems.

In addition to conductivity and relaxation time analysis, impedance spectroscopy also allows the estimation of the volumetric charge density associated with mobile carriers in the material. This parameter is particularly relevant because it provides complementary information on how Li doping affects the concentration of charge carriers, thereby offering further insight into the mechanisms underlying the observed conductivity enhancement [63]. The volumetric charge density (ρ_Q) was estimated from impedance data using the relation:

$$\rho_Q = \frac{\varepsilon_0 \varepsilon' E}{d} \tag{13}$$

where ε_0 is the vacuum permittivity, ε' is the real part of the dielectric constant, E is the applied electric field, and d is the sample thickness. This parameter provides an indication of the population of mobile charges contributing to polarization. The values increase systematically with Li doping, from approximately $10^{-7}C/cm^3$ for the undoped sample to about $10^{-4}C/cm^3$ for the 3 % Li-doped sample (measured at 10 Hz). This pronounced enhancement is consistent with an increased concentration of mobile ionic carriers, further supporting the predominance of ionic conductivity in these materials [64].

3.2. Theoretical results and discussion

The sonochemical synthesis of lithium-doped sodium titanate samples enabled the identifica- tion of three distinct phases: $Na_2Ti_3O_7$, $Na_2Ti_6O_{13}$, and $NaLiTi_3O_7$. Following this identification, detailed calculations were performed for the three phases considering the energetics, structural characteristics, and electronic properties. Initially, the experimental structure was considered for the calculations, and the cell parameters and volume were calculated and found to agree with Table 2 of the manuscript. Thereafter, the structures were completely relaxed and were demonstrated to have a lower energy than those of the experimental structures. The difference in the energies per atom has been used to calculate the stability, and is given by 0.063 eV, 0.084 eV, and 0.056 eV in $Na_2Ti_3O_7$, $Na_2Ti_6O_{13}$, and $NaLiTi_3O_7$, respectively. Moreover, on Li doping, the third phase leads to the formation of Li—O, Na—Na, and Ti—Ti bonds.

The arrangement demonstrates that doping leads to the occupation of Li in place of Na in $Na_2Ti_3O_7$, leading to the phase $NaLiTi_3O_7$. Na—O bond length in $Na_2Ti_3O_7$ is 2.23 Å, whereas the Li—O bond length in $NaLiTi_3O_7$ is 1.84 Å, which could be understood based on the ionic radius of the atoms. The Na—Na bond length is 2.84 Å, and the Ti—Ti bond length varies between 2.87 Å and 2.84 Å depending on the position of the atoms. Ti—O bond length varies around 1.84 Å and 2.15 Å, similar to those of $Na_2Ti_3O_7$.

The gap values of the three phases, as well as the effective values based on the HOMO and LUMO of the three phases, were calculated following [65]. It is important to understand the individual contribution of each of the components in the Li-doped sample. The gap values of the three phases of the unrelaxed structures are 2.47 eV, 2.77 eV, and 2.24 eV for $Na_2Ti_3O_7$, $Na_2Ti_6O_{13}$, and $NaLiTi_3O_7$, respectively. However, for the relaxed structures, the respective gap values are a little higher and are given by 3.14 eV, 3.07 eV, and 2.70 eV. The effective values of the mixed systems were calculated using the highest value of HOMO and the lowest value of LUMO of the three phases. For 0 %, the effective gap value is 2.37 (2.90) eV for the unrelaxed (relaxed) structures. With the addition of Li, a decrease in the values is observed, reaching 1.92 (2.42) eV, respectively. Among the three phases, the largest gap is observed for $Na_2Ti_6O_{13}$, while the smallest is for $NaLiTi_3O_7$. Therefore, the appearance of the third phase is fundamental to the reduction of the gap in the sample. Moreover, a decrease in the gap values is evident, and thereby an increase in the electrical conductivity due to Li doping is expected.

Fig. 11 presents the total projected density of states (PDOS, black solid line) for the three phases: (a) $Na_2Ti_3O_7$, (b) $Na_2Ti_6O_{13}$, and (c) $NaLiTi_3O_7$. The atomic contributions are also exhibited, with Na in olive, Ti in blue, O in red, and Li in purple. For all plots, the valence band maximum (VBM) is taken as the reference energy. The band gap values corresponding to each phase are evident as discussed above. In the valence band of all three systems, oxygen contributions dominate, far exceeding those from other elements. However, the conduction band mainly contains contributions from the titanium atoms, with minor contributions from the oxygen atoms. Sodium contributions are evident in the valence band of $Na_2Ti_3O_7$ and $Na_2Ti_6O_{13}$, while in $NaLiTi_3O_7$, the same region shows contributions from lithium and sodium instead. Moreover, the contribution from the Na atom in $NaLiTi_3O_7$ is lower than that of Li.

It is interesting to note that the addition of lithium to the solution led to the substitution of Na by Li during the formation of $NaLiTi_3O_7$. The above substitution of Na can be understood from the smaller bond lengths of Li—O compared to those of Na—O, as can be seen above. In case of occupation of the interstitial sites, the bond lengths could be much longer as Li—O distances could be set by the cavity size rather than purely ionic size. Furthermore, the change in Löwdin charges of Na in $NaLiTi_3O_7$ relative to $Na_2Ti_3O_7$ is about 0.05 e, consistent with the substitution of Na by Li. In addition, the PDOS in Fig. 11 shows no significant Li-related features near the Fermi energy, and the Fermi level shift between $NaLiTi_3O_7$ and $Na_2Ti_3O_7$ is minimal, only 0.3 eV.

The promising results obtained here provide a solid foundation for these future analyses, reinforcing the potential of lithium-doped sodium titanate materials synthesized by sonochemistry.

4. Conclusions

The synthesis route applied in this work proved to be viable, as the main crystalline phase ($Na_2Ti_3O_7$) consistently predominated in all samples and exhibited higher purity results compared to previous studies. The emergence of a third phase in the 2 % sample suggests a saturation of lithium that was previously lodged in the interstitial sites of the $Na_2Ti_3O_7$ and $Na_2Ti_6O_{13}$ structures. The FTIR spectra demonstrated the presence of bands corresponding to Ti—O, O—Ti— O, and Na—O bond vibrations and are in agreement with the XRD results. The SEM showed a morphological pattern already reported for this material, indicating that the synthesized samples maintain the characteristic microstructural features of sodium trititanate. UV–Vis measurements showed a decrease in the band gap of the samples, also presenting a band gap value consistent with sodium trititanate, suggesting that lithium incorporation modifies the electronic environment of the Ti—O framework and may facilitate improved charge transport properties.

Complex impedance spectroscopy analyses showed that the material's electrical conductivity increased from the order of 10^{-7} S/cm in the undoped sample to the order of 10^{-5} S/cm in the 3 % lithium-doped sample. Another significant result was the increase in charge density with the addition of lithium, along with an increase in permittivity and a

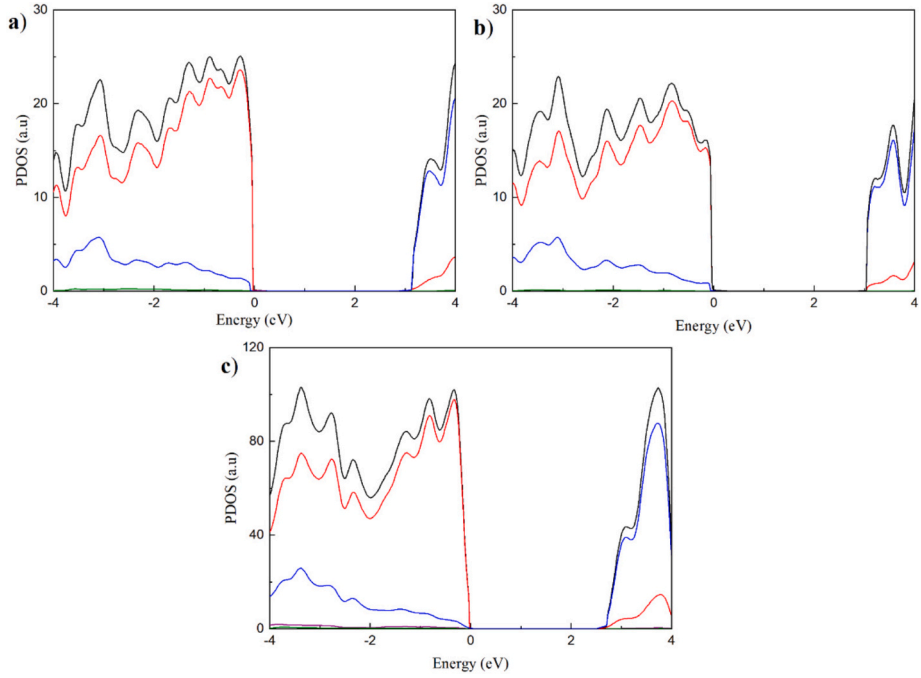


Fig. 11. The total projected density of states (PDOS) of the three phases (a) $Na_2Ti_3O_7$, (b) $Na_2Ti_6O_{13}$, and (c) $NaLiTi_3O_7$. The individual atomic PDOS are also displayed, with contributions from Na (olive), Ti (blue), O (red), and Li (purple). (For interpretation of the references to colour in this figure legend, the reader is referred to the web version of this article.)

decrease in relaxation time, which suggests an increase in electrical conductivity. Experimental evidence and literature reports indicate that ionic conductivity predominates in the samples, suggesting it is the primary transport mechanism. Nevertheless, the use of blocking electrodes in future studies could improve the analysis regarding the predominant type of conductivity.

The theoretical analysis using DFT showed agreement with the structural analyses performed through X-ray diffraction. Furthermore, the calculated band gap values showed a decreasing trend with the addition of lithium, consistent with the values determined from UV–Vis measurements. In summary, all these results suggest an improvement in the electrical properties of the material, making it promising for use in energy storage applications.

CRediT authorship contribution statement

Jardson Braz da Silva: Writing – original draft, Methodology, Investigation, Formal analysis, Conceptualization. **Juliana Pereira da Silva:** Writing – original draft, Methodology, Formal analysis. **Rodrigo Lavareda dos Santos:** Methodology, Investigation, Formal analysis. **Salomão dos Santos Costa:** Validation, Methodology, Formal analysis. **Francisco Xavier Nobre:** Writing – original draft, Methodology, Formal analysis. **Monica Tirado:** Writing – review & editing, Supervision, Methodology. **Angsula Ghosh:** Writing – review & editing, Supervision, Software, Formal analysis. **Lianet Aguilera Domínguez:** Writing – review & editing, Methodology, Formal analysis, Conceptualization. **Yurimiler Leyet Ruiz:** Writing – review & editing, Supervision, Methodology, Conceptualization.

Declaration of competing interest

The authors declare that they have no known competing financial interests or personal relationships that could have appeared to influence the work reported in this paper.

Acknowledgements

This study was financed in part by the “Coordenac¸ão de Aperfeic¸oamento de Pessoal de Nível Superior - Brasil (CAPES)” - Finance Code 001.The authors would like to thank “Fundac¸ão de Amparo à Pesquisa do Estado do Amazonas”, “Conselho Nacional de Desenvolvimento Científico e Tecnológico”and “Financiadora de Estudos e Projetos” for their financial support.

Data availability

Data will be made available on request.

References

[1] P. Kurzweil, Gaston Plate and his invention of the lead–acid battery—the genesis of the first practical rechargeable battery, J. Power Sources 195 (14) (2010) 4424–4434.
[2] H. Sun, S. Kang, L. Cui, Prospects of LLZO type solid electrolyte: from material design to battery application, Chem. Eng. J. 454 (2023) 140375.
[3] Z. Xu, X. Hu, B. Fu, K. Khan, J. Wu, T. Li, H. Zhou, Z. Fang, M. Wu, Co-doping strategy enhanced the ionic conductivity and excellent lithium stability of garnet-type $Li_7La_3Zr_2O_{12}$ electrolyte in all solid-state lithium batteries, J. Mater. 9 (4) (2023) 651–660.
[4] H.K. Tran, B.T. Truong, B.-R. Zhang, R. Jose, J.-K. Chang, C.-C. Yang, Sandwich-structured composite polymer electrolyte based on PVDF-HFP/PPC/Al-doped LLZO for high-voltage solid-state lithium batteries, ACS Appl Energy Mater 6 (3) (2023) 1475–1487.
[5] Y.-S. Choi, S.I. Costa, N. Tapia-Ruiz, D.O. Scanlon, Intrinsic defects and their role in the phase transition of Na-ion anode $Na_2Ti_3O_7$, ACS Appl Energy Mater 6 (1) (2022) 484–495.
[6] F. Chen, H. Li, X. Qiao, R. Wang, C. Hu, T. Chen, Y. Niu, B. Zhong, Z. Wu, X. Guo, The chance of sodium titanate anode for the practical sodium-ion batteries, Chin. J. Chem. Eng. 72 (2024) 226–244.
[7] A. Melo, J. da Silva, F. Nobre, S. Costa, J. Sales Jr., J. Anglada-Rivera, F. Guerrero, M. da S. Paula, R. de Souza, R. Pena-Garcia, et al., Synthesis microwave-assisted: fast method to obtain lithium-doped sodium titanate, J. Mater. Sci. Mater. Electron. 34 (6) (2023) 537.
[8] J. da Silva, S. Costa, F. Nobre, E. Sanches, M.d.S. Paula, L. Aguilera, M. Torikachvili, Y. Leyet, Poly (o-methoxyaniline) modified by the biphasic ceramic system $Na_2Ti_3O_7/Na_2Ti_6O_{13}$, J. Inorg. Organomet. Polym. Mater. 33 (5) (2023) 1381–1387.

[9] K. Eggestad, S.M. Selbach, B.A. Williamson, Doping implications of li solid state electrolyte $Li_7La_3Zr_2O_{12}$, J Mater Chem A 12 (26) (2024) 15666–15675.

[10] L.J. Miara, S.P. Ong, Y. Mo, W.D. Richards, Y. Park, J.-M. Lee, H.S. Lee, G. Ceder, Effect of Rb and Ta doping on the ionic conductivity and stability of the garnet $Li_7(La_{3-x}Rb_x)(Zr_{2-y}Ta_y)o_{12}$ ($0 \leq x \leq 0.375$, $0 \leq y \leq 1$) superionic conductor: A first principles investigation, Chem. Mater. 25 (15) (2013) 3048–3055.

[11] F.A. Altayaran, The Effects of Doping on the lithium Ionic Conductivity of LLZO Solid-State Electrolyte, Master's thesis,, North Dakota State University, 2020.

[12] Y. Leyet, F. Guerrero, J. Anglada-Rivera, R. De Souza, W. Brito, L. Aguilera, L. Pocrifka, R. Pena-Garcia, E. Padrón-Hernández, J. De La Cruz Pe'rez, Synthesis of $Na_2Ti_3O_7$ nanoparticles by sonochemical method for solid state electrolyte applications, J. Solid State Electrochem. 22 (2018) 1315–1319.

[13] J. Da Silva, M. Biondo, F. Nobre, J. Anglada-Rivera, A. Almeida, J. Agostinho-Moreira, E. Sanches, M.d.S. Paula, L. Aguilera, Y. Leyet, Structure and electrical properties of the composite $Na_2Ti_3O_7/Na_2Ti_6O_{13}$/poma: a study of the effect of adding poma, J. Alloys Compd. 867 (2021) 159025.

[14] I.N.D. Yahya, N. Sofyan, D.S. Khaerudini, G.E. Timuda, S. Priyono, Characteristics of sodium lithium titanate synthesized at different solid-state reaction temperature for lithium-ion battery anode, J. Mater. Explor. Find. 2 (3) (2023) 3.

[15] P. Wang, P. Li, T.-F. Yi, X. Lin, Y.-R. Zhu, L. Shao, M. Shui, N. Long, J. Shu, Improved lithium storage performance of lithium sodium titanate anode by titanium site substitution with aluminum, J. Power Sources 293 (2015) 33–41.

[16] G. Matyszczak, K. Krawczyk, A. Yedzikhanau, K. Głuc, M. Szymajda, A. Sobiech, Z. Gackowska, Sonochemical synthesis of low-dimensional nanostructures and their applications—a review, Materials 17 (22) (2024) 5488.

[17] Q.T. Trinh, N. Golio, Y. Cheng, H. Cha, K.U. Tai, L. Ouyang, J. Zhao, T.S. Tran, T.-K. Nguyen, J. Zhang, et al., Sonochemistry and sonocatalysis: current progress, existing limitations, and future opportunities in green and sustainable chemistry, Green Chem. 27 (2025) 4926–4958.

[18] P. Giannozzi, S. Baroni, N. Bonini, M. Calandra, R. Car, C. Cavazzoni, D. Ceresoli, G.L. Chiarotti, M. Cococcioni, I. Dabo, et al., Quantum espresso: a modular and open-source software project for quantum simulations of materials, J. Phys. Condens. Matter 21 (39) (2009) 395502.

[19] M.C. Payne, M.P. Teter, D.C. Allan, T. Arias, a.J. Joannopoulos, Iterative minimization techniques for ab initio total-energy calculations: molecular dynamics and conjugate gradients, Rev. Mod. Phys. 64 (4) (1992) 1045.

[20] H.J. Monkhorst, J.D. Pack, Special points for brillouin-zone integrations, Phys. Rev. B 13 (12) (1976) 5188.

[21] A. Kokalj, Computer graphics and graphical user interfaces as tools in simulations of matter at the atomic scale, Comput. Mater. Sci. 28 (2) (2003) 155–168.

[22] X. Ma, Y. Liu, Y. Zhang, Y. Gong, Layered sodium titanate with a matched lattice: a single ion conductor in a solid-state sodium metal battery, Chem. Sci. 14 (47) (2023) 13812–13824.

[23] H. Zhong, F. Pan, S. Yue, C. Qin, V. Hadjiev, F. Tian, X. Liu, F. Lin, Z. Wang, J. Bao, Idealizing tauc plot for accurate bandgap determination of semiconductor with ultraviolet–visible spectroscopy: a case study for cubic boron arsenide, J. Phys. Chem. Lett. 14 (29) (2023) 6702–6708.

[24] R. Zárate, S. Fuentes, A. Cabrera, V. Fuenzalida, Structural characterization of single crystals of sodium titanate nanowires prepared by hydrothermal process, J. Cryst. Growth 310 (15) (2008) 3630–3637.

[25] S. Ghosh, Sonochemically synthesized $Na_2Ti_6O_{13}$ nanorod: an efficient electrode material for na-ion battery, Bull. Mater. Sci. 43 (1) (2020) 251.

[26] L. Basilio, J. Silva, F. Xavier, L. Aguilera, F. Guerrero, E. Antonelli, J. Anglada-Rivera, J. Garcia, R. Silva, Y. Leyet, Toward a new ptcr material based on the $Na_2Ti_6O_{13}/Na_2Ti_3O_7$ system, Mater. Res. Bull. 140 (2021) 111311.

[27] S. Chaar, J. Da Silva, F. Nobre, J. Passos, L. Aguilera, J. Silva, R. Silva, F. Guerrero, F. Pontes, Y. Leyet, Sonochemical synthesis and characterization of the biphasic compound $Na_2Ti_3O_7/Na_2Ti_6O_{13}$, Mater. Res. 24 (Suppl. 1) (2021) e20210011.

[28] L. Basilio, F. Xavier, J. Sales Jr., J. Andrade, J. Anglada-Rivera, L. Aguilera, R. Silva, J. Rodriguez-Hernandez, J.P. de la Cruz, Y. Leyet, Fast synthesis of $Na_2Ti_3O_7$ system synthesized by microwave-assisted hydrothermal method: electrical properties, Ceram. Int. 46 (15) (2020) 23834–23839.

[29] W. Zhao, Y. Zhu, Q. Yan, Z. Yang, Q. Zhang, Synthesis and electrochemical performance of defected nano-micro structure sodium/lithium titanate composites materials for lithium-ion batteries, Vacuum 177 (2020) 109402.

[30] P. Kumari, Y. Li, R. Boston, An ionic liquid synthesis route for mixed-phase sodium titanate ($Na_2Ti_3O_7$ and $Na_2Ti_6O_{13}$) rods as an anode for sodium-ion batteries, Nanoscale 15 (28) (2023) 12087–12094.

[31] C.D. de Abreu Lima, R. dos Santos Sousa, A.W. Miranda, J.V.B. Moura, G. de Sousa Pinheiro, B.C. Viana, I.S. Lima, T.M.B.F. Oliveira, O. Baffa, J.F.D.F. Araujo, et al., Synthesis, characterization, and thermal stability study of sodium and sodium–aluminum titanate nanotubes, Solid State Sci. 138 (2023) 107134.

[32] S. Ali, H. Granbohm, Y. Ge, V.K. Singh, F. Nilsén, S.-P. Hannula, Crystal structure and photocatalytic properties of titanate nanotubes prepared by chemical processing and subsequent annealing, J. Mater. Sci. 51 (2016) 7322–7335.

[33] B.C. Viana, O.P. Ferreira, A.G. Souza Filho, A.A. Hidalgo, J. Mendes Filho, O. L. Alves, Alkali metal intercalated titanate nanotubes: a vibrational spectroscopy study, Vib. Spectrosc. 55 (2) (2011) 183–187.

[34] M. Shirpour, J. Cabana, M. Doeff, New materials based on a layered sodium titanate for dual electrochemical na and li intercalation systems, Energy Environ. Sci. 6 (8) (2013) 2538–2547.

[35] F.L.R. Silva, A.A.A. Filho, M.B. Silva, K. Balzuweit, J.-L. Bantignies, E.W. S. Caetano, R.L. Moreira, V.N. Freire, A. Righi, Polarized raman, ftir, and dft study of $Na_2Ti_3O_7$ microcrystals, J. Raman Spectrosc. 49 (3) (2018) 538–548.

[36] P.R. Griffiths, Fourier transform infrared spectrometry, Science 222 (4621) (1983) 297–302.

[37] T. Putjuso, S. Putjuso, A. Karaphun, E. Swatsitang, Influence of li concentration on structural, morphological and electrochemical properties of anatase-tio2 nanoparticles, Sci. Rep. 14 (1) (2024) 11200.

[38] P.W. Atkins, R.S. Friedman, Molecular Quantum Mechanics, Oxford University Press, 2011.

[39] R.M. Badger, A relation between internuclear distances and bond force constants, J. Chem. Phys. 2 (3) (1934) 128–131.

[40] J. Cioslowski, G. Liu, R.A.M. Castro, Badger's rule revisited, Chem. Phys. Lett. 331 (5–6) (2000) 497–501.

[41] E. Kurita, H. Matsuura, K. Ohno, Relationship between force constants and bond lengths for cx (x= c, si, ge, n, p, as, o, s, se, f, cl and br) single and multiple bonds: formulation of badger's rule for universal use, Spectrochim. Acta A Mol. Biomol. Spectrosc. 60 (13) (2004) 3013–3023.

[42] A.H. Larsen, J.J. Mortensen, J. Blomqvist, I.E. Castelli, R. Christensen, M. Dułak, J. Friis, M.N. Groves, B. Hammer, C. Hargus, et al., The atomic simulation environment—a python library for working with atoms, J. Phys. Condens. Matter 29 (27) (2017) 273002.

[43] P.R. Jubu, O. Obaseki, D. Ajayi, E. Danladi, K.M. Chahrour, A. Muhammad, S. Landi Jr., T. Igbawua, H. Chahul, F. Yam, Considerations about the determination of optical bandgap from diffuse reflectance spectroscopy using the tauc plot, J. Opt. 53 (5) (2024) 5054–5064.

[44] A.K. Mishra, S. Sau, Y. Patel, N. Shaikh, H. Odedra, B. Vagadiya, A. Ray, S. Mitra, I. Mukhopadhyay, Stabilization of cubic $Li_7La_3Zr_2O_{12}$ phase solid electrolyte by gallium doping and its effect on structural and energy storage properties, J Energy Storage 121 (2025) 116537.

[45] M.B. Pramanik, M.A. Al Rakib, M.A. Siddik, S. Bhuiyan, Doping effects and relationship between energy band gaps, impact of ionization coefficient and light absorption coefficient in semiconductors, European, J. Eng. Technol. Res. 9 (1) (2024) 10–15.

[46] L. Yesappa, M. Niranjana, S. Ashokkumar, H. Vijeth, M. Basappa, P. VC, S. Ganesh, H. Devendrappa, et al., Optical properties and ionic conductivity studies of an 8 mev electron beam irradiated poly (vinylidene fluoride- co-hexafluoropropylene)/ liclo 4 electrolyte film for opto-electronic applications, RSC Adv. 8 (28) (2018) 15297–15309.

[47] N.H. Gaukås, T.O. Sunde, B. Arstad, A.H. Reksten, E. Stefan, A. Thøgersen, M. K. Pedersen, T. Norby, Y. Larring, Effects of different doping strategies on cubic $Li_7La_3Zr_2O_{12}$ solid-state li-ion battery electrolytes, ACS Appl Energy Mater 7 (24) (2024) 12141–12154.

[48] M.Y. Shah, Y. Lu, N. Mushtaq, M. Yousaf, M. Akbar, S. Rauf, Y. Dong, P.D. Lund, B. Zhu, M.I. Asghar, Enabling high ionic conductivity in semiconductor electrolyte membrane by surface engineering and band alignment for lt-cfcs, J. Membr. Sci. 668 (2023) 121264.

[49] S. Dos Santos Costa, J. Pereira da Silva, M. Moraes Biondo, E.A. Sanches, M.M. Da Silva Paula, F. Xavier Nobre, J. Anglada Rivera, Y. Alexis Zulueta, M. S. Torikachvili, D. Vieira Sampaio, et al., Temperature dependence of the electrical properties of $Na_2Ti_3O_7/Na_2Ti_6O_{13}$/poma composites, Molecules 27 (18) (2022) 5756.

[50] P. Braun, C. Uhlmann, A. Weber, H. Störmer, D. Gerthsen, E. Ivers-Tiffée, Separation of the bulk and grain boundary contributions to the total conductivity of solid lithium-ion conducting electrolytes, J. Electroceram. 38 (2017) 157–167.

[51] R.K. Hona, G.S. Dhaliwal, R. Thapa, Investigation of grain, grain boundary, and interface contributions on the impedance of Ca_2FeO_5, Appl. Sci. 12 (6) (2022) 2930.

[52] C. Uhlmann, P. Braun, J. Illig, A. Weber, E. Ivers-Tiffe'e, Interface and grain boundary resistance of a lithium lanthanum titanate ($Li_{3x}La_{2/3-x}TiO_3$, LLTO) solid electrolyte, J. Power Sources 307 (2016) 578–586.

[53] D.M. Babiker, Z.R. Usha, C. Wan, M.M.E. Hassaan, X. Chen, L. Li, Recent progress of composite polyethylene separators for lithium/sodium batteries, J. Power Sources 564 (2023) 232853.

[54] A. Tsyganov, N. Morozova, M. Vikulova, A. Asmolova, D. Artyukhov, I. Zotov, A. Gorokhovsky, N. Gorshkov, The effect of lithium doping on the dielectric properties of solid solutions $Li_xCa_{(1-x)}Cu_3Ti_4O_{12}$ (x= 0.01–0.1), J. Compos. Sci. 7 (7) (2023) 282.

[55] S. Aydi, S. Chkoundali, A. Oueslati, A. Aydi, Effect of lithium doping on the structural, conduction mechanism and dielectric property of $MnNbO_4$, RSC Adv. 13 (29) (2023) 20093–20104.

[56] M. Xue, W. Lu, S. Xue, C. Zhang, Enhanced al/ta co-doped $Li_7La_3Zr_2O_{12}$ ceramic electrolytes with the reduced ta doping level for solid-state lithium batteries, J. Mater. Sci. 56 (2021) 19614–19622.

[57] R.A. Talewar, S. Mahamuda, A. Rao, S. Moharil, Novel Mn^{4+} −activated $NaLiTi_3O_7$ far-red emitting phosphors, JOL 255 (2023) 119591.

[58] D. Li, D. Yang, L. Li, L. Wang, K. Wang, Electrochemical impedance spectroscopy based on the state of health estimation for lithium-ion batteries, Energies 15 (18) (2022) 6665.

[59] E. Barsoukov, J.R. Macdonald, Impedance Spectroscopy: Theory, Experiment, and Applications, second ed., John Wiley & Sons, Inc., Hoboken, NJ, 2005.

[60] M.A. Dar, I.A. Alnaser, D.-W. Kim, Progress in sodium-ion batteries: a focus on phosphate-based cathodes and their interaction with electrolytes, Int. J. Energy Res. 2024 (1) (2024) 9198966.

[61] J. Pan, N. Wang, D. Lv, W. Dong, J. Yang, F. Huang, Layered structure $Na_2Ti_3O_7$ as a promising anode material for sodium-ion batteries, Adv. Energy Sustain. Res. 2 (6) (2021) 2000095.

[62] M. Dynarowska, J. Kotwin'ski, M. Leszczynska, M. Marzantowicz, F. Krok, Ionic conductivity and structural properties of $Na_2Ti_3O_7$ anode material, Solid State Ionics 301 (2017) 35–42.

[63] B. Pu, Z. Zou, J. Liu, B. He, D. Chen, D. Wang, Y. Liu, M. Avdeev, S. Shi, Direct calculation of effective mobile ion concentration in lithium superionic conductors, npj Comput. Mater. 11 (1) (2025) 37.
[64] Y. Li, S. Guo, Z. Cao, J. Liu, L. Wang, G. Li, High ionic conductivity and critical current density of $Li_{7-x}La_{2.95}Yb_{0.05}Zr_{2-x}Ta_xO_{12}$ solid electrolyte by modulation of Li^+ distribution, J. Eur. Ceram. Soc. 44 (3) (2024) 1665–1677.
[65] S.I. Costa, Y.-S. Choi, A.J. Fielding, A.J. Naylor, J.M. Griffin, Z. Sofer, D.O. Scanlon, N. Tapia-Ruiz, Surface engineering strategy using urea to improve the rate performance of $Na_2Ti_3O_7$ in na-ion batteries, chemistry–a, Eur. J. Dermatol. 27 (11) (2021) 3875–3886.

ANNEX B – PUBLISHED ARTICLE — NLTO: LITHIUM DOPING AND ORGANIC-PHASE EFFECTS

This annex presents the published article reporting the investigation of the synergistic effects of lithium doping and retained organic phases on the structural, electrical, and dielectric properties of sodium titanate.

Solid State Sciences 168 (2025) 108036

Contents lists available at ScienceDirect

Solid State Sciences

journal homepage: www.elsevier.com/locate/ssscie

Synergistic effects of lithium doping and organic phases on the electrical and dielectric properties of sodium titanate solid-state electrolytes

Jardson Braz da Silva [a,b], Juliana Pereira da Silva [b], Rodrigo Lavareda dos Santos [b], Salomão dos Santos Costa [a,b], Yan Matheus Colares Pinto [a,b], Marcos Vinicius Passos Colares [b], Ruan Carlos Ambrosio Raposo [b], Francisco Xavier Nobre [c], Monica Tirado [d], Angsula Ghosh [a], Lianet Aguilera Domínguez [b], Ramo'n Raudel Peña Garcia [e], Yurimiler Leyet Ruiz [b,*]

[a] Departamento de Física de Materiais, Universidade Federal do Amazonas (UFAM), Manaus, AM, Brazil
[b] Laboratório de Processamento de Materiais Tecnológicos, Departamento de Engenharia de Materiais, Universidade Federal do Amazonas (UFAM), Manaus, AM, Brazil
[c] Instituto Federal de Educação, Ciência e Tecnologia do Amazonas, Manaus, AM, 69020-120, Brazil
[d] Universidad Nacional de Tucumán (UNT), Facultad de Ciencias Exactas y Tecnología (FACET) and Instituto de Física del Noroeste Argentino: INFINOA (UNT-CONICET), Avenida Independencia 1800, 4000, Tucumán, Argentina
[e] Universidade Federal Rural de Pernambuco, Unidade Acadêmica do Cabo de Santo Agostinho, Cabo de Santo Agostinho, PE, Brazil

ARTICLE INFO

Keywords:
Sodium titanate
Lithium doping
Organic phases
Solid-state electrolyte
Ionic conduction

ABSTRACT

Energy storage technologies have attracted widespread attention due to the growing global demand. In this context, we present a detailed study of the structural, electrical, and dielectric properties of sodium titanate samples, with $Na_2Ti_3O_7$ as the predominant crystalline phase and $Na_2Ti_6O_{13}$ as the secondary phase, following lithium addition. Additionally, the synthesis route also produced samples capable of retaining organic phases, derived from the solvents used, even after thermal treatment at 900 °C. The above materials were characterized using X-ray diffraction (XRD) with Rietveld refinement, scanning electron microscopy (SEM), Fourier transform infrared spectroscopy (FTIR), complex impedance spectroscopy, distribution of relaxation times analysis (DRT), and density-functional calculations. In samples with retained organic phases, the presence of $C_{20}H_{10}O_2$ was observed in the sample without lithium addition, whereas, lithium hydrogen maleate ($C_4H_7LiO_6$) and $C_{20}H_{10}O_2$ were detected in the sample on lithium addition. Density functional analysis was performed to obtain detailed information on the various phases. Moreover, the gap values of the phases demonstrated an increase in conductivity due to the presence of the organic phases. Scanning electron microscopy revealed a morphology already known for sodium titanate. It is characterized by uniform rod-like structures, with particle sizes ranging between 1 μm and 2 μm in samples without organic phases. In contrast, samples with organic phases exhibited a distinct morphology, with low uniformity and significant variations in particle sizes. FTIR spectroscopy revealed the predominance of bands below 920 cm^{-1}, characteristic of Ti – O, Ti – O – Ti, and Na – O bonds. Furthermore, complex impedance spectroscopy revealed a two- order-of-magnitude increase in conductivity for the 1 % lithium sample containing organic phases, compared to the pure ceramic sodium titanate sample. Dielectric analysis reveals a synergistic effect between lithium incorporation and organic phase retention, leading to enhanced energy storage capacity. Distribution of relaxation times (DRT) analysis shows strong agreement with the equivalent circuit models obtained via ZView software from the complex impedance data. The above results confirm the feasibility of the use of sodium titanate in solid-state electrolytes.

1. Introduction

The flammability, volatility, chemical instability, and explosion risk associated with the liquid electrolyte used in commercial lithium-ion batteries [1] have stimulated intensive research into the development of solid-state electrolytes. In addition, solid-state electrolytes — both inorganic and polymeric — demonstrate high electrochemical stability and enable high energy density [2]. In this context, titanates have

* Corresponding author.
E-mail address: yurileyet@gmail.com (Y. Leyet Ruiz).

https://doi.org/10.1016/j.solidstatesciences.2025.108036
Received 22 June 2025; Received in revised form 25 July 2025; Accepted 27 July 2025
Available online 31 July 2025
1293-2558/© 2025 Elsevier Masson SAS. All rights are reserved, including those for text and data mining, AI training, and similar technologies.

attracted significant attention in the literature due to their versatile structural, electrical, and optical properties. The term titanate refers to a family of compounds composed of titanium and oxygen-based structures, which can exhibit various structural arrangements, including spinel, layered, and tunnel-type frameworks. These structural variations are crucial for tuning the functional properties of solid-state devices, including ionic mobility, electrochemical stability, and interfacial behavior. Recent studies have investigated lithium titanate compounds [3,4] demonstrating their promising characteristics for optoelectronic and electrochemical applications. Sodium titanates, $Na_2Ti_nO_{2n+1}$, have also been of considerable interest due to their potential use as solid-state electrolytes. In these compounds, sodium ions occupy distinct structural sites depending on the phase: in $Na_2Ti_3O_7$, Na^+ ions are located between the TiO_6 octahedra layers (lamellar structure), whereas in $Na_2Ti_6O_{13}$, they reside within the tunnels formed by interconnected TiO_6 octahedras (tunnel structure).

Titanium- and sodium-based materials are naturally abundant, leading to lower costs for devices that incorporate sodium titanates. Moreover, these materials exhibit low toxicity, which enhances their economical and ecological viability [5]. However, Na^+ ions tend to exhibit lower ionic conductivity compared to Li^+ ions due to their lower diffusivity. The above characteristics are attributed to the difference in their ionic radii (approximately 102 p.m. for Na^+ and 76 p.m. for Li^+) [6]. In addition, sodium titanate presents sluggish ion deintercalation kinetics and interfacial instability, resulting in inferior cycling stability [7]. It also shows low initial Coulombic efficiency and poor performance at high charge/discharge rates [7]. Hence, to overcome these limitations, researchers have doped sodium trititanate with conductive elements such as Nb^{5+}, F^-, and Li^+ [5]. The electrical conductivity of $Na_2Ti_3O_7$ and $Na_2Ti_6O_{13}$ have been reported to be of the order of 1.0×10^{-6} S cm^{-1} [8]. Additionally, doping these compounds with Li^+ tends to increase their conductivity by at least one order of magnitude [6]. In addition to doping strategies, several studies have analyzed these materials in composite systems incorporating organic materials, particularly polymeric materials [8–10].

In this study, we propose the use of the sonochemical method to synthesize pure sodium titanate, as well as its lithium-doped variant (Li = 1 %) named as the NTO and NLTO-1 samples, respectively. Additionally, two more samples with the same lithium concentrations were synthesized, retaining the organic phases, referred to as NTO/Org and NLTO-1/Org, respectively. Furthermore, a comprehensive structural and electrical characterization were performed. The key feature in the present study lies in the use of a sonochemical synthesis approach, where, instead of forming a composite with defined proportions, the drying temperature is adjusted to enable the encapsulation of the organic material originating from precursors and isopropyl alcohol as the solvent, thereby preserving it even after thermal treatment at 900 °C. Thus, the objective of this study is to analyze the synergistic effects of lithium doping and organic phase retention, which emerge during the synthesis process, on enhancing the electrical and dielectric properties for solid-state electrolytes applications.

2. Experimental methods

2.1. Synthesis and characterization

The pure (NTO) and lithium-doped samples (NLTO-1) were synthesized following the methodology described in the works of [6,11]. Titanium isopropoxide ($C_{12}H_{28}O_4Ti$) (Aldrich, > 97 %) was diluted in isopropyl alcohol and mixed with sodium hydroxide, NaOH (Synth, 98 %), previously dissolved in distilled water at a molar concentration of 1 M. Magnetic stirring was performed until complete homogenization was reached.

Subsequently, the mixture was subjected to sonication at a fixed frequency of 40 kHz for 15 min, with a power of 487.5 W (65 % of the nominal output), resulting in a power density of 14.17 W mL^{-1}, for the mixture volume of approximately 34.4 mL. Thereby, the samples were dried in an oven for 24 h at 100 °C. The thermal treatment of the resulting powder was carried out at 900 °C for 1 h. The synthesis was carried out using the following proportion given by eq. (1):

$$2\,NaOH + 3\,C_{12}H_{28}O_4Ti \rightarrow Na_2Ti_3O_7 + 3\,C_{12}H_{28}O_2 + H_2O \quad (1)$$

The lithium-doped sodium titanate samples, in turn, were prepared following the exact stoichiometry as the pure sample, but with partial substitution of sodium by lithium, leading to the formation of $Na_{2-x}Li_xTi_3O_7$. The lithium source used was lithium acetate dihydrate ($C_2H_3LiO_2 \cdot {}_2H_2O$, Sigma-Aldrich, 97 %). Here, x represents the lithium concentration (0.01) for lithium doped samples.

Moreover, to produce pure sodium titanate samples in the presence of an organic phase (NTO/Org), as well as samples doped with 1 % lithium in the presence of an organic phase (NLTO- 1/Org), all the above steps were repeated with a single modification. After the sonication process, the samples were dried in an oven at 60 °C.

X-ray diffraction (XRD) measurements were performed using a Panalytical Empyrean diffractometer equipped with copper (Cu) and molybdenum (Mo) radiation sources, operated in Bragg-Brentano geometry. The instrument was configured with Cu K_α radiation (λ = 1.5406 Å). Data were collected over a 2θ range of 5° to 80°. The Rietveld refinement was carried out using the GSAS-II software.

The scanning electron microscopy (SEM) measurements were performed using a JEOL JSM IT500 HR microscope equipped with a Secondary Electron Detector (SED). For the NTO and NLTO-1 samples, the acceleration voltage was set at 5 kV, the working distance (WD) was between 3.6 and 3.7 mm, the magnification was 7000 × , and the scale bar was 2 μm. For the NTO/Org and NLTO-1/Org samples, the acceleration voltage was set at 5 kV, while the working distance (WD) was between 4.69 and 4.70 mm. The magnification was 1500 × , and the scale bar was 2 μm.

The FTIR measurements were performed using a Fourier Transform Infrared Spectrometer (Cary 630, Agilent Technologies, USA). The scans were performed over a spectral range of 4000 to 650 cm^{-1} using Attenuated Total Reflectance (ATR) with a zinc selenide (ZnSe) crystal by horizontally positioning the sample close to a prism (d = 1.8 mm).

The complex impedance spectroscopy measurements were performed using a Solartron 1260 impedance analyzer, operating at an amplitude of 500 mV at room temperature over a frequency range of 10 Hz to 1 MHz. A Solartron 12962A sample holder was employed, featuring two parallel plate stainless steel blocking electrodes—one fixed and the other adjustable to accommodate sample thickness—while applying slight mechanical pressure to ensure good electrical contact. A micrometer integrated into the holder was used to determine the sample thickness during measurement accurately. The pellets were painted on both sides by conductive silver paint. The samples consisted of pellets with a diameter of 10 mm and thicknesses of 1.39 mm (NTO), 1.41 mm (NLTO-1), 1.69 mm (NTO/Org), and 1.77 mm (NLTO-1/Org), sintered at 900 °C for an hour. Due to experimental limitations, it was not possible to separately analyze the ionic and electronic contributions to conductivity.

The relaxation time distribution analysis was performed based on the complex impedance data. The method was implemented using Tikhonov regularization, which relies on the numerical inversion of the relationship between complex impedance and the relaxation time distribution function through the Ridge regression technique. The experimental data were processed in Python using the NumPy, Pandas, Matplotlib, and Scikit-learn libraries. Regularization allowed for signal smoothing and noise reduction.

The model was adjusted by separating the real and imaginary contributions to facilitate the analysis of resistive and capacitive processes. Peaks were identified using the find peaks method (SciPy), and associated relaxation times were compared with the equivalent circuits modeled in ZView.

2.2. Calculation details

To gain a deeper insight into the features observed during lithium addition and the presence of organic phases formed during synthesis, first-principles calculations based on density functional theory (DFT) were performed using the Quantum ESPRESSO package [12] to investigate the four phases obtained in this study under Li doping. The NTO and NLTO-1 samples exhibited the formation of two phases: $Na_2Ti_3O_7$ and $Na_2Ti_6O_{13}$. In contrast, the NTO/Org and NLTO- 1/Org samples, which retained organic phases, contained the above two inorganic phases along with organic compounds identified as $C_{20}H_{10}O_2$ and $C_4H_7LiO_6$. Notably, the latter organic phase, $C_4H_7LiO_6$, was observed exclusively in the NLTO-1/Org sample. The structures of all the above phases were obtained from experimental data and imported via crystallographic information files (CIF files). Ultrasoft pseudopotentials were employed in conjunction with the generalized gradient approximation (GGA) using the Perdew-Burke-Ernzerhof (PBE) exchange-correlation functional [13]. The convergence was performed with a kinetic energy cut-off of 0.4 keV and a charge-density cut-off of 4 keV for the inorganic phases, whereas the above cut-offs for the organic phases are given by 1.4 keV and 14 keV. Brillouin-zone sampling of the supercells was performed using a Monkhorst-Pack k-point grid mesh [14]. The k-point sampling and the number of atoms in the cell for the inorganic phases are given as follows Na_2Ti_3O7 - 4 × 8 × 4 (24 atoms), $Na_2Ti_6O_{13}$ - 8 × 8 × 8 (21 atoms), whereas those for organic phases are given as follows: $C_{20}H_{10}O_2$ - 12 × 12 × 8 (64 atoms) and $C_4H_7LiO_6$ - 8 × 8 × 8 (72 atoms). The structural and electronic properties of the four phases were calculated using structures obtained from the crystallographic information files and also with the geometries of all the systems, which were completely relaxed without any constraint. The convergence thresholds were considered to be 10^{-3} eV/Å for the total force and 10^{-4} eV for the total energy. The total projected density of states, along with the contributions of the constituent atoms, was calculated. The graphic representation of the cells was performed using Xcrysden [15] and VESTA [16].

3. Results and discussion

3.1. Structural and electronic characterization

Fig. 1 displays the X-ray diffraction patterns of all the samples. The black curve corresponds to NTO, the red curve to NLTO-1, the blue curve to NTO/Org, and the dark olive-green curve to NLTO-1/Org.

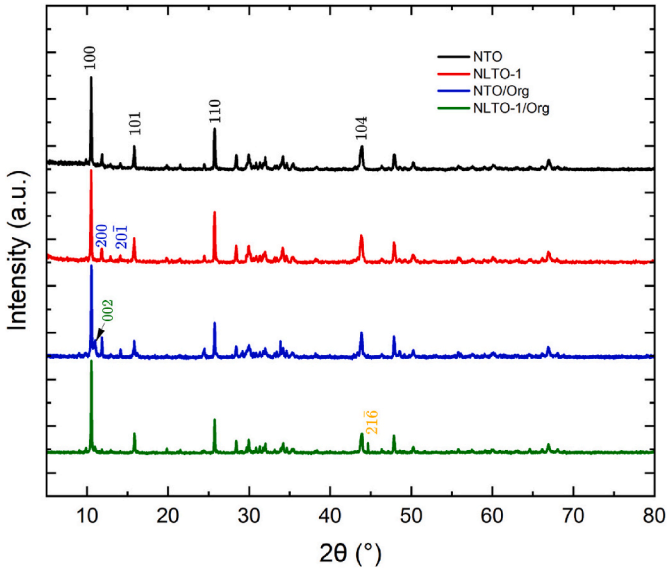


Fig. 1. X-ray Diffraction (XRD) patterns of all powder samples.

The most intense peak, which is also the first peak, occurs around 10.5° and indicates the predominance of the crystalline phase of $Na_2Ti_3O_7$ in all the samples, associated with the (100) plane [17–19]. The (200) and (201) planes, highlighted in the red curve, correspond to the $Na_2Ti_6O_{13}$ crystalline phase [19–21]. These peaks are present in all the samples, indicating their occurrence as a secondary phase, as also observed in other related works in the literature [11,22–24]. However, corresponding to NLTO-1/Org (green curve), these peaks appear to be less prominent. This finding is consistent with the data in Table 1, which indicates that this sample exhibits a lower concentration of this phase and a higher one of the primary phase, $Na_2Ti_3O_7$.

The Miller index (002), at approximately 10.9° in 2θ, corresponds to the organic phase $C_{20}H_{10}O_2$, which is likely a remnant of the precursors and the solvent used to dissolve titanium isopropoxide, isopropyl alcohol. This phase remained in the sample despite its treatment at a temperature of 900 °C. This phenomenon is most likely caused due to the encapsulation effet induced by the ceramic material. For the green curve of Fig. 1, the Miller index (216), corresponding to the organic compound $C_4H_7LiO_6$, is highlighted. This material is likely formed due to the incorporation of lithium into the residual organic phase.

Fig. 2 presents the Rietveld refinement plots of all the samples. The analysis revealed the existence of two monoclinic phases of the NTO sample. The lattice parameters of sodium trititanate, $Na_2Ti_3O_7$, with space group $P2_1/m$ (ICSD 15463), are $a = 8.575$ Å, $b = 3.796$ Å, $c = 9.130$ Å, and $\beta = 101.581°$, as shown in Table 1. Additionally, the lattice parameters of sodium hexatitanate, $Na_2Ti_6O_{13}$, with space group $C2/m$

Table 1
Lattice parameters and refinement parameters obtained from the Rietveld refinement of all samples.

Phase	Parameter	NTO	NLTO-1	NTO/Org	NLTO-1/Org
$Na_2Ti_3O_7$	**a (Å)**	8.575(2)	8.577(3)	8.578(3)	8.573(2)
	b (Å)	3.796(1)	3.796(1)	3.7995(3)	3.7998(2)
	c (Å)	9.130(2)	9.131(2)	9.140(2)	9.135(2)
	V (Å3)	291.14(5)	291.29(5)	291.89(5)	291.51(3)
	β (°)	101.581 (8)	101.569 (9)	101.54(1)	101.580 (6)
	ρ (g/cm^3)	3.441	3.440	3.432	3.437
	% wt	87.27 ± 0.36	86.27 ± 0.38	72.47 ± 0.54	89.65 ± 0.66
$Na_2Ti_6O_{13}$	**a (Å)**	15.121(8)	15.143(8)	15.143(6)	15.13(2)
	b (Å)	3.746(1)	3.746(1)	3.7515(7)	3.746(2)
	c (Å)	9.161(5)	9.153(5)	9.168(4)	9.15(1)
	V (Å3)	512.5(2)	512.7(2)	514.3(3)	511.7(5)
	β (°)	99.08(3)	99.12(3)	99.10(2)	99.24(7)
	ρ (g/cm^3)	3.509	3.506	3.496	3.514
	% wt	12.73 ± 0.36	13.73 ± 0.38	16.22 ± 0.39	3.58 ± 0.28
C20H10O2	**a (Å)**	–	–	16.08(2)	16.07(2)
	b (Å)	–	–	4.874(4)	4.978(6)
	c (Å)	–	–	16.20(1)	16.14(1)
	V (Å^3)	–	–	1269(1)	1291(2)
	β (°)	–	–	91.9(1)	91.4(2)
	ρ (g/cm^3)	–	–	1.478	1.452
	% wt	–	–	11.31 ± 0.47	4.72 ± 0.36
$C_4H_7LiO_6$	**a (Å)**	–	–	–	5.869(14)
	b (Å)	–	–	–	5.937(6)
	c (Å)	–	–	–	18.47(10)
	V (Å3)	–	–	–	643(3)
	β (°)	–	–	–	92.0(3)
	ρ (g/cm^3)	–	–	–	1.632
	% wt	–	–	–	2.05 ± 0.59
Refinement Parameters					
χ^2	1.31	1.41	1.59	1.53	
Rwp (%)	16.68	18.31	12.80	12.57	
Rexp (%)	14.57	15.42	10.15	10.16	

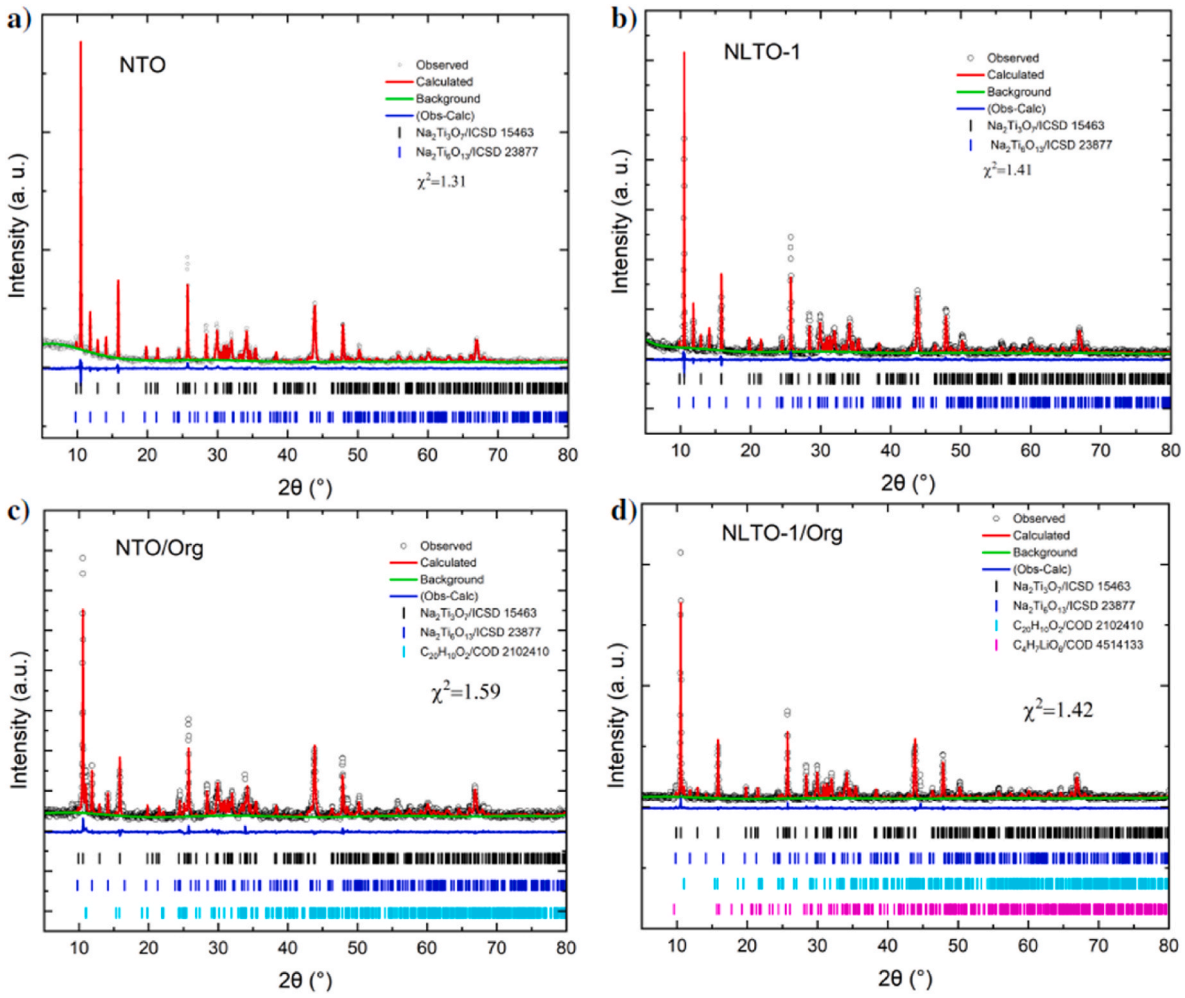


Fig. 2. Rietveld refinement plots of X-ray diffraction (XRD) data for (a) NTO, (b) NLTO-1, (c) NTO/Org and (d) NLTO-1/Org.

(ICSD 23877), are $a = 15.121$ Å, $b = 3.746$ Å, $c = 9.161$ Å, and $\beta = 99.08°$, as described in Table 1. The analysis also indicated that the dominant phase is $Na_2Ti_3O_7$, representing 87.27 ± 0.36 %, while $Na_2Ti_6O_{13}$ comprised only 12.73 ± 0.36 %.

The NLTO-1 sample also exhibits similar behavior, containing the same two crystalline phases with lattice parameters closely matching those of the NTO sample, as shown in Table 1. There is a slight increase in the amount of the secondary phase ($Na_2Ti_6O_{13}$), which accounts for 13.73 ± 0.38 %, while the main phase represents 86.27 ± 0.38 %, as shown in Table 1. The NTO/Org sample contains three monoclinic phases, $Na_2Ti_3O_7$, $Na_2Ti_6O_{13}$, and $C_{20}H_{10}O_2$, with space group *C 2/c* (COD 2102410). An increase was observed in all lattice parameters of the $Na_2Ti_3O_7$ crystalline phase compared to the samples without the organic phase, resulting in a unit cell volume of 291.89(5) Å^3. This increase can be attributed to the interaction between the trititanate and the organic phase [25]. Another possible explanation is that $Na_2Ti_3O_7$ has a layered structure, allowing the intercalation of atoms from other materials within its structure, which could lead to an increase in volume [26]. Additionally, van der Waals forces might influence this behavior due to the presence of hydrogen bonds in the $C_{20}H_{10}O_2$ structure. A significant change in the lattice parameters was also observed for the $Na_2Ti_6O_{13}$ phase in the NTO/Org sample. The unit cell volume is 514.3 (2) Å^3, while the NTO and NLTO-1 samples exhibited values of 512.5(2) Å^3 and 512.7(7) Å^3, respectively.

In the case of $Na_2Ti_6O_{13}$ for the NTO/Org sample, this result could be related to the interaction of sodium titanate atoms with $C_{20}H_{10}O_2$, through intermolecular interactions such as van der Waals forces. Another significant result, related to the NTO/Org sample, is the significant decrease of the %wt of the main crystalline phase compared to the NTO and NLTO-1 samples. The above reduction is approximately 15 percentage points. Although the appearance of a new phase with a considerable presence (11.31 ± 0.47 %) contributed to this reduction, the difference between the layered structure of $Na_2Ti_3O_7$ and the three-dimensional structure of $Na_2Ti_6O_{13}$ [5] could have also played a role in this behavior. Furthermore, this sample exhibited an increase in the %wt of sodium hexatitanate by approximately 16 %.

In the NLTO-1/Org sample, $Na_2Ti_3O_7$ exhibited, as shown in Table 1, a slight decrease in lattice parameters compared to the NTO/Org sample, as its unit cell volume reduced to 291.51(3) Å^3. This reduction can be attributed to the decrease in the amount of $C_{20}H_{10}O_2$ (to 4.72 ± 0.36 %), resulting in a subsequent decrease in interactions between the two phases. Another consequence of this reduction in the %wt of $C_{20}H_{10}O_2$ is the significant increase in the %wt of the main crystalline phase, $Na_2Ti_3O_7$, which rose to 89.65 ± 0.66 %. In comparison, the crystalline phase $Na_2Ti_6O_{13}$ significantly decreased (to 3.58 ± 0.28 %). The emergence of a new phase, $C_4H_7LiO_6$ - a monoclinic phase belonging to the space group $P2_1/n$, might also have influenced this behavior. This process occurs because the structure of $Na_2Ti_6O_{13}$ appears to be less stable in the presence of lithium ions, while the structure of $Na_2Ti_3O_7$ demonstrates greater stability in these interactions.

Fig. 3 presents the structural representations in order to highlight the internal atomic organization. The red spheres represent oxygen atoms, the blue spheres indicate titanium atoms, the yellow spheres represent sodium atoms, and the green spheres represent lithium atoms. The

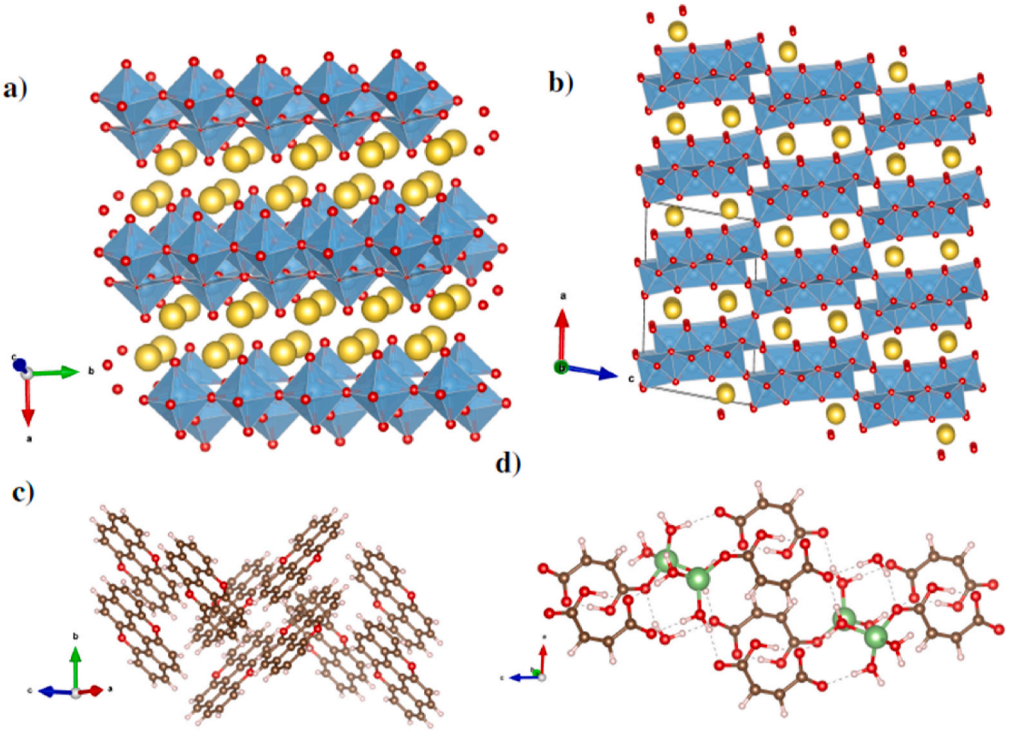


Fig. 3. Structural representations of the observed crystalline phases. (a) Crystal structure of $Na_2Ti_3O_7$. (b) Crystal structure of $Na_2Ti_6O_{13}$. (c) Crystal structure of $C_{20}H_{10}O_2$. (d) Crystal structure of $C_4H_7LiO_6$.

brown spheres represent carbon atoms, and the white spheres represent hydrogen atoms. The structures correspond to the following compounds: (a) $Na_2Ti_3O_7$, (b) $Na_2Ti_6O_{13}$, (c) $C_{20}H_{10}O_2$, and (d) $C_4H_7LiO_6$. The structure of $Na_2Ti_3O_7$ consists of layers of TiO_6 octahedra forming lamellae, between which the sodium atoms (Na) are located [6,27–29]. This conformation, shown in Fig. 3a, might facilitate the incorporation of other materials, promoting the interaction of this crystalline phase with other components present in the sample. The structure of $Na_2Ti_6O_{13}$, in turn, consists of TiO_6 octahedra interconnected to form a three-dimensional structure with tunnels, where the Na atoms are located [6,23,30,31], as shown in Fig. 3b. This configuration may hinder the insertion of other materials into this crystalline phase, as corroborated by the XRD results, as no significant changes in the lattice parameters were observed upon the appearance of $C_{20}H_{10}O_2$ in the NTO/Org sample. Fig. 3c shows the crystal structure of the $C_{20}H_{10}O_2$ phase. It consists of an organic molecular chain. Fig. 3d exhibits the crystal structure of the $C_4H_7LiO_6$ phase which corresponds to another organic molecular chain structure. In contrast, the lithium atoms are incorporated into the structure, probably due to substitution in the $C_{20}H_{10}O_2$ crystal lattice. These structures have a direct impact on the structural and morphological transformations, as well as on the electrical behavior of the material under study.

The two organic phases detected are likely not stable crystalline phases but rather the result of partial decomposition of the organic precursors used in the synthesis process, such as titanium isopropoxide (a hydrolysis-sensitive organometallic compound), lithium acetate (an organic salt that can generate compounds like $C_4H_7LiO_6$ through incomplete hydrolysis and/or oxidation), and isopropyl alcohol. In the case of titanium isopropoxide, contact with water leads to the release of alcohol as a byproduct. When this hydrolysis process is incomplete, residual organic species may remain, which could explain the formation of compounds such as $C_{20}H_{10}O_2$. After hydrolysis, Lithium acetate can release CH_3COO^- ions, which may react with Li^+ to form organolithium compounds. These fragments can undergo mild oxidation due to their exposure to atmospheric oxygen, leading to the formation of compounds such as $C_4H_7LiO_6$, which persist as residual phases in the final material.

The sonochemical synthesis of lithium-doped sodium titanate samples enables the identifica-tion of two distinct phases: $Na_2Ti_3O_7$ and $Na_2Ti_6O_{13}$, in NTO and NLTO-1 samples. However, the NTO/Org and NLTO-1/Org samples, which retained the organic phases, not only contained the two aforementioned inorganic phases but also exhibited the organic compounds identified as $C_{20}H_{10}O_2$ and $C_4H_7LiO_6$. DFT calculations were performed for all phases, considering their en-ergetics, structural characteristics, and electronic properties. Initially, the experimental structures were used for the calculations, and the resulting cell parameters and volume showed good agreement with those reported in Table 1 of the manuscript. Thereafter, the structures were completely relaxed without any constraint. The optimized structures demonstrated a lower energy than those obtained from the CIF files. The differences in per-atom energies between the optimized structures and the corresponding CIF-derived structures are given by 0.063 eV, 0.084 eV, 0.13 eV, and 0.007 eV in $Na_2Ti_3O_7$, $Na_2Ti_6O_{13}$, $C_{20}H_{10}O_2$, and $C_4H_7LiO_6$, respectively. The gap values of all phases, as well as the effective values based on the HOMO and LUMO of the inorganic and or-ganic phases, were calculated following [54]. The gap values of the two inorganic phases of the NTO (NLTO-1) samples obtained from experimental CIF files are 2.47 (2.46) eV and 2.77 (2.77) eV, for $Na_2Ti_3O_7$and $Na_2Ti_6O_{13}$, respectively. However, for the relaxed structures, the respective gap values of $Na_2Ti_3O_7$and $Na_2Ti_6O_{13}$ are slightly higher, at 3.14 eV and 3.07 eV for both NTO and NLTO-1. The effective values of the mixed systems were calculated using the highest value of HOMO and the lowest value of LUMO of the phases. For NTO, the effective gap value is 2.37 (2.90) eV for the unrelaxed (relaxed) structures, whereas for NLTO-1, the gaps are 2.37 (2.89) eV. The NTO/Org and NLTO-1/Org samples with the presence of the organic phases demonstrate the presence of $C_{20}H_{10}O_2$ in NTO/Org and $C_{20}H_{10}O_2$ and $C_4H_7LiO_6$ in NLTO-1/Org sample. The gap values for the NTO/Org samples are 2.46 (3.13) eV, 2.76 (3.07) eV, and 1.88 (1.83) eV for $Na_2Ti_3O_7$, $Na_2Ti_6O_{13}$, and $C_{20}H_{10}O_2$, respectively. The effective gap value of the inorganic phase is 2.38 (2.90) eV for the unrelaxed (relaxed) structures. Therefore, the

appearance of the third phase is fundamental for reducing the gap in the sample and increasing the conductivity of the NTO/Org compared to NTO and NLTO-1. Considering the NLTO-1/Org system, we observe the fourth phase due to Li doping $C_4H_7LiO_6$, which has a gap of 3.17 (2.86) eV. $Na_2Ti_3O_7$, $Na_2Ti_6O_{13}$, and $C_{20}H_{10}O_2$ show gap values of 2.46 (3.13) eV, 2.79 (3.07) eV, and 1.90 (1.85) eV for the unrelaxed (relaxed) samples. Considering the inorganic phases, the effective gap is 2.34 (2.86) eV. For the organic phases, the effective gap can also be similarly calculated to be 0.64 (0.35) eV for the unrelaxed (relaxed) systems. Hence, in the presence of the organic sample and upon Li doping, the effective gap should be significantly less than in all the other systems considered, thereby demonstrating the highest conductivity, as can be observed in Fig. 7 of the manuscript. This process is observed primarily because doping can modify the material's structure, promoting the formation of vacancies, creating preferential pathways for ionic migration, and increasing the concentration of mobile charge carriers (Li^+). Several studies have addressed the influence of doping on enhancing the ionic conductivity of materials intended for use as solid electrolytes, including superionic conductors of the LISICON (LIthium Super Ionic CONductor) type [32–34]. Secondly, the presence of organic phases can induce structural defects that increase the density of electronic states available for conduction. Furthermore, these phases may facilitate interfacial polarization, which contributes to the improvement of the material's electrical properties.

Although the band gap values were theoretically calculated using DFT, this study does not include experimental measurements that allow direct estimation of the band gap, such as UV–Vis spectroscopy or similar techniques. Therefore, a direct quantitative comparison between theoretical and experimental re-sults is not possible. However, the DFT-obtained values were used comparatively across different samples, enabling a qualitative correlation between the reduction in the band gap and the increase in electrical conductivity — an approach commonly adopted in the literature [32–34]. The total projected density of states (PDOS) of the four phases (a) $Na_2Ti_3O_7$, (b) $Na_2Ti_6O_{13}$, (c) $C_{20}H_{10}O_2$, and (d) $C_4H_7LiO_6$are exhibited in Fig. 4. The individual atomic PDOS are also displayed, with contributions from Na (olive), Ti (blue), C (black), H (orange), O (red), and Li (purple). The va-lence band maximum (VBM) was taken as the reference energy for all calculations. The resulting plots present the band gap values corresponding to the different phases examined in this study. In the valence band of $Na_2Ti_3O_7$, $Na_2Ti_6O_{13}$, and $C_4H_7LiO_6$, the density of states is dominated by contributions from oxygen atoms, significantly surpassing those from other elements.

For $Na_2Ti_3O_7$ and $Na_2Ti_6O_{13}$, the conduction band is predominantly composed of titanium states, with a minor contribution from oxygen, while the role of sodium is negligible in both valence and conduction bands. In contrast, $C_{20}H_{10}O_2$ exhibits a dominant contribution from carbon atoms in both the valence and conduction bands. For $C_4H_7LiO_6$, the conduction band displays a nearly equal contribution from oxygen and carbon atoms.

Table 2 presents the experimental and calculated optimized bond

Table 2
Average bond lengths for sodium titanate phases.

Sample	Crystalline Phase	Exp. Ti–O (Å)	Exp. Na–O (Å)	Theo. Ti–O (Å)	Theo. Na–O (Å)
NTO	$Na_2Ti_3O_7$	1.9713 (1)	2.6500 (12)	1.9944	2.6439
	$Na_2Ti_6O_{13}$	1.9587 (2)	2.7004 (3)	1.9950	2.6787
NLTO-1	$Na_2Ti_3O_7$	1.9717 (1)	2.6505 (1)	1.9886	2.6446
	$Na_2Ti_6O_{13}$	1.9589 (2)	2.7012 (3)	1.9948	2.6802
NTO/ Org	$Na_2Ti_3O_7$	1.9731 (1)	2.6523 (1)	1.9940	2.5956
	$Na_2Ti_6O_{13}$	1.9609 (2)	2.7038 (3)	1.9962	2.6845
NLTO- 1/Org	$Na_2Ti_3O_7$	1.9722 (1)	2.6511 (1)	1.9936	2.5504
	$Na_2Ti_6O_{13}$	1.9575 (6)	2.6994 (9)	1.9873	2.6768

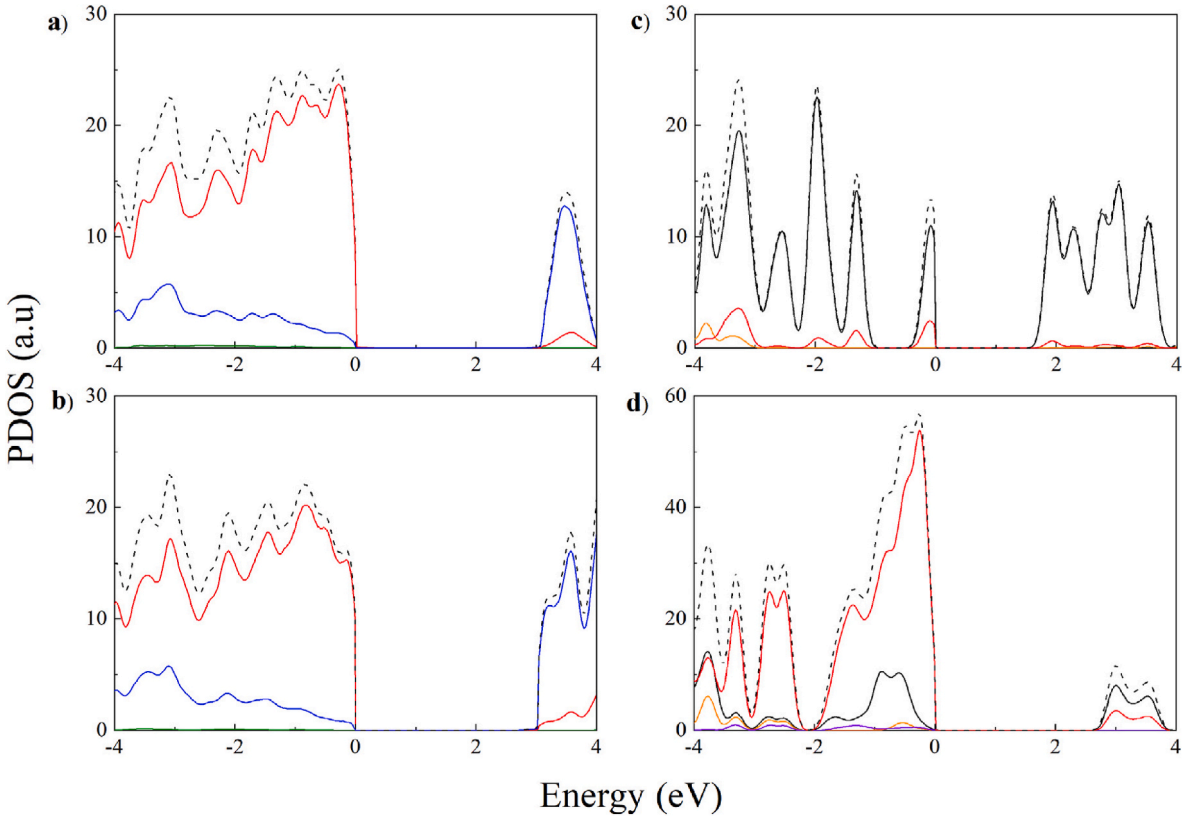


Fig. 4. The total projected density of states (PDOS) of the four phases (a) $Na_2Ti_3O_7$, (b) $Na_2Ti_6O_{13}$, (c) $C_{20}H_{10}O_2$, and (d) $C_4H_7LiO_6$ are exhibited in Fig. 4. The individual atomic PDOS are also displayed, with contributions from Na (olive), Ti (blue), C (black), H (orange), O (red), and Li (purple). (For interpretation of the references to colour in this figure legend, the reader is referred to the Web version of this article.)

lengths of the crystalline phases $Na_2Ti_3O_7$ and $Na_2Ti_6O_{13}$ for each sample. The first two columns, labeled as Exp. Ti– O (Å) and Exp. Na–O (Å), correspond to experimental measurements, while the last two columns, labeled as Theo. Ti–O (Å) and Theo. Na–O (Å), represents the bond lengths obtained through density functional theory (DFT) calculations. It is worth noting that the bond lengths of the experimental samples and the optimized structures are in excellent agreement. From the NTO sample to the NLTO-1 sample, the bond lengths in both crystalline phases undergo small variations: the average Ti–O bond length changes from 1.9713(1) Å to 1.9717(1) Å for the $Na_2Ti_3O_7$ phase and from 1.9587(2) Å to 1.9589(2) Å for the $Na_2Ti_6O_{13}$ phase, while the Na–O bond length varies from 2.6500(12) Å to 2.6505(1) Å in sodium trititanate and from 2.7004(3) Å to 2.7012(2) Å in sodium hexatitanate. In the optimized sample, the variations are from 1.9944 Å to 1.9986 Å in $Na_2Ti_3O_7$ phase, whereas for $Na_2Ti_6O_{13}$ phase, the above bond length suffers nearly no variation. The optimized Na-O bond length exhibits a slight increase, as also observed in experimental measurements. This observation suggests that the addition of 1 % lithium has a minimal impact on the structure of these two crystalline phases. This result is in agrrement with those in Table 1, which shows that the variations in unit cell volumes and other lattice parameters are not significant. The unit cell volume increased from 2191.14(5) $Å^3$ to 2191.29(5) $Å^3$ for $Na_2Ti_3O_7$, and from 512.5(2) $Å^3$ to 512.7(2) $Å^3$ for $Na_2Ti_6O_{13}$. In the NTO/Org sample, the crystalline phase exhibits a more significant increase in the Ti–O bond length compared to the NTO sample, increasing from 1.9713(1) Å to 1.9731(1) Å, and in $Na_2Ti_3O_7$, a slight increase is observed from 1.9587(2) Å to 1.9609(2) Å for $Na_2Ti_6O_{13}$. In the optimized structures, although we observe very little modification in $Na_2Ti_3O_7$, an increase in the Ti-O bond length is evident in $Na_2Ti_6O_{13}$. The Na–O bond also exhibits a greater increase in NTO/Org sample compared to the NTO sample, varying from 2.6500(12) Å to 2.6523(1) Å in $Na_2Ti_3O_7$ and from 2.7004(3) Å to 2.7038(3) Å in $Na_2Ti_6O_{13}$. This finding is in consonnance with the results presented in Table 1, reinforcing the hypothesis of interactions between the organic material ($C_{20}H_{10}O_2$) and the structures of sodium trititanate and sodium hexatitanate present in this sample. The NTO-1/Org sample shows a reduction in the Na–O bond length of the $Na_2Ti_6O_{13}$ phase compared to the NTO/Org sample. In this sample, the bond length is 2.6994(9) Å, whereas in the NTO/Org sample, the value is 2.7037(3) Å. This behavior might indicate a weaker interaction between the organic structures and the $Na_2Ti_6O_{13}$ phase, resulting in reduced stress on the bonds and, consequently, shorter bond lengths. This effect is possibly related to the significant decrease in the $C_{20}H_{10}O_2$ phase, which dropped from 11.31 $\pm$ 0.47 % to 4.72 $\pm$ 0.36 %.

3.2. Morphological characterization by SEM

Fig. 5 displays the scanning electron microscopy (SEM) images of the four samples. Fig. 5a and b are for the NTO e NLTO-1 samples, which are in agreement with those obtained in Ref. [6]. These images predominantly display rod-like or needle-like particles, with sizes ranging between 1 and 2 μm. Figures show similar morphologies, with particles of comparable size and shape. The particles appear relatively smooth, indicating a material with few imperfections.

Fig. 5c and d, corresponding to the NTO/Org and NLTO-1/Org samples, exhibit significant differences compared to the morphological pattern observed in the NTO and NLTO-1 samples. The samples exhibit highly irregular and agglomerated structures, with a rougher surface. The NLTO- 1/Org sample appears even more agglomerated compared to the NTO/Org sample. Moreover, it is irregularly shaped, and fewer granular particles are exhibited. The increased particle agglomeration behavior in hybrid inorganic-organic materials has already been

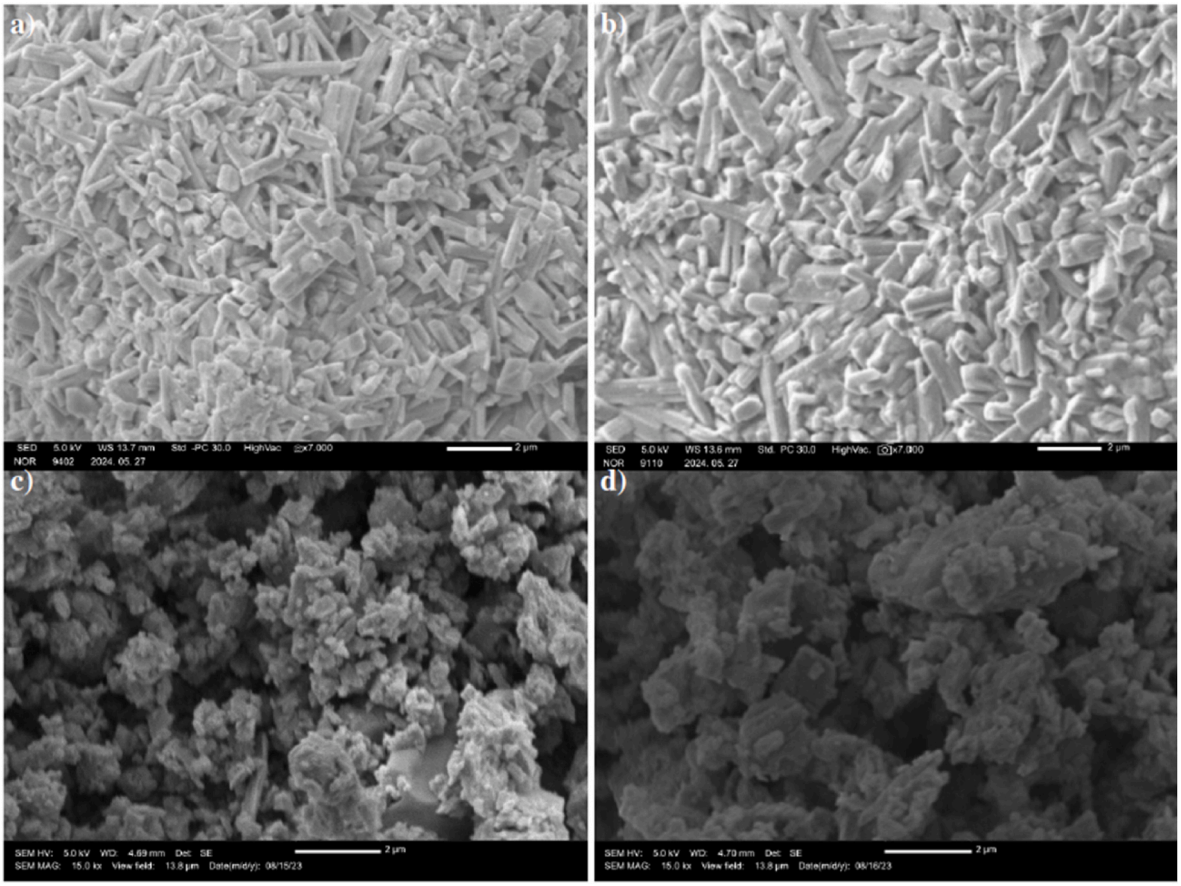


Fig. 5. SEM for all Samples. a) NTO. b) NLTO-1. c) NTO/Org. d) NLTO-1/Org.

described in the literature [35,36]. This behavior indicates that the addition of lithium has a more significant influence on the morphology of the NLTO-1/org sample compared to the NLTO-1 sample, relative to the NTO sample. This finding is most likely due to the emergence of a new material, $C_4H_7LiO_6$, which might have affected the structural organization of the system.

3.3. FTIR spectroscopy analysis

Fig. 6a exhibits the Fourier-transform infrared spectroscopy (FTIR) measurements of all samples. The measurements primarily reveal bands below 1000 cm^{-1}, a characteristic of Ti–O, Ti–O–Ti, and Na–O bonds. The bands observed between 650 and 800 cm^{-1} have been previously reported in the literature as surface phonon modes associated with Ti–O and Ti–O–Ti bonds [37]. The bands between 900 and 918 cm^{-1} corresponding to Ti–O bonds were also observed in Ref. [38]. Moreover, the peak at 743 cm^{-1} is related to the Na–O bond involved in a complex lattice vibration mode [39]. The presence of sodium was also detected at 876 cm^{-1}, attributed to the Na–O bond of the crystalline phase $Na_2Ti_3O_7$. The band at 860 cm^{-1} can be assigned to the Ti–O–Ti stretching of $Na_2Ti_3O_7$. The bands at 891 cm^{-1} and 910 cm^{-1} can be associated with the Ti–O bond vibrations involving less-coordinated oxygen atoms, which could directly interact with sodium ions [40,41].

Fig. 6b shows the FTIR spectrum between 900 and 2800 cm^{-1} for the NTO/Org and NLTO- 1/Org samples. This region highlights the presence of the organic phases. Below 2000 cm^{-1}, the observed vibrations can be attributed to C=C stretching [42], more specifically around 1650 cm^{-1} due to a bond present in $C_{20}H_{10}O_2$ structure. Bands in the range of 1450–1600 cm^{-1} in aromatic compounds are predominantly assigned to the stretching of C=C bonds in the ring skeleton [43]. The band observed at 2152 cm^{-1} can be attributed to the combination of C–H and C–C stretching [42]. The bands between 1000 and 1200 cm^{-1} might indicate C–O–C stretching vibrations, associated with the $C_{20}H_{10}O_2$ molecule [42]. Furthermore, the presence of bands around 1700 cm^{-1} in the NLTO-1/Org sample indicate C=O stretching, a characteristic feature of the $C_4H_7LiO_6$ compound. Overall, the bands observed in this region support the presence of crystalline organic phases previously identified by the X-ray diffraction analysis.

Furthermore, the spectrum of NTO and NLTO-1 samples show significant differences in the region between 650 and 710 cm^{-1}. Fig. 6c and d show the deconvolution of this region for the two samples mentioned above. It is observed that the intensity of the absorption bands is relatively low, as they are associated with vibrations involving the Ti-O bonds. Such vibrations are generally intense due to the rigidity of the crystalline structure, which results in weaker vibration modes. Band splitting related to O–Ti–O stretching occurs between 660 and 702 cm^{-1}. The analysis was performed using symmetric Lorentzian functions characterized by a Full Width at Half Maximum (FWHM) below 2.2 cm^{-1} for NTO and below 7.0 cm^{-1} for NLTO-1, indicating an adequate fit for well-defined bands. Between 650 and 660 cm^{-1}, the O–Ti–O wagging mode is observed in the hexatitanate phase. Ti–O stretching occurs between 670 and 680 cm^{-1} in the trititanate phase, whereas, between 680 and 690 cm^{-1}, the O–Ti–O bending mode is identified. Since the absorption intensity is related to the number of bonds corresponding to that wavelength [44], the interference of lithium in these bonds is already noticeable. A slight shift in the first peak from 654

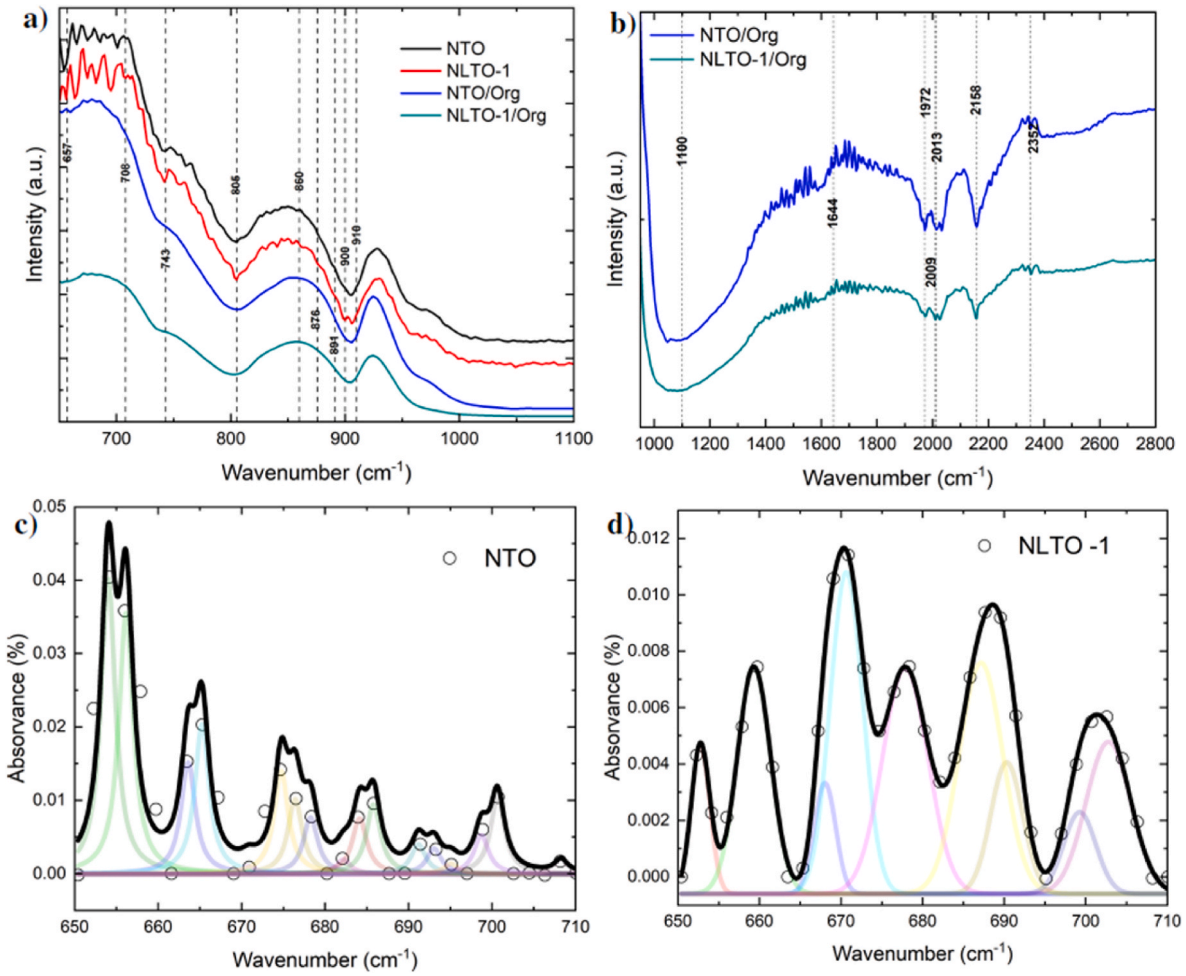


Fig. 6. (a) FTIR for all samples. (b) and (c) Deconvolution of the 650 to 710 cm^{-1} region for the NTO and NLTO-1 samples.

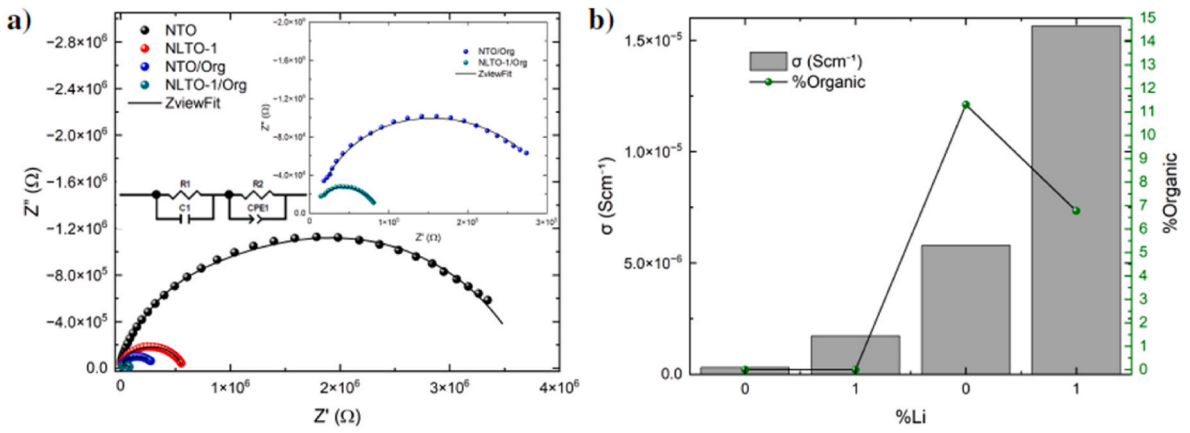


Fig. 7. (a)Cole-Cole plots (Z'' vs. Z') of the NTO, NLTO-1, NTO/Org, and NLTO-1/Org samples, along with the equivalent circuit model used for fitting. The inset shows a zoomed-in view of the NTO/Org and NLTO-1/Org impedance data. (b) Electrical conductivity (σ) as a function of lithium content (%Li), represented by gray bars, and the organic material percentage (%Organic) as a function of %Li, shown by the green curve. (For interpretation of the references to colour in this figure legend, the reader is referred to the Web version of this article.)

cm^{-1}–652.6 cm^{-1} suggests a change in bond strength. Additionally, the band splitting shifts from 685.8 cm^{-1} and 700.6 cm^{-1} to 687.1 cm^{-1} and 702.8 cm^{-1}, indicating alterations in the stretching vibrations of the O–Ti–O bond. These changes enhance the stretching polarization while reducing the lateral wagging motion.

3.4. Complex impedance spectroscopy

Fig. 7a displays the Cole-Cole plot obtained from complex impedance spectroscopy data. The largest semicircle, represented by black dots, corresponds to the NTO sample, which contains neither lithium addition nor organic material. The red curve displays the data for the NLTO-1 sample, while the blue curve corresponds to the NTO/Org sample. The smallest curve, in green, refers to the NLTO-1/Org sample, indicating that it exhibits the lowest electrical resistance. In other words, the addition of lithium, combined with the presence of organic materials in the sample, contributed concomitantly to the decrease in the electrical resistance of sodium titanate. The image inserted on the left side of Fig. 7a shows an equivalent circuit generated in the ZView program, which represents the electrical behavior of the samples. This configuration corresponds to a model known as the grain boundary model [45]. The resistor R_1 and the capacitor C_1 form a parallel circuit that models the behavior of the grains, which constitute the predominant part of the material. The resistor R_2 and the constant phase element (CPE1) represent the behavior of the material surrounding the grains, known as the grain boundary. CPE1 is used to describe the non-ideal capacitive behavior [46–48]. In the present study, the ionic and electronic contributions to conductivity were not individually analyzed. For this purpose, future studies may include measurements using ion- and electron-blocking electrodes to investigate these contributions separately.

However, to gain a deeper understanding of the electrical characteristics, it is necessary to calculate its electrical conductivity using Equation (2) [49,50], as electrical resistance is a property of the sample rather than the material.

$$\sigma = \frac{e}{R_b \cdot A} \tag{2}$$

where e is the thickness of the pellet corresponding to the solid-state electrolyte in the battery configuration, with its values given in Section 2. A is the cross-sectional area, and R_b is the bulk resistance (also referred to as grain resistance, R_1), obtained from the high-frequency semicircle in the Cole–Cole plots.

Fig. 7b displays the conductivity as a function of the percentage of lithium addition and the percentage of organic material present in the sample, as listed in Table 1. The gray bars represent the measured conductivity, while the curve with green points and a black line indicates the percentage of organic phases (%Org). It is possible to observe that the first 2 bars correspond to samples without the presence of an organic phase, namely NTO and NLTO-1, respectively, while the last two correspond to samples containing organic phases. The presence of organic material is observed to act in conjunction with lithium, improving the material's conductivity. There is an increase in electrical conductivity by two orders of magnitude in the NLTO-1/Org sample compared to the NTO sample, with conductivity rising from 3.05×10^{-7} $S\ cm^{-1}$ for the NTO sample to 1.57×10^{-5} $S\ cm^{-1}$ for the NLTO-1/Org sample.

Furthermore, even in the NTO/Org sample, which does not contain lithium, an increase of one order of magnitude is observed compared to the NTO sample (reaching 5.79×10^{-6} S cm^{-1}), and a electrical conductivity more than three times higher than that of the NLTO-1 sample (whose conductivity is 1.73×10^{-6} S cm^{-1}). The above characteristics could also be understood from the band-gap analysis of our DFT calculations.

In Fig. 8a, it is possible to observe the behavior of the real impedance component (Z') as a function of frequency. For the NTO sample, the real component reaches 3×10^6 Ω at very low frequencies. For the NLTO-1 sample, this component is approximately 5×10^5 Ω, whereas in the NTO/Org sample, it is above 2.5×10^5 Ω. In the NLTO-1 sample, the above value is of the order of 10^4Ω. These results are consistent with the resistance values of the samples at low frequencies, calculated using the ZView software fit ($R_1 + R_2$) (3.71×10^6 Ω, 5.61×10^5 Ω, 3.08×10^5 Ω, and 9.03×10^4 Ω, respectively). Fig. 8b shows the variation of the imaginary component of the impedance as a function of frequency. This graph is important as it enables the determination of the peak frequency (f_{peak}). Based on the peak frequency, the relaxation time (τ) can be calculated through Equation (3) [51].

$$\tau = \frac{1}{2\pi f_{peak}} \tag{3}$$

The relaxation time is given by Equation (4), where τ is found to be inversely proportional to the DC conductivity. This relationship arises because the relaxation time demonstrates the time required for a charge carrier, the ions, to return to their initial state after the removal of an applied electric field. Thus, the shorter the time, the higher the ion velocity, the greater the ionic diffusivity, and, consequently, the higher the ionic conductivity.

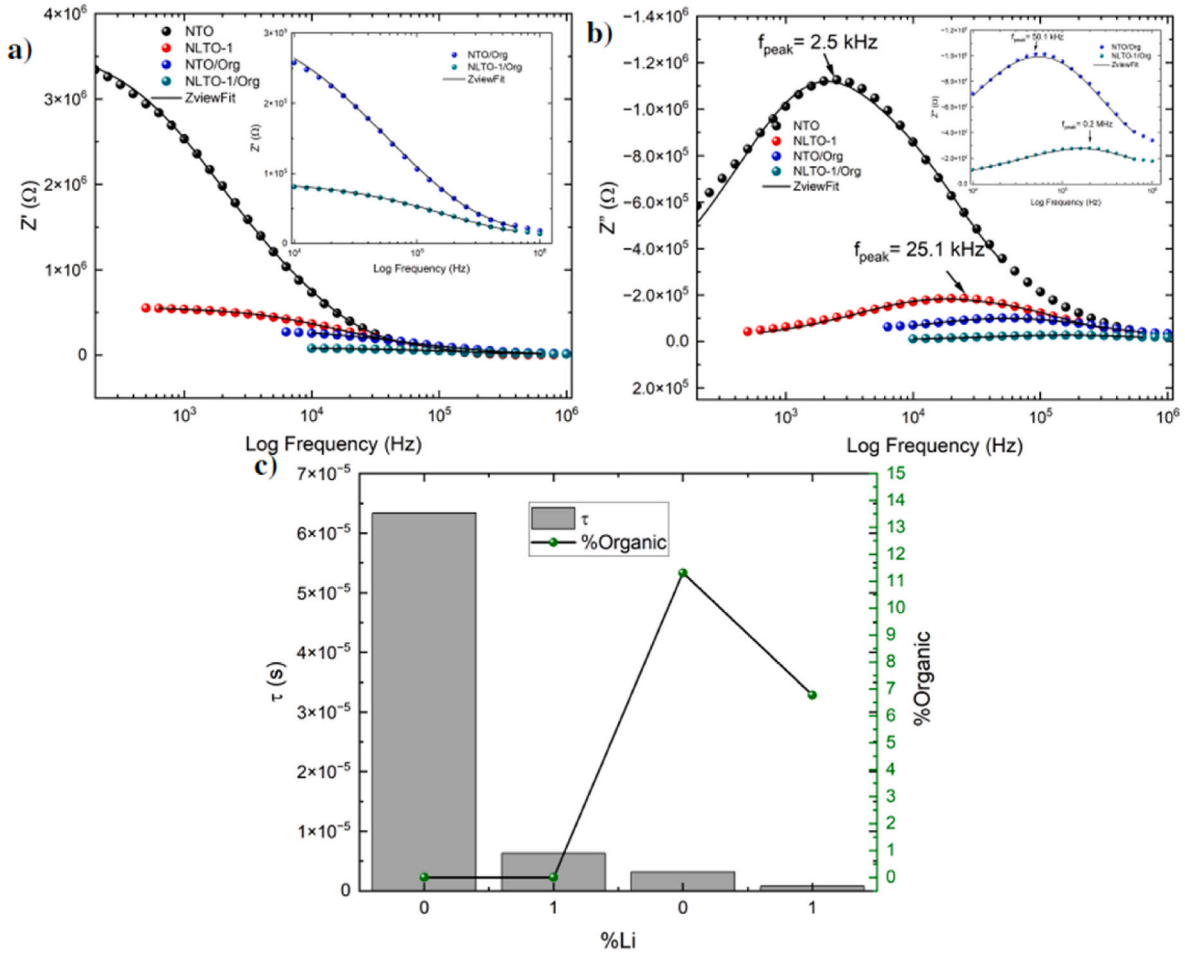


Fig. 8. Plots of Impedance Spectroscopy for all samples: (a) Real Impedance (Z') vs. Log Frequency. (b) Imaginary Impedance (Z'') vs. Log Frequency. (c) Relaxation time vs. %Li and %Organic %Organic phases.

$$\tau = \frac{\varepsilon_0 \varepsilon'}{\sigma_{DC}} \tag{4}$$

where τ is the relaxation time, ε_0 is the vacuum permittivity (8.854×10^{-12} F/m), ε' is the real part of the material's permittivity, and σ_{DC} is the DC conductivity.

Using the peak frequency data shown in Fig. 8b and applying Equation (3), it was possible to plot the graph presented in Fig. 8c. This graph shows the variation of the relaxation time as a function of the lithium content and the percentage of organic phases in the material. A clear decrease in relaxation time is observed, from 6.3×10^{-5} s in the NTO sample to 6.3×10^{-6} s in the NLTO-1 sample. In the samples containing organic material, these values are even lower. For the NTO/Org sample, the value is 3.2×10^{-6} s, whereas for NLTO-1/Org sample, it is 8.0×10^{-7} s. Two important aspects can be highlighted from these results. First, the presence of organic material alone, without lithium addition, was able to reduce the relaxation time. Second, the combination of lithium addition with the presence of organic phases further decreased the relaxation time by two orders of magnitude. These results are consistent with the conductivity values presented in Fig. 7c.

Another relevant analysis is that of the dielectric properties of the material, achieved through the study of the material's electric permittivity, given by Equation (5):

$$\varepsilon^* = \frac{1}{j\omega C_0 Z^*} \tag{5}$$

where j is the imaginary unit, ω is the angular frequency, and $C_0 = \frac{\varepsilon_0 A}{d}$ is the geometric capacitance of the sample (ε_0 is the permittivity of vacuum, A is the electrode area, and d is the sample thickness).

The real (ε') and imaginary (ε'') components of the permittivity are given, respectively, by Equations (6) and (7):

$$\varepsilon' = \frac{Z''}{\omega C_0 \left(Z'^2 + Z''^2\right)} \tag{6}$$

$$\varepsilon'' = \frac{Z'}{\omega C_0 \left(Z'^2 + Z''^2\right)} \tag{7}$$

The dielectric loss factor, given by Equation (8), addresses the energy dissipation of the material [52,53]. For example, it enables the identification of conditions under which the material operates more efficiently in terms of energy utilization.

$$\tan\delta = \frac{\varepsilon''}{\varepsilon'} \tag{8}$$

The increase in this quantity is also related to the increase in conductivity, as predicted by Equation (9).

$$\tan\delta = \frac{\sigma}{\omega \varepsilon'} \tag{9}$$

In summary, the above equations, combined with the complex spectroscopy data, enabled the dielectric analysis of the material as exhibited in Fig. 9. Fig. 9a presents the Nyquist diagram (ε'' vs. ε') for all samples. The black curve, corresponding to NTO, represents a lower growth rate of ε'' relative to ε', indicating lower dielectric losses. In contrast, the red

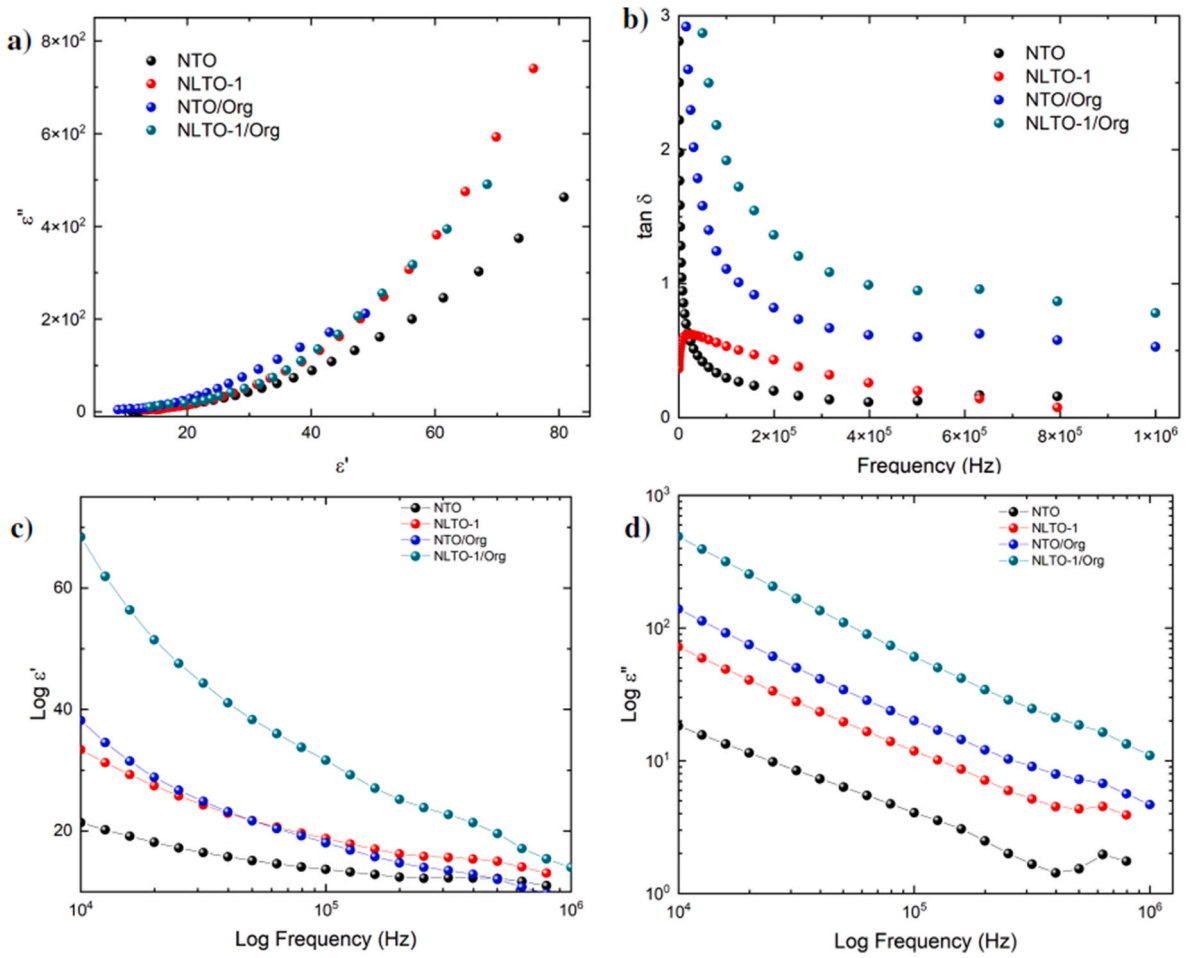


Fig. 9. (a) Nyquist plots (ε'' vs. ε') for all samples. (b) Dielectric loss factor (tan δ) as a function of frequency. (c) and (d) Frequency dependence of the imaginary permittivity (ε'') and real permittivity (ε').

curve, representing NLTO-1, exhibits a higher rate of dielectric losses. The blue and green curves, corresponding to NTO/Org and NLTO-1/Org, exhibit a slightly lower inclination compared to the NLTO-1 curve. This change indicates a more moderate increase in ε'' relative to ε', suggesting a more controlled increase in dielectric losses for these samples. Fig. 9b highlights the behavior of the dielectric loss factor tan δ as a function of frequency. Although the organic samples, in the graph of Fig. 9a, exhibited a modest increase in ε'' relative to ε' when compared to NLTO-1, the dielectric loss factor is higher for the organic phases. Hence, although the increase in imaginary permittivity is less pronounced compared to the real permittivity, the difference between these two quantities is greater for the organic phases, resulting in higher loss factors. This effect might result in new dielectric response mechanisms acquired by the material due to the presence of organic phases, such as Maxwell-Wagner-Sillars interfacial polarization [54]. Fig. 9c and d display an increase in the real component (ε') of the permittivity in the NLTO-1 sample (red curve) compared to the NTO sample. NTO/Org sample exhibits higher values than NLTO-1 at low frequencies and lower values at high frequencies. This behavior likely occurs due to the polarization mechanism induced by the presence of organic phases. At high frequencies, the rapid changes in the electric field polarity hinder the additional polarization. Meanwhile, the NLTO-1/Org sample, represented by the green curve, exhibits higher ε' values across all frequencies, probably due to its combination of the polarization mechanisms of the organic phases with that of ionic doping [55], which are more efficient over a wider frequency range [56,57]. Fig. 9d presents the graph of the imaginary permittivity (ε'') for all samples. In this case, ε'' shows the highest values for the NLTO-1/Org sample and the lowest values for the NTO sample. The NTO/Org sample exhibits ε'' values higher than those of the NLTO-1 sample across all frequencies. This quantity is related to energy dissipation. In other words, as the energy storage capacity increases (indicated by the rise in ε'), there is also an increase in energy dissipation. Furthermore, the increase in ε'' also suggests an improvement in AC conductivity, as described by Equation (10).

$$\sigma_{AC} = \omega \varepsilon_0 \varepsilon'' \tag{10}$$

The improvement in electrical response due to the retention of organic phases might have occurred primarily because the compound $C_{20}H_{10}O_2$, as shown in Fig. 3c, contains functional groups that facilitate charge transport, in addition to the specific arrangement of its molecular network [58].

Fig. 10 shows the dependence of the AC conductivity (σ_{AC}) on frequency. It can be seen that σ_{AC} follows the same trend as σ_{DC} (Fig. 7c). Comparing the most conductive sample (NLTO-1/Org) with the least conductive sample (NTO), there is an increase of two orders of magnitude at low frequencies (from 5.1×10^{-6} Scm^{-1} to 2.7×10^{-4} Scm^{-1}). At high frequencies, this increase is of one order of magnitude (from 7.7×10^{-5} Scm^{-1} to 6.1×10^{-4} Scm^{-1}).

In organic materials, electrical conductivity is often associated with conjugated systems, in which π-electrons can move along the structure, thereby reducing electrical resistance. Furthermore, intermolecular interactions, such as hydrogen bonding, may favor proton transport [59], which also contributes to the observed electrical response. The molecular organization — especially in the case of $C_{20}H_{10}O_2$, which has aromatic rings in its structure — could create internal pathways that assist

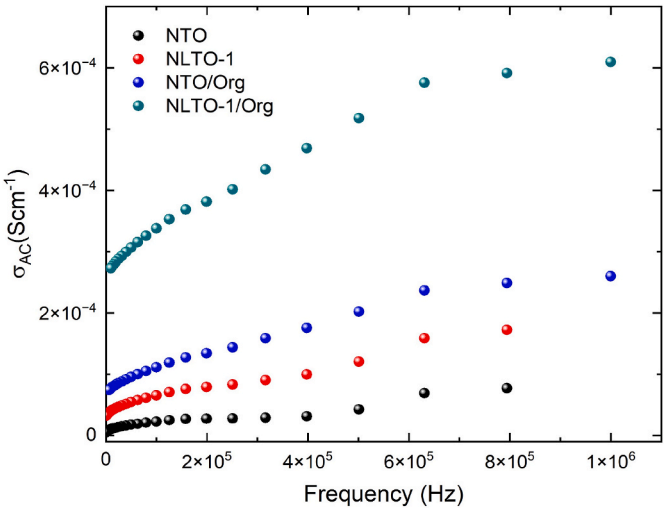


Fig. 10. AC conductivity (σ_{AC}) as a function of frequency for all samples.

in charge mobility. Although it is not a metallic or predominantly ionic mate-rial, these characteristics explain the electrical behavior observed in the tests. On the other hand, the structure shown in Fig. 3d ($C_4H_7LiO_6$) exhibited a superior electrical response, primarily due to the presence of lithium ions. Li^+ is very mobile in solid-state materials, particularly when the crystalline network provides well-defined pathways for its diffusion. The interaction between lithium and oxygen atoms in the structure creates a favorable environment for charge transport, thus enhancing ionic conduction [60].

In summary, the electrical analysis of the studied material indicates an improvement in its electrical properties for use as a solid-state electrolyte, facilitated by lithium doping while retaining the organic materials in the structure. There was an increase in both DC and AC conductivities, as well as a decrease in relaxation time, resulting in an enhancement in ionic conductivity. Additionally, the dielectric behavior analysis revealed an increase in real permittivity, indicating a greater energy storage capacity.

3.5. Distribution of relaxation times (DRT) analysis

Complex impedance spectroscopy data enables us to understand the material's behavior through the distribution of relaxation time analysis. In this context, the complex impedance $Z(\omega)$ can be described in terms of a distribution of relaxation times $g(\tau)$ using Equation (11) [48,61].

$$Z(\omega) = R_s + \int_{-\infty}^{\infty} \frac{g(\tau)}{1 + j\omega\tau} d\ln\tau \tag{11}$$

in which $Z(\omega)$ is the complex impedance measured experimentally, $g(\tau)$ is the Distribution of Relaxation Time (DRT), which we aim to determine, and R_s represents the series resistance of the material.

It is therefore possible to determine $g(\tau)$ from a discrete set of experimentally measured $Z(\omega)$ values by approximating Equation (11) using a finite and discrete summation, in which the DRT is represented on a grid of values τ_i, as shown in Equation (12):

$$Z(\omega_k) \approx \sum_{i=1}^{N} G_{ki} g_i \tag{12}$$

where g_i is the DRT value associated with the relaxation time τ_i; G_{ki} is the basis matrix representing the contribution of each g_i to the impedance $Z(\omega)$; and k represents the different measured frequency values.

The problem can then be written as the linear system described by Equation (13):

$$\mathbf{Z} = \mathbf{Gg} \tag{13}$$

where $\mathbf{Z}$ is the complex impedance vector, $\mathbf{G}$ is the DRT basis matrix, and $\mathbf{g}$ is the DRT vector. Given the definitions in Equations (14)–(17) [62].

$$\mathbf{Z} = \begin{bmatrix} Z(\omega_1) \\ Z(\omega_2) \\ \vdots \\ Z(\omega_K) \end{bmatrix} \tag{14}$$

$$\mathbf{G}_{\text{real}} = \begin{bmatrix} \frac{1}{1+(\omega_1\tau_1)^2} & \frac{1}{1+(\omega_1\tau_2)^2} & \cdots & \frac{1}{1+(\omega_1\tau_N)^2} \\ \frac{1}{1+(\omega_2\tau_1)^2} & \frac{1}{1+(\omega_2\tau_2)^2} & \cdots & \frac{1}{1+(\omega_2\tau_N)^2} \\ \vdots & \vdots & \ddots & \vdots \\ \frac{1}{1+(\omega_K\tau_1)^2} & \frac{1}{1+(\omega_K\tau_2)^2} & \cdots & \frac{1}{1+(\omega_K\tau_N)^2} \end{bmatrix} \tag{15}$$

$$\mathbf{G}_{\text{imag}} = \begin{bmatrix} \frac{\omega_1\tau_1}{1+(\omega_1\tau_1)^2} & \frac{\omega_1\tau_2}{1+(\omega_1\tau_2)^2} & \cdots & \frac{\omega_1\tau_N}{1+(\omega_1\tau_N)^2} \\ \frac{\omega_2\tau_1}{1+(\omega_2\tau_1)^2} & \frac{\omega_2\tau_2}{1+(\omega_2\tau_2)^2} & \cdots & \frac{\omega_2\tau_N}{1+(\omega_2\tau_N)^2} \\ \vdots & \vdots & \ddots & \vdots \\ \frac{\omega_K\tau_1}{1+(\omega_K\tau_1)^2} & \frac{\omega_K\tau_2}{1+(\omega_K\tau_2)^2} & \cdots & \frac{\omega_K\tau_N}{1+(\omega_K\tau_N)^2} \end{bmatrix} \tag{16}$$

$$\mathbf{g} = \begin{bmatrix} g(\tau_1) \\ g(\tau_2) \\ \vdots \\ g(\tau_N) \end{bmatrix}, \tag{17}$$

The purpose of this method is to solve this linear system to find $\mathbf{g}$. However, the system $\mathbf{Z} = \mathbf{Gg}$ is ill-conditioned, which means that slight variations in the data $Z(\omega)$ can result in significant variations in $g(\tau)$. To stabilize the solution, Tikhonov regularization can be applied, adding a smoothing term, as shown in Equation (18):

$$\mathbf{g}^* = \underset{\mathbf{g}}{\text{argmin}} \| \mathbf{Z} - \mathbf{Gg} \|^2 + \alpha \| \mathbf{Lg} \|^2 \tag{18}$$

where α is the regularization parameter, and $\mathbf{L}$ is the regularization matrix, which can be the identity matrix or a finite difference matrix to smooth $g(\tau)$. The regularization problem is solved numerically (Equation (19)), using Ridge regression.

$$\mathbf{g}^* = \left(\mathbf{G}^T\mathbf{G} + \alpha\mathbf{I}\right)^{-1}\mathbf{G}^T\mathbf{Z} \tag{19}$$

Fig. 11 exhibits the real and imaginary DRT $g(\tau)$ distributions for each sample. If we consider the imaginary $g(\tau)$ distributions, each peak corresponds to an existing process in the material [63–65]. Considering the model of resistors in parallel with capacitors (or constant phase elements - CPE), the relaxation time associated with each peak can be defined according to Equation (20).

$$\tau_{\text{peak}} = \omega_{\text{peak}}^{-1} = (R \cdot \text{CPE})^{\frac{1}{n}} \tag{20}$$

$$n = \frac{\ln(\tau_{\text{peak}})}{\ln(R \cdot \text{CPE})} \tag{21}$$

In Equation (20), CPE represents the behavior of an ideal capacitor for $n = 1$. For values of n lower than 1, CPE characterizes a non-ideal capacitance. Lower values of n may indicate structural defects, rough interfaces, or variations in local permittivity. Additionally, values lower than 1 might also be associated with ionic transport in porous electrodes and heterogeneous surfaces. As n approaches zero, there is an indication of predominant resistive behavior, and for $n = 0$, the behavior is purely resistive. Each peak in the imaginary $g(\tau)$ graphs indicates a distinct electrochemical process. Each of these processes can be represented by an equivalent circuit that best describes its behavior.

Comparing the DRT results, presented in Fig. 11, with the equivalent

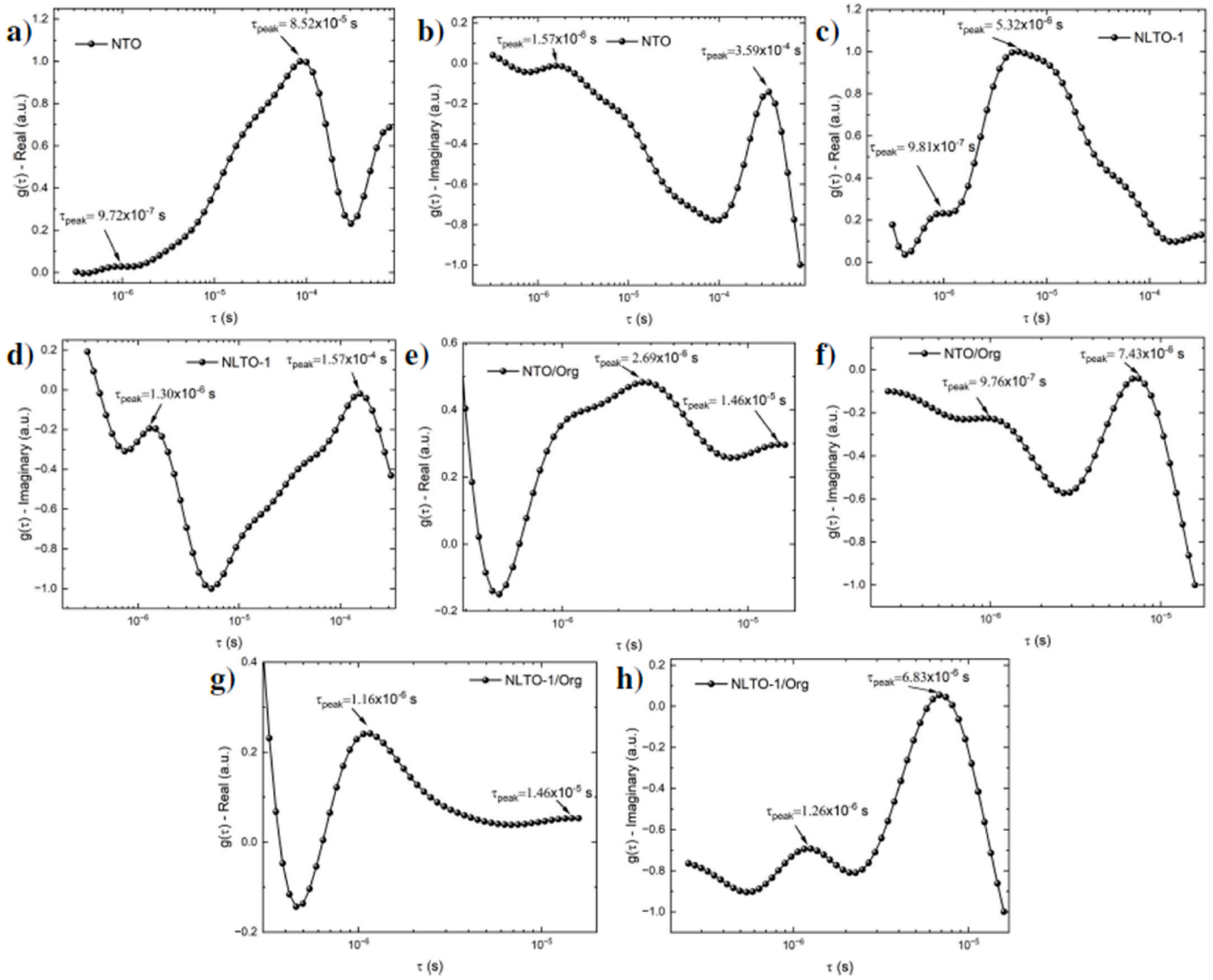


Fig. 11. Distribution of Relaxation Times (DRT) for Different Samples. (a, b) DRT for the NTO sample: (a) real part $g(\tau)_{real}$ and (b) imaginary part $g(\tau)_{imag}$. (c, d) DRT for the NLTO-1 sample: (c) real part $g(\tau)_{real}$ and (d) imaginary part $g(\tau)_{imag}$. (e, f) DRT for the NTO/Org sample: (e) real part $g(\tau)_{real}$ and (f) imaginary part $g(\tau)_{imag}$. (g, h) DRT for the NLTO-1/Org sample: (g) real part $g(\tau)_{real}$ and (h) imaginary part $g(\tau)_{imag}$.

circuit results obtained through ZView, it is observed that the imaginary $g(\tau)$ exhibits two peaks, indicating the presence of two distinct processes. This result agrees with the equivalent circuit found through the fitting process in the ZView software (Fig. 7a), which consists of an $R//C$ circuit in series with an $R//CPE_1$ circuit. For a more detailed analysis, it is easy to see that Equation (21) can be derived from Equation (20). Using Equation (21) and considering all capacitors as CPE, it is possible to compare the results of the adopted DRT approach with the equivalent circuit values obtained using ZView, as shown in Table 3, by analyzing n. For the NTO sample, the obtained values are $n = 0.87(1)$ and $n = 0.91(2)$. Therefore, the first value of n is more related to structural defects and rough interfaces, which can be attributed to the behavior of the grain boundary region, where the heterogeneity of the materials in the sample plays a significant role. On the other hand, the second value of n is closer to 1, indicating a behavior similar to that of an ideal capacitor. This result suggests a greater homogeneity of the material in this region, which can be associated with the grain behavior of the material.

For the NLTO-1 sample, n_1 ($n = 0.97(1)$) indicates a behavior close to that of an ideal capacitor. However, the difference compared to n_2 ($n = 1.00(2)$), which represents an ideal capacitor, suggests that the material exhibits a less homogeneous region, with a characteristic grain boundary behavior. On the other hand, for the NTO/Org sample, $n_1 = 0.99(1)$ and $n_2 = 0.74(1)$. In this case, n_2 reflects a greater deviation from ideal capacitive behavior, suggesting increased heterogeneity at the grain

Table 3
Equivalent circuit parameters and DRT analysis results for the studied samples.

Sample	R_1 (Ω)	C_1 (F)	R_2 (Ω)	CPE_1 (F)	n_1	n_2
NTO	5.80×10^5 (41)	1.64×10^{-11} (9)	3.05×10^6 (6)	2.41×10^{-10} (10)	0.87 (1)	0.91 (2)
NLTO-1	1.04×10^5 (6)	1.96×10^{-11} (9)	4.60×10^5 (5)	2.80×10^{-10} (26)	0.97 (1)	1.00 (2)
NTO/Org	3.71×10^4 (3)	3.02×10^{-11} (3)	2.89×10^5 (4)	5.79×10^{-10} (14)	0.99 (1)	0.74 (1)
NLTO-1/Org	1.44×10^4 (1)	1.08×10^{-11} (1)	6.95×10^4 (1)	1.94×10^{-10} (10)	1.00 (1)	0.94 (1)

boundaries. Thus, this result is consistent with the image in Fig. 5c, which shows a less uniform morphology compared to the NTO and NLTO-1 samples. In contrast, n_1 represents the behavior of an ideal capacitor and is associated with the grain region. For the NLTO-1/Org sample, one of the results suggests the proximity to the behavior of an ideal capacitor ($n_1 = 1.00(1)$). The other result ($n_2 = 0.94(1)$), although also close to an ideal capacitor, indicates a behavior associated with a more heterogeneous region, related to the grain boundary.

The real contributions are important when analyzed together with the imaginary contributions. All $g(\tau)$-real graphs, as well as the $g(\tau)$-imaginary graphs, exhibited two peaks. This characteristic suggests that, in these regions, a coexistence of resistive and capacitive processes exists. All results agrees with the equivalent circuits, as they confirm the existence of two electrochemical processes, each with capacitive and resistive contributions. The real component is more closely related to resistive processes, while the imaginary component is more closely associated with capacitive behaviors. The difference between the peaks can indicate greater or lesser dispersive behavior in the region. The more dispersive the behavior, the greater the difference between the peaks of the real and imaginary components, which corresponds to an $R//$CPE circuit. All samples exhibit both more and fewer coincident peaks, indicating regions where capacitance behavior is closer to or further from the ideal. This supports the equivalent circuit model derived using ZView. For the NLTO-1/Org sample, the difference for the first peak is approximately 9 %, while for the second peak, it is around 53 %. This observation suggests a less dispersive region, associated with grain behavior, and a more dispersive region, related to grain boundary behavior.

Furthermore, the analysis of the relaxation time distribution allowed the estimation of the predominant relaxation time for each sample, based on the identification of the most intense peaks in the real part of the $g(\tau)$ function, relative to a defined baseline. A progressive decrease in the relaxation time is observed, with values of 8.52×10^{-5} s, 5.32×10^{-5} s, 2.69×10^{-6} s, and 1.16×10^{-6} s for the NTO, NLTO-1, NTO/Org, and NLTO-1/Org samples, respectively. This reduction in relaxation time is directly related to the increased charge carrier mobility in the material. In structures with a high ion density, such faster dynamics typically indicate an enhancement in ionic conductivity. These features are highly desirable for solid-state energy storage applications, where efficient ionic conduction and fast interfacial response are essential. Additionally, the presence of two distinct relaxation peaks in the hybrid and doped samples suggests the coexistence of multiple transport mechanisms, possibly associated with grain and grain boundary contributions, or interfacial polarization effects.

The performance improvement observed across all characterizations and theoretical calculations may result from several mechanisms. First, the residual presence of organic phases at the interfaces or grain boundaries may induce structural disorder and the formation of defects [66] that facilitate the movement of charge carriers. This disorder can increase the density of states near the Fermi level, thereby reducing the activation energy and consequently enhancing electrical conductivity. Moreover, the dielectric contrast between the inorganic matrix and the residual or-ganic materials may favor the formation of localized charge accumulation regions, promoting po-larization and improving the dielectric response of the material under an applied electric field [67]. Additionally, charge transport might occur through *hopping* mechanisms across organic/inorganic interfaces, particularly if organic fragments with π-conjugated systems—originating from the par-tial decomposition of solvents—remain integrated into the structure [68]. In this case, such inter-faces can act as bridges that facilitate the tunneling of charge carriers. In summary, the coexistence of these mechanisms contributes to the enhancement of both conductivity and dielectric properties of the materials.

The results obtained in this study demonstrate a clear improvement in the electrical performance of sodium titanate-based materials, attributed to the combined effects of lithium doping and the partial retention of organic phases. Compared to previous studies, this approach provides competitive or even superior properties. Melo et al. [6], for instance, investigated lithium-doped $Na_2Ti_3O_7$ synthesized via microwave-assisted methods, and reported a maximum conductivity value of 4.0×10^{-5} S cm^{-1}, without considering organic phase retention. In that case, the lithium addition was 5 %, whereas in the present study, only 1 % lithium was added. Yet, when combined with the retention of organic phases, this resulted in electrical conductivity of the order of 10^{-4} S cm^{-1}. Similarly, Da Silva et al. [9] investigated sodium titanate-based composites and obtained conductivity values on the order of 10^{-5} S cm^{-1} by adding 50 % of the organic material poly (o-methoxyaniline) (POMA), a known conducting polymer. In a more recent study, Da Silva et al. [8] reported the addition of 35 % sodium titanate into a POMA polymer matrix, which also resulted in conductivity values on the order of 10^{-5} S cm^{-1}. Thus, the combination of lithium doping and the retention of organic phases derived from the solvents used during synthesis appears to be an effective strategy to enhance the material's conductivity, achieved through a simple modification in the synthesis route — specifically, by changing the drying temperature of the solution.

4. Conclusions

In this work, we investigated the synthesis and characterization of lithium-doped sodium titanate solid-state electrolytes examining samples both with and without retained organic phases. The synthesis route proved effective in obtaining the desired crystalline phase, $NaTi_3O_7$ - the predominant one in all samples. Furthermore, a simple modification of the route enabled the retention of organic material, which significantly improved the material's electrical properties. This change also offers an energy-saving benefit by lowering the oven drying temperature from 100 to 60 °C.

The *FTIR* spectra demonstrated the presence of bands corresponding to the vibrations of the Ti – O, Na – O, and Ti – O – Ti bonds, as well as bands related to C – C bonds, the stretching of the C – C bond, and the stretching of the C – O – C bond present in the $C_{20}H_{10}O_2$ and $C_4H_7LiO_6$ phases, and bands associated with C – O bonds present in $C_4H_7LiO_6$, as expected, in agreement with the results obtained by *XRD*. Scanning electron microscopy (*SEM*) revealed a morphological pattern previously attributed in the literature to sodium trititanate [6] in NTO and NLTO-1 samples, with significant changes observed in NTO/Org and NLTO-1/Org samples, clearly demonstrating the influence of retained organic phases on the material's morphology.

Complex impedance spectroscopy analysis showed that the electrical conductivity of the material increased in the sample doped with 1 % lithium and containing organic phases in its composition. The organic residues, although they are probably not stable crystalline phases, appear to be crucial for the increase in conductivity. This improvement is likely attributed, among other factors, to their contribution in enhancing interfacial charge carrier transport. The AC conductivity, in turn, exhibited a one-order-of-magnitude increase at high frequencies. Furthermore, the presence of lithium and retained organic phases reduces the relaxation time, thereby enhancing conductivity. Together, these results indicate an improvement in ionic conductivity because of the synergistic effect of doping and the presence of organic phases. The DFT calculations confirm the increase in conductivity through the band gap values obtained from all phases in the four systems considered in this study. Another significant result is the increase in real permittivity, indicating an improvement in energy storage capacity as lithium and organic materials are added.

The DRT analysis revealed the existence of two distinct electrochemical processes in all samples. Furthermore, the agreement with the equivalent circuits modeled using ZView confirmed the grain and grain boundary behavior of the samples.

In summary, both experimental and theoretical results consistently indicate improved properties for solid-state electrolyte applications,

following lithium doping and the use of a technique that preserves organic phases even after high-temperature thermal treatment. Due to experimental constraints, this study did not distinguish between ionic and electronic contributions to the overall conductivity. This limitation represents an area for improvement of the present work, as the use of ion- and electron-blocking electrodes would allow a more accurate decoupling of these transport mechanisms. Therefore, future studies should include such configurations to enable a detailed analysis of the dominant conduction pathways.

CRediT authorship contribution statement

Jardson Braz da Silva: Writing – original draft, Methodology, Investigation, Formal analysis, Conceptualization. **Juliana Pereira da Silva:** Writing – original draft, Methodology, Investigation. **Rodrigo Lavareda dos Santos:** Validation, Investigation, Formal analysis. **Salomão dos Santos Costa:** Methodology, Investigation, Conceptualization. **Yan Matheus Colares Pinto:** Investigation, Formal analysis, Data curation. **Marcos Vinicius Passos Colares:** Methodology, Investigation, Data curation. **Ruan Carlos Ambrosio Raposo:** Methodology, Investigation, Formal analysis. **Francisco Xavier Nobre:** Methodology, Formal analysis, Conceptualization. **Monica Tirado:** Writing – review & editing, Methodology, Formal analysis. **Angsula Ghosh:** Writing – review & editing, Supervision, Investigation, Formal analysis. **Lianet Aguilera Domínguez:** Writing – review & editing, Investigation, Conceptualization. **Ramo'n Raudel Peña Garcia:** Investigation, Formal analysis, Data curation. **Yurimiler Leyet Ruiz:** Writing – review & editing, Supervision, Methodology, Conceptualization.

Declaration of competing interest

The authors declare that they have no known competing financial interests or personal relationships that could have appeared to influence the work reported in this paper.

Acknowledgements

This study was financed in part by the "Coordenacão de Aperfeicoamento de Pessoal de Nível Superior - Brasil (CAPES)" - Finance Code 001. The authors would like to thank "Fundac,a~o de Amparo a' Pesquisa do Estado do Amazonas" and "Conselho Nacional de Desenvolvimento Científico e Tecnolo'gico" for their financial support.

Data availability

Data will be made available on request.

References

[1] H. Sun, S. Kang, L. Cui, Prospects of LLZO type solid electrolyte: from material design to battery application, Chem. Eng. J. 454 (2023) 140375, https://doi.org/10.1016/j.cej.2022.140375.

[2] H.K. Tran, B.T. Truong, B.-R. Zhang, R. Jose, J.-K. Chang, C.-C. Yang, Sandwich-structured composite polymer electrolyte based on pvdf-hfp/ppc/al-doped llzo for high-voltage solid-state lithium batteries, ACS Appl. Energy Mater. 6 (3) (2023) 1475–1487, https://doi.org/10.1021/acsaem.2c03363.

[3] F.H. Alkallas, S.M. Alghamdi, O. Albeydani, E.A. Rashed, E. Alsubhe, A.B. G. Trabelsi, E.A. Mwafy, W. Elsharkawy, A.M. Mostafa, Studying the effect of addition of lithium titanate on crystallinity and electrical properties of ppy-c/pva nanocomposite for optoelectronic applications, J. Mater. Res. Technol. 28 (2024) 3414–3421, https://doi.org/10.1016/j.jmrt.2023.12.241.

[4] N.S. Al-Kadhi, R.A. Pashameah, E.A. Mwafy, A.N. Al-Ahmadi, H.A. Ahmed, A. M. Mostafa, F.S. Alamro, R.A. Rezk, Spinel lithium titanate anode/polyether sulfone nanocomposite synthesized by pulsed laser ablation method for optoelectronic applications, J. Saudi Chem. Soc. 27 (3) (2023) 101626, https://doi.org/10.1016/j.jscs.2023.101626.

[5] Y.-S. Choi, S.I.R. Costa, N. Tapia-Ruiz, D.O. Scanlon, Intrinsic defects and their role in the phase transition of na-ion anode $Na_2Ti_3O_7$, ACS Appl. Energy Mater. 6 (1) (2022) 484–495, https://doi.org/10.1021/acsaem.2c02090.

[6] A.D. Melo, J.P. da Silva, F.X. Nobre, S. Costa, J.C.C. Sales Jr., J. Anglada-Rivera, F. Guerrero, M.M. da S. Paula, R.F.B. de Souza, R. Pena-Garcia, et al., Synthesis microwave-assisted: fast method to obtain lithium-doped sodium titanate, J. Mater. Sci. Mater. Electron. 34 (6) (2023) 537, https://doi.org/10.1007/s10854-023-09948-w.

[7] C. Wu, Y. Xia, K. Song, Y. Cao, C. Huang, J. Chen, Y. Wang, C. Xu, Improving $Na_2Ti_3O_7$ anode performance in sodium-ion batteries via a al doping, Nanomaterials 15 (12) (2025) 885, https://doi.org/10.3390/nano15120885.

[8] J.P. da Silva, S. Costa, F.X. Nobre, E.A. Sanches, M.M.d.S. Paula, L. Aguilera, M. S. Torikachvili, Y. Leyet, Poly (o-methoxyaniline) modified by the biphasic ceramic system $Na_2Ti_3O_7/Na_2Ti_6O_{13}$, J. Inorg. Organomet. Polym. Mater. 33 (5) (2023) 1381–1387, https://doi.org/10.1007/s10904-023-02608-w.

[9] J. Da Silva, M. Biondo, F. Nobre, J. Anglada-Rivera, A. Almeida, J. Agostinho-Moreira, E. Sanches, M.d.S. Paula, L. Aguilera, Y. Leyet, Structure and electrical properties of the composite $Na_2Ti_3O_7/Na_2Ti_6O_{13}$/poma: a study of the effect of adding poma, J. Alloys Compd. 867 (2021) 159025, https://doi.org/10.1016/j.jallcom.2021.159025.

[10] S. Dos Santos Costa, J. Pereira da Silva, M. Moraes Biondo, E.A. Sanches, M.M. Da Silva Paula, F. Xavier Nobre, J. Anglada Rivera, Y. Alexis Zulueta, M. S. Torikachvili, D. Vieira Sampaio, et al., Temperature dependence of the electrical properties of $Na_2Ti_3O_7/Na_2Ti_6O_{13}$/poma composites, Molecules 27 (18) (2022) 5756, https://doi.org/10.3390/molecules27185756.

[11] Y. Leyet, F. Guerrero, J. Anglada-Rivera, R. De Souza, W. Brito, L. Aguilera, L. Pocrifka, R. Peña-Garcia, E. Padrón-Hernández, J. De La Cruz Pérez, Synthesis of $Na_2Ti_3O_7$ nanoparticles by sonochemical method for solid state electrolyte applications, J. Solid State Electrochem. 22 (2018) 1315–1319, https://doi.org/10.1007/s10008-017-3697-x.

[12] P. Giannozzi, S. Baroni, N. Bonini, M. Calandra, R. Car, C. Cavazzoni, D. Ceresoli, G.L. Chiarotti, M. Cococcioni, I. Dabo, et al., Quantum espresso: a modular and open-source software project for quantum simulations of materials, J. Phys. Condens. Matter 21 (39) (2009) 395502, https://doi.org/10.1088/0953-8984/21/39/395502.

[13] M.C. Payne, M.P. Teter, D.C. Allan, T. Arias, a.J. Joannopoulos, Iterative minimization techniques for ab initio total-energy calculations: molecular dynamics and conjugate gradients, Rev. Mod. Phys. 64 (4) (1992) 1045, https://doi.org/10.1103/RevModPhys.64.1045.

[14] H.J. Monkhorst, J.D. Pack, Special points for brillouin-zone integrations, Phys. Rev. B 13 (12) (1976) 5188, https://doi.org/10.1103/PhysRevB.13.5188.

[15] A. Kokalj, Computer graphics and graphical user interfaces as tools in simulations of matter at the atomic scale, Comput. Mater. Sci. 28 (2) (2003) 155–168, https://doi.org/10.1016/S0927-0256(03)00104-6.

[16] K. Momma, F. Izumi, Vesta 3 for three-dimensional visualization of crystal, volumetric and morphology data, Applied Crystallography 44 (6) (2011) 1272–1276, https://doi.org/10.1107/S0021889811038970.

[17] R.N. Karunarathne, T. Pathirana, H. Wijayasinghe, M. Dissanayake, $Na_2Ti_3O_7$ nano fibres as an anode material for rechargeable na-ion batteries, Ceylon Journal of Science 47 (2) (2018) 125–128, https://doi.org/10.4038/cjs.v47i2.7507.

[18] X. Ma, Y. Liu, Y. Zhang, Y. Gong, Layered sodium titanate with a matched lattice: a single ion conductor in a solid-state sodium metal battery, Chem. Sci. 14 (47) (2023) 13812–13824, https://doi.org/10.1039/D3SC04355J.

[19] H. Zhong, F. Pan, S. Yue, C. Qin, V. Hadjiev, F. Tian, X. Liu, F. Lin, Z. Wang, J. Bao, Idealizing tauc plot for accurate bandgap determination of semiconductor with ultraviolet–visible spectroscopy: a case study for cubic boron arsenide, J. Phys. Chem. Lett. 14 (29) (2023) 6702–6708, https://doi.org/10.1021/acs.jpclett.3c01416.

[20] R.A. Zárate, S. Fuentes, A.L. Cabrera, V.M. Fuenzalida, Structural characterization of single crystals of sodium titanate nanowires prepared by hydrothermal process, J. Cryst. Growth 310 (15) (2008) 3630–3637, https://doi.org/10.1016/j.jcrysgro.2008.05.020.

[21] S. Ghosh, Sonochemically synthesized $Na_2Ti_6O_{13}$ nanorod: an efficient electrode material for Na-ion battery, Bull. Mater. Sci. 43 (1) (2020) 251, https://doi.org/10.1007/s12034-020-02215-2.

[22] L. Basilio, J. Silva, F. Xavier, L. Aguilera, F. Guerrero, E. Antonelli, J. Anglada-Rivera, J. Garcia, R. Silva, Y. Leyet, Toward a new ptcr material based on the $Na_2Ti_6O_{13}/Na_2Ti_3O_7$ system, Mater. Res. Bull. 140 (2021) 111311, https://doi.org/10.1016/j.materresbull.2021.111311.

[23] S. Chaar, J. Da Silva, F. Nobre, J. Passos, L. Aguilera, J. Silva, R. Silva, F. Guerrero, F. Pontes, Y. Leyet, Sonochemical synthesis and characterization of the biphasic compound $Na_2Ti_3O_7/Na_2Ti_6O_{13}$, Mater. Res. 24 (suppl 1) (2021) e20210011, https://doi.org/10.1590/1980-5373-mr-2021-0011.

[24] L. Basilio, F. Xavier, J. Sales Jr., J. Andrade, J. Anglada-Rivera, L. Aguilera, R. Silva, J. Rodriguez-Hernandez, J.P. de la Cruz, Y. Leyet, Fast synthesis of $Na_2Ti_3O_7$ system synthesized by microwave-assisted hydrothermal method: electrical properties, Ceram. Int. 46 (15) (2020) 23834–23839, https://doi.org/10.1016/j.ceramint.2020.06.160.

[25] M. Albert, A. Clifford, I. Zhitomirsky, O. Rubel, Adsorption of maleic acid monomer on the surface of hydroxyapatite and TiO_2: a pathway toward biomaterial composites, ACS Appl. Mater. Interfaces 10 (29) (2018) 24382–24391, https://doi.org/10.1021/acsami.8b05128.

[26] J.S. Ko, V.V. Doan-Nguyen, H.-S. Kim, G.A. Muller, A.C. Serino, P.S. Weiss, B. S. Dunn, $Na_2Ti_3O_7$ nanoplatelets and nanosheets derived from a modified exfoliation process for use as a high-capacity sodium- ion negative electrode, ACS Appl. Mater. Interfaces 9 (2) (2017) 1416–1425, https://doi.org/10.1021/acsami.6b10790.

[27] J. Pan, N. Wang, D. Lv, W. Dong, J. Yang, F. Huang, Layered structure $Na_2Ti_3O_7$ as a promising anode material for sodium-ion batteries, Adv. Energy Sustain. Res. 2 (6) (2021) 2000095, https://doi.org/10.1002/aesr.202000095.

[28] H. Pan, X. Lu, X. Yu, Y.-S. Hu, H. Li, X.-Q. Yang, L. Chen, Sodium storage and transport properties in layered na2ti3o7 for room-temperature sodium-ion batteries, Adv. Energy Mater. 3 (9) (2013) 1186–1194, https://doi.org/10.1002/aenm.201300139.

[29] W. Yin, J. Ahn, G. Barim, J. Alvarado, M.M. Doeff, Tailoring stepped layered titanates for sodium-ion battery applications, Acc. Mater. Res. 5 (8) (2024) 933–943, https://doi.org/10.1021/accountsmr.4c00080.

[30] A. Rudola, K. Saravanan, S. Devaraj, H. Gong, P. Balaya, $Na_2Ti_6O_{13}$: a potential anode for grid-storage sodium- ion batteries, Chem. Commun. 49 (67) (2013) 7451–7453, https://doi.org/10.1039/C3CC44381G.

[31] S. Stanchovska, M. Kalapsazova, S. Harizanova, V. Koleva, R. Stoyanova, Design of sodium titanate nanowires as anodes for dual li, na ion batteries, Batteries 9 (5) (2023) 271, https://doi.org/10.3390/batteries9050271.

[32] K. Eggestad, S.M. Selbach, B.A. Williamson, Doping implications of li solid state electrolyte $Li_7La_3Zr_2O_{12}$, J. Mater. Chem. A 12 (26) (2024) 15666–15675, https://doi.org/10.1039/D4TA01487A.

[33] L.J. Miara, S.P. Ong, Y. Mo, W.D. Richards, Y. Park, J.-M. Lee, H.S. Lee, G. Ceder, Effect of rb and ta doping on the ionic conductivity and stability of the garnet $Li_{7+x-y}(La^{3+-x}Rb^x)(Zr^{2-y}Ta^y)O_{12}$ (0 x 0.375, 0 y 1) superionic conductor: a first principles investigation, Chem. Mater. 25 (15) (2013) 3048–3055, https://doi.org/10.1021/cm401232r.

[34] M.M. Raju, F. Altayran, M. Johnson, D. Wang, Q. Zhang, Crystal structure and preparation of li7la3zr2o12 (llzo) solid-state electrolyte and doping impacts on the conductivity: an overview, Electrochem 2 (3) (2021) 390–414, https://doi.org/10.3390/electrochem2030026.

[35] M.T. Hayajneh, F.M. AL-Oqla, M.M. Al-Shrida, Hybrid green organic/inorganic filler polypropylene composites: morphological study and mechanical performance investigations, E-Polymers 21 (1) (2021) 710–721, https://doi.org/10.1515/epoly-2021-0074.

[36] M. Dulski, K. Malarz, M. Kuczak, K. Dudek, K. Matus, S. Sułowicz, A. Mrozek-Wilczkiewicz, A. Nowak, An organic–inorganic hybrid nanocomposite as a potential new biological agent, Nanomaterials 10 (12) (2020) 2551, https://doi.org/10.3390/nano10122551.

[37] C.D. de Abreu Lima, R. dos Santos Sousa, A.W. Miranda, J.V.B. Moura, G. de Sousa Pinheiro, B.C. Viana, I.S. Lima, T.M.B.F. Oliveira, O. Baffa, J.F.D.F. Araujo, et al., Synthesis, characterization, and thermal stability study of sodium and sodium–aluminum titanate nanotubes, Solid State Sci. 138 (2023) 107134, https://doi.org/10.1016/j.solidstatesciences.2023.107134.

[38] S. Ali, H. Granbohm, Y. Ge, V.K. Singh, F. Nilsén, S. Hannula, Crystal structure and photocatalytic properties of titanate nanotubes prepared by chemical processing and subsequent annealing, J. Mater. Sci. 51 (15) (2016) 7322–7335, https://doi.org/10.1007/s10853-016-0014-5.

[39] F.L.R. Silva, A.A.A.A. Filho, M.B. Silva, K. Balzuweit, J.-L. Bantignies, E.W. S. Caetano, R.L. Moreira, V.N. Freire, A. Righi, Polarized raman, ftir, and dft study of $Na_2Ti_3O_7$ microcrystals, J. Raman Spectrosc. 49 (3) (2018) 538–548, https://doi.org/10.1002/jrs.5316.

[40] M. Doeff, M. Shirpour, J. Cabana, New materials based on a layered sodium titanate for dual electrochemical na and li intercalation systems, Energy Environ. Sci. 6 (2013) 2538–2547, https://doi.org/10.1039/C3EE41037D.

[41] B.C. Viana, O.P. Ferreira, A.G. Souza Filho, A.A. Hidalgo, J. Mendes Filho, O. L. Alves, Alkali metal intercalated titanate nanotubes: a vibrational spectroscopy study, Vib. Spectrosc. 55 (2) (2011) 183–187, https://doi.org/10.1016/j.vibspec.2010.11.007.

[42] B.H. Stuart, Infrared Spectroscopy: Fundamentals and Applications, 1st Edition, Analytical Techniques in the Sciences, John Wiley & Sons, Hoboken, NJ, USA, 2004, https://doi.org/10.1002/0470011149.

[43] R.M. Silverstein, F.X. Webster, D.J. Kiemle, D.L. Bryce, Spectrometric Identification of Organic Compounds, eighth ed., John Wiley & Sons, Hoboken, NJ, 2014.

[44] P.R. Griffiths, Fourier transform infrared spectrometry, Science 222 (4621) (1983) 297–302, https://doi.org/10.1126/science.6623077.

[45] L. Zhao, H. Dai, F. Pei, P. Ming, X. Wei, J. Zhou, A comparative study of equivalent circuit models for electro- chemical impedance spectroscopy analysis of proton exchange membrane fuel cells, Energies 15 (1) (2022) 386, https://doi.org/10.3390/en15010386.

[46] M. Schalenbach, Y.E. Durmus, H. Tempel, H. Kungl, R.-A. Eichel, Double layer capacitances analysed with impedance spectroscopy and cyclic voltammetry: validity and limits of the constant phase element parameterization, Phys. Chem. Chem. Phys. 23 (37) (2021) 21097–21105, https://doi.org/10.1039/D1CP03381F.

[47] Y. Xiao, X. Huang, J. Meng, Y. Zhang, V. Knap, D.-I. Stroe, Electrochemical impedance spectroscopy-based characterization and modeling of lithium-ion batteries based on frequency selection, Batteries 11 (1) (2024) 11, https://doi.org/10.3390/batteries11010011.

[48] Y. Zhao, V. Kumtepeli, S. Ludwig, A. Jossen, Investigation of the distribution of relaxation times of a porous electrode using a physics-based impedance model, J. Power Sources 530 (2022) 231250, https://doi.org/10.1016/j.jpowsour.2022.231250.

[49] L. Yesappa, M. Niranjana, S. Ashokkumar, H. Vijeth, M. Basappa, P. Vc, S. Ganesh, H. Devendrappa, et al., Optical properties and ionic conductivity studies of an 8 mev electron beam irradiated poly (vinylidene fluoride- co-hexafluoropropylene)/$LiClO_4$ electrolyte film for opto-electronic applications, RSC Adv. 8 (28) (2018) 15297–15309, https://doi.org/10.1039/C8RA00970H.

[50] D.M. Babiker, Z.R. Usha, C. Wan, M.M.E. Hassaan, X. Chen, L. Li, Recent progress of composite polyethylene separators for lithium/sodium batteries, J. Power Sources 564 (2023) 232853, https://doi.org/10.1016/j.jpowsour.2023.232853.

[51] E. Barsoukov, J.R. Macdonald, Impedance Spectroscopy: Theory, Experiment, and Applications, second ed., John Wiley & Sons, Hoboken, NJ, USA, 2005 https://doi.org/10.1002/0471716243.

[52] M. Molina-Ruiz, Y. Rosen, H. Jacks, M. Abernathy, T. Metcalf, X. Liu, J. DuBois, F. Hellman, Origin of mechanical and dielectric losses from two-level systems in amorphous silicon, Phys. Rev. Mater. 5 (3) (2021) 035601, https://doi.org/10.1103/PhysRevMaterials.5.035601.

[53] L. Lei, C. Chen, H. Nie, X. Wu, D.Q. Tan, Dielectric loss and electrical conductivity behaviors of epoxy composites containing semiconducting zno varistor particles, Molecules 27 (18) (2022) 6067, https://doi.org/10.3390/molecules27186067.

[54] M. Samet, A. Kallel, A. Serghei, Maxwell-wagner-sillars interfacial polarization in dielectric spectra of composite materials: scaling laws and applications, J. Compos. Mater. 56 (20) (2022) 3197–3217, https://doi.org/10.1177/00219983221090629.

[55] D. Scheunemann, E. Järsvall, J. Liu, D. Beretta, S. Fabiano, M. Caironi, M. Kemerink, C. Müller, Charge transport in doped conjugated polymers for organic thermoelectrics, Chemical Physics Reviews 3 (2) (2022) 021309, https://doi.org/10.1063/5.0080820.

[56] M. Comin, S. Fratini, X. Blase, G. d'Avino, Doping-induced dielectric catastrophe prompts free-carrier release in organic semiconductors, Adv. Mater. 34 (2) (2022) 2105376, https://doi.org/10.1002/adma.202105376.

[57] L. Yuan, Y. Xia, T. Zhang, D. Han, C. Fang, D. Zuo, Effect of doping ion concentration on the microstructure and dielectric properties of $(Na_{1/2}Eu_{1/2})_xCa_{1-x}Cu_3Ti_4O_{12}$ ceramics, J. Mater. Sci. Mater. Electron. 35 (11) (2024) 751, https://doi.org/10.1007/s10854-024-12485-9.

[58] T.A. Skotheim, J.R. Reynolds (Eds.), Handbook of Conducting Polymers, third ed., CRC Press, Boca Raton, FL, USA, 2007 https://doi.org/10.1201/b12346, 2.

[59] K.-D. Kreuer, Proton conductivity: materials and applications, Chem. Mater. 8 (3) (1996) 610–641, https://doi.org/10.1021/cm950192a.

[60] J.B. Goodenough, K.-S. Park, The li-ion rechargeable battery: a perspective, J. Am. Chem. Soc. 135 (4) (2013) 1167–1176, https://doi.org/10.1021/ja3091438.

[61] C. Plank, T. Rüther, L. Jahn, M. Schamel, J.P. Schmidt, F. Ciucci, M.A. Danzer, A review on the distribution of relaxation times analysis: a powerful tool for process identification of electrochemical systems, J. Power Sources 594 (2024) 233845, https://doi.org/10.1016/j.jpowsour.2023.233845.

[62] M. Hahn, S. Schindler, L.-C. Triebs, M.A. Danzer, Optimized process parameters for a reproducible distribution of relaxation times analysis of electrochemical systems, Batteries 5 (2) (2019) 43, https://doi.org/10.3390/batteries5020043.

[63] D.Y. Semerukhin, A. Kubarkov, V. Sergeyev, O. Semenikhin, E. Antipov, Analysis of the distribution of relaxation times (drt) responses of li-ion cells as a function of their preparation conditions, Electrochim. Acta 486 (2024) 144092, https://doi.org/10.1016/j.electacta.2024.144092.

[64] T. Paul, P. Chi, P.M. Wu, M. Wu, Computation of distribution of relaxation times by tikhonov regularization for li ion batteries: usage of l-curve method, Sci. Rep. 11 (1) (2021) 12624, https://doi.org/10.1038/s41598-021-91871-3.

[65] E. Goldammer, J. Kowal, Determination of the distribution of relaxation times by means of pulse evaluation for offline and online diagnosis of lithium-ion batteries, Batteries 7 (2) (2021) 36, https://doi.org/10.3390/batteries7020036.

[66] Y. Lin, C. Chai, Z. Liu, J. Wang, S. Jin, Y. Yang, Y. Gao, M. Hao, X. Li, Y. Hou, et al., Large low-field- driven electrocaloric effect in organic-inorganic hybrid tmcm-$CdCl_3$, Nat. Commun. 16 (1) (2025) 4009, https://doi.org/10.1038/s41467-025-58914-z.

[67] F. Wu, A. Xie, L. Jiang, S. Mukherjee, H. Gao, J. Shi, J. Wu, H. Shang, Z. Sheng, R. Guo, et al., Inorganic– organic hybrid dielectrics for energy conversion: mechanism, strategy, and applications, Adv. Funct. Mater. 33 (28) (2023) 2212861, https://doi.org/10.1002/adfm.202212861.

[68] M. Romero, D. Mombrú, F. Pignanelli, R. Faccio, A.W. Mombrú, Hybrid organic-inorganic materials and interfaces with mixed ionic-electronic transport properties: advances in experimental and theoretical approaches, Front. Chem. 10 (2022) 892013, https://doi.org/10.3389/fchem.2022.892013.

ANNEX C – PUBLISHED ARTICLE — LLZO/POMA COMPOSITE SYSTEM

This annex presents the published article reporting the investigation of the LLZO/POMA composite system discussed in this thesis.

Journal of Applied Polymer Science

WILEY

Applied Polymer SCIENCE

RESEARCH ARTICLE

Interfacial Driven Electrical Transport in Mg/Sr-Doped LLZO/POMA Hybrid Composites

Jardson Braz da Silva[1,2] | Juliana Pereira da Silva[2] | Yan Matheus Colares Pinto[2] | Ronald Zico de Aguiar Nunes[2] | Fidel Guerrero Zayas[1] | Francisco Xavier Nobre[3] | Monica Tirado[4] | Ramon Raudel Peña Garcia[5] | Eduardo Antonelli[6] | Lianet Aguilera Dominguez[2] | Yurimiler Leyet Ruiz[2]

[1]Departamento de Física de Materiais, Instituto de Ciências Exatas, Universidade Federal do Amazonas (UFAM), Manaus, State of Amazonas, Brazil | [2]Laboratório de Processamento de Materiais Tecnológicos, Departamento de Engenharia de Materiais, Universidade Federal do Amazonas (UFAM), Manaus, State of Amazonas, Brazil | [3]Instituto Federal de Educação, Ciência e Tecnologia do Amazonas, Manaus, State of Amazonas, Brazil | [4]Universidad Nacional de Tucumán (UNT), Facultad de Ciencias Exactas y Tecnología (FACET) and Instituto de Física del Noroeste Argentino: INFINOA (UNT-CONICET), San Miguel de Tucumán, Argentina | [5]Universidade Federal Rural de Pernambuco, Unidade Acadêmica do Cabo de Santo Agostinho, Cabo de Santo Agostinho, State of Pernambuco, Brazil | [6]Department of Science and Technology, Polymer and Biopolymer Technology Laboratory (TecPBio), Federal University of São Paulo (UNIFESP), São José dos Campos, São Paulo, Brazil

Correspondence: Yurimiler Leyet Ruiz (yurileyet@yahoo.es)

Received: 9 March 2026 | **Revised:** 24 June 2026 | **Accepted:** 29 June 2026

Keywords: electrical conductivity | impedance spectroscopy | Mg/Sr doped LLZO | polymer/ceramic interfaces | POMA composites

ABSTRACT

In contrast to previous LLZO/POMA studies, this work investigates a distinct Mg/Sr-doped LLZO composition using a multiscale characterization approach combining Rietveld bond-length analysis, DSC-based thermal mapping, and impedance modeling. This strategy provides new insights into the structural mechanisms governing the electrical behavior of POMA-modified garnet composites. The materials were characterized by x-ray diffraction (XRD) with Rietveld refinement, scanning electron microscopy (SEM), Fourier transform infrared spectroscopy (FTIR), energy dispersive x-ray spectroscopy (EDS), thermogravimetric analysis (TG/DTG), differential scanning calorimetry (DSC), and complex impedance spectroscopy. XRD results revealed the predominance of cubic $Li_7La_3Zr_2O_{12}$, with minor tetragonal LLZO and secondary phases (Li_2CO_3 and LiOH), consistent with LLZO reactivity toward atmospheric moisture and CO_2. SEM analysis showed notable morphological changes after POMA incorporation, while EDS and FTIR confirmed the elemental composition and vibrational signatures of the identified phases. TG/DTG results indicated increasing mass loss with higher POMA content. Impedance spectroscopy revealed a two-order-of-magnitude increase in grain conductivity, reaching $2.66 \times 10^{-6}\,S{\cdot}cm^{-1}$. These results highlight the effectiveness of POMA incorporation in enhancing the electrical performance of LLZO-based composites.

1 | Introduction

Lithium lanthanum zirconate ($Li_7La_3Zr_2O_{12}$, LLZO) has been extensively investigated due to its high ionic conductivity and chemical stability against metallic lithium, characteristics that make it one of the most promising solid electrolytes for next-generation solid-state batteries [1, 2]. Since the pioneering study by [1] reporting fast Li^+ transport in LLZO, numerous works have explored the influence of synthesis routes, dopant chemistry, and defect engineering strategies on stabilizing the cubic garnet phase, which presents ionic conductivities several orders of magnitude higher than those of the tetragonal modification [1, 3]. Despite these advances, persistent challenges remain, including limited densification, lithium volatilization during high temperature processing, and thermal instability, thereby motivating the development of refined doping strategies and improved processing control [3, 4]. In particular, Mg/Sr co-doping has emerged as a promising strategy for enhancing the

© 2026 Wiley Periodicals LLC.

All rights reserved, including rights for text and data mining and training of artificial intelligence technologies or similar technologies.

structural stability and overall performance of LLZO-based materials [5–7].

In parallel, conducting polymers have gained increasing attention in the context of solid state battery materials. These polymers offer intrinsically lower interfacial resistances than purely ceramic electrolytes, while being lightweight, easily synthesized, and compatible with flexible processing routes. Importantly, they retain the key safety advantages of solid electrolytes, namely the absence of leakage and flammability hazards, making them attractive candidates for forming hybrid polymer ceramic composites [8].

In this context, POMA an o-methoxy derivative of polyaniline (PANI) stands out due to its relatively high electrical conductivity, with reported values on the order of 10^{-2} S·cm^{-1} [9]. This behavior originates from its conjugated backbone, which, upon protonation or oxidative doping, forms polarons: quasiparticles consisting of a localized charge (electron or hole) coupled to a distortion of the polymer chain. Electroneutrality is maintained by counterions introduced during the doping process. Under an external electric field, these polarons migrate along the conjugated chain through successive rearrangements of single and double bonds, enabling efficient charge transport (Figure 1b) [9, 10].

Ceramic and polymeric materials each exhibit characteristic advantages and limitations when employed as solid electrolytes. Consequently, polymer/ceramic composites have attracted growing interest, as they combine the mechanical and thermal robustness of ceramics with the improved interfacial and processing properties of polymers. In the specific case of POMA, an additional benefit has been reported: its incorporation can enhance the electrical performance of LLZO based systems [11]. While polymer addition to ceramic matrices often decreases conductivity [12], the inclusion of LLZO in polymer matrices typically leads to conductivity enhancement [13]. Although charge transport in POMA is primarily electronic, the polymer introduces interfacial regions where charge-carrier mobility is significantly modified. At these polymer/ceramic interfaces, a localized weakening of Li—O interactions may occur, increasing the mobility of Li^+ ions near the LLZO grain surfaces (Figure 1c). As a result, the composite may exhibit improved overall electrical conductivity due to synergistic interfacial effects [14].

This work differs fundamentally from previous LLZO/polymer composite studies, including Reference [14] and systems based on PVDF, PEO, PAN, or PVDF-HFP, by investigating a distinct Mg/Sr co-doped LLZO composition and adopting a substantially more comprehensive multiscale characterization strategy. In contrast to our earlier publication, the present study integrates full Rietveld refinement with bond length and polyhedral distortion analyses, detailed TG/DTG/DSC thermal mapping, and a combined two ZARC and Jonscher impedance modeling approach to decouple grain, grain-boundary, and interfacial relaxation processes.

Moreover, a broader range of POMA incorporation (1–15 wt%) is examined, revealing previously unreported morphological evolution pathways and polymer–ceramic interfacial effects. Collectively, these compositional and methodological advances provide new insights into structure–property relationships that were not captured in earlier LLZO/POMA studies.

In summary, this work reports the synthesis of Mg/Sr co-doped LLZO and chlorine-doped POMA (POMA-Cl), as well as the preparation of LLZO/POMA composites with different polymer loadings. A comprehensive multiscale characterization approach was employed to investigate the structural, morphological, thermal, and electrical modifications of the ceramic phase resulting from polymer incorporation.

2 | Experimental Methods

The synthesis of doped LLZO was carried out using high-purity commercial reagents: La_2O_3 (Dinaˆmica, 99.9%), ZrO_2 (Sigma-Aldrich, 99%, 5 μm), Li_2CO_3 (Labsynth, 99%), MgO (Vetec and Sigma-Aldrich, 95%), and Sr $(C_2H_3O_2)_2$ (Vetec, 98%). The stoichiometry was calculated based on cation substitution, following the formula $Li_{6.95}Mg_{0.15}La_{2.75}Sr_{0.25}Zr_2O_{12}$, which exhibits satisfactory electrical conductivity and densification above 90% [15]. To compensate for possible lithium losses during the process, an excess of 12.9% Li_2CO_3 was added, corresponding to 0.4 g per 10 g of the final product. The reagents were homogenized by ball milling for 36 h, dried, and calcined at 1000°C for 4 h. The calcined powder was subsequently remilled for 36 h to improve homogeneity and control particle size. To minimize lithium evaporation during calcination, the crucible was covered

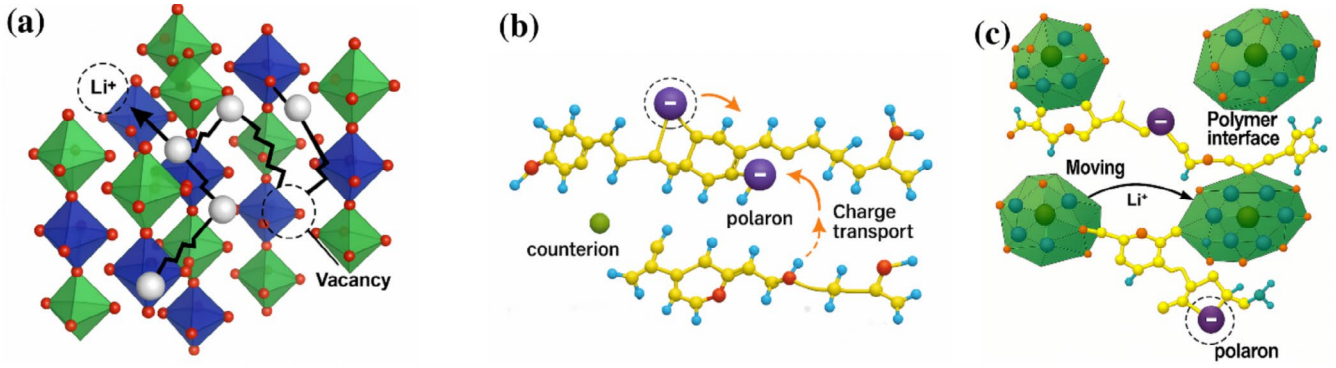


FIGURE 1 | Schematic representation of the charge transport mechanisms in the studied systems: (a) Lithium-ion migration through vacancies in the LLZO lattice, (b) electronic transport by polarons along the polymeric chain, and (c) interfacial charge transfer and Li^+ migration across the ceramic–polymer interface. [Color figure can be viewed at wileyonlinelibrary.com]

and sealed with a layer of alumina powder containing polyvinyl alcohol (PVA).

The synthesis of POMA was carried out following the method described by [16, 17]. A solution containing 28 mL of o-anisidine ($CH_3OC_6H_4NH_2$, Sigma-Aldrich, 99%) in 300 mL of hydrochloric acid (HCl, Synth, 37%) at 1 mol L^{-1} was prepared. Then, a solution of 11.64 g of ammonium persulfate ($(NH_4)_2S_2O_8$, Sigma-Aldrich, 98%) in 200 mL of 1 mol L^{-1} HCl was added dropwise to the o-anisidine solution. Subsequently, the mixture was stirred for 3 h. The resulting solution was vacuum filtered using an oil-less diaphragm pump and washed with distilled water to remove excess acid. Finally, the sample was dried in a vacuum chamber for 5 days, resulting in a final powder.

For the production of the composites, the LLZO ceramic matrix was mixed with POMA in different mass percentages of POMA in 0, 1, 5, 10, and 15 wt% for the samples LLZO, LLZO/POMA-1, LLZO/POMA-5, LLZO/POMA-10, and LLZO/POMA-15, respectively. The dispersion was carried out in 10 mL of distilled water per gram of the powder mixture. The mixture was homogenized in an ultrasonic bath for 15 min and then dried in an oven at 40°C for 24 h to obtain the final powder.

X-ray diffraction (XRD) measurements were conducted using a Panalytical Empyrean diffractometer equipped with copper (Cu) and molybdenum (Mo) radiation sources. The instrument was configured with Cu K_α radiation ($\lambda = 1.5406$ Å) and operated in Bragg-Brentano geometry. Data collection was carried out over a 2θ range from 5° to 80°.

Scanning electron microscopy (SEM) images were obtained using a JSM-IT500HR microscope operated at 5 kV. Polymeric samples were coated with a 10 nm gold layer prior to analysis.

The FTIR measurements were carried out using a Fourier Transform Infrared Spectrometer (Cary 630, Agilent Technologies, USA). The scans were performed over a spectral range of 4000–650 cm^{-1} using Attenuated Total Reflectance (ATR) with a zinc selenide (ZnSe) crystal, with the sample horizontally positioned close to the prism ($d = 1.8$ mm).

The thermal analyses were performed using a TA Instruments SDT Q600. The samples, with an approximate mass of 10 mg, were heated at 10°C min^{-1} from room temperature to 1200°C, with a 10 min isothermal hold. The experiment was conducted under a nitrogen gas flow (N_2 5.0) at a rate of 30 mL min^{-1}. A 90 μL alumina crucible without a lid was used.

Complex impedance measurements were carried out in ambient air at room temperature using a Solartron 1260 impedance analyzer, with an excitation amplitude of 500 mV and a frequency range from 10 Hz to 1 MHz. The pellets were prepared by uniaxial pressing under a load of 1.5 tons, and brass electrodes from a Solartron 12962A sample holder were used during the measurements. All samples had a diameter of 15 mm and a thickness of approximately 1.50 mm. No metallic coating was applied to the samples prior to the impedance measurements.

3 | Results and Discussion

Figure 2 presents the x-ray diffraction patterns, Rietveld refinement profiles of all samples, and the corresponding unit cell representations generated in VESTA [18] using experimentally refined crystallographic information files (CIFs). In Figure 2a, the black curve corresponds to unmodified LLZO, while the red, blue, dark yellow, and purple curves represent LLZO containing 1, 5, 10, and 15 wt% of POMA, respectively.

Several characteristic reflections were highlighted using Miller indices to illustrate the evolution of the crystalline phases as the POMA content increases. The first intense peak, located at $2\theta \approx 16.6°$, corresponds to the (211) reflection of $Li_7La_3Zr_2O_{12}$, which is common to both the cubic and tetragonal polymorphs [19]. Its strong intensity in all samples confirms that the LLZO garnet structure remains the dominant crystalline phase throughout the composite series.

Reflections indexed as (220) ($2\theta \approx 19.1°$) and (004) ($2\theta \approx 28.1°$), highlighted in green in the LLZO/POMA-5 pattern, are characteristic of the tetragonal modification of LLZO. The presence of these peaks in all samples indicates the persistence of a minor tetragonal fraction, a phenomenon widely reported in the literature for garnets synthesized under similar conditions [20, 21].

Additional reflections at $2\theta \approx 21.4°$ and 23.9°, indexed as (110) and (200) and highlighted in blue, correspond to Li_2CO_3. The detection of these peaks in all samples is consistent with previous reports describing the spontaneous formation of Li_2CO_3 on LLZO surfaces exposed to atmospheric CO_2 and moisture [22–25]. Similarly, the reflection at $2\theta \approx 20.3°$, indexed as (001) (yellow), is attributed to LiOH, which forms according to Equation (1) through the reaction of LLZO with water [24]:

$$Li_7La_3Zr_2O_{12} + xH_2O \rightarrow Li_{7-x}H_xLa_3Zr_2O_{12} + xLiOH \quad (1)$$

Subsequently, LiOH reacts with CO_2 in air to produce Li_2CO_3, as described in Equation (2) [24]:

$$LiOH + \frac{1}{2}CO_2 \rightarrow \frac{1}{2}Li_2CO_3 + \frac{1}{2}H_2O \quad (2)$$

Therefore, the coexistence of LiOH and Li_2CO_3 in the diffraction patterns is attributed to the well-known surface reactivity of LLZO toward ambient humidity and CO_2, which leads to the formation of these secondary phases.

Figure 2f–k show the Rietveld refinement plots for the LLZO sample and all LLZO/POMA samples. The cubic phase of lithium lanthanum zirconate is predominant in all samples, as shown in Table 1. Additionally, all samples contain the tetragonal phase of LLZO, Li_2CO_3, and, except for the LLZO/POMA-5 and LLZO/POMA-15 samples, LiOH.

In the LLZO sample, the cubic phase of $Li_7La_3Zr_2O_{12}$, with space group $I\bar{3}d$, appears with 53.56 ± 0.95 wt% and lattice parameters $a = 13.1023$ (6) Å and $V = 2249.3$ (3) $Å^3$. The tetragonal phase of $Li_7La_3Zr_2O_{12}$, with space group $I4_1/acd$, appears with 17.24 ± 0.50 wt% and lattice parameters $a = 13.056$ (2) Å, $c = 12.852$ (2) Å, and

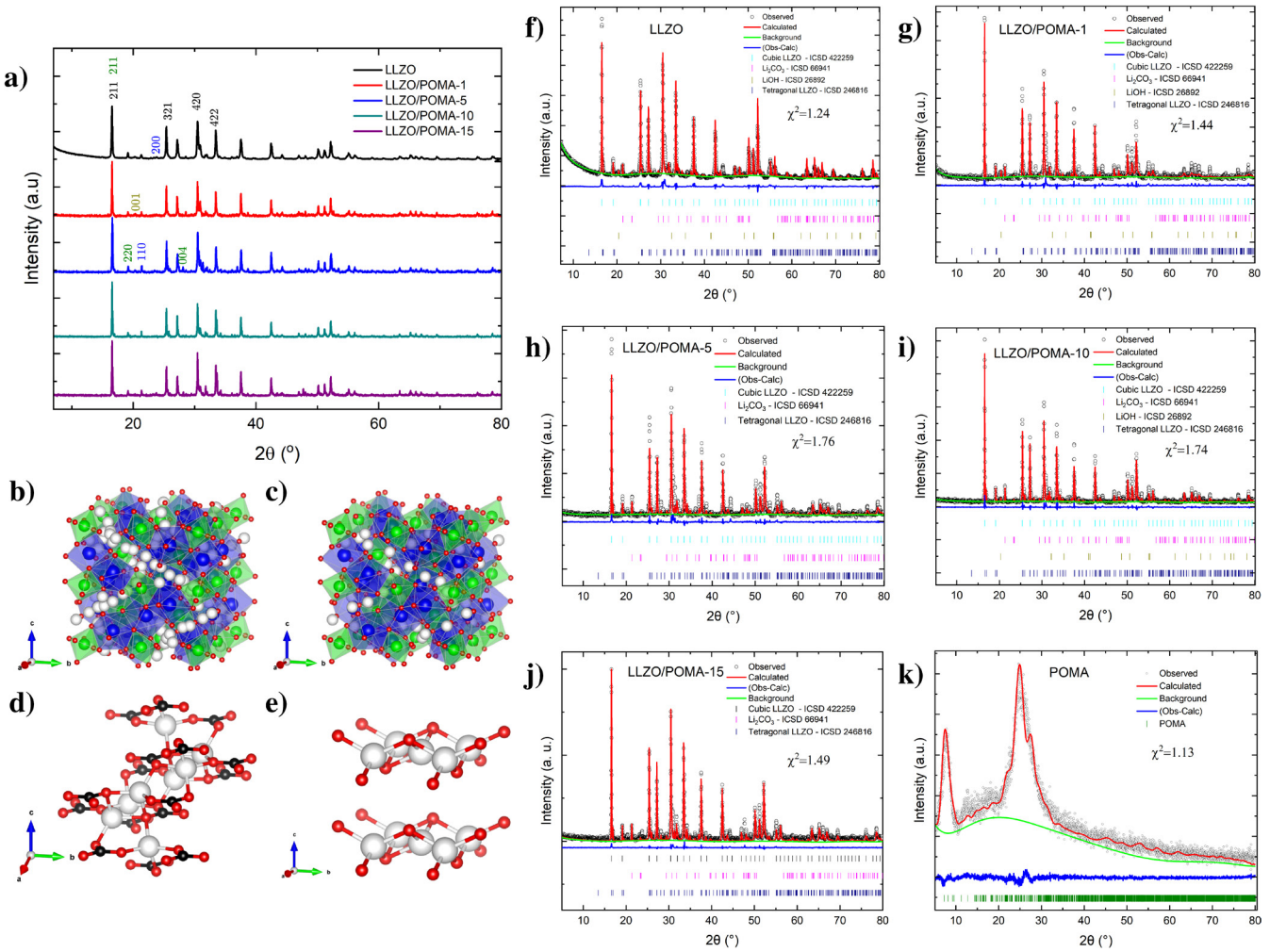


FIGURE 2 | (a) Experimental XRD diffractogram of LLZO and LLZO/POMA composites. Crystal structures: (b) Cubic LLZO, (c) tetragonal LLZO, (d) Li_2CO_3, and (e) LiOH. Rietveld refinements: (f) LLZO, (g) LLZO/POMA-1, (h) LLZO/POMA-5, (i) LLZO/POMA-10, and (j) LLZO/POMA-15. Le Bail refinement: (k) POMA. Color code: O (red), Zr (green), La (blue), Li (white), and C (black). [Color figure can be viewed at wileyonlinelibrary.com]

$V = 2190.6\ (5)$ Å^3. The crystalline phase of Li_2CO_3, monoclinic with space group $C12/c1$, appears with 25.50 ± 1.11 wt% and lattice parameters $a = 8.34\ (3)$ Å, $b = 4.971\ (2)$ Å, $c = 6.16\ (2)$ Å, and $V = 233.0\ (1)$ Å^3. Finally, LiOH, which is tetragonal at room temperature [26] with space group $P4/nmm$, appears with 3.70 ± 0.69 wt% and lattice parameters $a = 3.560\ (3)$ Å, $c = 4.354\ (3)$ Å, and $V = 55.2\ (1)$ Å^3.

The LLZO/POMA-1 sample shows an increase in the cubic phase of $Li_7La_3Zr_2O_{12}$ (58.11 ± 1.18 wt%), in the Li_2CO_3 phase (27.72 ± 1.29 wt%), and in the LiOH phase (4.97 ± 0.79 wt%), along with a significant decrease in the tetragonal phase of $Li_7La_3Zr_2O_{12}$. A slight increase is also observed in the lattice parameters of the cubic phase of LLZO, with a change from 13.1023 (6) to 13.109 (1) Å and V from 2249.3 (3) to 2252.6 (5) Å^3. Although POMA can interact with LLZO at the interface consistent with behavior commonly observed in ceramic/polymer composites, in which macromolecules generally cannot occupy interstitial sites or substitute lattice atoms [12, 13, 27] the observed structural changes suggest that the polymer may exert an indirect influence on the LLZO crystalline framework. At the investigated concentrations, POMA appears to promote a slight expansion of the cubic lattice and may contribute to stabilizing this polymorph, as reflected by its increased relative abundance in the Rietveld refinements.

The concurrent increase in Li_2CO_3 and LiOH fractions is consistent with the surface degradation reactions discussed above. This effect may arise from procedural steps during composite preparation that transiently expose the powder to moisture, or from POMA incorporation, which increases the effective surface area and may facilitate access of CO_2 and H_2O to LLZO grain boundaries. Such secondary phase formation is widely reported for LLZO based materials and is consistent with their well-documented susceptibility to surface degradation under ambient conditions.

In the LLZO/POMA-5 sample, the weight fraction of the cubic $Li_7La_3Zr_2O_{12}$ phase remains comparable to that of pristine LLZO, while the tetragonal fraction decreases less markedly than in LLZO/POMA-1. A pronounced increase in the Li_2CO_3 phase is observed (from 25.50% ± 1.11% to 33.20% ± 1.15%), and no LiOH is detected in the refinement. This behavior suggests a more extensive conversion of LiOH into Li_2CO_3 during surface degradation. The substantial growth of the Li_2CO_3 fraction may also account for the absence of further cubic-phase enhancement in this composition: the formation of Li_2CO_3 consumes near-surface lithium species and reduces the amount of LLZO available for refinement, counteracting the stabilizing tendency attributed to POMA.

TABLE 1 | Lattice parameters for LLZO/POMA samples.

Sample	LLZO	LLZO/POMA-1	LLZO/POMA-5	LLZO/POMA-10	LLZO/POMA-15
Cubic LLZO					
a (Å)	13.1023 (6)	13.109 (1)	13.111 (1)	13.1089 (8)	13.1084 (4)
V (Å^3)	2249.3 (3)	2252.6 (5)	2253.5 (6)	2252.7 (4)	2252.4 (2)
ρ (g/cm^3)	4.960	4.953	4.951	4.952	4.953
% wt	53.56 ± 0.95	58.11 ± 1.18	53.56 ± 1.02	53.18 ± 1.02	55.31 ± 1.01
Tetragonal LLZO					
a (Å)	13.056 (2)	13.034 (4)	13.117 (3)	13.120 (3)	13.120 (3)
c (Å)	12.852 (2)	12.889 (5)	12.698 (3)	12.680 (3)	12.681 (3)
V (Å^3)	2190.6 (5)	2190 (1)	2185 (1)	2182.6 (8)	2182.8 (9)
ρ (g/cm^3)	5.092	5.095	5.106	5.111	5.111
% wt	17.24 ± 0.50	9.20 ± 0.51	13.24 ± 0.64	12.60 ± 0.57	12.75 ± 0.58
Li_2CO_3					
a (Å)	8.34 (3)	8.35 (4)	8.37 (4)	8.35 (3)	8.36 (3)
b (Å)	4.971 (2)	4.973 (3)	4.972 (2)	4.973 (2)	4.969 (2)
c (Å)	6.16 (2)	6.18 (2)	6.18 (2)	6.18 (1)	6.18 (2)
V (Å^3)	233.0 (1)	233.6 (1)	234.2 (2)	234.0 (1)	233.8 (1)
β (°)	114.17 (5)	114.47 (7)	114.45 (6)	114.43 (5)	114.45 (5)
ρ (g/cm^3)	2.106	2.101	2.096	2.098	2.100
% wt	25.50 ± 1.11	27.72 ± 1.29	33.20 ± 1.15	31.20 ± 1.14	31.94 ± 1.15
LiOH					
a (Å)	3.560 (3)	3.564 (5)	—	3.604 (8)	—
c (Å)	4.354 (3)	4.346 (2)	—	4.369 (3)	—
V (Å^3)	55.2 (1)	55.2 (2)	—	56.7 (3)	—
ρ (g/cm^3)	4.688	4.686	—	4.559	—
% wt	3.70 ± 0.69	4.97 ± 0.79	—	3.02 ± 0.63	—
Refinement parameters					
χ^2	1.24	1.44	1.76	1.74	1.49
R_{wp} (%)	15.96	19.83	20.16	19.66	18.94
R_{exp} (%)	14.32	16.53	15.20	14.90	15.52

The LLZO/POMA-5 sample also exhibits a slight increase in the cubic-phase lattice volume compared with pristine LLZO (from 2249.3 (3) to 2253.5 (6) Å^3), whereas the tetragonal phase shows a reduction in lattice parameters. This trend persists up to LLZO/POMA-10, suggesting that POMA incorporation may indirectly influence the tetragonal framework by modifying local environments at grain surfaces or boundaries.

The LLZO/POMA-10 and LLZO/POMA-15 samples display similar weight fractions for the cubic (~53%) and tetragonal (~13%) phases, as well as comparable amounts of Li_2CO_3 (~31%). The main distinction between these two compositions is the absence of LiOH in LLZO/POMA-15. Their lattice parameters also remain nearly unchanged, indicating that structural modifications induced by POMA tend to saturate beyond ~10 wt%.

Given that the POMA employed in this study was synthesized in its HCl-doped (POMA-Cl) form, chloride ions may influence the system's early evolution by modifying local charge compensation or interfacial electrostatics. However, the convergence of phase fractions and lattice parameters for POMA contents above 5–10 wt% suggests that the LLZO/POMA interface reaches a structurally stable regime, beyond which additional polymer or counterions no longer produce significant crystallographic changes.

Figure 2k shows the refinement of the POMA sample using the Le Bail method. The initial lattice parameters used for

TABLE 2 | Average Li—O, La—O, and Zr—O bond lengths for the cubic phase of $Li_7La_3Zr_2O_{12}$, by VESTA from CIF files from Rietveld refinement of the XRD data.

Sample	La—O (Å)	Zr—O (Å)	Li_1—O (Å)	Li_2—O (Å)
LLZO	2.57821 (3)	2.12895 (3)	1.92446 (3)	2.11280 (3)
LLZO/POMA-1	2.58065 (9)	2.13093 (7)	1.92625 (8)	2.11477 (8)
LLZO/POMA-5	2.58095 (11)	2.13122 (7)	1.92652 (9)	2.11506 (9)
LLZO/POMA-10	2.58063 (6)	2.13095 (6)	1.92627 (6)	2.11478 (7)
LLZO/POMA-15	2.58054 (3)	2.13087 (3)	1.92619 (3)	2.11470 (3)

the refinement, based on the work of [9], were: $a = 6.0233$ Å, $b = 11.9863$ Å, $c = 18.9307$ Å, $\alpha = 83.1724°$, $\beta = 84.1401°$, and $\gamma = 88.8810°$. After refinement, the obtained values were: $a = 6.10326$ (35) Å, $b = 12.2273$ (115) Å, $c = 18.6559$ (251) Å, $\alpha = 83.1112$ (138)°, $\beta = 95.1501$ (365)°, and $\gamma = 95.1501$ (88)°, with $\chi^2 = 1.13$, $R_{wp} = 12.98\%$, and $R_{exp} = 12.21\%$.

Another important observation is the systematic increase in Li_2CO_3 content up to the LLZO/POMA–5 sample (25.50% ±1.11% for LLZO, 27.72% ±1.29% for LLZO/POMA–1, and 33.20% ±1.15% for LLZO/POMA–5). From LLZO/POMA–10 onward, the Li_2CO_3 fraction stabilizes at approximately 30 wt%. This behavior suggests that the initial incorporation of POMA increases the effective exposure of the LLZO surface to CO_2 and H_2O during handling and composite preparation, thereby promoting Li_2CO_3 formation through the well-known ambient degradation reactions of LLZO. Beyond ~10 wt% POMA, however, this surface reactivity appears to reach a saturation regime. In contrast, LiOH does not exhibit a monotonic trend with increasing POMA content. Because LiOH readily converts to Li_2CO_3 upon exposure to CO_2, even small amounts formed at early stages may not remain detectable in the final XRD refinements. Consequently, variations in the relative amounts of Li_2CO_3 and LiOH primarily reflect surface degradation phenomena rather than intrinsic modifications of the LLZO bulk structure. Therefore, the structural evolution of the composite is more appropriately assessed through the relative fractions of the cubic and tetragonal $Li_7La_3Zr_2O_{12}$ phases, lattice parameters, and bond-length variations, which provide direct information on modifications within the garnet framework.

Importantly, the presence and evolution of these secondary phases do not correlate with the enhancement of electrical conductivity observed in the composites. Instead, the improved electrical transport is attributed to polymer–ceramic interfacial effects introduced by POMA, which are known to locally modify Li^+ mobility near grain surfaces and boundaries. Accordingly, the evolution of Li_2CO_3 and LiOH is interpreted as a consequence of LLZO surface reactivity, rather than a determining factor governing the observed conductivity trends.

Figure 2b–e show the graphical representation of the unit cells of the crystalline structures identified in the samples, drawn using VESTA [18] from experimental data and imported through crystallographic information files (CIF). The first, Figure 2b, shows the cubic phase of $Li_7La_3Zr_2O_{12}$. It is possible to observe the large amount of lithium in the interstices of the material, which contributes to the high conductivity of this crystalline phase, along with the fact that the distribution of lithium sites and vacancies in the structure is more disordered than in the tetragonal structure [28, 29].

In turn, Figure 2c shows the structure of the tetragonal phase of $Li_7La_3Zr_2O_{12}$. In this phase, the sites are arranged in a more orderly manner [28, 29], contributing to greater structural stability. This arrangement hinders the diffusion of ions within the material, resulting in lower ionic conductivity compared to the cubic phase.

According to [20], the number of vacancies in the cubic phase is much higher than in the tetragonal phase. Lithium ions in the cubic phase occupy only two types of sites, 24d and 96h (where the number indicates the quantity of available sites, and the letter represents the symmetry type of the site) [30, 31]. This fact means there are 120 available sites for lithium ions, a much larger number than the 56 lithium ions in the cubic LLZO unit cell. Thus, in this phase, there is a significant number of vacancies, facilitating ion movement within the structure (Figure 1a).

In the tetragonal phase, lithium ions occupy three types of sites, 8a, 16f, and 32g [30, 31], totaling 56 available sites, exactly matching the number of lithium ions. Thus, theoretically, there would be no vacancies in this structure, which significantly hinders ionic movement. Additionally, the distance between these sites is much greater in the tetragonal structure than in the cubic structure [28], further hindering the movement of lithium ions within the structure. In summary, the structural differences between the two crystalline forms influence ionic conductivity.

The structures of Li_2CO_3 and LiOH are shown in Figure 2d,e. These phases result from the degradation process of part of the sample, as indicated by Equations (1) and (2). The presence of these materials can be detrimental, as they interfere with the material's conductivity and create interfacial issues with metallic lithium-ion electrodes, due to the chemical instability and low ionic conductivity of LiOH and Li_2CO_3 [32].

Table 2 summarizes the variations in the average atomic bond lengths of the predominant crystalline phase, the cubic $Li_7La_3Zr_2O_{12}$ garnet, calculated using VESTA [18] from the CIF files obtained through Rietveld refinement of the XRD data. A slight modification of the local coordination environment is observed upon POMA incorporation. Up to the LLZO/POMA-5 composition, the Li—O, La—O, and Zr—O bond distances exhibit a subtle increase, suggesting mild

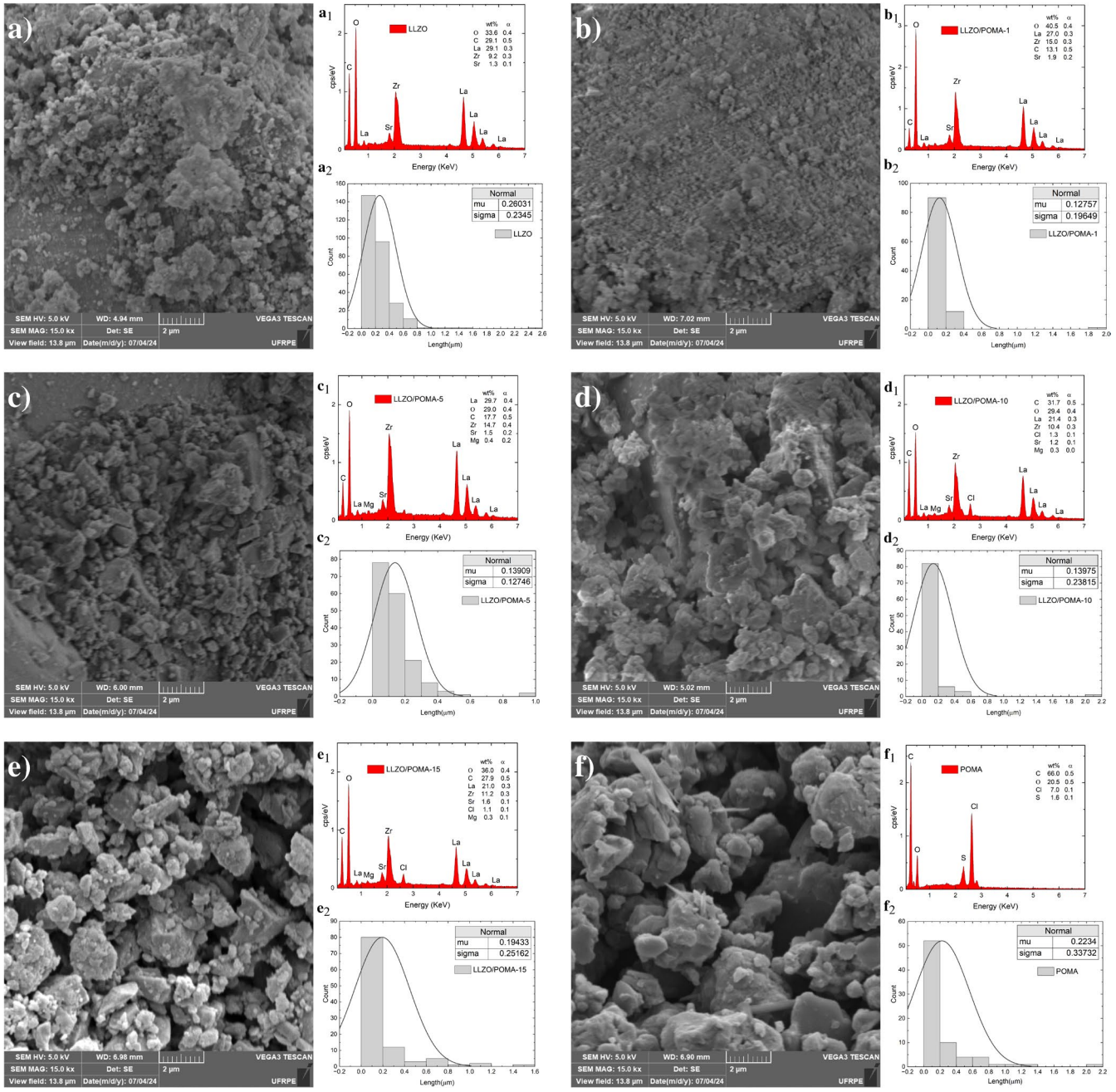


FIGURE 3 | SEM micrographs of samples (a–f). The left panel shows the main SEM image, while the right panels (1) and (2) correspond to the EDS spectrum and particle-size distribution analyzed with ImageJ (Fiji), respectively. [Color figure can be viewed at wileyonlinelibrary.com]

lattice expansion and/or increased local structural distortion. At higher POMA contents (LLZO/POMA-10 and above), the average bond lengths show a marginal reduction, indicating that the structural response becomes less pronounced as the polymer content increases.

Figure 3 shows the scanning electron microscopy images, EDS, and particle-size distribution of the analyzed powder samples. The image in Figure 3a presents the LLZO sample. A morphological conformation with low uniformity and significant particle-size differences can be observed. This trend was also observed in the particle size distribution, as shown in Figure $3a_2$. Although most particles are up to 0.2 μm, there are particles distributed in size ranges extending up to 1.4 μm, with no incidence in the range from 1.6 to 2.4 μm and with an incidence in the range from 2.4 to 2.6 μm. This behavior has already been reported in the literature [33–35].

Figure 3b shows the image of the LLZO/POMA-1 sample. Greater surface uniformity can be observed, as well as an improvement in the uniformity of particle size. This tendency is also confirmed by the particle size distribution in Figure $3b_2$, where it can be observed that there is no great variety in size, since the particles are distributed only within ranges up to 0.4 μm and an incidence in the range of 1.8–2.0 μm. The initial addition of 1% POMA may have contributed to this behavior, as the polymer, in a small amount,

due to its greater flexibility compared to ceramic materials, can act as a glue between the material's particles.

Figure 3c shows the image of the LLZO/POMA-5 sample. It is possible to observe more dispersed particles. This structure suggests the presence of more voids between molecules, resulting in a more porous microstructure. In addition to a wide diversity of particle sizes, which, as can be seen in the particle size distribution graph in Figure $3c_2$, are distributed in sizes ranging from 0.1 μm to ranges extending up to 1.0 μm. In the LLZO/POMA-10 sample, the addition of POMA leads to an irregular conformation, more similar to the morphology of polymeric materials, with a variety of particle sizes in two predominant size ranges (≳ 0–0.2 μm and 0.2–0.6 μm), with an incidence at 2.2 μm. This trend continues in the LLZO/POMA-15 sample, where voids become even more evident, and the diversity of particle sizes is evident, which are also distributed in several ranges reaching up to 1.6 μm, as shown in Figure $3e_2$. The POMA sample exhibits a conformation previously reported [9, 16, 36], characterized by more irregular agglomerations typical of polymers, and a significant variation in particle size distribution, as shown in Figure $3f_2$.

Table 3 presents the data corresponding to the mean particle size (Mean size, μm), standard deviation (Std. dev., μm), and coefficient of variation (CV = σ/μ). These parameters provide quantitative support for the analysis of microstructural evolution induced by incorporating POMA into the ceramic matrix. The use of statistical descriptors to complement qualitative morphological observations is a common approach in the quantitative characterization of micro- and nanoscale structures [37, 38]. The initial addition of POMA promotes a reduction in the average particle size, with μ decreasing from 0.260 μm for the LLZO sample to approximately 0.13–0.14 μm for the LLZO/POMA-1 and LLZO/POMA-5 samples. Among all compositions, LLZO/POMA-5 exhibits the lowest standard deviation (σ = 0.127 μm) and one of the lowest coefficients of variation (CV = 0.91), indicating a more homogeneous particle-size distribution. At higher POMA contents, the simultaneous increase in σ and CV suggests a broader particle-size distribution, consistent with the greater porosity and morphological heterogeneity observed in the SEM micrographs.

TABLE 3 | Particle-size distribution parameters obtained from ImageJ/Fiji analysis of the SEM micrographs.

Sample	Mean size (μm)	Standard deviation (μm)	CV (σ/μ)
LLZO	0.260	0.235	0.90
LLZO/POMA-1	0.128	0.196	1.53
LLZO/POMA-5	0.139	0.127	0.91
LLZO/POMA-10	0.140	0.238	1.70
LLZO/POMA-15	0.194	0.252	1.30
POMA	0.223	0.337	1.51

Figure $3a_1$–f_1 (EDS) confirm the presence of the chemical elements identified in the XRD. Additionally, the results show other elements, such as Mg, Sr, Cl, and S. Mg and Sr are present due to the $Li_7La_3Zr_2O_{12}$ doping with these elements. The Cl is present due to POMA doping, while S is part of one of the POMA precursors.

Except for the LLZO sample, the amount of carbon increases with the addition of POMA. This mass percentage increases from 13.1 (5)% in the LLZO/POMA-1 sample to about 30% in LLZO/POMA-10 and LLZO/POMA-15 samples, and 66.0 (5)% in the POMA sample. This behavior clearly illustrates the influence of POMA addition on the elemental composition of the analyzed samples. The LLZO sample showed an unexpected behavior. This result may have occurred due to the high reactivity of LLZO with CO_2 and water, both of which are present in the atmospheric composition [39] to varying degrees depending on the experimental conditions.

For a more quantitative analysis, Table 1 and the mass proportions of the chemical elements in samples shown in Figure $3a_1$–f_1 can be observed. For the LLZO/POMA-1 sample, for example, a proportion of La around 32%, Zr around 14%, oxygen around 37%, and carbon around 6% is expected. Analyzing Figure $3b_1$, we observe 40.5 (4)% oxygen, 27.0 (3)% La, 15.0 (3)% Zr, and 13.1 (5)% carbon. The most significant discrepancy was in oxygen levels. This difference could be attributed to the tendency for surface formation of Li_2CO_3 [23, 40], which would also explain all the deviations, as this reaction would increase the amount of oxygen, which in turn would decrease the proportion of Zr due to the increase in the quantities of other chemical elements. However, considering these conditions of material reactivity and the inherent differences of each characterization technique, it can be said that the EDS measurements corroborate the x-ray diffraction results regarding the structures formed during the syntheses, since the elements detected by EDS are the same as those that constitute the structures identified by XRD, in proportions reasonably consistent with the mass fractions obtained from the Rietveld refinement.

Figure 4 shows the Fourier-transform infrared spectroscopy (FTIR) measurements of all samples. There are several bands that can be attributed to POMA. For example, the band at 1460 cm^{-1} is attributed to the C—H deformation of the —OCH3 group [9, 41]. The band at 1290 cm^{-1} corresponds to C—N stretching [9, 42, 43], while bands associated with the 1,4-substituted benzene ring, one of the structural units of POMA, are observed in the region between 1203 and 793 cm^{-1} [9]. In addition, the band located at 1255 cm^{-1} corresponds to C—O—C stretching [44], whereas the band at 746 cm^{-1} is attributed to the out-of-plane C—H deformation of mono- and 1,2-disubstituted aromatic rings [45]. The band at 1352 cm^{-1} may indicate residual APS [9], a precursor of POMA. This residual presence corroborates the presence of S in the POMA sample, as shown by EDS (Figure $3f_1$). According to [46], the band at 688 cm^{-1} is attributed to the Zr—O group, and the band at 681 cm^{-1} is attributed to the La—O group, both of which indicate the formation of LLZO. Additionally, the band at 1438 cm^{-1} is associated with the asymmetric stretching vibration mode of C═O, corroborating the Li_2CO_3 and confirming the XRD results indicating the presence of this crystalline phase in the samples.

Figure 5 displays the TG, DTG, and DSC curves for all samples. In the TG plot (Figure 5a), a progressive mass loss is observed as

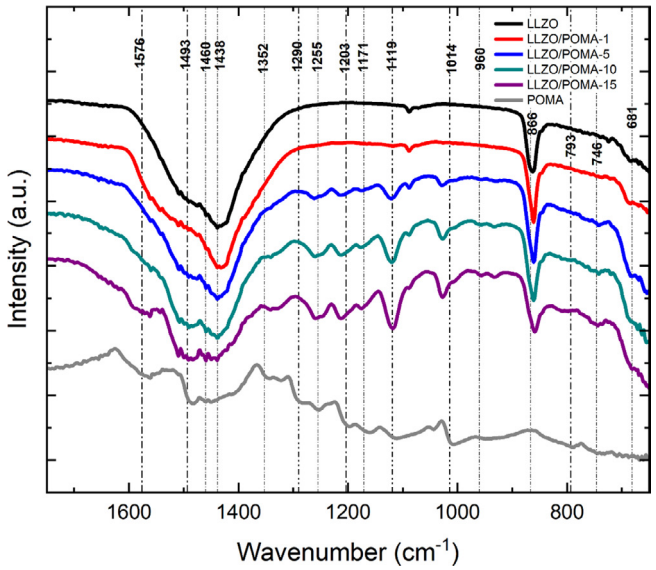


FIGURE 4 | FTIR spectra of all powder samples. [Color figure can be viewed at wileyonlinelibrary.com]

a function of temperature. The LLZO sample exhibits the lowest mass variation, retaining approximately 83% of its initial mass at 1200°C, whereas the LLZO/POMA–15 sample shows the highest degradation, retaining about 73%. This difference of approximately 10 wt% between pristine LLZO and LLZO/POMA–15 suggests that not all of the added polymer is volatilized; instead, a fraction likely decomposes into thermally stable residual phases rather than being completely eliminated. The POMA sample, in turn, undergoes almost complete thermal decomposition at around 835°C. The DTG curves (Figure 5b) represent the rate of mass loss as a function of temperature, enabling the identification of discrete thermal events and degradation stages. For the pristine LLZO sample (black curve), the first major DTG peak appears at approximately 364°C and corresponds to the most significant mass loss process. Up to this temperature, the sample exhibits excellent thermal stability. A second peak of higher intensity is observed at slightly higher temperatures, indicating an additional mass-loss event; beyond this region, no further substantial variations are detected up to 1200°C.

In the composite samples, this first major DTG peak progressively shifts toward lower temperatures with increasing POMA content. For instance, in the LLZO/POMA-15 sample, the peak occurs at approximately 329°C, indicating that the onset of the primary degradation process takes place earlier in the presence of POMA. This shift reflects the expected behavior with the incorporation of an organic polymer phase, whose decomposition typically initiates at lower temperatures than that of the LLZO ceramic matrix.

In addition, a low temperature DTG feature (~40°C–80°C) becomes increasingly pronounced as the POMA fraction increases. This event is attributed to the release of physically adsorbed water and residual solvents associated with the polymeric component. The presence of this low temperature mass loss is consistent with the higher $LiOH/Li_2CO_3$ contents identified by XRD, as moisture exposure promotes surface reactions on LLZO leading to the formation of these secondary phases. Composites with higher POMA content exhibit a larger interfacial area and increased moisture sensitivity, which may further contribute to this behavior.

In all composite samples, a significant DTG peak is observed around 743°C. There are no significant differences in the intensity of this peak, indicating that at this temperature range, the influence of POMA is no longer significant. This observation is supported by the graph in Figure 5a, which shows that at this temperature, only about 10% of the initial POMA mass remains.

The gray curve in Figure 5b shows the DTG curve of POMA. A very pronounced initial peak is observed, indicating a high mass loss rate in this temperature region, around 63°C. The mass loss in this range is likely due to the evaporation of adsorbed water and residual solvents. The peaks near 200°C–300°C are associated with the degradation of the polymer, which begins with the cleavage of the side groups [47], specifically the COH_3 group. The peaks at higher temperatures, between 500°C and 800°C, are associated with the oxidation of carbonaceous residues [47], completing the material's total degradation.

Figure 5c–h show the energy flow curves over time for all samples. For the LLZO sample, three endothermic peaks were identified (at 692.8°C, 758.2°C, and 1196.4°C). The first process starts at 663.8°C and ends at 704°C, the second process begins at 713.2°C and finishes at 770.9°C, and the third process occurs between 1193.8°C and 1198.2°C. These processes are attributed to transitions between the tetragonal and cubic crystalline phases. The two processes observed between 663.8°C and 770.9°C are likely due to the transition from the tetragonal to the cubic phase, as heating around 650°C triggers this transition by releasing internal stresses in the LLZO crystal lattice [48]. The process observed between 1193.8°C and 1198.2°C corresponds to the reverse transformation from the cubic phase back to the tetragonal phase [49]. In addition to these three endothermic peaks, the composite samples exhibit an exothermic peak ranging from 763.1°C for the LLZO/POMA-5 sample to 948.2°C, also for the LLZO/POMA-5 sample. This peak corresponds to the complete degradation of POMA [50]. A similar behavior is observed in the graph of Figure 5h, corresponding to the POMA sample, which exhibits a peak at 836.1°C.

In summary, the incorporation of POMA reduces the overall thermal stability of the composites. Nevertheless, for solid-state electrolyte applications, this decrease is not critical, as all composites exhibit negligible mass loss events up to approximately 300°C, well above the typical operational temperature window of solid-state batteries (20°C–40°C) [51]. Furthermore, the thermal analysis supports the interpretation that POMA increases the effective exposure of LLZO surfaces to H_2O and CO_2 during composite preparation and handling. This exposure promotes the initial formation of LiOH, which subsequently converts to Li_2CO_3 via the reaction described in Equation (2). The observation that the Li_2CO_3 content saturates at approximately 30 wt% for POMA fractions above 10 wt% suggests that, at higher polymer loadings, part of the LLZO surface becomes shielded by the polymer matrix, thereby limiting further surface reactions.

Importantly, the formation of Li_2CO_3, a largely insulating secondary phase, does not correlate with the enhancement of

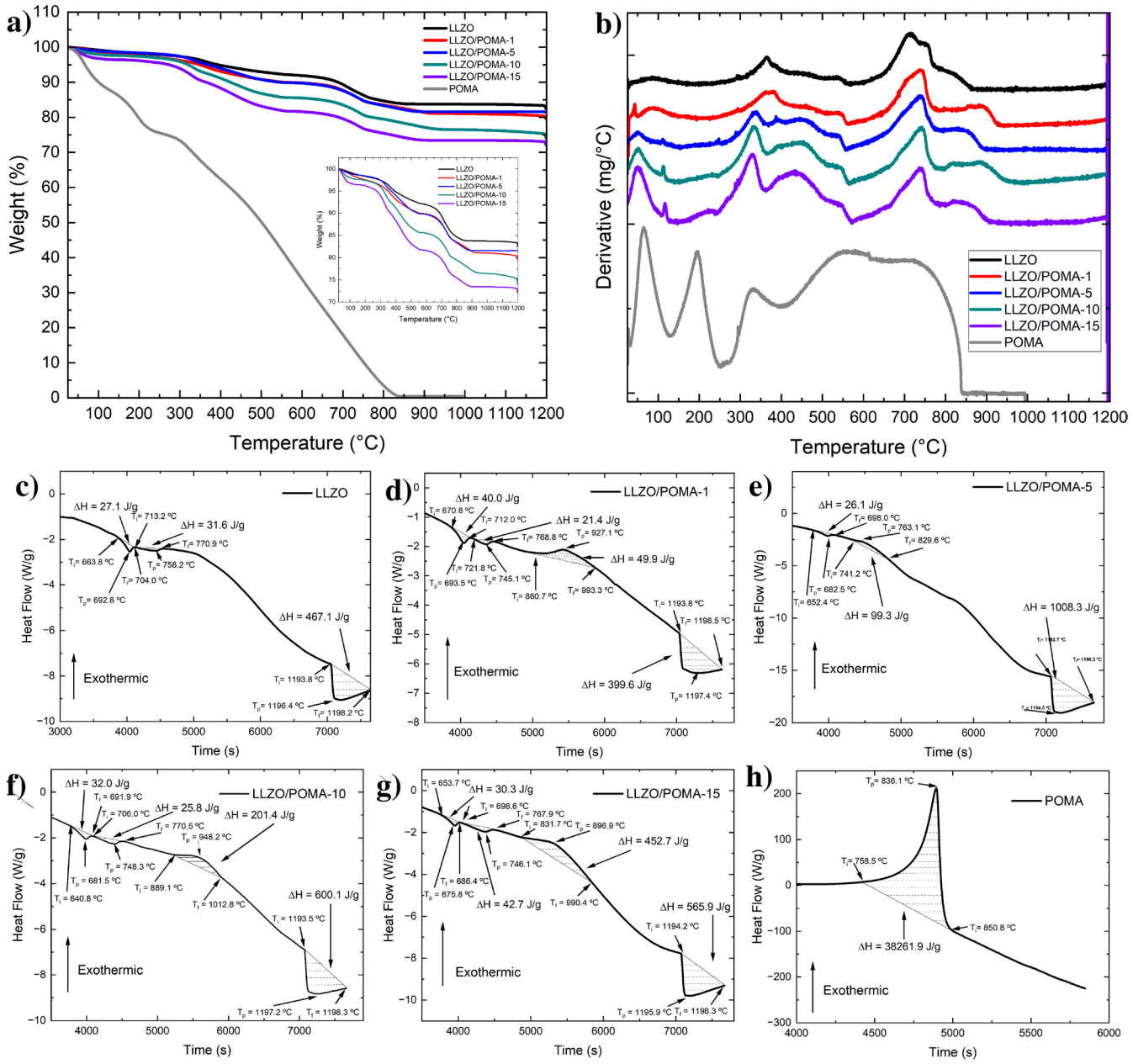


FIGURE 5 | (a) TGA curves and (b) DTG curves of LLZO and LLZO/POMA composites. DSC thermograms for: (c) LLZO, (d) LLZO/POMA-1, (e) LLZO/POMA-5, (f) LLZO/POMA-10, (g) LLZO/POMA-15, and (h) POMA, recorded in the high-temperature region. [Color figure can be viewed at wileyonlinelibrary.com]

electrical transport observed in the composites. Instead, the improved conductivity is attributed primarily to polymer–ceramic interfacial effects introduced by POMA, which modify local Li^+ mobility near grain surfaces and boundaries. This interpretation is consistent with the trends revealed by the Jonscher analysis (Figure 6b), which indicate changes in relaxation dynamics rather than contributions from secondary phases.

Figure 6a shows the Nyquist (Z'' vs. Z') plot obtained from complex impedance spectroscopy. The largest semicircle, represented by black points, corresponds to the LLZO sample, that is, the purely ceramic sample without the addition of POMA. The red curve corresponds to the LLZO/POMA-1 sample, while the blue curve represents the LLZO/POMA-5 sample. The green curve refers to the LLZO/POMA-10 sample, and the purple semicircle corresponds to the LLZO/POMA-15 sample. Finally, the smallest curve, in gray, refers to the pure POMA sample. A decrease in the size of the semicircles formed by Z'' is observed with the addition of POMA, indicating a reduction in the electrical resistance of the pellets as more POMA is added.

The equivalent circuit shown in the insert in Figure 6a represents the electrical behavior of the LLZO samples and all composite samples. The resistor R_1 and capacitor C_1 form a parallel circuit that models the behavior of the grains, which constitute the material's predominant part. The resistor R_2 and the constant phase element (CPE1) model the behavior of the material surrounding the grains, known as the grain

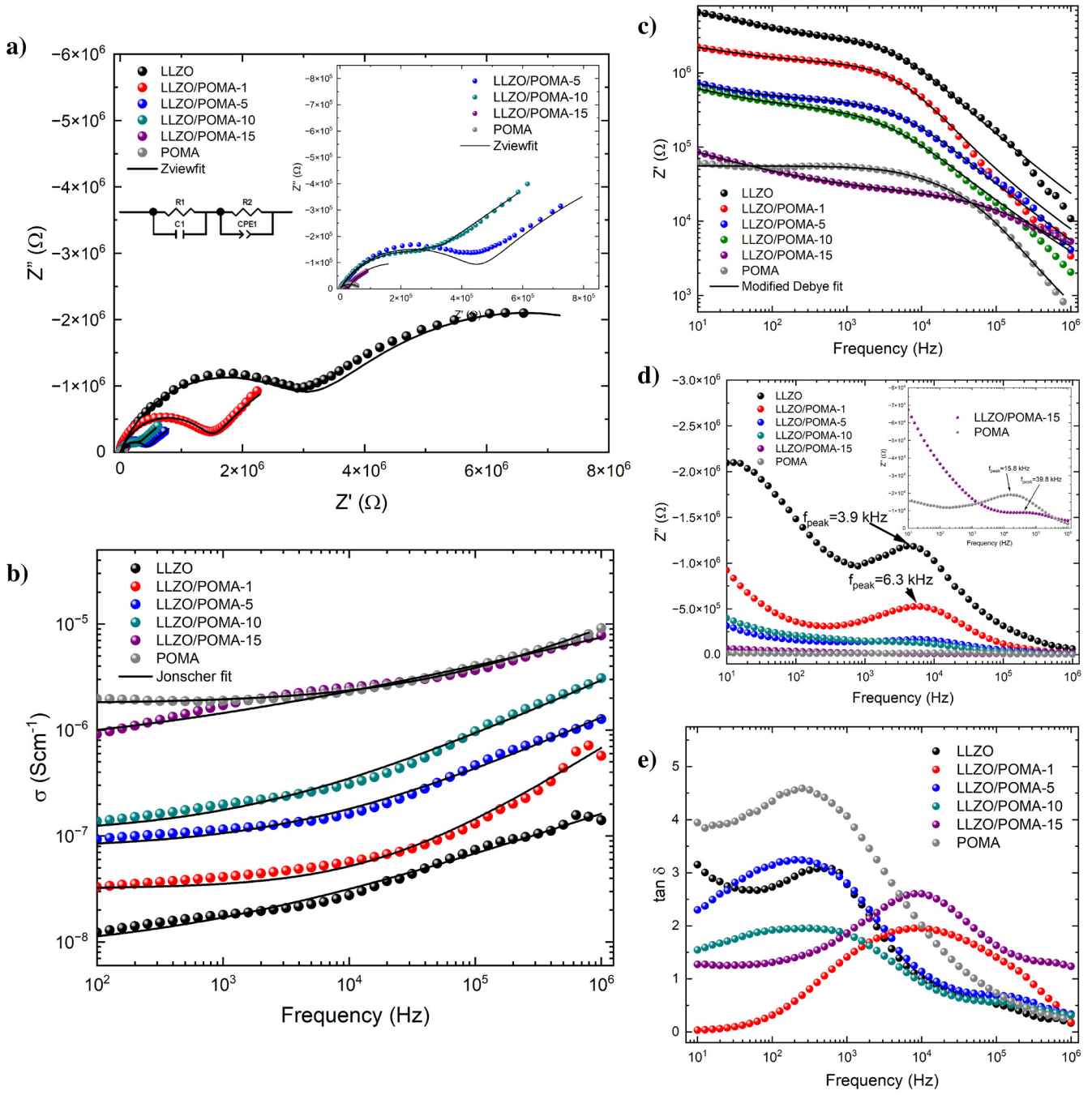


FIGURE 6 | (a) Nyquist plots with equivalent-circuit fitting (inset). (b) AC conductivity as a function of frequency fitted with Jonscher's law. (c) Real part of impedance (Z') as a function of frequency fitted with the modified Debye model, (d) imaginary part of impedance (Z''), and (e) dielectric loss (tan δ) for LLZO and LLZO/POMA composites. [Color figure can be viewed at wileyonlinelibrary.com]

boundary. The constant phase element (CPE1) is used to depict non-ideal capacitive behavior [52–54]. In pristine LLZO, the R_2/CPE contribution primarily represents the ceramic grain boundaries, whereas in the LLZO/POMA composites it also encompasses the interfacial regions formed between the ceramic matrix and the polymer phase. This equivalent circuit was selected because the Nyquist plots exhibit two depressed and partially overlapping semicircular responses, which are commonly associated with grain and grain boundary/interfacial contributions in ceramic electrolytes and composite materials. The use of a constant phase element (CPE) is justified by the depressed nature of the semicircles, indicating a distribution of relaxation times and non-Debye behavior. Similar equivalent-circuit models have been widely employed for LLZO-based solid electrolytes and polymer–ceramic composites reported in the literature [55].

Table 4 presents the equivalent circuit parameters obtained using ZView. A decreasing trend is observed with the addition of POMA for both the grain resistance (R_1) and the grain boundary resistance (R_2). There is only an apparent deviation from this trend between the LLZO/POMA-5 and LLZO/POMA-10 samples, due to a slight increase in R_1 (from 4.40×10^5 to 4.71×10^5 Ω). The grain, grain-boundary, and total conductivities exhibit

a systematic increase with increasing POMA content. For instance, the grain conductivity increases by approximately two orders of magnitude when comparing pristine LLZO and LLZO/POMA–15 (from 1.89×10^{-8} to 2.66×10^{-6} S·cm^{-1}). Table 6 shows a continuous increase in the DC electrical conductivity with the addition of POMA. Such a trend is expected, as a conducting polymer, POMA can form partial percolation pathways [56], reduce grain-boundary barrier heights, and improve interfacial contact.

Figure 6c shows the behavior of the real impedance component (Z') as a function of frequency. It can be observed that for the LLZO sample, the DC component approaches 6.6×10^6 Ω at very low frequencies, while for the LLZO/POMA-15 sample, this component is on the order of 10^4 Ω. This result is consistent with the low-frequency resistance values of the samples, calculated using ZView fit (on the order of 10^6 and 10^4 Ω, respectively).

The plots in Figure 6c can be further analyzed by fitting them to the modified Debye model. In this framework, multiple relaxation processes ($R \parallel$ CPE) with a series resistance are described by Equation (3) [57].

$$Z'(\omega) = R_s + \sum_{k=1}^{2} \frac{R_k\left[1 + \left(\omega\tau_k\right)^{n_k}\cos\left(n_k\pi/2\right)\right]}{1 + 2\left(\omega\tau_k\right)^{n_k}\cos\left(n_k\pi/2\right) + \left(\omega\tau_k\right)^{2n_k}}. \tag{3}$$

where $Z'(\omega)$ is the real impedance; R_s is the series resistance; R_k is the process (arc) resistance; τ is the characteristic relaxation time; n is the constant–phase exponent ($0 < n \leq 1$, with $n = 1$ recovering Debye); and $\omega = 2\pi f$ is the angular frequency with f the frequency.

The constant phase element (CPE) is characterized by Q and n, with $Y_{\mathrm{CPE}}(\omega) = Q\,(j\omega)^n$. For the branch $R \parallel$ CPE, the characteristic time satisfies $\tau^n = RQ$, that is, $\tau = (RQ)^{1/n}$. For $n = 1$, the ZARC model reduces to the pure Debye case ($R \parallel C$), $\tau = RC$.

The curves in Figure 6c were fitted in Python (NumPy, Pandas, SciPy, and Matplotlib). The $Z'(f)$ data were read from CSV files containing the experimental complex-impedance measurements, and a nonlinear fit to the chosen model (modified Debye/ZARC) was performed using *scipy.optimize.curve_*fit. From the fit, we extracted the equivalent-circuit parameters: R_s (series resistance) and, for each process k (grain/boundary), R_k (resistance), τ_k (characteristic time), and n_k (CPE exponent, $0 < n_k \leq 1$), together with the parameter uncertainties (standard errors) estimated from the covariance matrix.

The parameters obtained from fitting $Z'(f)$ are listed in Table 5. The series resistance was fixed at $R_s = 0$, as determined by the equivalent-circuit models determined using ZView. The values of R_1 are close to those reported in Table 4, and R_2 agrees at least in order of magnitude. Taken together, these results indicate a clear grain/grain boundary response and a systematic decrease in electrical resistance with increasing POMA fraction, with good consistency between the fitting approaches.

In turn, the graph in Figure 6d shows the variation in the imaginary component of impedance with frequency. This

TABLE 4 | Equivalent circuit parameters and derived electrical conductivities for the LLZO/POMA samples.

Sample	R_1 (Ω)	C_1 (F)	R_2 (Ω)	CPE_1 (F)	σ_{grain} (S/cm)	σ_{gb} (S/cm)	σ_{total} (S/cm)
LLZO	2.99×10^6 (8)	1.31×10^{-11} (1)	7.40×10^6 (73)	7.87×10^{-9} (58)	1.89×10^{-8} (5)	7.65×10^{-9} (75)	5.45×10^{-9} (38)
LLZO/POMA-1	1.49×10^6 (2)	2.91×10^{-10} (5)	4.99×10^6 (10)	4.58×10^{-9} (12)	3.80×10^{-8} (5)	1.13×10^{-8} (2)	8.73×10^{-9} (14)
LLZO/POMA-5	4.40×10^5 (10)	1.03×10^{-9} (6)	2.07×10^6 (4)	1.38×10^{-7} (5)	1.29×10^{-7} (29)	2.73×10^{-8} (5)	2.25×10^{-8} (10)
LLZO/POMA-10	4.71×10^5 (31)	2.36×10^{-9} (5)	2.06×10^6 (22)	1.05×10^{-7} (15)	1.20×10^{-7} (8)	2.75×10^{-8} (29)	2.24×10^{-8} (20)
LLZO/POMA-15	2.62×10^4 (16)	5.56×10^{-10} (73)	3.05×10^5 (22)	2.15×10^{-7} (22)	2.66×10^{-6} (16)	2.28×10^{-7} (16)	2.10×10^{-7} (14)
POMA	1.45×10^4 (10)	1.30×10^{-10} (8)	5.17×10^4 (23)	1.18×10^{-8} (7)	7.69×10^{-6} (53)	2.16×10^{-6} (10)	1.68×10^{-6} (6)

TABLE 5 | 2XZARC fit parameters from $Z'(f)$: For each sample, the smaller resistance is labeled R_1 (with its corresponding τ_1 and n_1).

Sample	R_1 (Ω)	τ_1 (s)	n_1	R_2 (Ω)	τ_2 (s)	n_2
LLZO	2.92×10^{6} (3)	2.82×10^{-5} (4)	0.765 (4)	5.92×10^{6} (19)	8.72×10^{-3} (5)	0.638 (12)
LLZO/POMA–1	1.31×10^{6} (1)	2.83×10^{-5} (4)	0.826 (fixed)	2.27×10^{6} (18)	3.06×10^{-2} (67)	0.520 (fixed)
LLZO/POMA–5	4.39×10^{5} (1)	2.40×10^{-5} (2)	0.718 (fixed)	1.25×10^{6} (17)	7.33×10^{-2} (17)	0.620 (fixed)
LLZO/POMA–10	3.05×10^{5} (1)	3.63×10^{-5} (6)	0.717 (fixed)	1.51×10^{6} (1)	1.73×10^{-1} (fixed)	0.491 (fixed)
LLZO/POMA–15	2.32×10^{4} (1)	1.23×10^{-6} (3)	0.606 (fixed)	3.49×10^{5} (30)	3.83×10^{-1} (86)	0.432 (fixed)
POMA	2.01×10^{4} (18)	2.53×10^{-6} (34)	0.879 (fixed)	3.57×10^{4} (19)	1.48×10^{-5} (fixed)	0.792 (fixed)

Note: Units: R in Ω, τ in s. Numbers in parentheses indicate the uncertainty in the last digit(s) of the mantissa.

TABLE 6 | Jonscher fitting parameters: σ_{dc}, A, and s (uncertainty on the last digits in parentheses).

Sample	σ_{dc} (S cm^{-1})	A	s
LLZO	$7.58\,(46)\times10^{-9}$	$2.76\,(53)\times10^{-10}$	0.404 (11)
LLZO/POMA–1	$3.19\,(14)\times10^{-8}$	4.67 (fixed)$\times10^{-12}$	0.756 (11)
LLZO/POMA–5	$7.63\,(26)\times10^{-8}$	$2.73\,(65)\times10^{-10}$	0.538 (14)
LLZO/POMA–10	$1.039\,(45)\times10^{-7}$	6.89 (fixed)$\times10^{-10}$	0.532 (15)
LLZO/POMA–15	$5.44\,(90)\times10^{-7}$	6.82 (fixed)$\times10^{-8}$	0.295 (16)
POMA	$1.78\,(2)\times10^{-6}$	$1.33\,(25)\times10^{-9}$	0.551 (13)

graph is important because the peak frequency (f_{peak}) can be determined. Based on the peak frequency, the relaxation time $\left(\tau = \frac{1}{2\pi f_{peak}}\right)$ [58].

The relaxation time (τ) is related to the time it takes for charge carriers to return to their original state after the removal of an electric field applied to the material. In other words, this quantity is associated with ionic mobility, where a shorter relaxation time indicates a greater ability of ions to move within the material and, consequently, a higher ionic conductivity.

It is noticeable in Figure 6d that from the LLZO sample to the LLZO/POMA-1 sample, there is an increase in the peak frequency (from 3.9 to 6.3 kHz), which indicates a decrease in the relaxation time (from 4.0×10^{-5} to 2.5×10^{-5} s). This trend becomes more evident in the LLZO/POMA-15 sample, with a peak frequency of 39.8 kHz.

Complex impedance spectroscopy also allows the analysis of the dielectric properties of the material, as the electrical permittivity of the material is given by Equation (4) [59, 60].

$$\varepsilon^{*} = \frac{1}{j\omega C_0 Z^{*}} \tag{4}$$

where $j = \sqrt{-1}$ is the imaginary unit, $\omega = 2\pi f$ is the angular frequency, and $C_0 = \frac{\varepsilon_0 A}{d}$ is the geometric capacitance of the sample, where ε_0 is the permittivity of vacuum, A is the electrode area, and d is the sample thickness.

Figure 6e shows the behavior of the dielectric loss factor (tan δ) as a function of frequency. The imaginary permittivity is related to energy dissipation, while the real permittivity is associated with energy storage. In this context, the dielectric loss factor can provide valuable insights into the material's electrical properties. An increase in this factor may indicate higher ionic conductivity, but it may also reflect an increase in energy dissipation, leading to greater electrical losses [61].

The graph in Figure 6e indicates that, at high frequencies, the dielectric loss factor (tan δ) increases with the addition of POMA to the LLZO ceramic matrix. At low frequencies, a different behavior is observed; except for the LLZO/POMA-5 sample, the tan δ curves remain below those of pristine LLZO, an effect consistent with Maxwell–Wagner polarization, which raises ε' and suppresses losses in this range. Moreover, the real permittivity (calculated using Equation 4) at low frequencies for the LLZO/POMA-15 and POMA samples reaches significantly higher values (on the order of 10^5) compared to those obtained for the other composites (on the order of 10^2). This trend indicates an increase in energy storage capacity with the addition of POMA to the polymer matrix.

$$\sigma_{AC} = \omega\varepsilon_0\varepsilon'' \tag{5}$$

In the graph of Figure 6b, the trend of increasing AC conductivity (Equation 5, [60]) with the addition of POMA is evident. At high frequencies, this value increases from 1.41 $\times10^{-7}$ S·cm^{-1} for the LLZO sample to 7.47 $\times10^{-6}$ S·cm^{-1} for the LLZO/POMA-15 sample. For the POMA sample, the result is 8.30×10^{-6} S·cm^{-1}.

It is possible to fit the curves in Figure 6b to the Jonscher model, given by Equation (6) [62].

$$\sigma(\omega) = \sigma_{dc} + A\omega^{s}, \quad 0 < s < 1 \tag{6}$$

where $\sigma(\omega)$ is the effective conductivity as a function of angular frequency ω; σ_{dc} is the dc conductivity; A is the prefactor

scaling the dispersive (ac) contribution (fitted from data); ω is the angular frequency ($\omega = 2\pi f$, with f in Hz); and s is the dispersion exponent ($0 < s < 1$ in disordered media), linked to relaxation mechanisms. Fits were performed in Python (NumPy and SciPy) using scipy.*optimize.least_squares* for nonlinear least-squares fitting of the Jonscher model. Data were handled with pandas, and parameter uncertainties were estimated from the fit covariance matrix. The fitted parameters are summarized in Table 6. The results show a clear increase in the total DC conductivity, encompassing both grain and grain-boundary contributions, with increasing POMA content. Overall, an enhancement of approximately two orders of magnitude is observed, with the DC conductivity increasing from 7.58 (46) $\times 10^{-9}$ S·cm^{-1} in pristine LLZO to 5.44 (99) $\times 10^{-7}$ S·cm^{-1} in the LLZO/POMA-15 composite.

Another relevant result from Table 6 is the systematic reduction of the Jonscher exponent s in the composites, decreasing from 0.756 in LLZO/POMA-1 to 0.295 in LLZO/POMA-15. This parameter quantifies the degree of dispersion in the AC response, and values significantly below unity are characteristic of disordered systems in which charge transport is governed by localized hopping mechanisms. The progressive decrease in s therefore indicates that increasing POMA content introduces additional structural and interfacial heterogeneity, leading to a broader distribution of relaxation times.

Although this interpretation does not distinguish between ionic and electronic contributions, the increased heterogeneity is consistent with the observed enhancement in total DC conductivity. The incorporation of POMA generates a larger number of interfacial regions in which local disorder, weakened Li—O interactions, or polymer-induced defects may facilitate charge-carrier mobility, thereby contributing to the improved electrical transport properties of the composites.

Previous studies [58–65] have reported LLZO based composites incorporating different polymer matrices. For instance, a PVDF/LLZO composite engineered with a three-dimensional interconnected LLZO architecture exhibited an ionic conductivity of 1.51 $\times 10^{-4}$ S·cm^{-1} [58], whereas the same study reported a conductivity of 7.5 $\times 10^{-5}$ S·cm^{-1} for PVDF/LLZO composites containing LLZO as discrete particles. For LLZO/PEO systems with 20 wt% polymer, conductivities on the order of 10^{-5} S·cm^{-1} have been reported [9]. Composites incorporating Al-doped LLZO nanofibers in a PVDF-HFP matrix reached 3.26 $\times 10^{-4}$ S·cm^{-1} [59], and a similar value (2.9 $\times 10^{-4}$ S·cm^{-1}) has been reported for LLZO/PAN composites [60]. Overall, LLZO/polymer composites typically exhibit ionic conductivities in the 10^{-5}–10^{-4} S·cm^{-1} range.

In this context, the grain conductivity obtained for the LLZO/POMA-15 sample (2.66 $\times 10^{-6}$ S·cm^{-1}) falls within a close order of magnitude and demonstrates that POMA incorporation significantly improves the room temperature electrical performance of LLZO, yielding values comparable to those reported for state of the art LLZO-based composites.

In general, the measurements reveal a systematic increase in σ_{dc} with increasing POMA content, accompanied by a concurrent reduction in the Jonscher exponent s. This combination is characteristic of charge transport in increasingly heterogeneous microstructures and indicates a broader distribution of relaxation processes. Within this framework, POMA is understood to act primarily at polymer/ceramic interfaces, where local disorder, weakened Li—O interactions, and polymer-induced defects can reduce energy barriers for charge transport and improve connectivity between neighboring grains.

Because non-blocking electrodes were employed, the present data do not allow for an unambiguous separation of ionic and electronic contributions to σ_{dc}. Such a distinction would require additional measurements, including DC polarization with ion-blocking electrodes or transference-number experiments. Nevertheless, LLZO in its cubic phase is widely recognized as a predominantly ionic conductor due to its high Li^+ concentration, partially occupied lithium sublattices, and defect structures that promote Li^+ mobility [20, 62–67]. Thus, although the observed enhancement in total conductivity may include both ionic and electronic components, it is reasonable to expect that a significant contribution arises from improved Li^+ mobility at the polymer/ceramic interface. Taken together, the LLZO/POMA composites, particularly LLZO/POMA-15, exhibit competitive electrical performance while retaining good thermal stability, highlighting their potential for incorporation into solid-state electrolyte architectures for energy-storage devices.

The Jonscher exponent s provides valuable insight into relaxation mechanisms in disordered materials. In the present composites, all samples exhibit $s < 1$, which is characteristic of systems in which charge transport occurs via localized hopping processes rather than long range band conduction. In disordered ionic and electronic media, a decrease in s is commonly associated with broader distributions of relaxation times and with correlated barrier hopping (CBH) or quantum-mechanical tunneling mechanisms, as reported for polymer electrolytes and polymer–ceramic composites [68].

In this system, the progressive reduction of s with increasing POMA content is a robust experimental observation. This trend indicates enhanced dispersion of relaxation processes and increased structural and electronic disorder introduced by the polymer phase. Although this interpretation cannot be directly proven by the present measurements, such disorder may facilitate additional localized conduction pathways at LLZO/POMA interfaces, where weaker Li—O interactions and interfacial heterogeneity could promote charge-carrier mobility. These interfacial effects should therefore be regarded as interpretative hypotheses, complementary to the experimentally verified correlation between σ_{dc} and s.

Finally, it is important to emphasize that the electrical conductivity values reported here correspond to the total conductivity measured at room temperature using non-blocking electrodes. Because POMA is an electronically conductive polymer and selective electrodes were not employed, the present dataset does not allow for a quantitative separation of ionic and electronic contributions to σ_{dc}. Consequently, the conductivity enhancement observed in the LLZO/POMA composites should be interpreted as an improvement in total electrical conductivity rather than exclusively ionic transport. A rigorous determination of purely ionic conductivity would require additional experiments, such as DC polarization with ion-blocking electrodes, Li^+ transference-number measurements, or temperature-dependent

impedance spectroscopy to extract activation energies. These analyses are beyond the scope of the present work and will be addressed in future studies.

4 | Conclusions

The synthesis route employed in this work proved effective in producing the desired garnet type structure, with the cubic $Li_7La_3Zr_2O_{12}$ phase consistently dominating the crystalline composition of all samples. The formation of Li_2CO_3 and LiOH was attributed to the well known surface reactivity of LLZO toward atmospheric moisture and CO_2, as confirmed by XRD and supported by FTIR and TG/DTG analyses. FTIR spectra revealed vibrational bands associated with La—O and Zr—O lattice vibrations, as well as C—O stretching modes related to Li_2CO_3, in agreement with the XRD phase identification. Bands characteristic of POMA were also observed. SEM images displayed morphological features consistent with those reported for LLZO and POMA, while EDS analysis confirmed the presence of the constituent elements in proportions consistent with the Rietveld refinements. Impedance spectroscopy demonstrated a significant enhancement in total DC conductivity upon POMA incorporation, increasing from 7.58 $(46)\times10^{-9}$ S·cm^{-1} in pristine LLZO to 5.44 $(99)\times10^{-7}$ S·cm^{-1} in the LLZO/POMA–15 composite. The grain conductivity increased from 1.89×10^{-8} to 2.66×10^{-6} S·cm^{-1}, while the high-frequency AC conductivity increased from the 10^{-7} to the 10^{-6} S·cm^{-1} range across the same composition series. The POMA containing samples also exhibited higher permittivity and shorter relaxation times, consistent with increased interfacial heterogeneity and modified relaxation dynamics, as reflected by the reduction of the Jonscher exponent *s*. These results indicate that the improved electrical transport arises primarily from polymer–ceramic interfacial effects, which are associated with improved electrical transport and modified relaxation dynamics. Overall, the LLZO/POMA composites combine the structural and thermal stability of LLZO with the interfacial and transport advantages introduced by POMA. The synergistic interaction between the ceramic and polymer phases results in superior electrical performance compared with the individual constituents. Among the investigated compositions, LLZO/POMA-15 stands out as the most conductive while maintaining good thermal stability, highlighting its potential as a promising candidate for incorporation into solid-state electrolyte architectures for energy-storage devices.

Author Contributions

Jardson Braz da Silva: conceptualization, investigation, writing – original draft, methodology, formal analysis. **Juliana Pereira da Silva:** investigation, validation, methodology, visualization. **Ramon Raudel Peña Garcia:** investigation, writing – original draft, validation, visualization. **Lianet Aguilera Dominguez:** writing – review and editing, visualization, formal analysis, supervision. **Yan Matheus Colares Pinto:** conceptualization, methodology, data curation, validation. **Eduardo Antonelli:** investigation, methodology, validation, visualization. **Monica Tirado:** conceptualization, funding acquisition, validation, formal analysis. **Ronald Zico de Aguiar Nunes:** visualization, investigation, formal analysis. **Yurimiler Leyet Ruiz:** conceptualization, investigation, funding acquisition, methodology, supervision, formal analysis, writing – review and editing. **Fidel Guerrero Zayas:** investigation, validation, formal analysis, visualization, methodology. **Francisco Xavier Nobre:** conceptualization, investigation, methodology, formal analysis.

Acknowledgments

This study was financed in part by the "Coordenação de Aperfeiçoamento de Pessoal de Nível Superior—Brasil (CAPES)"—Finance code 001. The authors would like to thank "Fundac¸a~o de Amparo à Pesquisa do Estado do Amazonas", "Conselho Nacional de Desenvolvimento Científico e Tecnológico" and "Financiadora de Estudos e Projetos" for their financial support.

Funding

This work was supported by Coordination for the Improvement of Higher Education Personnel (CAPES), Brazil (Finance Code 001), Fundação de Amparo à Pesquisa do Estado do Amazonas (002), National Council for Scientific and Technological Development (CNPq), Brazil (003), Financiadora de Estudos e Projetos (004).

Conflicts of Interest

The authors declare no conflicts of interest.

Data Availability Statement

The data that support the findings of this study are available from the corresponding author upon reasonable request.

References

1. R. Murugan, V. Thangadurai, W. Weppner, et al., "Fast Lithium Ion Conduction in Garnet-Type $Li_7La_3Zr_2O_{12}$," *Angewandte Chemie International Edition* 46, no. 41 (2007): 7778.

2. Y. Zhang, F. Chen, R. Tu, Q. Shen, and L. Zhang, "Field Assisted Sintering of Dense al-Substituted Cubic Phase $Li_7La_3Zr_2O_{12}$ Solid Electrolytes," *Journal of Power Sources* 268 (2014): 960–964.

3. J. Awaka, N. Kijima, H. Hayakawa, and J. Akimoto, "Synthesis and Structure Analysis of Tetragonal $Li_7La_3Zr_2O_{12}$ With the Garnet-Related Type Structure," *Journal of Solid State Chemistry* 182, no. 8 (2009): 2046–2052.

4. M. Wood, X. Gao, R. Shi, et al., "Exploring the Relationship Between Solvent-Assisted Ball Milling, Particle Size, and Sintering Temperature in Garnet-Type Solid Electrolytes," *Journal of Power Sources* 484 (2021): 229252.

5. C. A. Geiger, E. Alekseev, B. Lazic, et al., "Crystal Chemistry and Stability of '$Li_7La_3Zr_2O_{12}$' Garnet: A Fast Lithium-Ion Conductor," *Inorganic Chemistry* 50, no. 3 (2011): 1089–1097.

6. M. Saccoccio, J. Yu, Z. Lu, et al., "Low-Temperature Pulsed Laser Deposition of Garnet $Li_{6.4}La_3Zr_{1.4}Ta_{0.6}O_{12}$ Films as All-Solid-State Lithium Battery Electrolytes," *Journal of Power Sources* 365 (2017): 43–52.

7. B.-J. Hwang and L. H. Abrha, "Cubic Garnet Solid Electrolyte With Superior Air Stability," in *Electrochemical Society Meeting Abstracts prime2020*, vol. 2 (Electrochemical Society, Inc., 2020), 494.

8. M. Lei, X. Wu, Y. Liu, K. Chen, J. Hu, and C. Li, "Polymer Electrolytes Reinforced by 2d Fluorinated Filler for All-Solid-State Li-Fe-F Conversion-Type Lithium Metal Batteries," *Nano Research* 16, no. 6 (2023): 8469–8477.

9. M. M. Biondo, L. M. de Oliveira, S. X. Lima, et al., "Chemically Synthesized Poly (O-Methoxyaniline): Influence of Counterions on the Structural and Electrical Properties," *Journal of Molecular Structure* 1205 (2020): 127588.

10. S. H. K. Paleti, Y. Kim, J. Kimpel, M. Craighero, S. Haraguchi, and C. Müller, "Impact of Doping on the Mechanical Properties of Conjugated Polymers," *Chemical Society Reviews* 53, no. 4 (2024): 1702–1729.

11. H. K. Tran, B. T. Truong, B.-R. Zhang, R. Jose, J.-K. Chang, and C.-C. Yang, "Sandwich-Structured Composite Polymer Electrolyte Based on PVDF-HFP/PPC/Al-Doped LLZO for High-Voltage Solid-State Lithium Batteries," *ACS Applied Energy Materials* 6, no. 3 (2023): 1475–1487.

12. P. Ghorbanzade, G. Accardo, K. Gomez, et al., "Influence of the LLZO–PPEO Interface on the Micro-and Macro-Scale Properties of Composite Polymer Electrolytes for Solid-State Batteries," *Materials Today Energy* 38 (2023): 101448.

13. M. Lechartier, L. Porcarelli, H. Zhu, et al., "Single-Lon Polymer/LlLZO Hybrid Electrolytes With High Lithium Conductivity," *Materials Advances* 3, no. 2 (2022): 1139–1151.

14. J. V. Garcia Milerio, J. B. da Silva, F. X. Nobre, et al., "Tuning Ionic Conductivity and Thermal Stability in Poma-Enriched LLZO Composites for Next-Generation Lithium-Ion Batteries," *Journal of Physical Chemistry C* 129, no. 19 (2025): 9127–9139.

15. A. J. Samson, K. Hofstetter, S. Bag, and V. Thangadurai, "A Bird's-Eye View of li-Stuffed Garnet-Type $Li_7La_3Zr_2O_{12}$ Ceramic Electrolytes for Advanced All-Solid-State li Batteries," *Energy & Environmental Science* 12, no. 10 (2019): 2957–2975.

16. J. Da Silva, M. Biondo, F. Nobre, et al., "Structure and Electrical Properties of the Composite $Na_2Ti_3O_7/Na_2Ti_6O_{13}$/POMA: A Study of the Effect of Adding POMA," *Journal of Alloys and Compounds* 867 (2021): 159025.

17. E. Sanches, J. Soares, R. Iost, et al., "Structural Characterization of Emeraldine-Salt Polyaniline/Gold Nanoparticles Complexes," *Journal of Nanomaterials* 2011, no. 1 (2011): 697071.

18. K. Momma and F. Izumi, "Vesta 3 for Three-Dimensional Visualization of Crystal, Volumetric and Morphology Data," *Journal of Applied Crystallography* 44, no. 6 (2011): 1272–1276.

19. J. W. Kim, J. L. Digol, S. Bong, and J. Lee, "Enhanced li-Ion Conductivity of $Li_7La_3Zr_2O_{12}$ by Simultaneous Substitution of Aluminum and Niobium Using a Modified Sol–Gel Method," *Battery Energy* 2, no. 2 (2023): 20220024.

20. M. M. Raju, F. Altayran, M. Johnson, D. Wang, and Q. Zhang, "Crystal Structure and Preparation of $Li_7La_3Zr_2O_{12}$ (LLZO) Solid-State Electrolyte and Doping Impacts on the Conductivity: An Overview," *Electrochem* 2, no. 3 (2021): 390–414.

21. E. Rangasamy, J. Wolfenstine, J. Allen, and J. Sakamoto, "The Effect of 24c-Site (a) Cation Substitution on the Tetragonal–Cubic Phase Transition in $Li_{7-x}La_{3-x}A_xZr_2O_{12}$ Garnet-Based Ceramic Electrolyte," *Journal of Power Sources* 230 (2013): 261–266.

22. S. Mohammadi, M. Golmohammad, A. SharifiRad, and S. M. Alizadeh, "Surface Modification and Chemical Stability of Garnet LLZO Solid Electrolyte by ZnO Coating Through a Facile and Practical Method," *Materials Chemistry and Physics* 308 (2023): 128235.

23. M. Sahal, J. Guo, C. K. Chan, and N. Rolston, "Surface Reduction of Li_2CO_3 on LLZO to Solid-State Electrolyte via Scalable Open-Air Plasma Treatment," *Batteries* 10, no. 7 (2024): 249.

24. S. Han, Z. Wang, Y. Ma, Y. Zhang, Y. Wang, and X. Wang, "Recent Advances in Solving Li_2CO_3 Problems in Garnet-Based Solid-State Battery: A Systematic Review (2020–2023)," *Journal of Energy Chemistry* 90 (2024): 58–76.

25. X. Yi, Y. Guo, S. Pan, et al., "Duality of Li_2CO_3 in Solid-State Batteries," *Transactions of Tianjin University* 29, no. 1 (2023): 73–87.

26. J. Kiat, G. Boemare, B. Rieu, and D. Aymes, "Structural Evolution of LLOH: Evidence of a Solid–Solid Transformation Toward ceLi_2O Close to the Melting Temperature," *Solid State Communications* 108, no. 4 (1998): 241–245.

27. M. Kozdra, D. Brandell, C. M. Araujo, and A. Mace, "The Sensitive Aspects of Modelling Polymer–Ceramic Composite Solid-State Electrolytes Using Molecular Dynamics Simulations," *Physical Chemistry Chemical Physics* 26, no. 7 (2024): 6216–6227.

28. L. Zhao, Y. Zeng, L. Fu, et al., "Constructing Low-Impedance $Li_7La_3Zr_2O_{12}$-Based Composite Cathode Interface for All-Solid-State Lithium Batteries," *Small Structures* 3, no. 12 (2022): 2200200.

29. E. Hirose, K. Niwa, K. Kataoka, J. Akimoto, and M. Hasegawa, "Structural Stability of the Li-Ion Conductor $Li_7La_3Zr_2O_{12}$ Investigated by High-Pressure In-Situ x-Ray Diffraction and Raman Spectroscopy," *Materials Research Bulletin* 107 (2018): 361–365.

30. K. Eggestad, S. M. Selbach, and B. A. Williamson, "Doping Implications of li Solid State Electrolyte $Li_7La_3Zr_2O_{12}$," *Journal of Materials Chemistry A* 12, no. 26 (2024): 15666–15675.

31. P. Gonzalez Puente, S. Song, S. Cao, et al., "Garnet-Type Solid Electrolyte: Advances of Ionic Transport Performance and Its Application in All-Solid-State Batteries," *Journal of Advanced Ceramics* 10 (2021): 1–40.

32. P. Ghorbanzade, P. López-Aranguren, and J. M. López del Amo, "A Vision for LLZO Carbonate Formation: Perspectives on Surface Treatment Approaches and Characterization Techniques," *ChemElectroChem* 11, no. 11 (2024): e202400136.

33. Z. Liu, A. Borodin, and F. Endres, "Ionic Liquid and Polymer Coated Garnet Solid Electrolytes for High-Energy Solid-State Lithium Metal Batteries," *Energy Technology* 10, no. 2 (2022): 2100907.

34. E. J. Cheng, T. Kimura, M. Shoji, H. Ueda, H. Munakata, and K. Kanamura, "Ceramic-Based Flexible Sheet Electrolyte for Li Batteries," *ACS Applied Materials & Interfaces* 12, no. 9 (2020): 10382–10388.

35. J. Tang, Y. Zhou, X. Li, X. Huang, W. Tang, and B. Tian, "In-Situ Li2o-Atmosphere Assisted Solvent-Free Route to Produce Highly Conductive $Li_7La_3Zr_2O_{12}$ Solid Electrolyte," *Energy Materials* 4, no. 2 (2024): 400022.

36. E. A. Sanches, L. C. Gomes, J. C. Soares, G. R. da Silva, and Y. P. Mascarenhas, "Characterization of Poly (o-Methoxyaniline) Emeraldine-Base Form Obtained at Different Time Neutralization," *Journal of Molecular Structure* 1063 (2014): 336–340.

37. S. Talu, *Micro and Nanoscale Characterization of Three Dimensional Surfaces: Basics and Applications* (Napoca Star Publishing House, 2015).

38. S. Talu and N. Patra, "Multiscale Stereometric Evolution of Zn0.7mg0.3O Thin Films From Peak Dominated Roughness to Porosity Driven Coarsening," *Journal of Alloys and Compounds* 1061 (2026): 187441.

39. N. Zhang, G. Ren, L. Li, et al., "Dynamical Evolution of CO_2 and H_2O on Garnet Electrolyte Elucidated by Ambient Pressure x-Ray Spectroscopies," *Nature Communications* 15, no. 1 (2024): 2777.

40. S. Vema, F. N. Sayed, S. Nagendran, et al., "Understanding the Surface Regeneration and Reactivity of Garnet Solid-State Electrolytes," *ACS Energy Letters* 8, no. 8 (2023): 3476–3484.

41. M. Elgegren, S. Kim, D. Cordova, et al., "Ultrasound-Assisted Encapsulation of Sacha Inchi (Plukenetia Volubilis Linneo.) Oil in Alginate-Chitosan Nanoparticles," *Polymers* 11, no. 8 (2019): 1245.

42. R. M. Silverstein and G. C. Bassler, "Spectrometric Identification of Organic Compounds," *Journal of Chemical Education* 39, no. 11 (1962): 546.

43. A. Nyczyk, M. Hasik, W. Turek, and A. Sniechota, "Nanocomposites of Polyaniline, Its Derivatives and Platinum Prepared Using Aqueous Pt Sol," *Synthetic Metals* 159, no. 7–8 (2009): 561–567.

44. B. Smith, "The Co Bond III: Ethers by a Knockout," *Spectroscopy* 32, no. 5 (2017): 22–26.

45. E. A. Sanches, J. M. da Silva, J. M. d. O. Ferreira, et al., "Nanostructured Polyaniline Emeraldine-Base Form (Eb-Pani): A Structural Investigation for Different Neutralization Times," *Journal of Molecular Structure* 1074 (2014): 732–737.

46. M. Aote and A. Deshpande, "Study of Ge-Doped Garnet Type $Li_7La_3Zr_2O_{12}$ as Solid Electrolyte for Li-Ion Battery Application," *Journal of Materials Science: Materials in Electronics* 35, no. 8 (2024): 586.

47. P. Gałka, J. Kowalonek, and H. Kaczmarek, "Thermogravimetric Analysis of Thermal Stability of Poly (Methyl Methacrylate) Films Modified With Photoinitiators," *Journal of Thermal Analysis and Calorimetry* 115 (2014): 1387–1394.

48. G. Larraz, A. Orera, and M. Sanjuán, "Cubic Phases of Garnet-Type $Li_7La_3Zr_2O_{12}$: The Role of Hydration," *Journal of Materials Chemistry A* 1, no. 37 (2013): 11419–11428.

49. M. Matsui, K. Takahashi, K. Sakamoto, et al., "Phase Stability of a Garnet-Type Lithium Ion Conductor $Li_7La_3Zr_2O_{12}$," *Dalton Transactions* 43, no. 3 (2014): 1019–1024.

50. C. Bernal, A. B. Couto, S. T. Breviglieri, and É. T. G. Cavalheiro, "Influence of Some Experimental Parameters on the Results of Differential Scanning Calorimetry-Dsc," *Química Nova* 25 (2002): 849–855.

51. Y. Ortiz, P. Arévalo, D. Peña, and F. Jurado, "Recent Advances in Thermal Management Strategies for Lithium-Ion Batteries: A Comprehensive Review," *Batteries* 10, no. 3 (2024): 83.

52. L. Zhao, H. Dai, F. Pei, P. Ming, X. Wei, and J. Zhou, "A Comparative Study of Equivalent Circuit Models for Electro-Chemical Impedance Spectroscopy Analysis of Proton Exchange Membrane Fuel Cells," *Energies* 15, no. 1 (2022): 386.

53. M. Schalenbach, Y. E. Durmus, H. Tempel, H. Kungl, and R.-A. Eichel, "Double Layer Capacitances Analysed With Impedance Spectroscopy and Cyclic Voltammetry: Validity and Limits of the Constant Phase Element Parameterization," *Physical Chemistry Chemical Physics* 23, no. 37 (2021): 21097–21105.

54. Y. Xiao, X. Huang, J. Meng, Y. Zhang, V. Knap, and D.-I. Stroe, "Electrochemical Impedance Spectroscopy-Based Characterization and Modeling of Lithium-Ion Batteries Based on Frequency Selection," *Batteries* 11, no. 1 (2024): 11.

55. S. Dos Santos Costa, J. Pereira da Silva, M. Moraes Biondo, et al., "Temperature Dependence of the Electrical Properties of na2ti3o7/na-2ti6o13/Poma Composites," *Molecules* 27, no. 18 (2022): 5756.

56. W. Bauhofer and J. Z. Kovacs, "A Review and Analysis of Electrical Percolation in Carbon Nanotube Polymer Composites," *Composites Science and Technology* 69, no. 10 (2009): 1486–1498.

57. T. M. Nahir, "Impedance Spectroscopy: Theory, Experiment, and Applications (Book Review)," (2005), Review of the Book Edited by E. Barsoukov and J. R. Macdonald.

58. J. R. Macdonald, W. B. Johnson, I. Raistrick, et al., *Impedance Spectroscopy: Theory, Experiment, and Applications* (John Wiley & Sons, 2018).

59. J. B. da Silva, J. P. da Silva, R. L. dos Santos, et al., "Tuning Electrical Conductivity in Lithium-Doped Sodium Titanate via Sonochemical Synthesis," *Materials Science and Engineering B* 323 (2026): 118836.

60. E. Barsoukov, *Impedance Spectroscopy Theory, Experiment, and Applications* (Wiley Online Library, 2005).

61. L. Lei, C. Chen, H. Nie, X. Wu, and D. Q. Tan, "Dielectric Loss and Electrical Conductivity Behaviors of Epoxy Composites Containing Semiconducting Zno Varistor Particles," *Molecules* 27, no. 18 (2022): 6067.

62. B. Belgacem, N. Nasri, M. B. Yahia, A. Oueslati, and R. B. Hassen, "First Principles Approach and Experimental Exploration of a New Double Perovskite Phase Sr 2 (In 0.33 Sn 0.33 Sb 0.33) 2 o 6: Evaluation of Structural, Optical, and Dielectric Properties," *RSC Advances* 14, no. 44 (2024): 32292–32303.

63. M. Wu, D. Liu, D. Qu, et al., "3d Coral-Like Llzo/Pvdf Composite Electrolytes With Enhanced Ionic Conductivity and Mechanical Flexibility for Solid-State Lithium Batteries," *ACS Applied Materials & Interfaces* 12, no. 47 (2020): 52652–52659.

64. J.-Y. Han, S. Kim, D. U. Park, et al., "Electrospun 1d Al-Llzo Incorporated Pvdf-Hfp Composite Electrolyte With Fast Li+ Pathway Derived From Highway Traction Effect for High Performance Lithium Metal Batteries," *Chemical Engineering Journal* 505 (2025): 159627.

65. X. Zhao, C. Wang, X. Fan, et al., "Addressing the Interface Issues of All-Solid-State Lithium Batteries by Ultra-Thin Composite Solid-State Electrolyte Combined With the Integrated Preparation Technology," *InfoMat* 7 (2025): e70012.

66. S.-K. Jung, H. Gwon, H. Kim, et al., "Unlocking the Hidden Chemical Space in Cubic-Phase Garnet Solid Electrolyte for Efficient Quasi-All-Solid-State Lithium Batteries," *Nature Communications* 13, no. 1 (2022): 7638.

67. J. Qu, X. Duan, K. Xue, and S. An, "Preparation and Electrochemical Characteristics of the Co-Doped $Li_7La_3Zr_2O_{12}$ Solid Electrolyte With fe3+ and bi3+," *Molecules* 30, no. 9 (2025): 2028.

68. A. K. Jonscher, *Dielectric Relaxation in Solids* (Chelsea Dielectrics Press, 1983).

ANNEX D – PUBLISHED ARTICLE — COMPLEMENTARY STUDY ON LLZO/POMA COMPOSITES

This annex presents a published article coauthored by the author of this thesis, reporting a complementary investigation of LLZO/POMA composites with different polymer contents and processing conditions.

THE JOURNAL OF PHYSICAL CHEMISTRY C
A JOURNAL OF THE AMERICAN CHEMICAL SOCIETY

Open Access
This article is licensed under CC-BY 4.0

pubs.acs.org/JPCC
Article

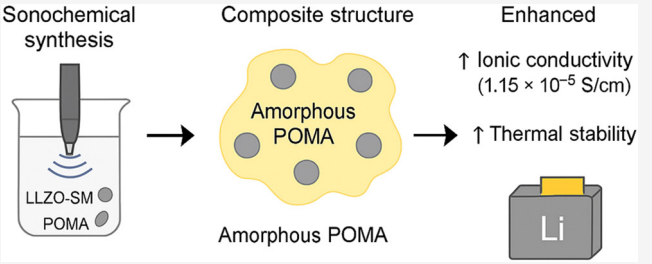
Tuning Ionic Conductivity and Thermal Stability in POMA-Enriched LLZO Composites for Next-Generation Lithium-Ion Batteries

José Victor Garcia Milério, Jardson Braz da Silva, Francisco Xavier Nobre, Rannier Marques Mendonça, Marcus Valerio Botelho do Nascimento, Eduardo Antonelli, Monica Tirado, Robert Saraiva Matos, Henrique Duarte da Fonseca Filho, Lianet Aguilera Dominguez, and Yurimiler Leyet Ruiz*

Cite This: J. Phys. Chem. C 2025, 129, 9127−9139

Read Online
ACCESS | Metrics & More | Article Recommendations

ABSTRACT: The garnet-type ceramic $Li_7La_3Zr_2O_{12}$ (LLZO) has garnered significant attention as a solid-state electrolyte for lithium-ion batteries due to its exceptional chemical stability, high ionic conductivity, and wide electrochemical window. Despite these advantages, practical applications of LLZO are hindered by challenges such as brittleness, interfacial resistance, and processing complexities. This study develops Sr- and Mg-doped LLZO enriched with poly(*o*-methoxyaniline) (POMA) composites. The composites were synthesized using a sonochemical approach, enabling uniform dispersion and integration of polymer and ceramic phases. Our results demonstrate that at an optimal 20% POMA content, the composite exhibited a remarkable enhancement in ionic conductivity (1.15×10^{-5} S/cm) along with exceptional thermal stability. X-ray diffraction (XRD) and Fourier transform infrared spectroscopy (FTIR) analyses confirmed the formation of amorphous domains that promote ion hopping, thermogravimetric analysis (TGA) highlighted the material's operational resilience. Further, morphological studies revealed synergistic interactions between the ceramic and polymer phases, facilitating efficient lithium-ion transport. These findings present a potentially scalable and innovative strategy to enhance solid-state electrolytes, paving the way for safer, higher-capacity, and more durable lithium-ion batteries for next-generation energy storage systems.

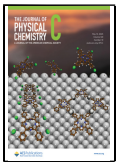


1. INTRODUCTION

The growing demand for electronic devices has driven the rapid expansion of battery production, necessitating the development of more robust devices with longer life cycles, faster charging, and enhanced safety. Solid-state lithium-ion batteries (SSLBs) represent a promising class of rechargeable batteries for next-generation devices,[1] primarily due to their potential to address the safety issues of current lithium-ion batteries (LIBs) that use organic liquid electrolytes (OLEs).[2] SSLBs are also expected to provide higher energy density, chemical stability, and longer service life.[3−6] These batteries consist of cathodes, anodes, and solid-state electrolytes (SSEs), which facilitate ionic conduction while minimizing leakage and fire hazards associated with liquid-based systems. Among SSEs, inorganic ceramic electrolytes (ICEs),[7] polymer electrolytes (PEs),[8] and solid composite electrolytes (SCEs)[7,9] have been extensively studied due to their distinct advantages in enhancing ionic conductivity and mechanical stability.

Deng et al. produced composite AlF_3-LLZTO solid electrolytes with F^- anions partially substituting for the O^{2-} ions in the grains and Al_2O_3/AlF_3 meliorating the grain boundaries were fabricated based on thermal AlF_3 decomposition and F/O displacement reactions. They unveiled the physicochemical effects of simultaneously modifying the grains and grain boundaries of garnet electrolytes, enlightening neoteric insights resolving interfacial issues in solid-state batteries.[10] By the way, Nasir et al. employed a microstructural engineering approach to control grain growth in $Li_{6.25}Ga_{0.25}La_3Zr_2O_{12}$ solid-state electrolytes, resulting in materials with high lithium-ion conductivity and air stability.[11] These advancements are promising for the development of more efficient and durable solid-state batteries. Specifically, garnet-type $Li_7La_3Zr_2O_{12}$ (LLZO) has emerged as a front-runner for ICE applications, offering high ionic conductivity and excellent chemical stability.[12,13] Additionally, advancements in conducting polymers like poly(*o*-methoxyaniline) (POMA) present a compelling alternative for polymer-based SSEs,[14] particularly when integrated with ceramic materials.

Received: February 5, 2025
Revised: April 28, 2025
Accepted: May 1, 2025
Published: May 6, 2025



ACS Publications
© 2025 The Authors. Published by American Chemical Society

https://doi.org/10.1021/acs.jpcc.5c00830
J. Phys. Chem. C 2025, 129, 9127−9139

Downloaded from pubs.acs.org/jpccck/article-pdf/129/19/9127/4096144/jp5c00830.pdf by guest on 09 September 2026

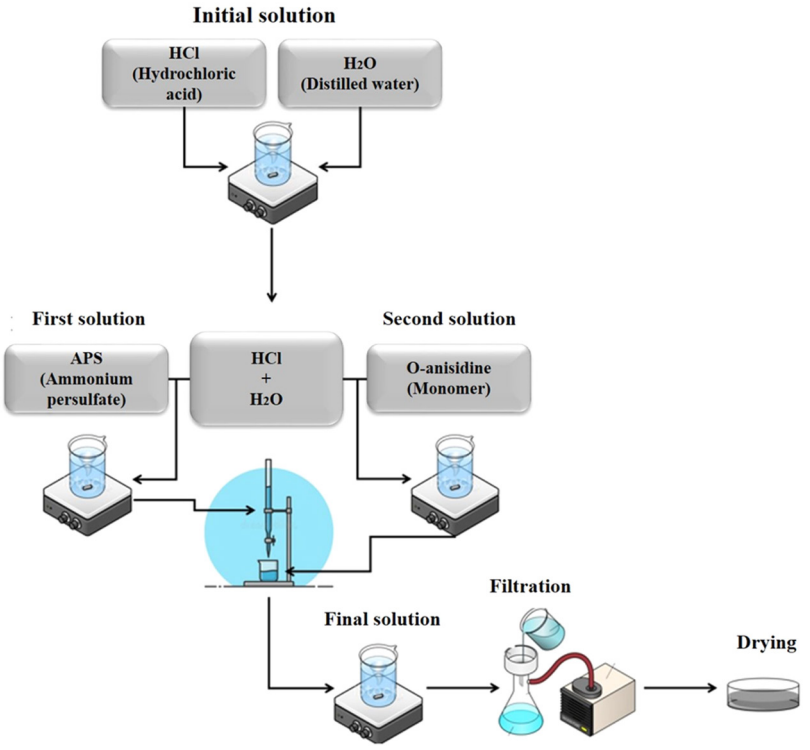


Figure 1. Schematic representation of the POMA preparation.

Despite significant advancements in SSLBs, several challenges persist that hinder their widespread adoption. The existing literature identifies three key limitations: the brittle nature of ICEs,[15,16] the moderate ionic conductivity of PEs,[4] and the difficulty in achieving an ideal balance between mechanical strength and ion transport efficiency in SCEs.[5,17] ICEs, while chemically stable, often suffer from interfacial resistance, limiting their application in flexible or high-performance devices. Conversely, PEs offer flexibility and ease of processing but fall short in terms of ionic conductivity, especially under extreme conditions. Recent research into SCEs, hybrid systems combining the strengths of ICEs and PEs, has highlighted their potential to address these challenges.[18,19] However, existing studies often report inconsistencies in structural stability and conductivity, influenced by factors such as dopant selection, material ratios, and processing conditions.[20−22] For instance, the ionic conductivity of garnet-based ceramics like LLZO can be significantly enhanced by doping with elements such as magnesium and strontium, yet achieving uniform integration with polymer matrices remains problematic.[23,24] Our study focuses on developing a novel LLZO−SM/POMA composite system, targeting improved ionic conductivity and thermal stability to meet the demands of next-generation energy storage applications.

Solid-state electrolytes have been a focal point of research due to their potential to improve the safety and performance of lithium-ion batteries. Among ICEs, garnet-type $Li_7La_3Zr_2O_{12}$ (LLZO) has attracted considerable attention for its high room-temperature ionic conductivity, chemical stability, and broad electrochemical window.[25,26] Studies have demonstrated that doping LLZO with elements like magnesium (Mg) and strontium (Sr) enhances ionic conductivity by creating vacancies in the crystal lattice and stabilizing the cubic phase.[27,28] However, the inherent brittleness and processing challenges of ceramics necessitate alternative approaches to improve their practical applicability. Polymer electrolytes, particularly those based on poly(ethylene oxide) (PEO)[29] and polyvinylidene fluoride (PVDF),[30] offer flexibility and ease of fabrication. However, their performance is constrained by relatively low ionic conductivity. Recent advancements in conductive polymers, such as poly(*o*-methoxyaniline) (POMA), show promise in bridging this gap. POMA exhibits unique properties, including high ionic conductivity when doped with acids and compatibility with ceramic phases, making it a suitable candidate for composite applications.[31]

Blending ICEs with PEs to form SCEs has emerged as a promising strategy to combine the strengths of both components. Research into garnet-polymer composites has shown that incorporating PEO, PVDF, or POMA into LLZO matrices can significantly enhance ionic conductivity while preserving mechanical integrity, e.g.,.[4,31−33] For instance, Yao et al.[33] reported that blending PVDF with LLZO resulted in 3D coral-like composite electrolytes with enhanced ionic conductivity and mechanical flexibility, achieving conductivities of up to 10^{-5} S/cm. Similarly, studies incorporating POMA into $Na_2Ti_3O_7/Na_2Ti_6O_{13}$ composites demonstrated that polymer additions can increase ionic mobility by introducing amorphous regions conducive to ion hopping.[31] Despite these advancements, challenges remain in achieving homogeneous dispersion of ceramic particles within polymer matrices, controlling interfacial interactions, and optimizing the balance between crystalline and amorphous phases for peak performance. This study introduces a novel LLZO−SM/POMA composite electrolyte, addressing critical gaps in the existing literature. Unlike conventional binary systems, it focuses on optimizing synergistic interactions between the ceramic and polymer phases, resulting in enhanced ionic conductivity, thermal stability, and mechanical properties. The use of a sonochemical method ensures homogeneous dispersion of ceramic particles, effectively overcoming key

Downloaded from pubs.acs.org/jpccck/article-pdf/129/19/9127/4096144/jp5c00830.pdf by guest on 09 September 2026

https://doi.org/10.1021/acs.jpcc.5c00830
J. Phys. Chem. C 2025, 129, 9127−9139

synthesis challenges. The LLZO−SM/POMA composite presents a scalable and efficient solution for next-generation solid-state lithium-ion batteries, resolving ICE brittleness and PE conductivity limitations.

Therefore, we developed and characterized LLZO−SM/POMA composites as advanced solid-state electrolytes for lithium-ion batteries. Using a sonochemical approach, composites with varying POMA content were synthesized targeting their best ionic conductivity and thermal stability. The structure, thermal stability, chemical interactions, and morphological changes of the composites were thoroughly examined using various experimental techniques. Furthermore, electrochemical impedance spectroscopy (EIS) analyses revealed a significant enhancement in the ionic conductivity of the composites, closely associated with their physical properties. Our findings highlight the composite's potential for energy storage applications and its pivotal role in advancing solid-state lithium-ion battery technologies.

2. MATERIALS AND METHODS

2.1. Raw Materials. The materials employed in this study included hydrochloric acid (HCl, Synth, 37%) for the preparation of a 2.0 M solution, distilled water as the solvent, ammonium persulfate ($(NH_4)_2S_2O_8$, Sigma-Aldrich, 98%) as the oxidizing agent, and *o*-anisidine monomer (C_7H_9NO, Sigma-Aldrich, 99%) as the precursor for the synthesis of poly(*o*-methoxyaniline) (POMA). Additionally, strontium- and magnesium-doped $Li_7La_3Zr_2O_{12}$ (LLZO−SM) ceramic material ($Li_{6.95}Mg_{0.15}La_{2.75}Sr_{0.25}Zr_2O_{12}$) was utilized as obtained from previous studies.[22,34]

2.2. POMA Synthesis. POMA was synthesized by preparing two separate solutions from an initial 2.0 M HCl solution (84 mL of HCl mixed with 916 mL of distilled water). Figure 1 illustrates the POMA production flowchart. In a typical procedure, the first solution was obtained by dissolving 0.0508 mol of ammonium persulfate ($(NH_4)_2S_2O_8$) in 200 mL of the HCl solution, stirring for 10 min without heating. Simultaneously, a second solution was prepared by mixing 300 mL of the HCl solution with 28 mL of o-anisidine monomer (C_7H_9NO) under the same stirring conditions. The first solution was then gradually added to the second under low-speed stirring, followed by 3 h of continuous mixing. The final product was filtered, air-dried at room temperature for 48 h, and collected as powdered POMA.

2.3. LLZO-SM/POMA Composite Obtention. For LLZO-SM/POMA composite production, a sonochemical method was employed to homogenize the materials. Samples were prepared according to predefined proportions (Table 1). POMA and LLZO-SM were first dispersed in distilled water and subjected to ultrasonic treatment at 40 kHz and 50 °C for 10 min. Subsequently, the LLZO-SM powder was added to POMA-containing samples (S2 to S5) and sonicated again under the same conditions. The resulting mixtures were dried at 50 °C until constant mass, producing particulate materials for subsequent characterization. Figure 2 outlines the synthesis process.

Table 1. Proportions of Materials Used in the Synthesis of Samples and Preparation of Powdered Test Specimens

samples	POMA (%)	LLZO−SM (%)
S1	0	100
S2	1	99
S3	5	95
S4	20	80
S5	50	50
S6	100	0

2.4. Characterization. The crystalline structure and phase composition of the materials were investigated using X-ray diffraction (XRD) on a Shimadzu XRD-7000 diffractometer (Shimadzu Corporation, Japan) equipped with copper Kα radiation (λ = 1.5606 Å). The instrument operated at 30 kV and 10 mA, scanning 2θ angles from 5 to 100°. The thermal stability and decomposition behavior of the samples were assessed through thermogravimetric analysis (TGA) using a Shimadzu TGA-50H instrument (Shimadzu Corporation, Japan) with a heating rate of 20 °C min^{-1} over a temperature range of 25 to 1000 °C, under a nitrogen flow of 30 mL/min. Functional groups in the samples were identified using Fourier transform infrared (FTIR) spectroscopy with an Agilent Cary 630 FTIR spectrometer (Agilent Technologies) equipped with an attenuated total reflectance (ATR) module, operating in the spectral range of 650−4000 cm^{-1} at a resolution of 8 cm^{-1}. The surface morphology and microstructural features were examined via scanning electron microscopy (SEM) using a JEOL JSM-IT500HR microscope (JEOL Ltd., Japan) with acceleration voltages ranging from 10 to 15 kV.

2.5. Complex Impedance Investigation. The electrical properties of the composites were investigated using complex impedance spectroscopy using cylindrical pellets (1 cm diameter and 0.6 g) using a Solartron 1260 impedance analyzer (AMETEK Scientific Instruments, United Kingdom). Measurements were conducted at room temperature with a potential of 500 mV across a frequency range from 10 Hz to 1 MHz. The pellets were only compacted without any thermal treatment or sintering due to the low degradation temperature of the polymeric component present in the samples.

3. RESULTS AND DISCUSSION

3.1. Characterization of the Materials. Initially, XRD analysis was conducted to assess the effects of sonication on the structural properties of polymeric and ceramic materials during composite formation, as shown in Figure 3. Figure 3(a) compares the XRD patterns of sonicated and nonsonicated POMA samples, revealing characteristic diffraction peaks in two distinct regions: 2θ = 7° and 2θ = 22−30°. The first peak, attributed to polymer chain alignment with OH^- or Cl^- ions, aligns with the use of HCl as a doping acid in POMA synthesis.[31] The broader peak in the second region results from multiple reflections linked to crystallinity, crystallite size, and benzene rings in the polymer structure.[31,35] Both XRD patterns reveal the presence of partial crystalline arrangements within the POMA chains. These results align with previous studies by Sanches et al.[35] and Biondo et al.,[36] which reported similar diffraction patterns, with slight variations influenced by the doping acid and synthesis duration. Notably, no significant structural differences were identified between the sonicated and nonsonicated samples, suggesting that the 10 min sonication process does not substantially alter the polymer's structural properties. On the other hand, the XRD patterns of LLZO−SM ceramics synthesized with and without sonochemical treatment (Figure 3(b)) showed diffraction peaks matching the ICSD#422259 database, confirming the cubic phase of LLZO. This phase, stabilized by Mg^{2+} substituting Li^+ and Sr^{2+} replacing La^{3+}, enhances ionic conductivity by

Downloaded from pubs.acs.org/jpcccck/article-pdf/129/19/9127/4096144/jp5c00830.pdf by guest on 09 September 2026

https://doi.org/10.1021/acs.jpcc.5c00830
J. Phys. Chem. C 2025, 129, 9127−9139

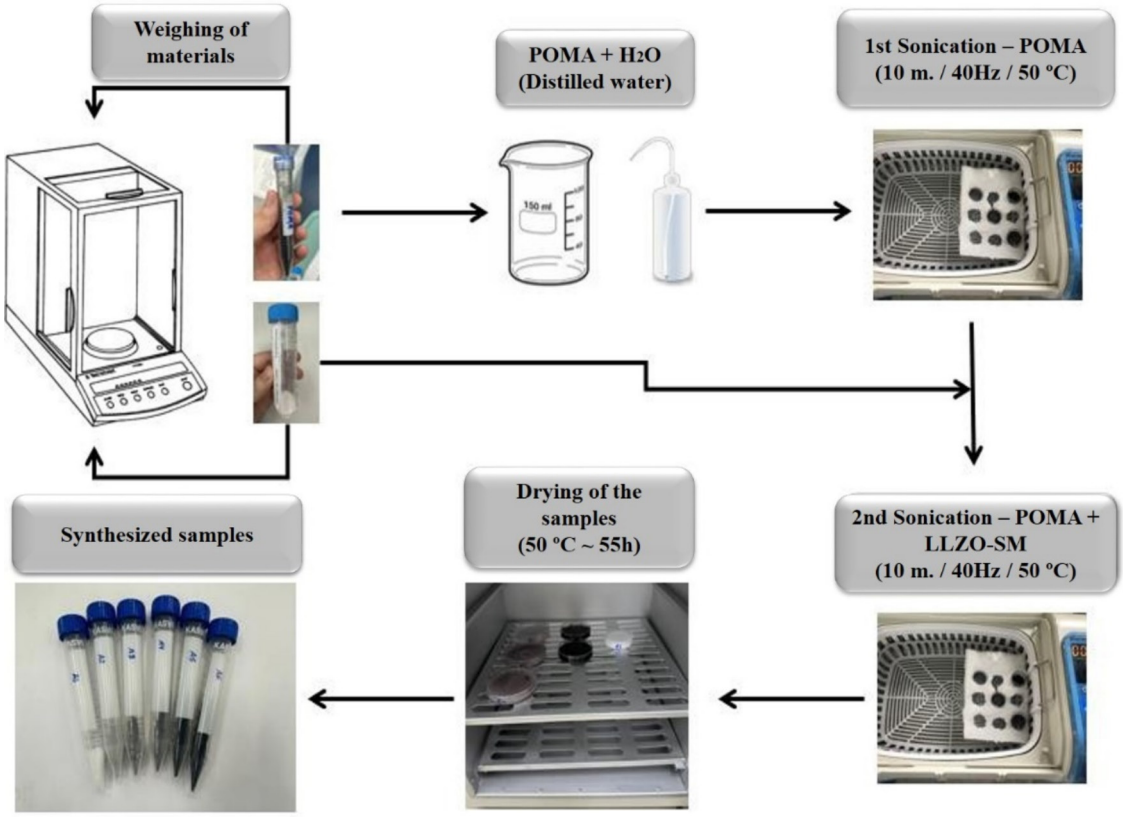


Figure 2. Sample composites synthesis flowchart.

creating vacancies and expanding the crystal lattice.[21] A minor shoulder peak at 2θ = 31°, corresponding to the tetragonal phase by the ICSD#246816 card, indicates a trace dual-phase structure with the cubic phase dominating. The similarities in XRD patterns suggest that the sonochemical treatment did not significantly alter the material's structure but primarily improved the homogenization of components. The predominance of the cubic phase is directly linked to cation substitutions, consistent with prior findings.[21,22] The molecular structure of POMA contains key functional groups, such as methoxy ($-OCH_3$) and amine (−NH or −N =), which can interact with the LLZO ceramic matrix. Possible interactions, such as hydrogen bonding and electrostatic interactions, may influence ionic conductivity.

Further, Figure 4 illustrates the structural effects resulting from the incorporation of POMA into LLZO−SM composites. The XRD patterns of all six samples consistently exhibited the characteristic peaks of LLZO−SM when low concentrations of POMA were integrated (S2−S3 samples), as compared to the pure LLZO−SM (S1). This consistency suggests that at these minimal polymer concentrations, POMA does not significantly disrupt the crystalline structure of the ceramic material or induce any substantial atomic rearrangements. These observations align with findings from Jiang et al.,[17] who reported that the integration of polymers, such as PVDF−HFP, into LLZO matrices preserved the material's characteristic peaks and structural integrity. At higher POMA concentrations, particularly in S4 (20% POMA), noticeable structural alterations were detected. The emergence of new, low-intensity peaks at 2θ = 23 and 24°, corresponding to POMA's crystalline regions (2θ = 22−30°), indicates the increasing influence of the polymer on the composite structure. Additionally, the distinct LLZO−SM "double peak" at 2θ = 31°, prominent in samples with lower polymer content, was reduced to a single peak in S4, signaling a shift toward greater amorphousness within the composite. Moreover, the disappearance of peaks at 2θ = 36 and 37°, which were observed in samples with lower POMA content, provides additional evidence that increasing POMA content significantly reduces the crystalline fraction of LLZO−SM.[17,37] Such structural transformations have been linked to improved ionic mobility, as a more amorphous phase often facilitates better electrical conductivity.[18,31] These trends became even more pronounced in S5 (50% POMA). The peaks at 2θ = 23, 24, and 29° intensified, underscoring the dominance of POMA's crystalline regions. Concurrently, the LLZO−SM "double peak" at 2θ = 31° was nearly eliminated, while the peaks at 2θ = 36 and 37°, associated with the amorphous portion of the composites,[17,37] remained absent. A baseline deviation between 2θ = 22 and 28° was also observed, attributed to reflections from the benzene rings and the crystallite size of POMA.[31] The results indicate that incorporating POMA above 20% significantly alters the composite structure, promoting a transition toward a more amorphous phase while simultaneously accentuating POMA's crystalline regions. At the highest concentration of 50% POMA, partial recovery of crystalline content was observed, potentially influencing the composites' electrical properties, e.g., conductivity.[5,17] These findings underscore the complex interplay between polymer content and structural phases, providing valuable insights for tailoring composite functionality to specific applications.

The thermal stability of LLZO−SM/POMA composite materials was investigated by our TGA analysis, as displayed in Figure 5. These curves display the thermal responses of the

Downloaded from pubs.acs.org/jpcccck/article-pdf/129/19/9127/4096144/jp5c00830.pdf by guest on 09 September 2026

https://doi.org/10.1021/acs.jpcc.5c00830
J. Phys. Chem. C 2025, 129, 9127−9139

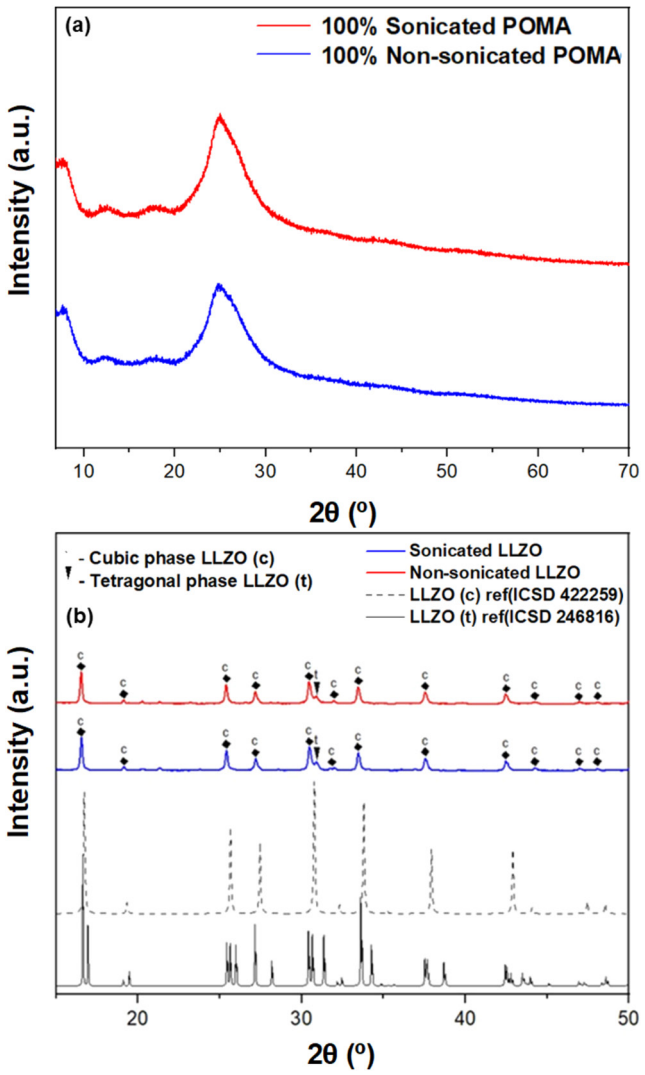


Figure 3. XRD patterns of (a) POMA and (b) LLZO−SM ceramics, comparing their structural characteristics with and without sonication treatment.

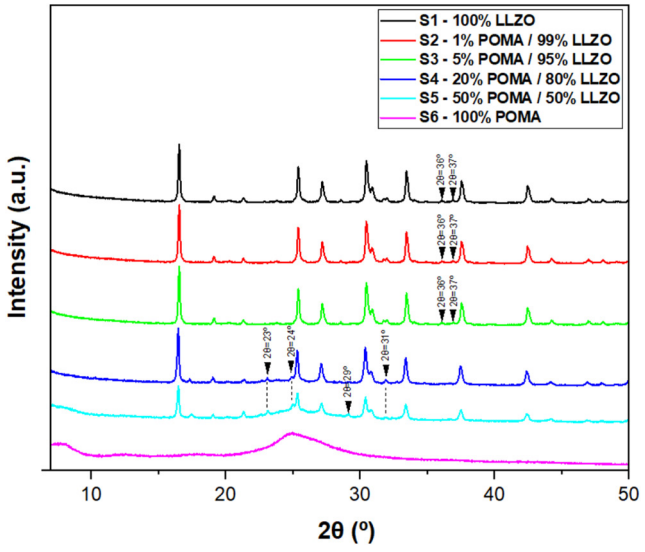


Figure 4. XRD patterns of LLZO−SM/POMA composites synthesized under different POMA contents.

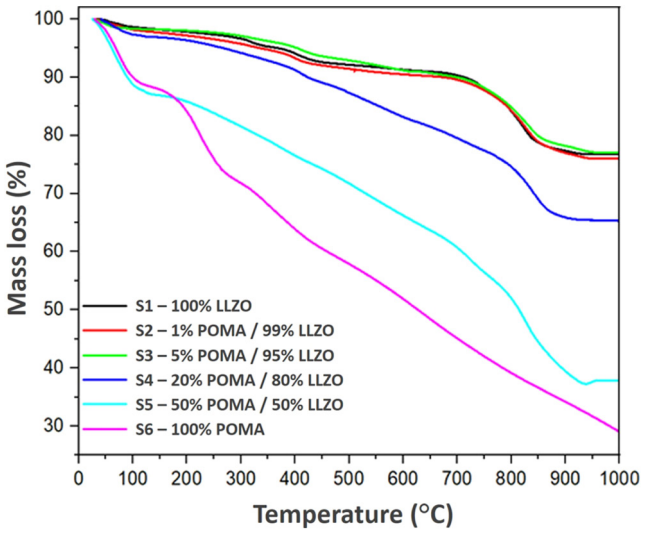


Figure 5. Comparative TGA curves of LLZO−SM/POMA composites synthesized under different POMA contents.

composites, revealing distinct degradation patterns influenced by the variation of POMA content in the composite matrix. The samples with low POM contents (S1, S2, and S3) displayed similar thermal profiles, characterized by minimal mass loss at low temperatures due to the evaporation of residual moisture (~2%). This trend is consistent with the intrinsic thermal stability of the LLZO−SM ceramic matrix, which remains largely unaffected by the inclusion of small amounts of polymer. Between 100 and 400 °C, these samples exhibited cumulative mass losses of 5−7%, primarily due to the decomposition of water molecules. However, for samples S2 and S3, this mass loss is also ascribed due to the initial degradation of POMA chains and the release of chlorine ions from HCl used in the polymer synthesis. This makes the three samples thermally stable at this temperature range, with the mass loss being relatively insignificant.[38−41] Further, their thermal behavior from 400 to 730 °C demonstrates their stability, evidenced by a small 11% mass reduction attributed to the partial decomposition of La_2O_3 precursors within the LLZO−SM structure, in addition to additional POMA polymer chains.[40,42] Above 730 °C, decomposition of $La_2O_2CO_3$ compounds formed by the presence of La_2O_3, coupled with CO_2 release during exothermic reactions,[43] led to a more significant mass loss of 23−24% overall. Despite this, these samples retained a substantial proportion of their initial mass, underscoring their excellent thermal resilience even at elevated temperatures.

Sample S4, containing 20% POMA, exhibited intermediate thermal stability between the ceramic-dominated and polymer-rich samples. Up to 100 °C, its mass loss of ~3% was slightly higher than that of S1−S3, reflecting the increased polymer content. Between 100 and 400 °C, a 9% reduction occurred, driven by polymer chain degradation and the release of HCl.[44] The mass loss from 400 to 730 °C was 11% greater than that observed for samples S1−S3, due to the degradation of lithium from the Li_2CO_3, in addition to POMA chains degradation.[42] However, this trend did not significantly compromise its overall stability; the total mass loss of 34% highlights its suitability for applications requiring moderate polymer incorporation. Importantly, these results demonstrate that the addition of up to 20% POMA does not drastically diminish

Downloaded from pubs.acs.org/jpccck/article-pdf/129/19/9127/4096144/jp5c00830.pdf by guest on 09 September 2026

https://doi.org/10.1021/acs.jpcc.5c00830
J. Phys. Chem. C 2025, 129, 9127−9139

thermal stability. However, the incorporation of higher POMA content significantly impacted thermal stability, as evidenced by the performance of S5 and S6 samples. Up to 140 °C, both samples exhibited accelerated mass loss due to increased moisture evaporation,[36,39] with S5 losing 13% of its initial mass. This trend intensified between 140 and 400 °C, with S5 showing a 24% reduction and S6 exhibiting the highest loss of 37%, attributable to extensive POMA chain degradation and the breakdown of HCl dopant.[44] Above 400 °C, the thermal behavior of S5 and S6 reflected the inherent instability of polymer-rich systems, with progressive degradation resulting in total mass losses of 62% and 71%, respectively, by 1000 °C. The substantial polymer content amplified the susceptibility of these samples to thermal degradation, confirming the inverse relationship between POMA ratio and thermal stability. These results reveal that while ceramic-dominated samples maintain superior thermal stability, higher polymer content compromises this stability significantly. This trade-off between thermal resilience and polymeric behavior offers a versatile platform for customizing composite properties to meet specific application demands.

We further evaluated the chemical structure of our LLZO-SM/POMA composites, as shown in our FTIR analysis (Figure 6). The pure LLZO-SM sample (S1) displays IR

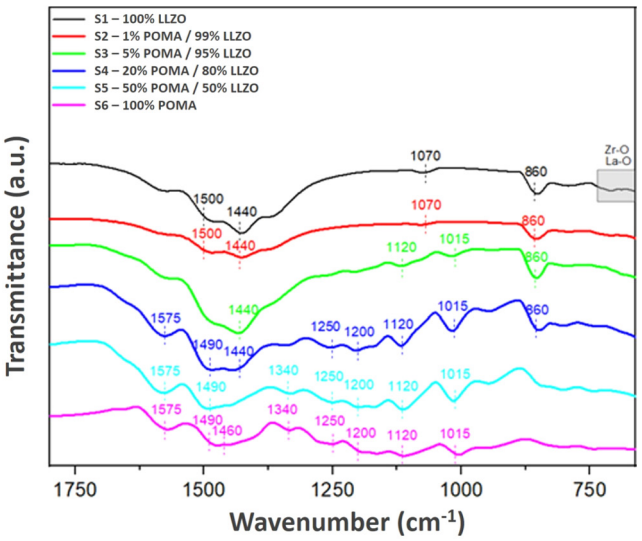


Figure 6. FTIR spectra of LLZO−SM/POMA composites synthesized under different POMA contents.

bands at 1440, 1070, and 860 cm^{-1} attributed to C−O stretching associated with Li_2CO_3 compound used in LLZO synthesis. Additionally, low-intensity bands below 750 cm^{-1} are assigned to Zr−O and La−O bond vibrations, consistent with the ceramic nature of LLZO-SM.[43,45] However, the sample S6 (100% POMA) exhibited distinct polymer-specific bands at 1575 and 1490 cm^{-1}, corresponding to N═Q═N (quinonoid) and N−B−N (benzenoid) vibrational modes, respectively.[40,46] The bands located at 1340 and 1250 cm^{-1} are ascribed to C−O−C stretching of alkyl aryl ether and C−H deformation of $-OCH_3$ molecules, respectively. Moreover, the bands positioned at 1200, 1120, and 1015 cm^{-1} arise due to substituted 1,4-benzene rings.[31,36] These differences provide a baseline for understanding the interactions between POMA and LLZO-SM in our composite materials.

The samples containing different POMA concentrations revealed progressive chemical structural changes indicative of interaction between the polymer and ceramic components. At 1% POMA (S2), the characteristic bands of LLZO−SM remained predominantly intact, indicating that the addition of a small amount of polymer had a negligible impact on the composite's structural framework. This observation aligns with previous studies, which report limited interaction and structural modifications at low polymer concentrations.[31,36,43] Further, at 5% POMA (S3), the emergence of polymer-specific bands at 1015 and 1120 cm^{-1}, associated with the substituted 1,4−benzene ring, along with the disappearance of the 1070 cm^{-1} band (C−O stretching of Li_2CO_3), marked the onset of detectable structural modifications within the composite. As the POMA concentration increased to 20% (S4), the chemical structural changes became significantly more pronounced, primarily due to the stronger contributions from polymeric bands such as N═Q═N (at 1575 cm^{-1}), N−B−N (at 1490 cm^{-1}), C−O−C (at 1250 cm^{-1}), and the substituted 1,4-benzene ring at 1200, 1120, and 1015 cm^{-1}. These prominent polymer-specific absorptions indicate an increasing interaction between POMA and the LLZO−SM matrix, reflecting substantial structural reorganization within the composite. These polymer-specific features were prominent alongside the retention of LLZO-SM bands, such as those at 1440 cm^{-1} and below 750 cm^{-1}. This indicates that the ceramic matrix remains structurally present but is increasingly influenced by the polymer content. On the other hand, at 50 and 100% POMA (S5 and S6), the FTIR spectra were dominated by polymeric bands, while most LLZO−SM-specific bands were significantly diminished, except for those associated with Zr−O and La−O vibrations. This suggests that high POMA concentrations induce extensive structural reorganization, where the polymer effectively overrides the ceramic matrix's vibrational characteristics. Such behavior aligns with earlier reports highlighting substantial structural alterations in ceramic systems with high polymer content.[31] Thus, the FTIR analysis reveals a clear progression of structural modifications driven by the incorporation of POMA into the LLZO−SM matrix, which is in accordance with our XRD results.

Furthermore, the morphology and structure of grains and particles within the composites reveal distinct trends across varying POMA compositions, as illustrated in Figure 7. The pure LLZO−SM material (S1, Figure 7(a)) exhibits densely packed particles ranging from nano- to micrometric scales, forming a tightly compact and uniformly aggregated structure. These particles form irregular spherical aggregates, which, while potentially enhancing lithium-ion transport through shorter diffusion paths, could compromise overall conductivity due to the formation of dense clusters that inhibit effective ion mobility.[44,47] This morphology aligns with similar observations reported in LLZO systems containing diverse dopants.[48−50] At 1% POMA (S2, Figure 7(b)), negligible morphological changes are observed compared to the pure sample, with the particle shape and surface characteristics remaining largely consistent. This confirms that low POMA content does not significantly alter the LLZO−SM matrix, aligning with previous studies that highlight the resilience of ceramic structures to minor polymeric additions. However, the incorporation of 5% POMA (S3, Figure 7(c)) introduces noticeable changes. As can be seen, the particles exhibit elongation and slightly larger aggregates, indicating that POMA begins to influence the composite's microstructure at this concentration. This

Downloaded from pubs.acs.org/jpcccck/article-pdf/129/19/9127/4096144/jp5c00830.pdf by guest on 09 September 2026

https://doi.org/10.1021/acs.jpcc.5c00830
J. Phys. Chem. C 2025, 129, 9127−9139

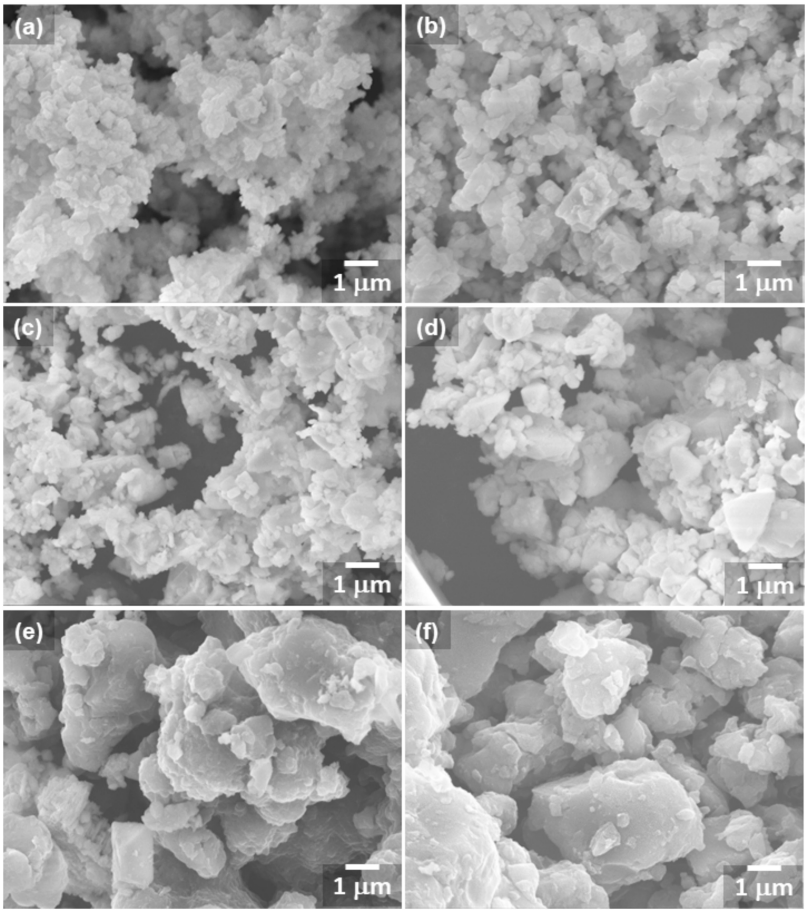


Figure 7. SEM images of (a) S1, (b) S2, (c) S3, (d) S4, (e) S5, and (f) S6 samples.

morphological shift could reflect increased interactions between the polymer and ceramic phases, initiating structural reorganization within the matrix. The trend becomes more evident at 20% POMA (S4, Figure 7(d)), where a distinct dual morphology develops, characterized by smaller, spherical particles associated with LLZO−SM and larger, irregularly shaped particles attributed to POMA. Such coexistence is characteristic of polymer-ceramic composites and has been documented in sodium titanate systems, e.g., $Na_2Ti_3O_7$/$Na_2Ti_6O_{13}$ composites loaded with 10 to 35% POMA.[31] This combination of morphologies is likely advantageous for ion conduction, as it leverages complementary pathways within the ceramic and polymeric phases, enhancing electrical performance through synergistic ion conduction mechanisms in both materials.[51] At 50% POMA (S5, Figure 7(e)), the morphology becomes distinctly dominated by POMA, characterized by larger and smoother particles exceeding 1 μm, consistent with observations reported in refs 31,36. This notable structural shift indicates that higher POMA content reduces the number of vacancies within the LLZO−SM framework, which could potentially impede ionic conductivity.[20,30] Finally, the pure POMA sample (S6, Figure 7(f)) reveals large, flat particles with smoother surfaces forming a "cauliflower-like" morphology. This unique structure, shaped by the dopant acid used during polymerization,[52] aligns with literature descriptions and reflects the intrinsic characteristics of the polymer. These findings underscore the critical influence of particle size, surface morphology, and aggregation on lithium-ion conduction pathways and the overall electrical behavior of the composites. The interplay between polymeric and ceramic components emerges as a key factor in determining ion transport mechanisms and optimizing material performance.

The significant differences observed in the SEM images of the six samples are primarily attributed to the varying POMA content in the LLZO−SM/POMA composites. The pure LLZO−SM sample (S1) exhibits a densely packed structure with micrometric particles, forming compact aggregates that enhance lithium-ion transport but may limit overall conductivity due to particle clustering. At a low POMA concentration (1% in S2), the morphology remains largely unchanged, indicating that minimal polymer incorporation does not significantly disrupt the ceramic matrix. However, at 5% POMA (S3), noticeable structural changes emerge, with elongated particles and larger aggregates forming, suggesting initial polymer influence on the composite's microstructure. A more distinct dual morphology appears at 20% POMA (S4), where spherical LLZO−SM particles coexist with irregular POMA domains, creating interconnected pathways that facilitate ionic conduction. As the POMA content increases to 50% (S5), the structure becomes polymer-dominated, with larger, smoother particles exceeding 1 μm, potentially reducing the availability of ceramic ion transport channels. Finally, in the pure POMA sample (S6), the morphology shifts entirely to a "cauliflower-like" structure with flat, smooth surfaces, characteristic of HCl-doped POMA. These variations indicate a gradual transition from a highly crystalline ceramic-dominated framework (S1) to an increasingly amorphous polymer-rich matrix (S6). The observed changes in morphology directly

Downloaded from pubs.acs.org/jpccck/article-pdf/129/19/9127/4096144/jp5c00830.pdf by guest on 09 September 2026

https://doi.org/10.1021/acs.jpcc.5c00830
J. Phys. Chem. C 2025, 129, 9127−9139

impact ion transport and mechanical stability, with an optimal POMA concentration of 20% balancing polymer flexibility and ceramic rigidity to enhance conductivity. Thus, the SEM differences reflect the interplay between the ceramic and polymer phases, which govern structural integrity, porosity, and ionic mobility in the composites.

3.2. Electrical Properties. The electrical properties of LLZO−SM/POMA disc-shaped composites were evaluated using Complex impedance spectroscopy at room temperature, with Nyquist (Cole−Cole) diagrams presented in Figures 8 and 9. These figures depict the impedance behavior of the composites with varying POMA content and bring crucial information about sample resistance and ionic conductivity.[39,40] The material's resistance was analyzed using the complex impedance (Z^*), defined as $Z^* = Z' - jZ''$, where Z' represents the real component and jZ'' denotes the imaginary component. The ionic conductivity (σ) was determined using the formula $\sigma = \frac{t}{Z_{re}A}$, where t represents the disc thickness, Z_{re} is the resistance obtained from the Nyquist plot, and A denotes the sample−electrode contact area.[53] The Cole−Cole diagram of pure LLZO−SM ceramic (Figure 8) reveals a large semicircular arc, indicating the highest resistivity among all samples. In this context, different parameters were determined through fitting with an equivalent circuit, including the electrical conductivity, as shown in Table 2. This behavior suggests limited charge carrier mobility and the absence of a well-defined conduction band, likely attributable to the highly crystalline nature of LLZO-SM. This occurs because the crystalline structure hinders lithium-ion transport by reducing vacancy availability and disrupting uniform ion distribution.[47,51]

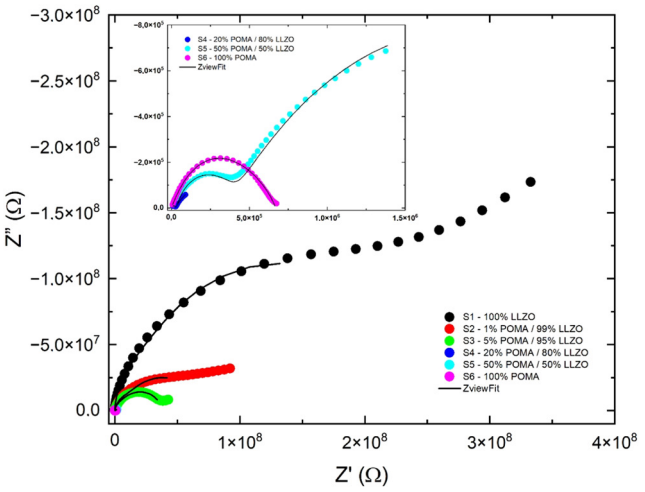


Figure 8. Comparative Cole−Cole diagram of samples S1 to S6 in tablet format measured at room temperature. The solid lines represent the adjustment derived from the employed circuit models.

The incorporation of POMA led to a decrease in the electrical resistance of the composites, as evidenced by the reduced diameter of the impedance semicircles. These improvements are attributed to the enhanced ionic transport facilitated by the amorphous regions introduced by POMA, which provide increased free volume and more flexible pathways for ion mobility. Furthermore, POMA improves grain boundary connectivity, leading to a significant enhancement in ionic conductivity. However, the crystalline domains of LLZO−SM still impose constraints on charge mobility, as evidenced by the persistence of semicircular features in the impedance spectra.

The most notable enhancement in electrical conductivity was observed at 20% POMA (S4), which is highlighted in Figure 9(b), where the semicircle diameter, corresponding to the electrical resistance, is the smallest. This composition achieves an optimal balance between crystalline and amorphous phases, reducing structural constraints while maintaining sufficient coordination sites for lithium-ion transport. The impedance data, supported by structural characterizations, suggest that the polymer chains disrupt crystallinity, creating pathways for ion conduction while preserving the contribution of LLZO−SM vacancies. Thus, these amorphous regions maximize the lithium-ion mobility as they form percolating networks while retaining the crystalline LLZO−SM domains for structural support, leading to peak ionic conductivity. This synergistic effect enhances ionic mobility, making S4 the most conductive composite in this study.

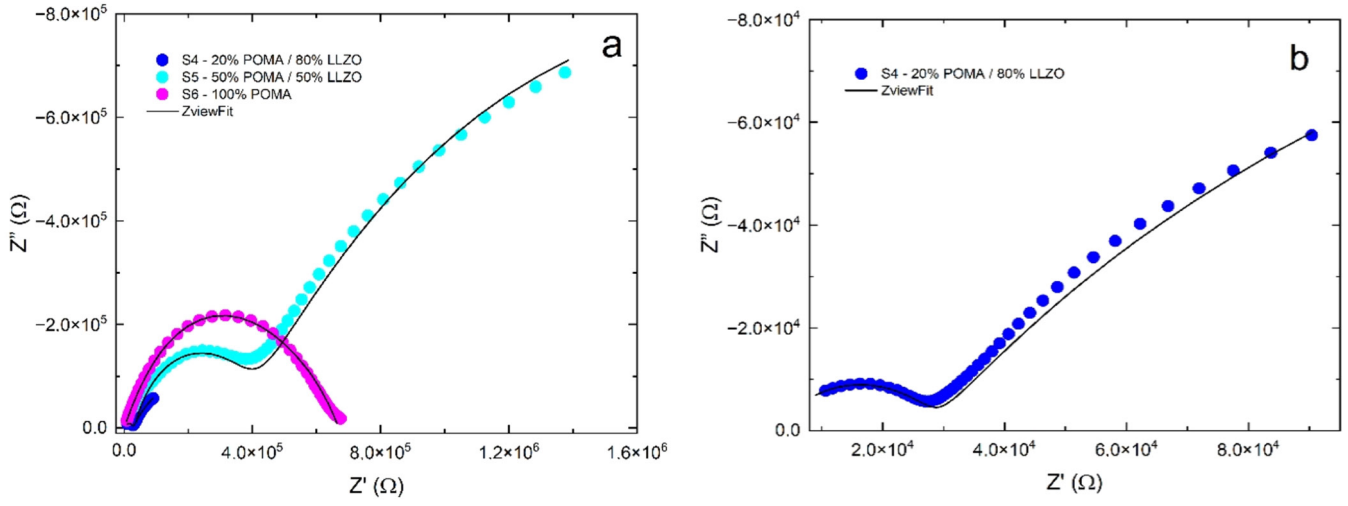


Figure 9. Room temperature Cole−Cole diagram of (a) S4 to S6 samples and (b) S4 in detail.

Downloaded from pubs.acs.org/jpccck/article-pdf/129/19/9127/4096144/jp5c00830.pdf by guest on 09 September 2026

https://doi.org/10.1021/acs.jpcc.5c00830
J. Phys. Chem. C 2025, 129, 9127−9139

Table 2. Parameters Obtained from the Equivalent Circuit Fitting of the Data for the LLZO−SM/POMA Composites

samples	$R1(\Omega)$	$R2$ (Ω)	C1(F)	$R3$ (Ω)	CPE1 (F)	σ (S/cm)
S1	-	2.14×10^{8}	4.89×10^{-12}	3.04×10^{7}	6.48×10^{-12}	1.60×10^{-9}
S2	-	8.13×10^{6}	6.92×10^{-12}	6.33×10^{7}	3.79×10^{-11}	4.07×10^{-8}
S3	-	3.39×10^{6}	8.13×10^{-12}	3.48×10^{7}	2.32×10^{-11}	1.14×10^{-7}
S4	3.22×10^{3}	2.47×10^{4}	5.48×10^{-10}	3.57×10^{5}	3.21×10^{-7}	1.60×10^{-5}
S5	3.19×10^{4}	3.48×10^{5}	2.01×10^{-10}	3.10×10^{6}	3.53×10^{-8}	1.42×10^{-6}
S6	-	1.51×10^{5}	1.58×10^{-10}	5.18×10^{5}	2.68×10^{-9}	5.06×10^{-6}

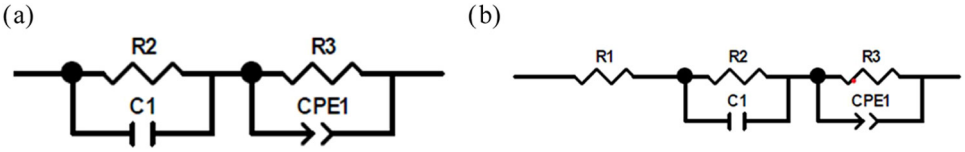


Figure 10. Equivalent electrical circuits used to fit the EIS data: (a) Circuit model used to describe the impedance response of samples S1, S2, S3, and S6; (b) Circuit model representing the electrical behavior of samples S4 and S5.

Table 3. Comparative Analysis of Synthesis Routes (SR) and Ionic Conductivity (σ) of Various LLZO/Polymer-Based Composites Reported in the Literature

composite	SR	σ (S/cm)	refs
$Li_{6.95}Mg_{0.15}La_{2.75}Sr_{0.25}Zr_2O_{12}$/20%POMA	sonochemical	1.15×10^{-5}	this work
PMMA/20%$LiClO_4$/10%$Li_{6.75}La_3Zr_{1.75}Nb_{0.25}O_{12}$	tape casting	2.2×10^{-5}	55
PAN/$LiClO_4$ and $Mg(ClO_4)_2$/$Li_{6.5}La_3Zr_{1.5}Ta_{0.5}O_{12}$	electrospinning	3.2×10^{-3}	56
PEO/LITFSI/10%LLZO	tape casting	2.39×10^{-4}	49
PEO/ANFs/$Li_7La_3Zr_2O_{12}$	solution casting method	1.36×10^{-3}	57
PEGMEA/TEGDA/LiTFSI$Li_{6.25}Ga_{0.25}La_3Zr_2O_{12}$	in situ radical polymerization	1.8×10^{-4}	58
PVDF/HFP/LiTFSI/10%LLZO	tape casting	9.5×10^{-4}	59

To deepen the understanding of the impedance behavior observed in the LLZO−SM/POMA composites, an equivalent circuit- modeling approach was employed. This complementary analysis allowed for a clearer interpretation of the electrical processes involved and the evolution of conduction mechanisms. The impedance spectra of the LLZO−SM/POMA composites were analyzed using equivalent circuit modeling, as shown in Figure 10. Two distinct circuit configurations were required to adequately describe the electrical response of the samples, depending on the POMA content. Samples S1, S2, S3, and S6 were best fitted using the model depicted in Figure 10(a), consisting of a resistor ($R2$) in parallel with a constant phase element (CPE1), preceded by a bulk capacitance ($C1$) and a resistor ($R3$) in parallel. This configuration reflects the dominance of bulk and interfacial processes in the absence of significant polymer phase continuity. On the other hand, samples S4 and S5, which contain intermediate concentrations of POMA, were better described by the circuit shown in Figure 10(b). This model includes an additional resistor ($R1$), attributed to the electrode/sample interface or surface resistance, as well as a third resistor ($R3$) associated with grain boundary effects. In both models, $R2$ represents the bulk resistance, $C1$ the bulk capacitance, and CPE1 captures the nonideal capacitive behavior at the interfaces. The evolution of these parameters across the sample series provides valuable insight into the role of POMA in modifying the ionic transport and dielectric properties of the LLZO-based composites.

Table 2 summarizes the parameters obtained from the equivalent circuit fitting of the data for the LLZO−SM/POMA composites. In all cases, the errors associated with the parameter determination were less than 5%. The evolution of the resistive and capacitive elements as a function of POMA content provides key insights into the role of the polymer phase in modulating ionic transport mechanisms. In the pure ceramic sample (S1), the bulk resistance ($R2$) is high ($\sim 2.14 \times 10^{8}$ Ω), indicating a highly resistive grain interior. As small amounts of POMA are introduced (S2 and S3), $R2$ decreases by 2 orders of magnitude, reaching 3.39×10^{6} Ω for S3. This reduction suggests that POMA incorporation enhances the connectivity within the grain regions, possibly due to improved lithium-ion mobility along the ceramic-polymer interface or increased defect concentration that facilitates charge transport. For S4 and S5, it was necessary to include an additional resistance element ($R1$) in the circuit. In S4, $R1$ is 3.22 x10^{3} Ω, and it increases to 3.19 x10^{4} Ω in S5. This behavior may be attributed to the formation of a resistive interfacial layer between the electrode and the sample, possibly due to surface enrichment of the polymer or less effective electrode contact in higher POMA-containing samples. A reduction is also observed in R3, which reflects the grain boundary resistance. From 3.04×10^{7} Ω in S1 to 3.57×10^{5} Ω in S4, this trend confirms the beneficial effect of POMA in reducing interfacial barriers and promoting lithium-ion transport across grain boundaries. The capacitance values ($C1$) increase progressively, from the picofarad range in S1−S3 to the nF range in S6 (1.58×10^{-10} F), suggesting a change in dielectric behavior due to the increased polymer content and potential interfacial polarization effects. This is consistent with the nature of conducting polymers, which tend to exhibit higher permittivity and increased polarizability.

The behavior of the constant phase element (CPE1) further reveals important information about the nonideal capacitive response at the interfaces. Its value increases significantly with POMA content, from 6.48×10^{-12} F in S1 to $\sim 10^{-7}$ to 10^{-9} F in S4−S6. This indicates the formation of heterogeneous or disordered interfaces, where ionic conduction may proceed

Downloaded from pubs.acs.org/jpccck/article-pdf/129/19/9127/4096144/jp5c00830.pdf by guest on 09 September 2026

https://doi.org/10.1021/acs.jpcc.5c00830
J. Phys. Chem. C 2025, 129, 9127−9139

through multiple parallel paths, leading to a dispersion of relaxation times. The sample with 20% POMA (S4) exhibits a good balance between low resistance ($R2$ and $R3$), high capacitance, and moderate interface complexity (CPE1), suggesting an optimal composition for potential application in solid-state lithium-ion batteries. In addition to the impedance-derived parameters, the ionic conductivity (σ) of the composites was calculated. The values presented in Table 3 show a clear trend: as the POMA content increases, the bulk resistance decreases significantly, resulting in a pronounced enhancement in ionic conductivity. Sample S4 (20% POMA) exhibited the highest ionic conductivity, reaching 1.60×10^{-5} S/cm, which is approximately 4 orders of magnitude higher than the conductivity of the pure LLZO sample (S1). This result highlights the synergistic effect between the ceramic and the polymer matrix, where POMA not only enhances the interfacial contact but also provides additional pathways for lithium-ion transport. While further increase in POMA content (S5 and S6) still maintains improved conductivity compared to the ceramic sample, a slight drop is observed, likely due to the excessive polymer phase hindering continuous conduction pathways or forming resistive domains.

Similar findings report peak conductivities for composites with optimal ceramic-polymer ratios, e.g., 1.6×10^{-5} S/cm for an 80% LLZO/20% polymer composite[S4] and 1.7×10^{-4} S/cm for a 75% ceramic composition.[18] However, increasing the POMA content to 50% (S5) led to a rise in resistance ($R2$) to 3.48×10^{5} Ω and a reduction in conductivity to 1.42×10^{-6} S/m. This behavior is likely due to the excessive amorphous content, which disrupts the structural balance, diminishing the contribution of crystalline LLZO−SM domains and introducing longer, less efficient pathways for lithium-ion transport. Additionally, the higher intrinsic resistivity of the POMA polymer at this concentration further reduces conductivity. This trend underscores that the electrical properties are optimized at 20% POMA, where the balance between crystalline and amorphous regions is ideal for efficient lithium-ion transport. Furthermore, the conductivity dropped to 5.06×10^{-6} S/cm for the pure POMA sample (S6). The absence of LLZO−SM in this composition limits conduction mechanisms to those intrinsic to POMA. The conductivity observed for this sample aligns with literature values for HCl-doped POMA materials, which ranges 5.18×10^{-7}−8.89×10^{-7} S/cm.[35] Factors such as polymer chain morphology, synthesis methods, and crystallinity significantly influence the conduction behavior of pure polymer samples.

The remarkable improvement in ionic conductivity observed in LLZO−SM/POMA composites up to 20% POMA is intrinsically linked to the interplay between their structural, chemical, and thermal properties. The incorporation of POMA introduces an amorphous phase into the highly crystalline LLZO−SM matrix, disrupting long-range order while enhancing the availability of free volume for ion transport. This disruption is evident from the attenuation of LLZO−SM's characteristic XRD peaks (Figure 4) and the emergence of polymer-specific bands in FTIR spectra (Figure 6), indicating a reduction in the density of energy barriers that impede lithium-ion mobility. Physically, this corresponds to an increased number of conduction pathways facilitated by the amorphous regions, where the absence of strict lattice constraints allows for greater ion hopping under an applied electric field. The interaction between the POMA chains and LLZO-SM introduces localized polar environments through functional groups such as $-OCH_3$ and C−N bonds, as revealed by FTIR (Figure 6). These groups enhance ionic dissociation by stabilizing Li^+ ions, thereby increasing the carrier concentration in the system. At the optimal POMA concentration of 20%, the balance between crystalline and amorphous domains maximizes the synergy between the fixed ionic sites provided by LLZO−SM and the flexible polymer matrix, forming a percolation network that supports continuous ion transport. This balance is critical; excessive polymer content beyond 20% disrupts the structural integrity of the LLZO−SM framework, reducing the density of coordination sites necessary for efficient conduction and increasing resistive pathways due to polymer aggregation. Furthermore, up to 20% POMA, the composite exhibits minimal mass loss and retains structural cohesion under thermal stress, as indicated by TGA results (Figure 5). The stability of the LLZO−SM framework ensures that the material's ionic vacancies remain functional over a wide temperature range, while the degradation of residual moisture and POMA chains at moderate temperatures reduces the risk of pore blockage or surface passivation. This thermal resilience, coupled with the increased disorder introduced by POMA, lowers the activation energy for lithium-ion migration, as evidenced by the substantial drop in impedance and the peak conductivity value of 1.6×10^{-5} S/cm for the 20% POMA composite. Thus, the improvement in ionic conductivity is a result of the optimal compromise between structural disorder, chemical interaction, and thermal stability. Structurally, the introduction of amorphous regions facilitates ion hopping; chemically, the stabilization of mobile ions enhances carrier density; and thermally, the system remains stable enough to sustain these effects. This multifaceted synergy underscores the importance of tuning the polymer-ceramic ratio to achieve maximal conductivity while maintaining the physical integrity of the composite. These findings offer critical insights into the fundamental mechanisms governing ionic transport in polymer-ceramic systems and their potential for next-generation energy storage technologies.

Therefore, the synthesis of LLZO/20%POMA composites through a sonochemical route has proven to be a highly effective method, achieving an ionic conductivity of 1.6×10^{-5} S/cm at room temperature. Compared to other synthesis techniques reported in the literature (Table 3), the sonochemical approach offers several advantages, including better dispersion of ceramic particles, reduced processing time, and scalability, which makes it suitable for industrial applications. When compared with composites such as PMMA/20%$LiClO_4$/10%$Li_{6.75}La_3Zr_{1.75}Nb_{0.25}O_{12}$ synthesized via tape casting ($\sigma = 2.2 \times 10^{-5}$ S/cm),[55] the ionic conductivity of our composite is slightly lower but still competitive. Notably, the enhanced thermal stability of the POMA-enriched composite compensates for the minor conductivity difference, addressing the brittleness of conventional ceramic-based composites. More complex methods, such as electrospinning for PAN/$LiClO_4$ and $Mg(ClO_4)_2$/$Li_{6.5}La_3Zr_{1.5}Ta_{0.5}O_{12}$, achieve significantly higher conductivity ($\sigma = 3.2 \times 10^{-3}$ S/cm).[56] However, these methods involve intricate procedures and require precise control over material properties, which could limit their scalability. Similarly, PEO/ANFs/$Li_7La_3Zr_2O_{12}$ prepared via solution casting offers high conductivity ($\sigma = 1.36 \times 10^{-3}$ S/cm),[57] but the thermal stability and processing requirements may not align with industrial-scale applications. In situ polymerization techniques, as seen in PEGMEA/TEGDA/LiTFSI$Li_{6.25}Ga_{0.25}La_3Zr_2O_{12}$

Downloaded from pubs.acs.org/jpccck/article-pdf/129/19/9127/4096144/jp5c00830.pdf by guest on 09 September 2026

https://doi.org/10.1021/acs.jpcc.5c00830
J. Phys. Chem. C 2025, 129, 9127−9139

composites, achieve a conductivity of 1.8×10^{-4} S/cm.[58] While effective, this method involves complex chemical reactions, which may introduce challenges in reproducibility and scalability. By contrast, the sonochemical synthesis employed in this study simplifies the fabrication process while maintaining competitive performance metrics. The comparison also highlights that tape casting methods for PEO/LiTFSI/10% LLZO ($\sigma = 2.39 \times 10^{-4}$ S/cm)[49] and PVDF/HFP/LiTFSI/10% LLZO ($\sigma = 9.5 \times 10^{-4}$ S/cm)[59] demonstrate higher conductivity levels than our LLZO/20% POMA composite. However, these systems face challenges related to polymer compatibility and the crystallinity of the polymer matrix, which may limit their long-term stability. Thus, our results demonstrate that LLZO/20%POMA synthesized via a sonochemical route not only achieves ionic conductivity comparable to other methods but also offers enhanced thermal stability. These attributes make it an attractive candidate for next-generation solid-state lithium-ion batteries, particularly for applications demanding a balance between performance, ease of fabrication, and cost-effectiveness. The synergy between POMA and LLZO in this composite system paves the way for further innovations in the development of solid-state electrolytes.

4. CONCLUSIONS

In summary, this study reports the successful development and characterization of LLZO−SM/POMA composites, integrating the ceramic's high ionic conductivity and structural robustness with the polymer's ionic transport enhancement. Optimizing the POMA content to 20% resulted in a composite with superior ionic conductivity (1.6×10^{-5} S/m) and thermal stability, surpassing pure LLZO−SM ceramic. The synergy between polymer and ceramic phases facilitates lithium-ion mobility via amorphous regions introduced by POMA, while maintaining the structural integrity of the LLZO−SM framework. XRD and FTIR analyses reveal progressive structural and chemical changes with increasing POMA content, where disrupted crystallinity improves ion transport. Thermal analysis confirms structural stability at moderate POMA levels, crucial for solid-state lithium-ion battery applications. SEM observations highlight morphological changes that enhance ion conduction pathways, particularly at the optimal 20% POMA composition. These results illuminate the mechanisms behind ionic transport in polymer-ceramic composites and provide a foundation for designing solid electrolytes for next-generation energy storage systems. By tailoring composite properties, our work addresses challenges in lithium-ion battery technology, such as improved safety, extended cycle life, and higher energy density. Scaling up synthesis, evaluating performance in practical cells, and investigating long-term stability under operational conditions are recommended for future studies. Exploring alternative dopants and polymers could further enhance ionic and mechanical properties, broadening the composites' applicability in solid-state energy storage. The insights gained here have immense potential to accelerate the adoption of sustainable and high-performance battery technologies.

AUTHOR INFORMATION

Corresponding Author

Yurimiler Leyet Ruiz − *Departamento de Engenharia de Materiais, Universidade Federal do Amazonas, Manaus, Amazonas 69080-900, Brazil; Instituto de Desenvolvimento Tecnológico, Manaus, Amazonas 69044-235, Brazil;* orcid.org/0000-0002-5774-5391; Email: yurileyet@yahoo.es

Authors

José Victor Garcia Milério − *Departamento de Engenharia de Materiais, Universidade Federal do Amazonas, Manaus, Amazonas 69080-900, Brazil; Instituto de Desenvolvimento Tecnológico, Manaus, Amazonas 69044-235, Brazil*

Jardson Braz da Silva − *Departamento de Engenharia de Materiais, Universidade Federal do Amazonas, Manaus, Amazonas 69080-900, Brazil; Departamento de Física de Materiais, Universidade Federal do Amazonas, Manaus, Amazonas 69080-900, Brazil*

Francisco Xavier Nobre − *Departamento de Química, Alimentos e Meio Ambiente (DQA), Instituto Federal de Educação, Ciência e Tecnologia do Amazonas, Campus Manaus Centro (CMC), Manaus, Amazonas 69020-120, Brazil*

Rannier Marques Mendonça − *Departamento de Engenharia de Materiais, Universidade Federal do Amazonas, Manaus, Amazonas 69080-900, Brazil*

Marcus Valerio Botelho do Nascimento − *Instituto de Desenvolvimento Tecnológico, Manaus, Amazonas 69044-235, Brazil;* orcid.org/0000-0002-5376-5643

Eduardo Antonelli − *Department of Science and Technology, Polymer and Biopolymer Technology Laboratory (TecPBio), Federal University of São Paulo (UNIFESP), São José dos Campos, SP 12231-280, Brazil*

Monica Tirado − *Universidad Nacional de Tucumán (UNT), Facultad de Ciencias Exactas y Tecnología (FACET) and Instituto de Física del Noroeste Argentino: INFINOA (UNT-CONICET), CP 4000 Tucumán, Argentina*

Robert Saraiva Matos − *Amazonian Materials Group, Federal University of Amapá (UNIFAP), Macapá, AP 68900-000, Brazil;* orcid.org/0000-0002-1219-8646

Henrique Duarte da Fonseca Filho − *Instituto de Desenvolvimento Tecnológico, Manaus, Amazonas 69044-235, Brazil;* orcid.org/0000-0001-9811-6391

Lianet Aguilera Dominguez − *Departamento de Engenharia de Materiais, Universidade Federal do Amazonas, Manaus, Amazonas 69080-900, Brazil*

Complete contact information is available at: https://pubs.acs.org/10.1021/acs.jpcc.5c00830

Author Contributions

All authors have equally contributed to this manuscript.

Funding

The Article Processing Charge for the publication of this research was funded by the Coordenacao de Aperfeicoamento de Pessoal de Nivel Superior (CAPES), Brazil (ROR identifier: 00x0ma614).

Notes

The authors declare no competing financial interest.

ACKNOWLEDGMENTS

This study was financed in part by the "Coordenação de Aperfeiçoamento de Pessoal de Nível Superior—Brasil (CAPES)"—Finance Code 001. The authors would like to thank "Fundação de Amparo à Pesquisa do Estado do Amazonas" and "Conselho Nacional de Desenvolvimento Científico e Tecnológico" for their financial support.

Downloaded from pubs.acs.org/jpccck/article-pdf/129/19/9127/4096144/jp5c00830.pdf by guest on 09 September 2026

REFERENCES

(1) Wu, D.; Chen, L.; Li, H.; Wu, F. Solid-State Lithium Batteries-from Fundamental Research to Industrial Progress. *Prog. Mater. Sci.* **2023**, *139*, No. 101182.

(2) Ma, J.; Li, Y.; Grundish, N. S.; Goodenough, J. B.; Chen, Y.; Guo, L.; Peng, Z.; Qi, X.; Yang, F.; Qie, L.; Wang, C.-A.; et al. The 2021 Battery Technology Roadmap. *J. Phys. D: Appl. Phys.* **2021**, *54* (18), No. 183001.

(3) Langer, F.; Bardenhagen, I.; Glenneberg, J.; Kun, R. Microstructure and Temperature Dependent Lithium Ion Transport of Ceramic−Polymer Composite Electrolyte for Solid-State Lithium Ion Batteries Based on Garnet-Type Li7La3Zr2O12. *Solid State Ionics* **2016**, *291*, 8−13.

(4) Li, Z.; Huang, H.-M.; Zhu, J.-K.; Wu, J.-F.; Yang, H.; Wei, L.; Guo, X. Ionic Conduction in Composite Polymer Electrolytes: Case of PEO:Ga-LLZO Composites. *ACS Appl. Mater. Interfaces* **2019**, *11* (1), 784−791.

(5) Fan, L.; Wei, S.; Li, S.; Li, Q.; Lu, Y. Recent Progress of the Solid-State Electrolytes for High-Energy Metal-Based Batteries. *Adv. Energy Mater.* **2018**, *8* (11), No. 1702657.

(6) Lu, W.; Xue, M.; Zhang, C. Modified Li7La3Zr2O12 (LLZO) and LLZO-Polymer Composites for Solid-State Lithium Batteries. *Energy Storage Mater.* **2021**, *39*, 108−129.

(7) Zhu, X.; Wang, K.; Xu, Y.; Zhang, G.; Li, S.; Li, C.; Zhang, X.; Sun, X.; Ge, X.; Ma, Y. Strategies to Boost Ionic Conductivity and Interface Compatibility of Inorganic - Organic Solid Composite Electrolytes. *Energy Storage Mater.* **2021**, *36*, 291−308.

(8) Wu, F.; Zhang, K.; Liu, Y.; Gao, H.; Bai, Y.; Wang, X.; Wu, C. Polymer Electrolytes and Interfaces toward Solid-State Batteries: Recent Advances and Prospects. *Energy Storage Mater.* **2020**, *33*, 26−54.

(9) Sheng, O.; Jin, C.; Ding, X.; Liu, T.; Wan, Y.; Liu, Y.; Nai, J.; Wang, Y.; Liu, C.; Tao, X. A Decade of Progress on Solid-State Electrolytes for Secondary Batteries: Advances and Contributions. *Adv. Funct. Mater.* **2021**, *31* (27), No. 2100891.

(10) Deng, S.; Zhu, H.; Zheng, Z.; Kong, Z.; Wang, Z.; Zhou, W.; Tang, R.; Wu, J.-F.; Liu, J. Synergistically Engineering Grains and Grain Boundaries toward Li Dendrite-Free Li 7 La 3 Zr 2 O 12. *Nano Lett.* **2024**, *24* (32), 9801−9807.

(11) Nasir, M.; Park, J. Y.; Heo, P.; Choi, K. H.; Park, H. J. Li-La-Zr-O Garnets with High Li-Ion Conductivity and Air-Stability by Microstructure-Engineering. *Adv. Funct. Mater.* **2023**, *33* (35), No. 2303397, DOI: 10.1002/adfm.202303397.

(12) Wang, Y.; Chen, Z.; Jiang, K.; Shen, Z.; Passerini, S.; Chen, M. Accelerating the Development of LLZO in Solid-State Batteries Toward Commercialization: A Comprehensive Review. *Small* **2024**, *20* (35), No. 2402035.

(13) Kravchyk, K. V.; Kovalenko, M. V. Perspective on Design and Technical Challenges of Li-Garnet Solid-State Batteries. *Sci. Technol. Adv. Mater.* **2022**, *23* (1), 41−48.

(14) Gonçalves, R.; Tozzi, K. A.; Pereira, E. C. Electroactive Polymers for Batteries. In *Electroactive Polymeric Materials*; CRC Press: New York, 2022; pp 203−218.

(15) Yu, X.; Manthiram, A. A Review of Composite Polymer-Ceramic Electrolytes for Lithium Batteries. *Energy Storage Mater.* **2021**, *34*, 282−300.

(16) Menkin, S.; Lifshitz, M.; Haimovich, A.; Goor, M.; Blanga, R.; Greenbaum, S. G.; Goldbourt, A.; Golodnitsky, D. Evaluation of Ion-Transport in Composite Polymer-in-Ceramic Electrolytes. Case Study of Active and Inert Ceramics. *Electrochim. Acta* **2019**, *304*, 447−455.

(17) Jiang, H.; Wu, Y.; Ma, J.; Liu, Y.; Wang, L.; Yao, X.; Xiang, H. Ultrathin Polymer-in-Ceramic and Ceramic-in-Polymer Bilayer Composite Solid Electrolyte Membrane for High-Voltage Lithium Metal Batteries. *J. Membr. Sci.* **2021**, *640*, No. 119840.

(18) Zhang, B.; Liu, Y.; Liu, J.; Sun, L.; Cong, L.; Fu, F.; Mauger, A.; Julien, C. M.; Xie, H.; Pan, X. "Polymer-in-Ceramic" Based Poly(ε-Caprolactone)/Ceramic Composite Electrolyte for All-Solid-State Batteries. *J. Energy Chem.* **2021**, *52*, 318−325.

(19) Luo, Y.; Dong, J.; Wang, Y.; Wang, Z.; Chen, Z.; Zhang, H. Enhanced Electrochemical Performance of Garnet Li7La3Zr2O12 Electrolyte by Efficient Incorporation of LiCl. *Ceram. Int.* **2024**, *50* (23), 51055−51064.

(20) Li, S.; Zhang, S.; Shen, L.; Liu, Q.; Ma, J.; Lv, W.; He, Y.; Yang, Q. Progress and Perspective of Ceramic/Polymer Composite Solid Electrolytes for Lithium Batteries. *Adv. Sci.* **2020**, *7* (5), No. 1903088.

(21) Chan, C. K.; Yang, T.; Mark Weller, J. Nanostructured Garnet-Type Li7La3Zr2O12: Synthesis, Properties, and Opportunities as Electrolytes for Li-Ion Batteries. *Electrochim. Acta* **2017**, *253*, 268−280.

(22) Seo, J.-H.; Nakaya, H.; Takeuchi, Y.; Fan, Z.; Hikosaka, H.; Rajagopalan, R.; Gomez, E. D.; Iwasaki, M.; Randall, C. A. Broad Temperature Dependence, High Conductivity, and Structure-Property Relations of Cold Sintering of LLZO-Based Composite Electrolytes. *J. Eur. Ceram. Soc.* **2020**, *40* (15), 6241−6248.

(23) Dang, M.-Z.; Rancourt, D. G.; Dutrizac, J. E.; Lamarche, G.; Provencher, R. Interplay of Surface Conditions, Particle Size, Stoichiometry, Cell Parameters, and Magnetism in Synthetic Hematite-like Materials. *Hyperfine Interact.* **1998**, *117* (1), 271−319.

(24) Zhang, Q.; Liu, K.; Wen, Y.; Kong, Y.; Wen, Y.; Zhang, Q.; Liu, N.; Li, J.; Ma, C.; Du, Y. Advances in Solid Lithium Ion Electrolyte Based on the Composites of Polymer and LLTO/LLZO of Rare Earth Oxides. *Eng. Rep.* **2022**, *4* (1), No. e12448.

(25) Thompson, T.; Yu, S.; Williams, L.; Schmidt, R. D.; Garcia-Mendez, R.; Wolfenstine, J.; Allen, J. L.; Kioupakis, E.; Siegel, D. J.; Sakamoto, J. Electrochemical Window of the Li-Ion Solid Electrolyte Li 7 La 3 Zr 2 O 12. *ACS Energy Lett.* **2017**, *2* (2), 462−468.

(26) Raju, M. M.; Altayran, F.; Johnson, M.; Wang, D.; Zhang, Q. Crystal Structure and Preparation of Li7La3Zr2O12 (LLZO) Solid-State Electrolyte and Doping Impacts on the Conductivity: An Overview. *Electrochem* **2021**, *2* (3), 390−414.

(27) Alam, T.; Das, A. Review on Impurity and Conductivity Issues of Garnet Type Li 7 La 3 Zr 2 O 12 : Mechanisms, Solutions, and Perspectives. *Energy Fuels* **2023**, *37* (20), 15267−15282.

(28) Il'ina, E. Recent Strategies for Lithium-Ion Conductivity Improvement in Li7La3Zr2O12 Solid Electrolytes. *Int. J. Mol. Sci.* **2023**, *24* (16), No. 12905.

(29) Abraham, K. M.; Jiang, Z.; Carroll, B. Highly Conductive PEO-like Polymer Electrolytes. *Chem. Mater.* **1997**, *9* (9), 1978−1988.

(30) Wang, Y.; Liu, T.; Liu, C.; Liu, G.; Yu, J.; Zou, Q. Solid-State Lithium Battery with Garnet Li7La3Zr2O12 Nanofibers Composite Polymer Electrolytes. *Solid State Ionics* **2022**, *378*, No. 115897.

(31) da Silva, J. P.; Biondo, M. M.; Nobre, F. X.; Anglada-Rivera, J.; Almeida, A.; Agostinho-Moreira, J.; Sanches, E. A.; da, M. M.; Aguilera, L.; Leyet, Y. Structure and Electrical Properties of the Composite Na2Ti3O7/ Na2Ti6O13/POMA: A Study of the Effect of Adding POMA. *J. Alloys Compd.* **2021**, *867*, No. 159025, DOI: 10.1016/j.jallcom.2021.159025.

(32) Kim, H.-K.; Barai, P.; Chavan, K.; Srinivasan, V. Transport and Mechanical Behavior in PEO-LLZO Composite Electrolytes. *J. Solid State Electrochem.* **2022**, *26* (9), 2059−2075.

(33) Yao, Z.; Qi, F.; Ye, L.; Sun, Q.; Gu, X.; Yang, X.; Zhu, K. Composite Polymer Electrolyte Based on Poly(Vinylidene Fluoride-Hexafluoropropylene) (PVDF-HFP) for Solid-State Batteries. *Heliyon* **2024**, *10* (6), No. e28097.

(34) Coutinho, L. S. Avaliação Do Processo de Sinterização a Frio Nas Propriedades Físicas e Elétricas de Materiais Cerâmicos: ZnO, ZnO/BaTiO3 e Li7La3Zr2O12 Dopado Com Sr e Mg, Ph.D. Thesis; Universidade Federal de São Paulo, 2023.

(35) Sanches, E. A.; Soares, J. C.; Mafud, A. C.; Trovati, G.; Fernandes, E. G.; Mascarenhas, Y. P. Structural and Morphological Characterization of Chloride Salt of Conducting Poly(o-Methoxyaniline) Obtained at Different Time Synthesis. *J. Mol. Struct.* **2013**, *1039*, 167−173.

(36) Biondo, M. M.; de Oliveira, L. M.; Lima, S. X.; Carolino, A.; de, S.; Rocha, A. L. F.; da Silva, J. P.; Ruiz, Y. L.; Giacon, V. M.; Campelo, P. H.; Sanches, E. A. Chemically Synthesized Poly(o-Methoxyani-

Downloaded from pubs.acs.org/jpccck/article-pdf/129/19/9127/4096144/jp5c00830.pdf by guest on 09 September 2026

https://doi.org/10.1021/acs.jpcc.5c00830
J. Phys. Chem. C 2025, 129, 9127−9139

line): Influence of Counterions on the Structural and Electrical Properties. *J. Mol. Struct.* **2020**, *1205*, No. 127588.
(37) Chen, F.; Yang, D.; Zha, W.; Zhu, B.; Zhang, Y.; Li, J.; Gu, Y.; Shen, Q.; Zhang, L.; Sadoway, D. R. Solid Polymer Electrolytes Incorporating Cubic Li7La3Zr2O12 for All-Solid-State Lithium Rechargeable Batteries. *Electrochim. Acta* **2017**, *258*, 1106−1114.
(38) Liu, W.-J.; Chang, Y.-H.; Hsu, S.-T.; Fern, C.-L.; Chen, Y.-T.; Tsao, S.-Y.; Lin, S.-H. Exploring the Correlation Between Surface Roughness, Surface Energy, Nano-Indentation, Electrical Properties, and Magnetic Characteristics of Annealed Co40Fe40Dy20 Thin Films Deposited on Si(100) Substrates. *J. Electron. Mater.* **2024**, *53* (8), 4498−4511.
(39) Costa, S. D. S.; da Silva, J. P.; Biondo, M. M.; Sanches, E. A.; Da Silva Paula, M. M.; Nobre, F. X.; Rivera, J. A.; Zulueta, Y. A.; Torikachvili, M. S.; Sampaio, D. V.; et al. Temperature Dependence of the Electrical Properties of Na2Ti3O7/Na2Ti6O13/POMA Composites. *Molecules* **2022**, *27* (18), No. 5756.
(40) da Silva, J. P.; Costa, S.; Nobre, F. X.; Sanches, E. A.; Paula, M. M.; da, S.; Aguilera, L.; Torikachvili, M. S.; Leyet, Y. Poly(o-Methoxyaniline) Modified by the Biphasic Ceramic System Na2Ti3O7/ Na2Ti6O13. *J. Inorg. Organomet. Polym. Mater.* **2023**, *33* (5), 1381−1387.
(41) Li, J.; Liu, Z.; Ma, W.; Dong, H.; Zhang, K.; Wang, R. Low-Temperature Synthesis of Cubic Phase Li7La3Zr2O12 via Sol-Gel and Ball Milling Induced Phase Transition. *J. Power Sources* **2019**, *412*, 189−196.
(42) Parascos, K.; Watts, J. L.; Alarco, J. A.; Chen, Y.; Talbot, P. C. Compositional and Structural Control in LLZO Solid Electrolytes. *RSC Adv.* **2022**, *12* (36), 23466−23480.
(43) Yow, Z. F.; Oh, Y. L.; Gu, W.; Rao, R. P.; Adams, S. Effect of Li +/H+ Exchange in Water Treated Ta-Doped Li7La3Zr2O12. *Solid State Ionics* **2016**, *292*, 122−129.
(44) Lin, C.; Huang, Y.; Deng, D.; Xiong, H.; Lu, B.; Weng, J.; Fan, X.; Li, G.; Zeng, Y.; Li, Y.; Wu, Q. Application of Li6.4La3Zr1.45-Ta0.5Mo0.05O12/PEO Composite Solid Electrolyte in High-Performance Lithium Batteries. *Materials* **2024**, *17* (13), No. 3094.
(45) Ghosh, K.; Wasim Raja, M. Engineered Li 7 La 3 Zr 2 O 12 (LLZO) for Pseudo-Solid-State Lithium Metal Batteries (SSLMBs): Tailor-Made Synthesis, Evolution of the Microstructure, Suppression of Dendritic Growth, and Enhanced Electrochemical Performance. *ACS Appl. Energy Mater.* **2023**, *6* (7), 4035−4052.
(46) Xu, F.; Jamal, R.; Ubul, A.; Shao, W.; Abdiryim, T. Characterization and Electrochemical Properties of Poly(Aniline-Co-o-Methoxyaniline)/Multi-Walled Carbon Nanotubes Composites Synthesized by Solid-State Method. *Fibers Polym.* **2013**, *14* (1), 8−15.
(47) Park, J.-Y.; Park, J.-W.; Doh, C.-H.; Ha, Y.-C.; Lee, S.-M.; Kim, S. Effect of Solvated Ionic Liquids on the Ion Conducting Property of Composite Membranes for Lithium Ion Batteries. *Res. Chem. Intermed.* **2018**, *44* (10), 6039−6051.
(48) Mukherjee, S.; Dönni, A.; Nakajima, T.; Mitsuda, S.; Tachibana, M.; Kitazawa, H.; Pomjakushin, V.; Keller, L.; Niedermayer, C.; Scaramucci, A.; Kenzelmann, M. E-Type Noncollinear Magnetic Ordering in Multiferroic o-LuMnO3. *Phys. Rev. B* **2017**, *95* (10), No. 104412.
(49) Wan, Z.; Lei, D.; Yang, W.; Liu, C.; Shi, K.; Hao, X.; Shen, L.; Lv, W.; Li, B.; Yang, Q.; et al. Low Resistance−Integrated All-Solid-State Battery Achieved by Li 7 La 3 Zr 2 O 12 Nanowire Upgrading Polyethylene Oxide (PEO) Composite Electrolyte and PEO Cathode Binder. *Adv. Funct. Mater.* **2019**, *29* (1), No. 1805301.
(50) Xu, Z.; Hu, X.; Fu, B.; Khan, K.; Wu, J.; Li, T.; Zhou, H.; Fang, Z.; Wu, M. Co-Doping Strategy Enhanced the Ionic Conductivity and Excellent Lithium Stability of Garnet-Type Li7La3Zr2O12 Electrolyte in All Solid-State Lithium Batteries. *J. Mater.* **2023**, *9* (4), 651−660.
(51) Zheng, J.; Tang, M.; Hu, Y. Lithium Ion Pathway within Li 7 La 3 Zr 2 O 12 -Polyethylene Oxide Composite Electrolytes. *Angew. Chem., Int. Ed.* **2016**, *55* (40), 12538−12542.
(52) Wang, X.; Ray, S.; Cooney, R. P.; Kilmartin, P. A.; Waterhouse, G. I. N.; Easteal, A. J. Synthesis and Characterization of Poly(o-Methoxyaniline)−Lignosulfonate Composites. *Synth. Met.* **2012**, *162* (13−14), 1084−1089.
(53) Das, A. K.; Badole, M.; Vasavan, H. N.; Saxena, S.; Gami, P.; Kumar, S. Highly Conductive Ceramic-in-Polymer Composite Electrolyte Enabling Superior Electrochemical Performance for All-Solid-State Lithium Batteries. *Ceram. Int.* **2023**, *49* (18), 29719−29728.
(54) Nkosi, F. P.; Valvo, M.; Mindemark, J.; Dzulkurnain, N. A.; Hernández, G.; Mahun, A.; Abbrent, S.; Brus, J.; Kobera, L.; Edström, K. Garnet-Poly(ε-Caprolactone- Co -Trimethylene Carbonate) Polymer-in-Ceramic Composite Electrolyte for All-Solid-State Lithium-Ion Batteries. *ACS Appl. Energy Mater.* **2021**, *4* (3), 2531−2542.
(55) Sun, J.; Li, Y.; Zhang, Q.; Hou, C.; Shi, Q.; Wang, H. A Highly Ionic Conductive Poly(Methyl Methacrylate) Composite Electrolyte with Garnet-Typed Li6.75La3Zr1.75Nb0.25O12 Nanowires. *Chem. Eng. J.* **2019**, *375*, No. 121922.
(56) Qiu, G.; Sun, C. A Quasi-Solid Composite Electrolyte with Dual Salts for Dendrite-Free Lithium Metal Batteries. *New J. Chem.* **2020**, *44* (5), 1817−1824.
(57) Yin, J.; Xu, X.; Jiang, S.; Wu, H.; Wei, L.; Li, Y.; He, J.; Xi, K.; Gao, Y. High Ionic Conductivity PEO-Based Electrolyte with 3D Framework for Dendrite-Free Solid-State Lithium Metal Batteries at Ambient Temperature. *Chem. Eng. J.* **2022**, *431*, No. 133352.
(58) Li, Z.; Xie, H.-X.; Zhang, X.-Y.; Guo, X. In Situ Thermally Polymerized Solid Composite Electrolytes with a Broad Electrochemical Window for All-Solid-State Lithium Metal Batteries. *J. Mater. Chem. A* **2020**, *8* (7), 3892−3900.
(59) Li, Y.; Zhang, W.; Dou, Q.; Wong, K. W.; Ng, K. M. Li 7 La 3 Zr 2 O 12 Ceramic Nanofiber-Incorporated Composite Polymer Electrolytes for Lithium Metal Batteries. *J. Mater. Chem. A* **2019**, *7* (7), 3391−3398.

Downloaded from pubs.acs.org/jpccck/article-pdf/129/19/9127/4096144/jp5c00830.pdf by guest on 09 September 2026

https://doi.org/10.1021/acs.jpcc.5c00830
J. Phys. Chem. C 2025, 129, 9127−9139